

For New Technology Network

NTN®

TECHNICAL REVIEW

No.
75

**Special Issue;
Automotive Environmental
Technologies**

October 2007

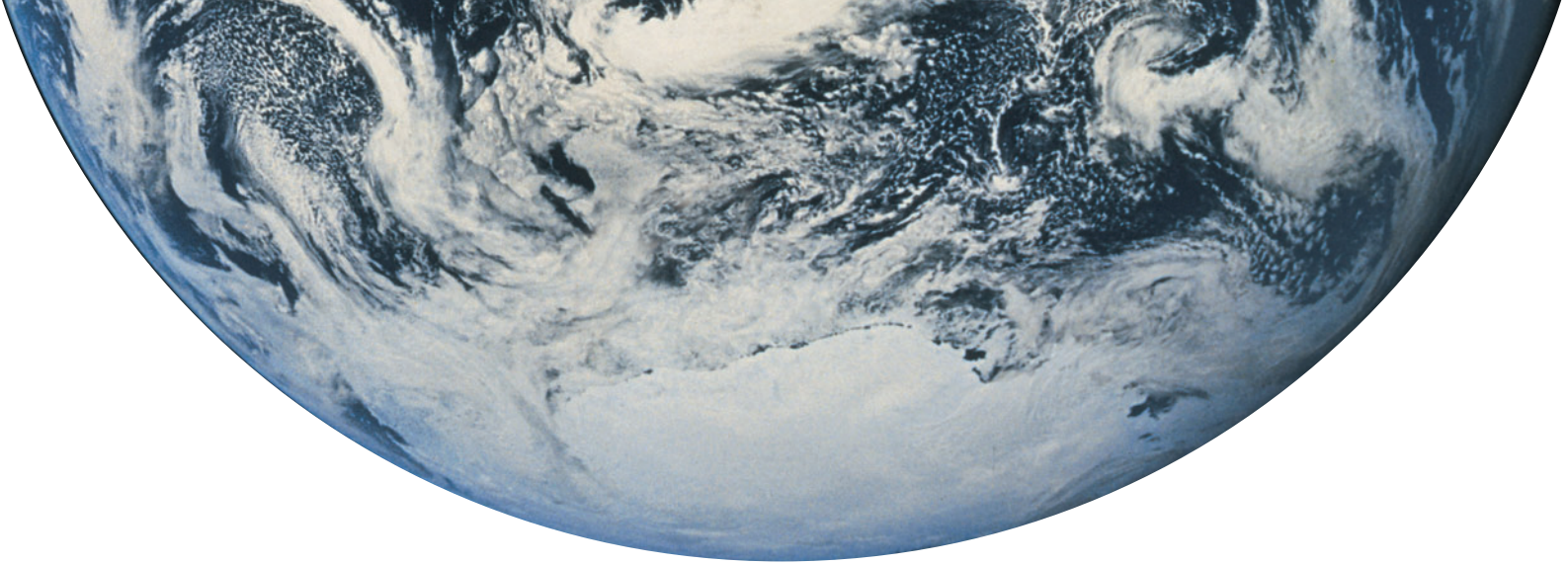


Weight reduction is one of the most important contributors to better handling and fuel economy. Cost, performance and durability in a variety of environments are equally important qualities.

NTN recognizes that achieving the optimal balance among all these conflicting requirements is the most successful approach.

To ensure our quality of life, it is essential that we maintain a high regard for the environment. We will continue to remain aware of the environmental influence of the automobile. NTN is working to create a better society with products that contribute to more efficient driving and greater fuel economy.

ISSN 0915-0528 OSAKA, JAPAN



NTN Bearings Turning our World “Blue”

Bearings are the “eco products” that reduce energy loss from rotating parts in all types of machinery from household appliances, medical equipment, and machine tools, to automobiles, trains, and aircraft.

At NTN, we are actively involved in an “eco” approach throughout the bearing manufacturing process, such as eliminating the use of hazardous substances, using clean natural energy, reducing CO₂ emission, and thoroughly recycling on a global level.

For a symbiotic relationship between humankind and the global environment, NTN continues to pursue the possibilities in “MONOZUKURI*” for the future.

*MONOZUKURI: A comprehensive concept of creating value throughout NTN's entire business process



NTN Blue = Ecology Blue

NTN®

www.ntn.co.jp





TECHNICAL REVIEW

No.75

Special Issue ● Automotive Environmental
Technologies

NTN TECHNICAL REVIEW No.75

CONTENTS

Preface

Kenji OKADA 1

Contribution

Saving Energy with Motor Vehicle Transmission Technologies

Haruo HOUJOH TOKYO INSTITUTE OF TECHNOLOGY Precision and Intelligence Laboratory

2

Driveline

Technical Trends in Constant Velocity Universal Joints and the Development of Related Products Shin TOMOGAMI	10
Fixed Constant Velocity Joint with a Super High Operating Angle of 54 Degrees (TUJ) Manabu HOSHINO and Masashi FUNAHASHI	16
Measurement of the Internal Forces of Ball Fixed Constant Velocity Joints Daiji OKAMOTO and Hirokazu OOBA	20
Technical Trends in Axle Bearings and the Development of Related Products Kiyotake SHIBATA and Takayuki NORIMATSU	29
Development of High Resolution Sensor Element MPS40S and Dual Track Magnetic Encoder for Rotational Speed and Position Measurement Pascal DESBIOLLES and Achim FRIZ	36
Tube Forming Simulation in a Generation 4 Hub joint Akitoshi IMOU and Takehiro TAKANO	42
Development of an In-Wheel Motor Axle Unit Minoru SUZUKI, Kayo SAKAI, Koichi OKADA and Yusuke MAKINO	46
Development of an Electromechanical Brake Tatsuya YAMASAKI, Masaaki EGUCHI and Yusuke MAKINO	53

Engine & Transmission

Engine Part Technical Trends and New Engine Products Yoshiaki RYOUNO, Kouichi ONIMARU, Kenichi KAWABATA and Shinji OOISHI	62
Ball-screw Unit for Variable Valve Event and Lift System Keisuke KAZUNO	72
Development of an End-Pivot Type Mechanical Lash Adjuster Eiji MAENO, Hiroshi BUNKO and Katsuhisa YAMAGUCHI	78
Transmission Technology Trends and Product Developments Takahiro KANAMOTO, Takashi UENO, Akihiko KATAYAMA and Masanori SATOU	86
Dynamic Analysis for Needle Roller Bearings Under Planetary Motion Tomoya SAKAGUCHI	94
Micro HL Tapered Roller Bearing Takashi UENO	100
High Speed Thrust Needle Roller Bearings Kosuke OBAYASHI	105

Accessory

Accessory Technology Trends and Product Developments Ikuo FUJINIWA, Makoto MURAMATSU and Tadahisa TANAKA	110
Development of NA103A Long-life Grease for Automotive Components Takayuki KAWAMURA and Hidenobu MIKAMI	116
Compact Clutch Integrated Pulley for Alternators Koji SATO and Isao MIKURIYA	124

Our Line of Award Winning Products

Society of Tribologists & Lubrication Engineers Captain Alfred E.Hunt Award Crack Propagation of Rolling Contact Fatigue in Ball Bearing Steel Due to Tensile Strain Noriyuki TSUSHIMA	128
JSME Young Engineers Award Logarithmic Profile of Rollers in Roller Bearings and Optimization of the Profiles Hiroki FUJIWARA and Tatsuo KAWASE	140
The 2005 Most Interesting Reading Award by Japan Society for Design Engineering Run-out Analysis for Rolling Element Bearing Tomoya SAKAGUCHI	149
Monodzukuri Manufacturing Award A prize for encouragement Improving Rolling Contact Fatigue Life of Bearing Steels Through Grain Refinement "Development of the FA bearing" Chikara OHKI	150
12th Advanced Display of the Year 2007(ADY) Excellent prize winning LCD Color Filter Repair System "NRS-3000 Series" Akihiro YAMANAKA	151

Our Line of New Products

152

Introduction to this Special Feature Issue –

About the 75th NTN Technical Review, Which Features NTN's Unique Eco-Conscious Automotive Technologies

Kenji OKADA
Executive Director



The targeted reduction in greenhouse gas emissions assigned to Japan according to “the Kyoto Protocol to the United Nations treaty on climate change” in effect in February 2005, is 6% decrease relative to the year 1990 level. Regrettably, the 2003 emission in Japan marked 8% increase over the 1990 level, rather than a decrease—many knowledgeable people are not confident about the fulfillment of this target. At the same time, global warming has been ever worsening, the evidences of which include damages inflicted by super-hurricanes in the U.S.; inundation in the U.K.; and an unprecedented long spell of very hot summer in this year in Japan—various regions in Japan experienced a record-high number of days above -30°C causing many Japanese to assert that “we are experiencing an abnormal summer”. The global environment is damaged to such an extent that our daily lives are increasingly jeopardized.

Automobiles are responsible for approximately 20% of CO₂ emissions in Japan (-FY2004 data). As more automobiles are sold in the BRICs and newly burgeoning markets, the total number of cars manufactured throughout the world in 2006 nearly reached 70 million. On the other hand, a series of global regulations for mitigating environmental impacts have been proposed, and the examples of which include “Establishment of 2015 fuel economy standard in Japan” and “CO₂ emissions control in Europe”. To address this situation, development work for various eco-conscious automotive technologies are in progress and will be further accelerated. Examples of these technologies include hybrid cars, ethanol cars, diesel cars and electric vehicles.

The Japanese version of this review featuring NTN's latest eco-conscious automotive technologies was issued, intended for presentation in the 40th Tokyo Motor Show that began on October 26 and ended on November 11. The main part of this review begins with a contribution titled “Saving Energy with Transmission Technology for a Motor Vehicle” from Professor Haruo HOUJOH, TOKYO INSTITUTE OF TECHNOLOGY, who is known as an authority in the research of automotive transmission system dynamics. Then our automobile-related technologies are presented in three application fields—<Drive line>, <Engine & transmission> and <Electrical equipment & auxiliaries>., wherein each section contains information about trends in eco-conscious engineering development efforts and an introduction to NTN's eco-friendly products and technologies.

In this review, our new engineering developments are categorized into three engineering fields: the “electric drive system” section presents an in-wheel motor unit and an electric brake unit; the “compact & light-weight technology” provides a pulley assembly for alternator w/ built-in compact clutch; and the “long service life technology” section offers knowledge about micro HL conical roller bearings and long-life grease for electrical auxiliary bearings.

The review presents various new technologies. The “sensor” section describes a technology for a high resolution velocity & position sensor; the “analysis” section offers examples of analysis that include dynamic analysis on bearings under planetary motion and analysis on internally working forces with constant velocity joints.

The review also includes information about NTN's five award winning technologies for FY2006 (STLE 2006 Captain Alfred E. Hunt Award, “Crack Propagation of Rolling Contact Fatigue in Ball Bearing Steel Due to Tensile Strain”; The Award for Prospective Researcher—The Japan Society of Mechanical Engineers, “Logarithmic Profile of Rollers in Roller Bearing and Optimization of the Profile”; The Monozukuri Buhin Taisho Shoreisho Award, “Improving Rolling Fatigue Life of Bearing Steels Through Grain Refinement—“Development of the FA bearing”).

NTN assigns the three years beginning with April 2007 to our new medium term business initiative “Sosei 21” which stands for “creativity”, “achievement” and “progress”. Based on this business concept, we, in terms of engineering commitments, will further enhance the value of the NTN brand by dramatically improving quality through robust design practices; more positive proposals to our customers and further accelerating product development.

In the field of environmental conservation, we will be more positively committed to the efforts for ecology: the examples of these efforts include more intensive development and marketing of eco-friendly products; attempts to totally ban use of environmentally impacting substances; positive utilization of clean natural energy sources; and recycling of otherwise disposed materials.

In accordance with NTN's creed: “For New Technology Network: contributing to the international society through creation of new technologies and development of new products”, NTN's commitment to develop eco-friendly products that contribute to “coexistence with the global environment” and drive to help achieve both realization of the sustainable society and better convenience that results from motorization.

Saving Energy with Motor Vehicle Transmission Technologies



Haruo HOUJOH

TOKYO INSTITUTE OF
TECHNOLOGY
Precision and Intelligence
Laboratory

Transmission technologies have been reviewed in this article from the viewpoint of global energy conservation. First, the importance of energy conservation is emphasized for a sustainable world not only because of global warming, but also because of historical planetary equilibrium. In addition, an assessment of future automobiles in the next 25 years is briefly introduced, predicting no promising systems among the various solutions for reducing fuel economy. Second, the energy consumption requirements of motor vehicles are discussed based on Newtonian mechanics to clarify the roles of both engines and transmissions. It follows that, although improvement of engine performance is the most essential, transmissions also play a large role in achieving better performance in regard to fuel consumption and drivability. Then, some key aspects for improving transmission energy consumption are briefly reviewed. Finally, the reuse of transmission units or parts is suggested as one effective way of saving energy.

1. Introduction

Many years have already elapsed since CO₂-induced global warming first posed a challenge for mankind. Now, environmental issues have been increasingly worsening. Energy saving is an outstanding challenge to be addressed for automobiles that are typical products in our consumption-oriented societies. Having specialized in automotive drive systems, the author has attempted to summarize the role of vehicle transmission technology in energy saving aspects together with his own private opinions.

1.1 The outstanding challenge is energy savings

A Japanese newspaper reported the content of the lecture that was presented, in the Agricultural Environmental Symposium held in Tokyo on May 23, 2007, hosted by Lester R. Brown, President, the Earth Policy Institute, USA. While use of biofuels was encouraged to mitigate emissions of greenhouse gases, he warned that the prices of food would dramatically rise and as a result the social environments with impoverished people around the world would be jeopardized.

His opinion appears to be true. The fossil fuels supporting the present-day motorization of modern society, typically, coal and petroleum*¹ are, figuratively speaking, "bank deposits" accumulated on the earth by solar energy in a time span as long as nearly a billion years after the birth of the earth, during which period the earth remained in an equilibrium state as the earth experienced several ice ages. During this

period, various living things somehow maintained their life activities through a long series of rises and declines on the surface of the earth in the equilibrium state. In other words, the solar energy reaching the earth is considered to be an indispensable thing to maintain the life activities on the earth in an equilibrium state.

An attempt to generate a plant-based hydrocarbon product such as a bioethanol and to use this product as a car fuel may be comparable to an act of stealing energy (figuratively, "daily income") that is needed for basic life activities. Deforestation activities to create farms for cultivating the sources of bioethanol also pose a challenge to the global environment. From this standpoint, even wind power generation and solar power generation may seem to help jeopardize the global environment. "Stealing" of energy in a very limited area on the earth may be acceptable. We cannot determine which factor can lead to disruption of the earth's equilibrium. I think dependency on a few alternative energy sources to replace a greater portion of necessary energies is not a wise option. We should use smaller amounts of energy from more diverse energy sources.

Therefore, in consideration of present-day energy-saving efforts, we need to develop a comprehensive energy saving measure rather than simply reducing CO₂ emissions.

*1 Some researchers have proposed "abiotic process" theories to explain the origin of petroleum. Regardless of the true origin, petroleum is the "bank deposit" that has long been possessed by the earth.

1.2 Energy is "money"

I am a layman in economics. Notwithstanding, I at least know that production of an industrial product unavoidably consumes energy. A machining process unavoidably involves the consumption of energy. However, various forms of human energies which may include a labor cost are transacted as commodities. To sum up, the price of a product may be considered to be an index that stands for the amount of energy consumed during the production process for the product in question. Accordingly, energy used to make a product can mean that the energy balance of a given product is measured by the money spent. We should consider that purchasing an expensive car means that a lot of energy has already been consumed to manufacture this car.

2. Cars of the future

Recently, I participated in a program sponsored by the Society of Automotive Engineers of Japan (JSAE), in developing a car industry engineering strategy and an engineering development scenario¹⁾. In this program, a questionnaire was presented to visitors in the Tokyo Motor Show 2005, asking what things are necessary for their daily lives. The top ranking answers were cars, computers and mobile phones, in that order. Similar questions were issued to university students in Japan, and the top ranking answers were mobile phones, computers, bicycles and then cars (the number of answers for cars was somehow equivalent to that of motorcycles).

These days, people who wish to purchase cars hope that their intended cars at least satisfy most

requirements of safety and eco-friendliness. In older days, ownership of cars meant "joy of driving", and car owners enjoyed the refreshing feelings and sensations from acceleration as well as a comfortable trip while they drove their cars. This view of cars seems to have changed. Most drivers of the present day seem to regard their cars only as a means of transportation, though they hope that driving in their cars is comfortable.

In its car industry engineering strategy for 2030 cars, JSAE set up the following six considerations as the benchmarks: **a)** energy saving (2L car), **b)** super low emission gas level (1/10 of the FY2005 level), **c)** low noise level (1/2 noise level of the FY2001 level), **d)** resources saving (100% recycling), **e)** safety (reduction of numbers of traffic accidents and casualties to 1/2), and **f)** information (media-free arrangement). Then, we issued, to knowledgeable people, a questionnaire about technologies needed for satisfying these benchmarks, wherein each respondent was expected to define these benchmarks in three levels development, commercialization and common use. One example of a post-edited result of the response is illustrated in Fig. 1. For more details, the readers are encouraged to refer to the related document. The particular information in this document, which seems to be most closely related to the author's contribution, is associated with efforts for energy and resource savings, and the information is hereunder summarized.

Some people expect that a 2L car (whose fuel consumption and CO₂ emissions for travel of 100 km are equivalent to those of 2 liters of gasoline consumed) will be commercialized and commonly

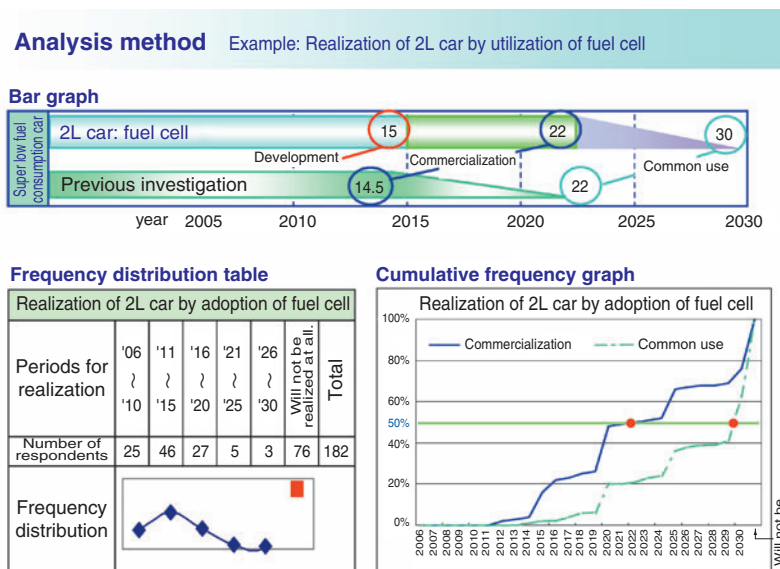


Fig.1 An questionnaire example done for assessing core technologies in next 25 years.²⁾

used by the year 2015. This epoch-making achievement will result from a HEV (Hybrid Electric Vehicle) design that also has a gasoline engine or an EV (Electric Vehicle) design. Commercialization of a FCV (Fuel Cell Vehicle) will take place in and after the year 2020; however, many people deny the possibility of common use of FCV even by the year 2030.

At the end of May 2007, a report about "next generation vehicle and fuel initiatives", a program mainly sponsored by The Ministry of Economy, Trade and Industry of Japan, was issued, wherein the report mentions that the automotive fuels will be diversified through use of batteries, clean diesel engines, hydrogen & fuel cells, and biofuels. As a result of study into the responses from the above-mentioned questionnaire, we find many pessimistic projections about commercialization and common use of techniques for production and provision of fuel cell. This trend coincides with the intention of researches for diversification in automotive fuels. It is expected that a variety of forms of so-called energy-efficient vehicles will be developed based on various technologies and techniques.

Incidentally, around the year 2020, commercialization will be realized for typical technologies that support energy saving cars, resulting from, reduction in frictional losses and the use of super-light high-strength non-metal and metal materials for drive systems. It appears that these particular technologies will be commercialized relatively soon. The strategy developed based on the findings from the above-mentioned investigation stresses importance of not only development of new power sources and further development of low fuel consumption cars based on the currently available technologies, but also of associated peripheral technologies and techniques.

In addition, we hope that the ratios of recycled or reused parts in the cars of the future exceed 90%. The old practice of purchasing a used car component from a junkyard can be practiced in a much more modernized way. A more modern car, at the end of its useful life, needs to be easily disassembled for recycling. Furthermore, to allow for reuse of components from used cars, importance in improving technologies for parts-compatibility design and accurate life-end recognition has been highlighted.

3. Discussions into energy consumption with automobiles

3.1 Thrust force and power needed by vehicles

Let us consider, based on Newtonian mechanics, the motion of a passenger car, where the car starts, accelerates and reaches a constant cruise speed. Then a relationship holds between the time and physical amounts as plotted in Fig. 2. If an acceleration curve is given and the mass of a vehicle is known, then the required thrust is defined and the required power (power) can be determined. In Fig. 2, two speed profile scenarios are covered from start to a cruise speed of 60 km/h and from start to a cruise speed of 120 km/h, wherein it is assumed that the vehicle (assumed to have a displacement of 2000 cc and a mass of 1.5 t, in accordance with the Automotive Engineering Handbook) is subjected to rolling resistance (which is not governed by the vehicle's speed) and aerodynamic resistance that is proportional to the square of the vehicle's speed. When the vehicle travels uphill, an additional resistance proportional to the degree of gradient will be added to the rolling resistance, the required thrust will be greater, and additional power will be needed. To cope with these physical amounts, the impedance of the output from the engine is adjusted such that the drive train including the transmission and final drive provides the thrust needed for an intended vehicle speed that also overcomes the rolling resistance in the vehicles tires.

The required thrusting force of a vehicle in acceleration is defined as a total of rolling resistance of the tires and the vehicle's aerodynamic resistance as well as the vehicle's "acceleration resistance"

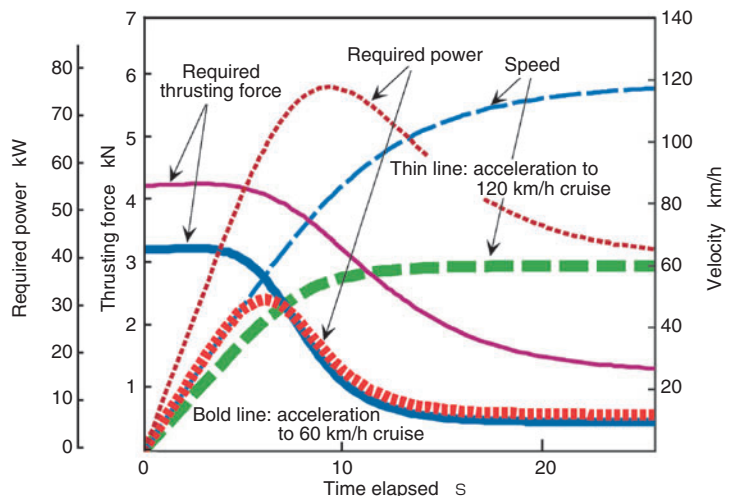


Fig.2 Typical example of thrusting force and power required during acceleration from standstill through cruise.

which is a sum of the vehicle's mass and the moment of inertia occurring on the vehicle's rotating portions. As to the rolling resistance of the tires and the vehicle's aerodynamic resistance, the work from the thrusting force is dissipated in the form of heat energy. The work relative to the acceleration resistance is conserved as the kinetic energy of the accelerating vehicle, and is dissipated as heat when the vehicle's brake is applied.

The peak at around the 10 seconds point in Fig. 2 occurs from the power consumption for this conserved energy. The power consumption corresponding with the sum of rolling resistance and aerodynamic resistance takes place in this period, wherein the rolling resistance proportionally increases, while the aerodynamic resistance increases in proportion with the cube of the vehicle's speed and accounts for the highest percentage of power consumed in the cruise mode after the 20 seconds period. Variation in the required power depending on the vehicle's velocity stems from the variation in aerodynamic resistance. As illustrated in Fig. 2, a significantly large output is consumed for acceleration, and the consumption of output maximizes in the transition region from acceleration to stable cruise.

This maximum value can vary greatly depending on the pattern of transition: with "mild acceleration", the required performance for the engine will be less demanding. Incidentally, a conventional engine provides maximum acceleration in the full-throttle setting; the engine does not develop its maximum output in an ordinary travel situation. Also, decreasing the above-mentioned dissipated energy will contribute to energy saving.

Conventionally, kinetic energy is stored in a vehicle and is dissipated as heat energy when the brake is actuated. On a hybrid electric vehicle, the kinetic energy is recovered and is used as an energy source to drive the electric motor, in order to start the vehicle and compensate for insufficiency in the required output in a situation such as acceleration for passing. With the so-called 10-15 mode, fuel economy with a hybrid electric vehicle is dramatically improved because in this mode acceleration and deceleration are frequently repeated and the resultant conserved energy is reused (such conserved energy is never reused on any conventional vehicle).

On the other hand, it is apparent that any modern automobile usually does not require much power since its engine runs at a lower speed of 2,000 rpm even when the vehicle is traveling at 100 km/h. Therefore, if a "less powerful, but highly efficient engine" is responsible for cruising at a given speed and an electric motor takes part in instantaneous positive

power-assist, the fuel economy of such an electric hybrid vehicle will be much more efficient.

However, from an "energy is money" standpoint, a car product may be regarded as an item that consumes much energy because the initial investment (that is, vehicle price) is high. In other words, a numerical value standing for improvement in fuel economy does not seem to directly stand for a degree of energy saving.

3.2 Operation of the engine, and energy

In the graphical plotting in Fig. 3, the engine speed values are taken on the horizontal axis while the engine torque values are along the vertical axis, wherein the engine performance graph is plotted with the engine equivalent efficiency curves assuming that the optimal efficiency taken at 100. Also, in Fig. 3, the equivalent output curves, determined by the engine speeds and torques, are hyperbolically plotted.

Next, suppose that the acceleration profile illustrated in Fig. 2, is realized with an ordinary 5-speed manual transmission system. Then, the operating trend with the engine (speed and torque) can be plotted with a bold dotted line. For instance, when a vehicle is accelerated to 60 km/h in this diagram, the vehicle's speed profile may consist of ① acceleration to 2200 rpm with the 1st gearshift, ② acceleration from 1300 rpm to 2700 rpm with the 2nd gearshift, ③ acceleration from 1800 rpm to 2800 rpm with the 3rd gearshift, and finally ④ cruise with the 4th gearshift. As apparent from this diagram, under these conditions, acceleration to 120 km/h means a driving mode that is 10% or more efficient.

Incidentally, the pattern of plotting can vary depending on the smoothness in start-up of

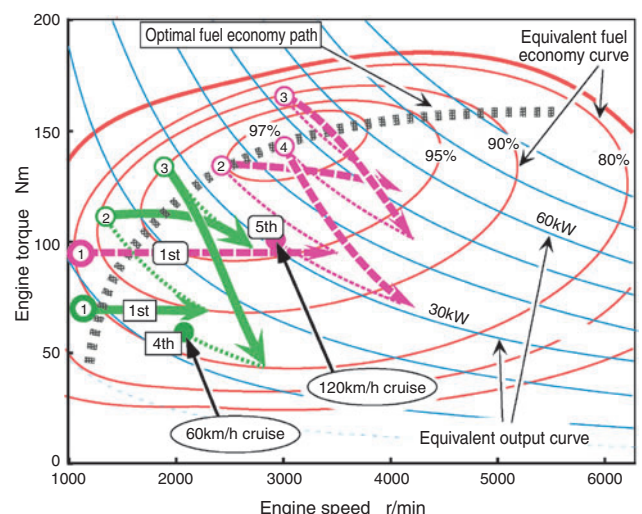


Fig.3 Engine performance of an ideal 2L gasoline engine and operation paths

acceleration and transition to a cruise: therefore, it should be noted that comprehensive discussions for a vehicle's efficiency under fixed conditions are meaningless. Additionally, some of the step ATs*2) recently very often used in Japan have the lock-up function, a vehicle's behavior immediately after starting travel may appear somewhat different. Of course, we need to take into account the number of gearshifts in evaluating the efficiency of a particular vehicle.

3.3 Expectation for drive system in contribution to energy saving

The engineering scenario¹⁾ that was developed in conjunction with the engineering technology includes discussions about drive systems in the future. When we attempt to predict the prospective technologies up to the year 2030, there appears to be a unique trend for each nation and no one best solution seems to be found for a particular region. Various travel profiles are possible in various nations and regions. Various solutions are possible for various cultures. Compared with cars in Europe and America, the vehicles in nations including Japan experience more stops and starts. The transmission systems used can be either AT or CVT. The drive systems most commonly used on the cars in the European market seem to be a variety of combinations of a diesel engine and MT or AMT (an automated MT): thus, one particular transmission type does not appear to prevail (Fig. 4). These transmission systems will be each selected

based on compatibility with particular diesel engines or gasoline engines, or hybrid electric systems.

a) Expectation for engine technology

As described above, when the intended vehicle employs either MT or AT, the running state of the engine of this vehicle is not always situated in the optimal efficiency region in Fig. 3. If the engine's running state falls in the region where the arrows each representing the state and when the efficiency of the engine is satisfactory in a wider speed range in Fig. 3, in other words, when the intervals between the contour lines are wider, the fuel economy of this vehicle will be still better. Thus, we want further improvement in the engine performance.

b) Expectation for transmission

Currently, CVTs are often used. A CVT can be adjusted such that the optimal operation path matches the intersections between the contour lines (efficiency) and equivalent output curves: as a result, the vehicle can be more efficient in terms of energy saving. However, a CVT can pose a problem in terms of layout (a belt-type CVT is suitable for a FF layout car while a troidal-type CVT is intended for a FR layout car) as well as in torque performance. In other words, a CVT may not be readily incorporated into any passenger car. Because there is a possible challenge about the efficiency resulting from a torque converter and/or hydraulic circuit: to address this problem, there has been an attempt to develop a clutchless CVT system that is referred to as the IVT.

At the same time, an increased number of stages have been applied to MT and step AT (wide range and close ratio) so that a vehicle can be run more frequently at an engine speed where the engine can run at higher efficiency to achieve better fuel economy. The effect of this effort is much apparent

*2) Step AT: An automatic transmission (AT) system that comprises a torque converter and a stepped transmission (usually, comprising a planetary reducer group and a multiple-disk clutch).

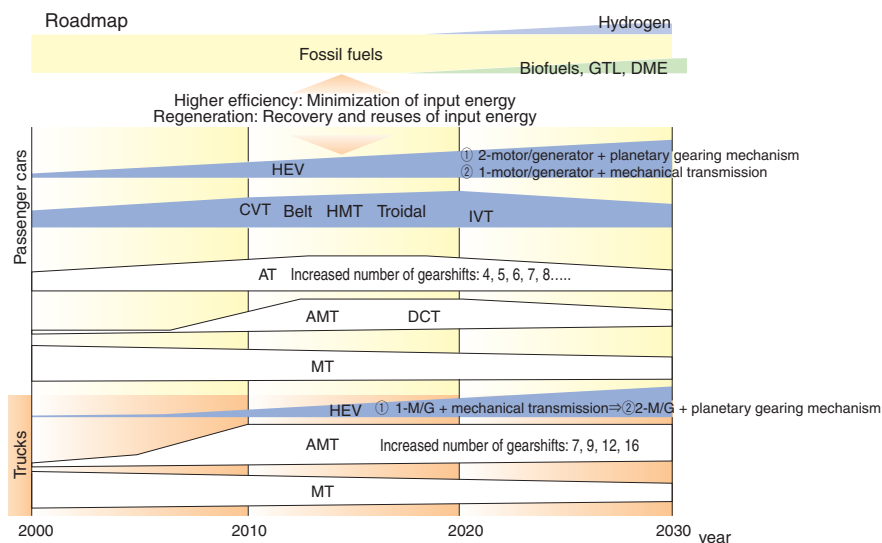


Fig.4 Sharing of various kinds of transmissions in next 25 years⁴⁾

with large trucks. A 12-stage transmission has been commercialized, and transmission of more increased stages will be marketed soon.

As discussed above, people are attempting to select an optimally performing drive system from a diversity of varieties. For this purpose, it is still necessary to make steady efforts for realizing both good fuel economy and running performance. Nevertheless, we hope that the automotive engines have more improved performance since improvement in engine efficiency helps realize further improvement in fuel economy as mentioned in a) above.

4. Energy saving and mechanical elements

For Figs. 2 and 3, no discussions were made about the efficiency of a drive system including a transmission. Currently, the transmission efficiency with MT appears to exceed 95%. On the other hand, the transmission efficiency with AT or CVT seems to fall in a range of 80% to 90%, though the efficiency can vary depending on the vehicle's running conditions. The factors that seem to be responsible for this variation in transmission efficiency are use of a torque converter and a hydraulic pump and greater drag on a multiple disk clutch. Gradual improvement will reflect these factors.

Elements including hypoid gears are indispensable for automobiles; however, some of these units still lead to a greater power loss. The efforts for improved efficiency are in progress, and some examples of these efforts are described below.

a) Lighter weight

When thinking of a simple dynamics, motion energy of a vehicle can be recovered by a generator; therefore, it may seem that the vehicle can be heavy. However, the battery on any vehicle has limitation in its capacity and the rolling resistance on the tires is usually proportional to the vehicle weight. Therefore, a lighter vehicle weight helps realize better fuel economy. Of course, energy regeneration accompanies a loss. Therefore, lowering the vehicle weight is very important, and achievable by improvement in materials, sophistication in individual elements and integration of elements.

b) Reduction in agitation loss and pump loss

The typical causes that are responsible for a larger portion of loss on a transmission and reducer are agitation loss with the lubricant and energy consumption by the hydraulic circuit. Investigation into the amount of such a loss has been of course available; however, the results of quantitative studies have been seldom published. Fig. 5 illustrates one

example of published achievement in efficiency improvement for a CVT system. A new transmission design boasts not only optimization of the system but also "lightening, reduced drag (clutch, bearing) and reduction in other losses". It is very hard to quantitatively determine the achieved improvements. As illustrated, contribution of each improvement is very minor. However, the improvement in hydraulic loss is a major contributing factor. Suppose that improvement in the hydraulic system is mandatory, and then the next challenge is an attempt for lower loss with individual elements.

c) More efficient bearings

-From test calculation for loss on bearing for hypoid pinion-

A hypoid gear is of course used on FR layout cars. In particular, two hypoid gears are usually used on 4WD layout cars. A tapered roller bearing used for hypoid drive pinion is often used with a greater thrust preload in order to fix the attitude of the shaft, and as a result, a greater dragging resistance occurs. Let us determine the approximate loss under the following conditions:

Tire speed:

10 r/s (63 rad/s, approximate vehicle speed; 72 km/h)

Reduction ratio with hypoid gear: 3

Dragging torque on bearing*3: 1 Nm by 2 pcs.

From a calculation under these conditions:

Power loss from dragging \approx 0.4 kW

Assuming that the maximum output of the engine is somewhat lower than 100 kW, the loss does not

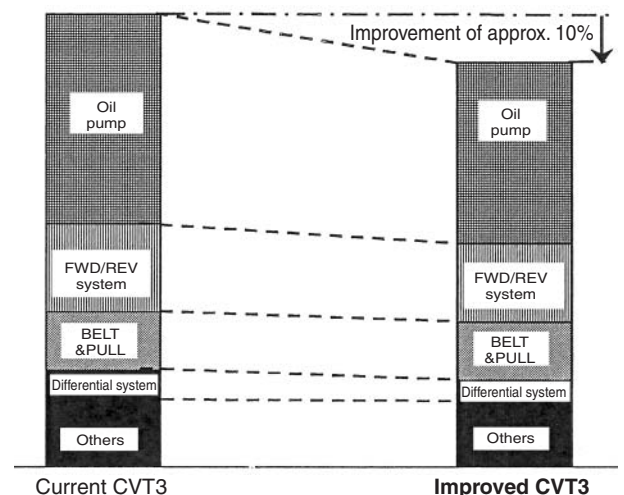


Fig.5 Loss reduction achievement by revising potential causes on a CVT unit (NISSAN) ³⁾

*3) Similar values are included in the reports from various bearing manufacturers, and this value has been set as a typical value.

appear to be too great.

Incidentally, the power required (determined as illustrated in Fig. 2) to compensate for the running resistance is approximately 8 kW. Within this power requirement, the loss from rolling resistance of the tires is as low as approximately 3 kW when the rolling resistance per tire is assumed to be approximately 35 N. At the same time, since the efficiency of a MT system is 95% and that of an AT system is approximately 85%, it is estimated that a loss of approximately 1 kW occurs under these running conditions. Considering these numerical values, the loss occurring on the bearing should not be neglected. To sum up, I hope that in the future we can publicly discuss the amount of power loss from dragging rather than the reduction in the dragging torque.

d) Motor/generator system and mechanical elements

Fig. 6 provides a cross-sectional view of a motor/transmission-reducer unit used on a TOYOTA's hybrid electric vehicle, where the maximum speed of the motor exceeds 12,000 rpm. This very high running speed with the electric motor has resulted from efforts for more compact size and higher motor speed to achieve a lighter power package since it was possible to assume that the motor output increases in proportion with the motor speed. When the vehicle starts to run and accelerates, the tire speed is very low and falls in a range of 100-200 rpm therefore, the transmission needs to have a reduction ratio of approximately 1/100. At the same time, so that this hybrid electric vehicle system can function as a parallel hybrid electric vehicle system, a power split mechanism involving a planetary gear mechanism is incorporated in order to allow the engine and the motor/generator to develop power either independent of each other or in cooperation, wherein the planetary gear mechanism employs a rolling bearing.

The transmission shown in Fig. 6 seems to be compact and light-weight. Since this transmission employs a larger rolling bearing that supports the ring gear, considerations about its efficiency are needed. Naturally, the planetary gear (pinion) and the needle roller bearing that supports the planetary gear appear to reflect various considerations and the planetary gear itself has been accordingly optimized. Though I don't know how high the level of the entire mechanical efficiency of this transmission is, I, as a specialist in mechanical elements think there will be various possibilities in further improving such a transmission system.

e) Expectation for oilless rolling bearing

Lubrication-induced loss is present on any rolling bearings. Therefore, running a rolling bearing without

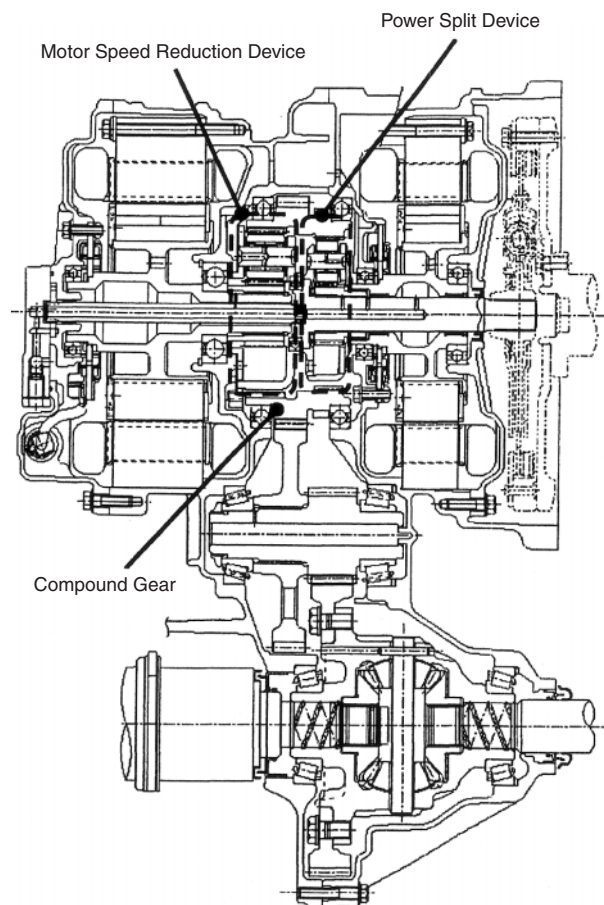


Fig.6 Cross sectional drawing of an up to date transmission for a hybrid car (TOYOTA)⁵⁾

a lubricant can help significantly improve efficiency of a transmission (currently, a near-impossible challenge). Of course, since contact-induced stress occurring inside a rolling bearing will deform the bearing, and this deformation lead to occurrence of hysteresis loss; as a result, complete avoidance of heat generation seems to be impossible.

5. Expectation for recycling or reuse

A drive system plays a vital role in transmitting the output from an engine to the road surface as a thrusting force. Currently, we seldom experience a failed transmission on a passenger car. The effective service life of a transmission for a passenger car will not be reached as long as the car is operated in a normal manner. In a transmission for a truck, the gears for low gearshift used for starting, acceleration and traveling uphill seem to be designed not to fail, through a finite life design technique that is based on run frequency data.

While an ordinary passenger car having traveled in excess of 100,000 km is often scrapped, a truck

having traveled more than 1,000,000 km with its full load capacity will continue to be used. However, in most cases, the transmission on such an aged truck rarely fails. Consequently, I expect that the following practices may be being observed:

a) Expectation for reuse

A few lucky still operable units may be recycled while most of still operable units are simply scrapped. This is a great waste. If still sound units are transferred to other vehicles, great energy savings can result. Such a practice, even though certain parts and components need to be replaced with new ones, will mean much mitigated environmental impacts.

As already described in Sec. 3.3, if the characteristic curve of a particular engine is flat, the car incorporating this engine will operate at a higher efficiency without a procedure for fine-adjustment of gears. This is true with a vehicle equipped with a CVT. Though a lighter vehicle weight is generally preferable, a certain increase in a vehicle weight may not adversely affect the fuel economy of the vehicle. If this assumption is true, transmission manufacturers in Japan need not manufacture more transmission types; instead, they may produce a limited number of standard transmission types. This arrangement will help a used transmission be transferred to another vehicle.

b) Improved reliability for life design

For present-day machine elements, failure of a machine element due to overloading is a simple problem in dynamics design; however, a more important problem is fatigue failure. The mode of fatigue failure is said to be governed not only by the composition and crystal structure of the material of the failed machine element but also by the inclusions in the material. Therefore, even now, fatigue failure needs to be discussed stochastically. In the engineering field of rolling bearings, the concept of life design has been accurately developed. Notwithstanding, we can predict the remaining life of a currently used part to an accuracy of "a specific number of days left" only when the operating conditions of that part are strictly limited.

The concept of finite life design appears to have been commonly accepted. I believe that further sophistication of this technique will help reduce waste of energy through recycling and reuse of machine parts.

6. Conclusion

From the viewpoint that energy saving is an issue to be addressed immediately, the author has discussed the present-day automotive drive system technologies. An automotive drive system develops its design role as its many mechanical elements work in cooperation with each other. I, as a specialist in mechanical elements, believe that we should remain committed to the permanent engineering challenge of reducing heat occurring on a mechanical element to near-zero. Also, we must develop a technology that addresses energy consumption in terms of global, long-term viewpoint, rather than only considering the lifecycle of each part in a machine element. While reconsidering a previous practice of "produce-and-scrap" with various industrial products including automobiles, I believe engineering people in Japan will further promote their research and development works, aiming at further evolution of their specialty element technologies. I hope that NTN's engineers and technicians will succeed in these challenges.

References

- 1) Society of Automotive Engineers of Japan, Inc.: Automobile technology strategy and technology development, Fuel scenario, May 2007.
- 2) Society of Automotive Engineers of Japan 2007 Spring Conference, Automobile Production Technology Forum Text, p.15.
- 3) Reference 1 above, part 2, p. 34.
- 4) Seiji Terauchi, Minoru Sawayama, Tatsuo Ochiai, Akihiro Makiyama, Masanori Ishido: Development of New Xtronic CVT for High-torque capacity, Symposium text of Society of Automotive Engineers of Japan, No.15-06 pp.18-22 (2006)
- 5) Hiroshi Hata, Masahiro Kojima, Hideto Watanabe, Tatsuhiko Mizutani, Munehiro Kiyama, Kenji Takizawa: Development of a Hybrid Transmission Engineers of Japan, No.10-05 pp.47-52 (2005)

<About the author>

Haruo HOUJOH

Professor, Tokyo Institute of Technology Precision and Intelligence Laboratory

Field of expertise: Dynamics of machine elements (especially gears)

Academic organization memberships:

Japan Society of Mechanical Engineers,
Society of Automotive Engineers of Japan

Technical Trends in Constant Velocity Universal Joints and the Development of Related Products

Shin TOMOGAMI*



Constant Velocity Universal Joints (CVJ) have come to be used widely for driveshafts and propeller shafts in vehicles, and are now being used for almost 100% of Japanese cars. CVJ performance has improved greatly with the evolution of vehicles. This paper will introduce recent technical trends and the development of products (parts) related to driveshaft CVJs.

1. Introduction

Forty-four years have already passed since NTN began production of the Constant Velocity Joint (hereinafter simply referred to as "CVJ"). The total number of CVJs produced thus far for driveshaft has nearly reached 400 million.

As Japan's auto industry has been expanding throughout this period, CVJs have been commonly used on driveshafts and propeller shafts of FF (Front-engine Front-drive) layout cars, IRS (Independent Rear Suspension) layout cars and 4WD (Four-Wheel Drive) layout cars. In today's market, virtually every passenger car designed in Japan incorporates the use of CVJs. The typical vehicle related areas in which the CVJs are applied have been illustrated in **Figs. 1** and **2**.

As automotive designs continually evolve, the performance of CVJs has been improved accordingly.

This paper describes the technical trend about the recent driveshaft CVJs as well as newly developed CVJ products.

2. Current requirements for CVJs

Around the world, the global environmental issues (including global warming) have been posing challenges that need to be immediately addressed. Automobile manufacturers and their suppliers have been committed to various efforts including improved fuel economy, introduction of hybrid car design, use of bio-fuel and development of high-performance diesel engines in order to reduce emissions of CO₂ which is a major contributing factor to global warming.

As a result of these initiatives, CVJs as drive train-related components are required to feature a lighter weight and offer better torque transmission efficiency in order to help improve fuel economy on the vehicle.

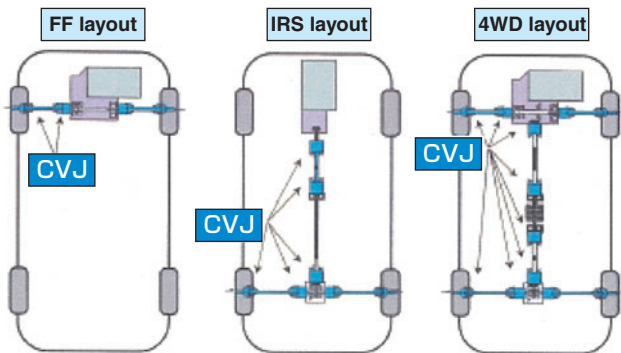


Fig. 1 CVJ application

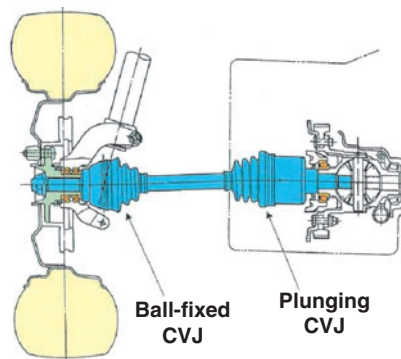


Fig. 2 Example: drive shaft of front axle

*Automotive Sales Headquarters C.V.Joint Engineering Dept.

In the next section, the author will present the history regarding weight reduction of driveshaft CVJs, Thereafter, the author will further explain functions, requirements and recent achievements about ball-fixed CVJ, plunging CVJs and CVJ components; each being a constituent of a driveshaft.

3. History of weight reduction for driveshaft CVJs

As the Holling-Kelly CAFE proposal seemed to be imposed in the US, the efforts for lighter weight component designs were strongly needed for every automotive manufacturer since the latter half of the 1980's. To cope with this need, NTN has been committed to light-weight, compact designs for its driveshaft CVJs with its unique technologies.

In the early 1990's, NTN developed a high-strength material and a long-life lubricant (grease) to realize a lighter-than-ever driveshaft CVJ. As a result of this effort, a lighter weight arrangement was achieved, whereas a CVJ of one nominal size smaller relative to a CVJ previously used on a given vehicle size could be employed.

In a time span from 1998 to the earlier half of 2000, NTN developed and mass-produced the next-generation CVJ products (E-series CVJ) that are much more compact compared with the previous CVJ series products, in order to meet the needs from the automakers. The change in size and weight with a typical CVJ (87 size) is graphically plotted in Fig. 3. Compared with weight levels in 1990, the weight of the present-day ball-fixed CVJ is 23% lighter while that of the present-day plunging CVJ is 17% lighter.

4. Ball-fixed CVJs

4.1 Functions of ball-fixed CVJs

A ball-fixed CVJ used on a front driveshaft of an FF or 4WD layout car is coupled to the front wheel hubs on a vehicle. This application results in a working angle while the steerable tires change the running direction as the steering wheel is operated, thereby transmitting the driving power from the engine to the tires while smoothly running at a constant velocity. Additionally, a ball-fixed CVJ directly affects the unsprung weight of a vehicle suspension.

4.2 Needs for ball-fixed CVJs

A need for a smaller turning radius with a vehicle, that is, a need for a greater steering angle with front wheels, has been significantly increasing as the recent car designs involve longer wheel bases and more diversified drive train layouts. In this context, a greater working angle is needed for ball-fixed CVJs whose working angles are governed by the steering angle of front wheels. Previously, the maximum working angles needed for ball-fixed CVJ were at approximately 47 degrees. However, larger working angles with ball-fixed CVJs on many car designs are currently needed with a (maximum working angle of up to 50 degrees).

At the same time, decreasing the weight of the car is necessary in order to help improve fuel economy, and under this circumstance, lighter CVJs are strongly needed. In particular, because of being situated near the tires, ball-fixed CVJs contribute to the unsprung weight of a vehicle. Therefore, a decrease in the weight of these CVJs positively contributes to a decrease in the overall vehicle weight.

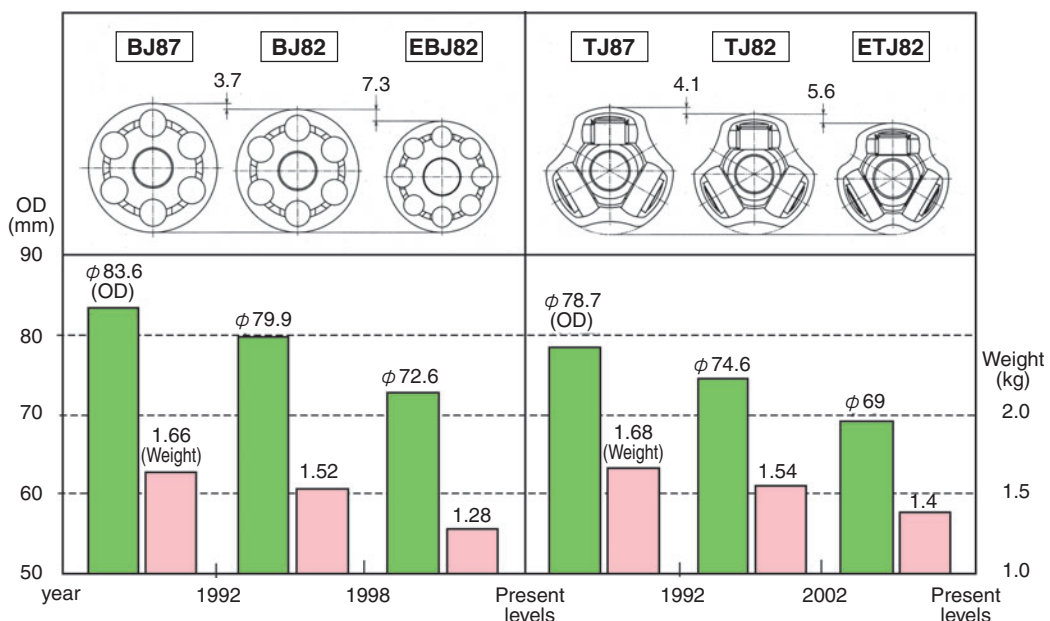


Fig. 3 Transition of outer diameter and weight of CVJ (Example of initial 87 size)

Generally, it is said that the effect by a decrease in unsprung weight is approximately 10 times effective as a decrease in sprung weight. Thus, lighter CVJs will greatly help improve fuel economy of the vehicles.

4.3 Latest ball-fixed CVJs

As the needs from car designs continue to evolve, the typical ball-fixed CVJ products that are currently used on the front driveshafts of FF cars and 4WD cars are matched with reduced size (compact) and light-weight joints with a maximum working angle of 50 degrees.

NTN offers a full lineup of the "EUJ series" compact, light-weight CVJs with a maximum working angle of 50 degrees for cars ranging from small-displacement engines to that of larger SUVs (Sports Utility Vehicles).

Compared with conventional 50-degree working angle capable CVJ designs, the "EUJ" series products boast approximately 7% reduction in the outside diameter and approximately 15% reduction in the weight (Photo 1).

Furthermore, the EUJ series products are light-weight, high-efficiency eco-friendly CVJs products that feature 25% reduction (working angle of 6 degrees) in the loss in driving force (torque loss) transmitted from an engine to the tires (Fig. 4).



Photo 1 Compact & light weight fixed CVJ with 50 degree working angle (EUJ)

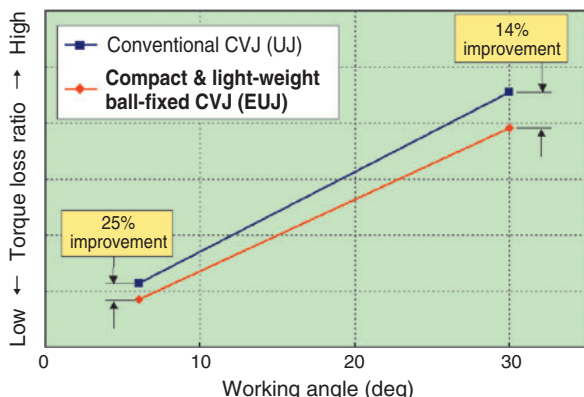


Fig. 4 Measurement data of torque loss for compact & light weight fixed CVJ (EUJ)

NTN additionally offers a lineup of the "EBJ series" with a maximum working angle of 47 degrees intended for vehicles on which the maximum working angle needed is less than 47 degrees. Compared with the "EUJ", the EBJ ball-fixed CVJ products feature a 3% smaller outside diameter and a 7% lighter weight while maintaining the high efficiency and performance of the EUJ series CVJs.

An automobile manufacturer can choose to use either an EUJ or EBJ product according to the maximum working angle needed by an intended vehicle design.

4.4 Vibration reducing techniques for ball-fixed CVJs

It is said that a plunging CVJ in a driveshaft affects the NVH (Noise, Vibration and Harshness) performance of a vehicle. Additionally through research, it has been determined that the characteristics of a ball-fixed CVJ also affects the NVH performance of a vehicle.

In particular, reducing the bending load (resistance occurring when a CVJ takes a working angle) on a ball-fixed CVJ can dampen the idling vibration on the vehicle. "Idling vibration" can be defined as minute vibration that is transmitted from the running engine to the vehicle body through the CVJ when the footbrake on an automatic transmission vehicle (A/T car) at a temporary stop is applied while the transmission is in a drive gear.

NTN achieves reduction in the bending load of its ball-fixed CVJs through optimization of the internal component design and dimensions (Fig. 5, Photo 2).

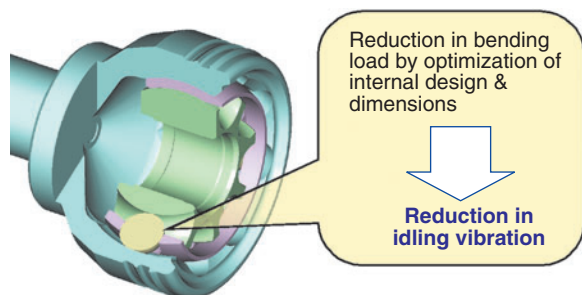


Fig. 5 Method of idling vibration reduction

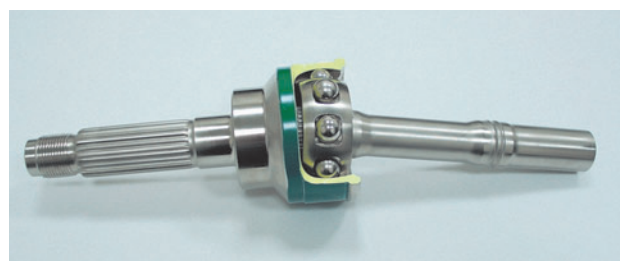


Photo 2 Less idling vibration CVJ

5. Plunging CVJs

5.1 Functions of plunging CVJs

Being coupled with a differential, a plunging CVJ transmits the driving power from an engine and a transmission to tires via a ball-fixed CVJ. A plunging CVJ is capable of absorbing the change in position relative to a ball-fixed CVJ that results from move of the suspension (axial displacement and angular displacement).

5.2 Requirements for plunging CVJs

It is widely known that the characteristics of any plunging CVJ affect the NVH characteristics of a given vehicle. Axial plunging resistance, which occurs when a plunging CVJ vibrates in the axial direction, is responsible for idling vibration of the vehicle. In addition, the axial force (known as "induced thrust") occurs on a plunging CVJ when the CVJ takes a working angle and runs while being subjected to a driving force. This force can contribute to a jerking phenomenon when the vehicle starts to travel as well as produce howling sound while the vehicle is running at a higher speed.

Therefore, plunging CVJs are required to have lower plunging resistance lower induced thrust and incorporate weight reduction design characteristics

5.3 Latest plunging CVJs

To cope with recent needs for improved quietness and riding comfort with vehicles, CVJ manufacturers are developing a diversity of plunging CVJ designs. Having developed an ultra low vibration plunging CVJ "PTJ" that boasts greatly reduced plunging resistance and induced thrust, NTN products contribute to improved NHV performance of vehicles.

Our "PTJ" is a tripod type plunging CVJ design, wherein three roller cassettes (each being a special roller bearing) are situated inside the outer ring that is

coupled with the differential. Moreover, the roller cassettes can stably roll on the rolling surface of the outer ring when the CVJ develops a working angle and/or axially plunges. This arrangement helps reduce the plunging resistance and internal friction so as to achieve ultra low vibration (Fig. 6).

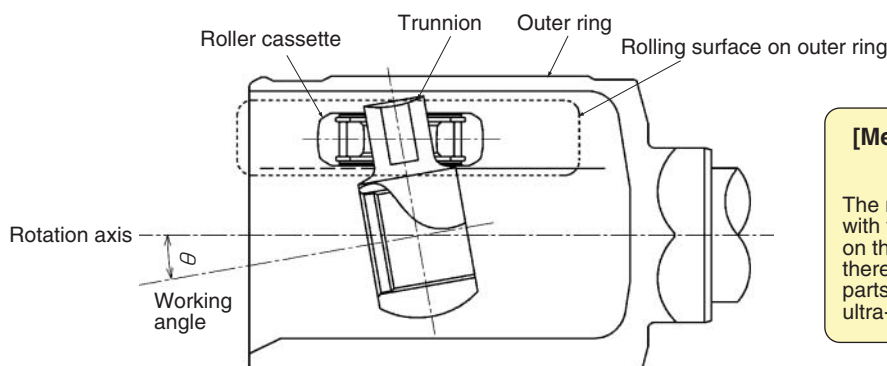
Our ultra-low vibration CVJ products excel in transmission efficiency for driving force (torque). When combined with the previously mentioned EUJ and EBJ, the PTJ will help minimize the torque loss on the driveshaft into which it is incorporated.

5.4 Ultra-low vibration CVJ of compact & light-weight design

To satisfy the market needs, NTN has commercialized compact, light-weight ultra-low vibration "EPTJ" series CVJ products that feature a structure and low vibration characteristics identical to that of the ultra-low vibration "PTJ" series CVJs. Further compared with the PTJ, the EPTJ boasts approximately 4% reduction in outside diameter and approximately 8% reduction in the weight. NTN offers the EPTJ series products for larger CVJs (NTN nominal size 95 or greater) with which a lighter weight provides many advantages (Photo 3).



Photo 3 Ultra low vibration CVJ with compact & lightweight design (EPTJ)



[Mechanism of ultra-low vibration arrangement]

The roller cassettes are held parallel with the rotation axis and stably roll on the rolling surface of the outer ring, thereby the friction force between parts is minimized so as to achieve ultra-low vibration.

Fig. 6 Structure of ultra low vibration plunging CVJ (PTJ)

6. CVJ components

6.1 Requirements for CVJ components

The requirements for CVJ components relative to the vehicle include lighter weights and enhanced rigidity (stiffness) against torsion on driveshafts. Greater rigidity on a drive system with CVJs will positively improve driver's feeling while maneuvering the vehicle. Therefore, highly rigid CVJ components are strongly needed especially for sporty and/or luxury passenger vehicles.

6.2 Latest technology with CVJ components—hollow design

A lighter, more compact component usually has lower rigidity. This is true with the components of CVJs too. In particular, rigidity is greatly affected by the shape of a shaft that connects a ball-fixed CVJ to a plunging CVJ. A recently available technology that satisfies conflicting requirements of lighter weight and higher rigidity is a hollow shaft design. A few examples of this technology are introduced below.

6.3 Hollow design—application to shaft

A shaft links a ball-fixed CVJ with a plunging CVJ to transmit engine torque to the wheels. Conventionally, a solid bar made of carbon steel for machinery is heat-treated and is used as a shaft (Fig. 7). Compared with the CVJs (both ball-fixed and plunging CVJs), the shaft typically has lower torsional rigidity. Therefore, it is an effective arrangement to increase the rigidity of the shaft in order to enhance the torsional rigidity of the entire driveshaft.

Reiterating that a larger diameter leads to increased rigidity of the shaft, one must also note that this arrangement in turn results in a much greater shaft weight.

Therefore, in order to realize both lighter weight and higher rigidity, a shaft being hollow over its entire length may be used (Fig. 8).

6.3.1 Features of hollow shaft

A length of steel pipe such as a one shown in Fig. 9 is swaged with a special machine (metal forming) to control the outside and inside diameters of the shaft while reducing the overall shaft diameter, whereby a hollow shaft is then formed.

Next, the hollow shaft is heat-treated (induction hardening, etc.) to increase its mechanical strength.

Upon completion of this unique design process, the hollow shaft can be up to 20 to 30% lighter compared with a conventional solid bar shaft whose torsional rigidity is equivalent. Additionally, a hollow shaft design also boasts increased bending rigidity, and thus can dampen the vibration resulting from bending resonance on the shaft.

6.4 Hollow design—application to plunging CVJ

With a transverse engine layout such as those on FF layout cars, the differential is offset relative to the centerline of the car. Consequently, the length of the right half of the driveshaft differs from that of the left half. With certain designs of driveshafts used on this type of car layout, the right and left stems to be installed to the differential of the plunging CVJ each have a unique length so that the length of the right half of the driveshaft is same as that of the left half of the driveshaft (equal shaft length design). With this arrangement, the working angle of the ball-fixed CVJ is same with the plunging CVJ on each of the right half and left half of driveshaft. As a result, the vehicle boasts better driving stability; therefore, an equal shaft length design is adopted for many FF and FF based 4WD vehicles.

With an equal shaft length design, the stem on the



Fig. 7 Solid bar shaft (Conventional design)

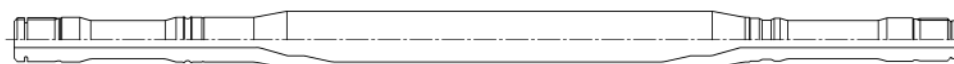


Fig. 8 Hollow shaft

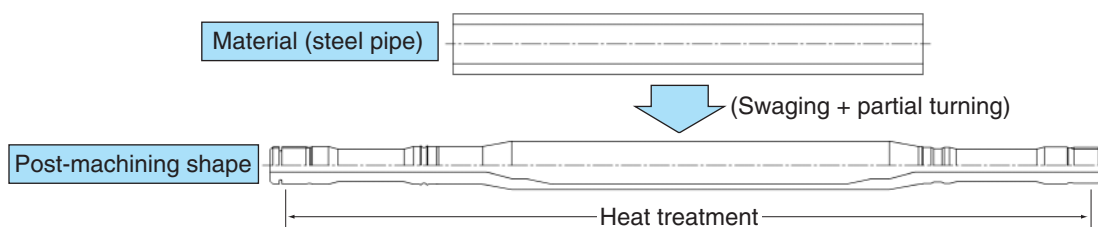


Fig. 9 Example of hollow shaft production process

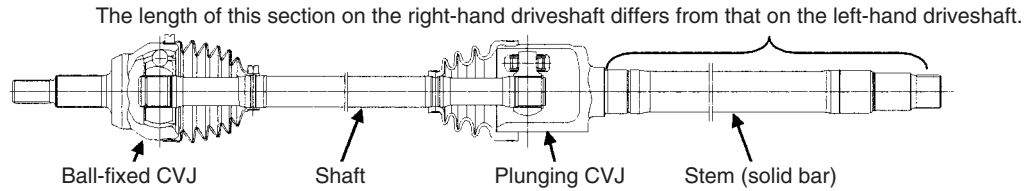


Fig. 10 Example of conventional drive shaft (Long stem design for plunging CVJ)

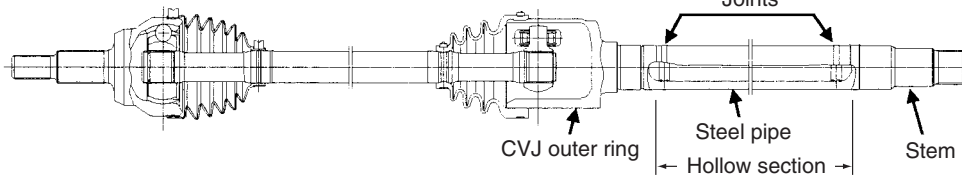


Fig. 11 Example of plunging CVJ with hollow type stem

right or left plunging CVJ is 20 to 30 cm longer compared with the other plunging CVJ and is of the solid stem type. If sufficient torsional rigidity is to be provided for a given driveshaft, the diameter on this longer stem section needs to be larger, and the resultant increased weight of this section leads to a heavier overall weight with the entire driveshaft assembly (**Fig. 10**).

6.4.1 Plunging CVJs with hollow stem

According to our new technology, a length of steel pipe is incorporated as an intermediate section for the stem between the plunging CVJ main body (outer ring) and the differential in order to realize an integrated structure (**Fig. 11**). The mechanical strength of this steel pipe section is increased by optimizing its composition and machining method; the outside diameters of the steel pipe and joints are sufficiently large and the steel pipe is not heat-treated.

With the shown example hollow driveshaft, the stem (having torsional rigidity same as with the solid plunging CVJ outer ring) is 0.8 kg (approximately 17%) lighter compared with the solid design.

7. Eco-friendly CVJs

Car manufacturers are committed to design and manufacture of "eco-friendly cars". In this context, we have been making efforts not only to design compact, light-weight and highly efficient CVJs that contribute to better fuel economy but also to eliminate any environmentally unfriendly chemicals or substances from the materials used to make our CVJ products.

In terms of eliminating environmentally unfriendly chemicals and substances, we have already eliminated grease containing lead, and paint with lead-free materials, and have adopted hexavalent chromium-free plated components instead of previous hexavalent chromium-plated components.

Additionally, in the latest CVJ production process at NTN, we employ a unique dry cutting process instead

of the previous wet grinding process that uses a grinding wheel.

The previous wet grinding process required a large amount of coolant (oil-based and/or water-soluble cutting fluid), which must be renewed and appropriately disposed at regular intervals. The dry cutting process does not need any such coolant. These are just some of the examples regarding NTN's commitment to reduction in environmental impacts.

8. Afterword

This paper has presented some examples of NTN's latest technology for driveshaft CVJs. Performance of automobiles improving. Functions and performance of constant velocity joints are directly or indirectly contributing to this performance improvement. As a specialist in constant velocity joint production, NTN is committed to developing and supplying constant velocity joint products that contribute to the progress of automobiles and are friendly to the global environment.

References

- 1) Tomoue: Latest technology trends for constant velocity joints, Tribology Monthly, No.218, pp.49-51 (2005)
- 2) Takeshi Ikeda: History of CVJ Design for Automobiles and Recent Technology, NTN Technical Review, No.70 (2002)

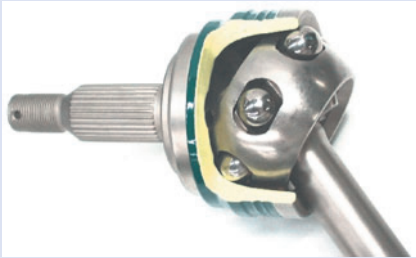
Photo of author



Shin TOMOGAMI
C.V. Joint Engineering Dept.
Automotive Sales Headquarters

Fixed Constant Velocity Joint with a Super High Operating Angle of 54 Degrees (TUJ)

Manabu HOSHINO*
Masashi FUNAHASHI*



NTN Corporation has succeeded in developing a fixed-type constant velocity joint called TUJ that has the world's highest maximum operating angle –54 degrees–for automobile drive shafts. TUJ will allow four-wheel drive and front-wheel drive cars to have a greater steering angle, enabling a very small turning radius. This report summarizes the concept, design and characteristics of TUJ.

1. Introduction

Recently, the needs from car users have been diversifying, and a greater variety of car designs have been marketed. In this context, the car manufacturers are attempting to market unique products by adding unique additional features.

Examples of such additional features may include sharp turning capability and increased passenger space. To satisfy these requirements, a vehicle must feature a smaller turning radius and an extended wheelbase. These requirements can be satisfied by a greater steering angle with the tires. This particular need has been strong for both FWD and 4WD vehicles where steering wheels also function as driving wheels. The tire steering angle is governed by the design limitations as well as the maximum bending angle (hereinafter referred to as "maximum operating angle") of the ball-fixed constant velocity universal joint; hereinafter referred to as "CVJ") in the tire side within the front driveshaft system that transmits the engine output from the differential gear to the driveshaft.

To address this need, we have recently developed a super high angle fixed CVJ "TUJ" (Tapered-track Undercut-free Joint) series capable of greater operating angle compared with conventional fixed CVJs in order to enhance the additional value and freedom of design on the vehicle side.

2. Driveshaft defined

A driveshaft is a power transmitting component that connects the engine power (revolutions and torque) to the tires. It remains capable of running at a constant speed and smoothly transmitting the torque even when an angle occurs between the running input shaft (differential gear shaft) and the rotating output shaft (tire shafts). Generally, a driveshaft assembly in each of the right and left sides comprises a shaft that links a fixed CVJ with a plunging CVJ, wherein the fixed CVJ cannot slide in the axial direction though being capable of a greater operating angle while the plunging CVJ can slide in the axial direction though being capable of only a limited operating angle. More specifically, the fixed CVJs are situated in the tire sides while the plunging CVJs are located near the differential gear (see Fig. 1).

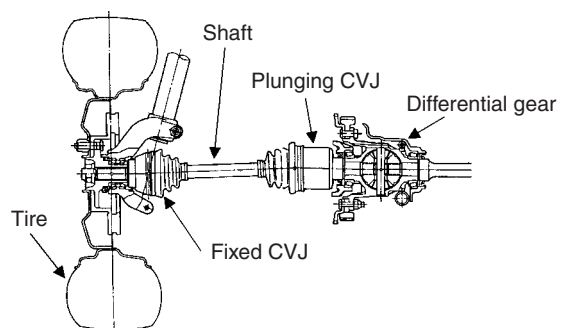


Fig. 1 Example of front drive shaft

*Automotive Sales Headquarters C.V.Joint Engineering Dept.

The maximum operating angle with the NTN's currently mass-produced EBJ (High Efficiency Ball fixed Joint) products, which feature light weight, compact size and high efficiency, is 47 degrees, while the maximum operating angle with the EUJ (High Efficiency Undercut-free Joint) products is 50 degrees.

3. Super high angle fixed CVJ "TUJ"

Compared with the conventional high angle fixed CVJs (maximum operating angle of 50 degrees), the TUJ series CVJ products boast a greater maximum operating angle. The TUJ series CVJs are described below.

3.1 Features of TUJ

The components of the TUJ are identical to those on conventional fixed CVJs, and are composed of outer ring and inner ring each having ball raceway track (hereinafter referred to as "ball track", six balls seated in the ball tracks and the cage that holds the balls (see Fig. 2).

The typical features of the TUJ are as follows:

- [1] **Maximum operating angle: 54 degrees**
- [2] **Functions (strength and durability): equivalent to those of conventional fixed CVJs**
- [3] **Transmission of torque is possible even at an operating angle of 54 degrees.**

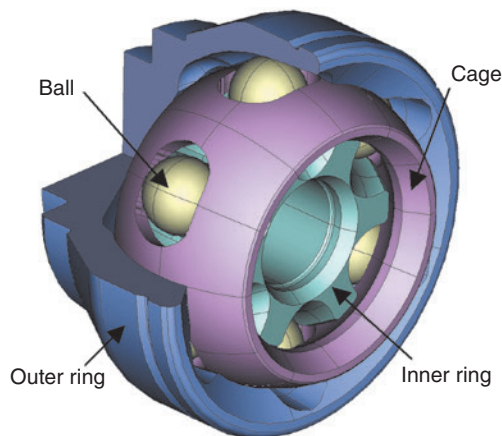


Fig. 2 Composition of TUJ

3.2 Basic structure of TUJ

In order to be able to transmit torque at a super high operating angle in excess of 50 degrees (an application not possible with conventional fixed CVJs), the TUJ incorporates NTN's unique design arrangements. The most unique points of this design are described below:

[1] Tapered ball track (patent pending)

On a fixed CVJ, the amount of axial travel of the

balls in the ball track is greater with a greater operating angle.

Therefore, to realize a greater operating angle, a greater axial length of the ball tracks is necessary. The range of axial travel of the balls at a higher angle situation is illustrated below, using the EBJ as an example (see Fig. 3).

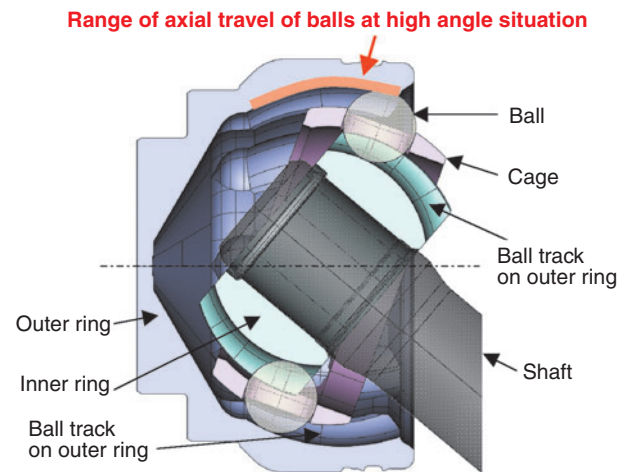


Fig. 3 Construction of EBJ at high-angle

The ball tracks on the EBJ are circular arc-shaped, and the maximum operating angle of the EBJ is 47 degrees. In contrast, the ball tracks on the EUJ (high-angle CVJ) are arc-shaped + straight-shaped, thereby a sufficient ball track length in the axial direction is realized and the maximum operating angle of 50 degrees is achieved. The newly developed TUJ, which is capable of an extremely high range of motion, has a unique ball track shape (arc + tapered) in order to incorporate the longer ball tracks (see Fig. 4).

[2] Adoption of offset cage (see Figs. 5 and 6)

The ball track shape adopted for the TUJ (arc + taper) causes the ball tracks on the inner ring and outer ring to force the balls toward the outer ring opening side when the TUJ is at a greater operating angle; consequently, a problem of insufficient strength occurs with the cage that holds the balls.

On fixed ball CVJs, due to the nature of their mechanism, an offset for controlling the balls is necessary (offsetting of the ball track centers on the outer and inner rings to the axial direction); accordingly, the ball tracks are offset relative to the center of sphere (hereinafter referred to as "ball track offset"). However, this ball track offset method is unfavorable due to structural limitations, the depth of ball track at the far side on the outer ring is shallower when the CVJ takes a greater operating angle.

The TUJ employs an offset cage (a cage with which the centers of the inner and outer spheres are axially

offset) to maintain a necessary offset by means of a cage, wherein the thickness of cage can be larger at the outer ring opening side where a greater cage strength is needed and, at the same time, possible decrease in the ball track depth can be prevented.

Thus, the TUJ design can solve not only insufficient joint strength at high angles situation but also possible problems resulting from an insufficient depth of ball tracks.

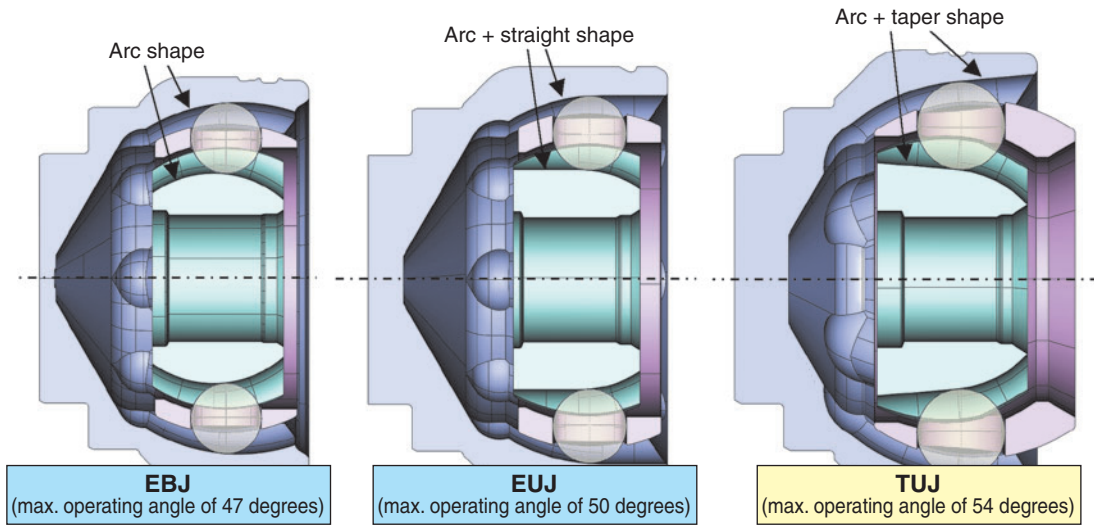


Fig. 4 Comparison of a ball track contour of fixed CVJs high-angle

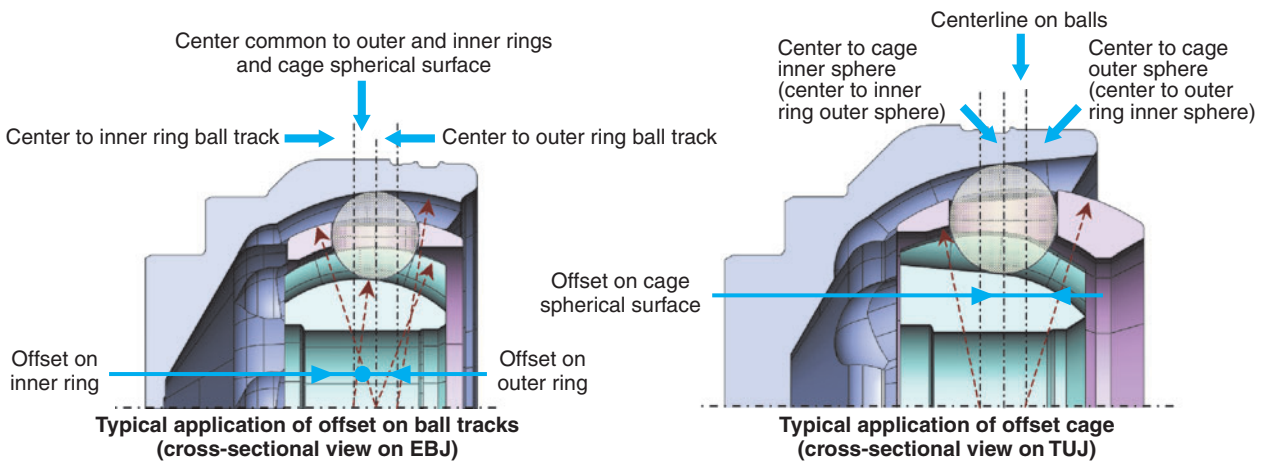


Fig. 5 Comparison of structure between ball track offset and cage offset

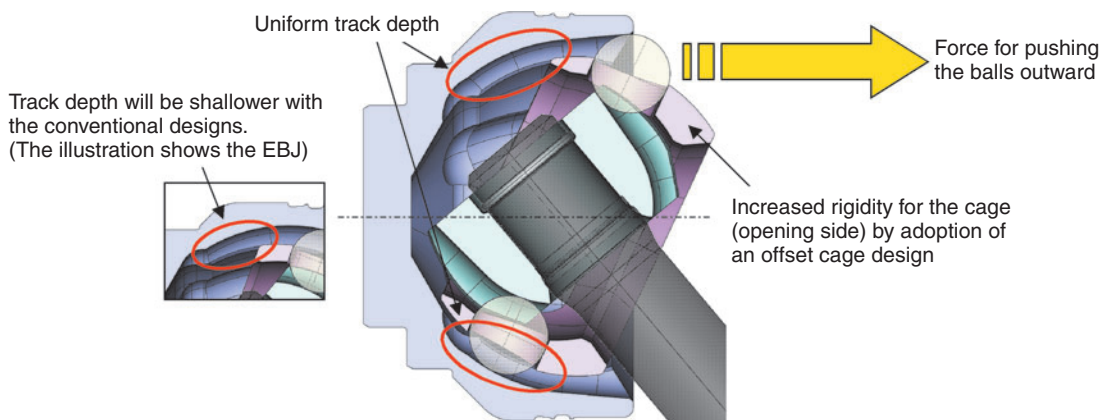


Fig. 6 Construction of TUJ at high angle

4. Joint functions

The TUJ features the performance comparable to that of conventional high angle fixed CVJs (maximum operating angle of 50 degrees). In consideration of an increased operating angle, we set the strength of the TUJ at a maximum operating angle equal to that of the conventional high angle fixed CVJs. More specifically, we have adopted the above-mentioned offset cage and fully utilized an FEM stress analysis (see Fig. 7)

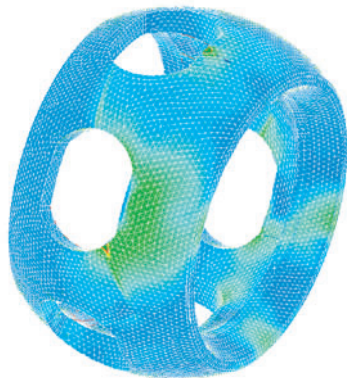
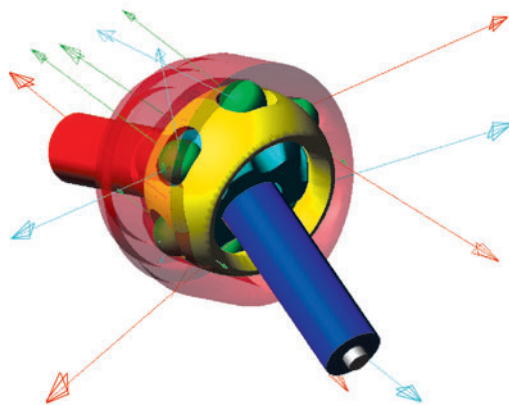


Fig. 7 FEM stress analysis for cage



Red : Load working between outer ring track and balls
 Blue : Load working between inner ring track and balls
 Green : Load working between balls and cage pockets

Fig. 8 Dynamic mechanism analysis

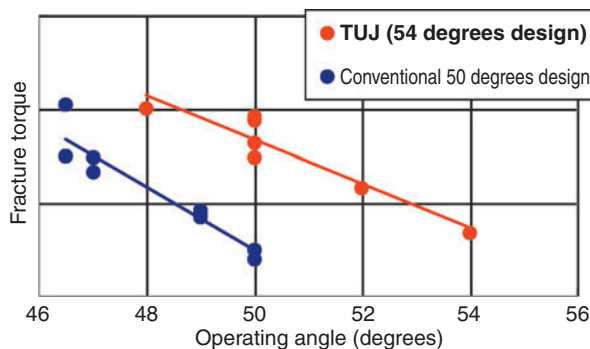


Fig. 9 Comparison of dynamic torsion strength

and dynamic mechanism analysis (see Fig. 8), thereby we have realized the mechanical strength at an operating angle of 54 degrees with the TUJ that is equivalent to the mechanical strength at an operating angle of 50 degrees with conventional fixed CVJs.

Fig. 9 provides comparison in terms of dynamic torsion strength.

5. Conclusion

By employing NTN's unique design, we have developed an innovative fixed CVJ featuring a maximum operating angle of 54 degrees while having the performance comparable to that of conventional CVJs (maximum operating angle of 50 degrees). This maximum operating angle (54 degrees) for automotive driveshaft is currently the highest in the automotive industry. The increase of 4 degrees in operating angle means that the minimum turning radius of an average medium-sized FF car can be decreased by approximately 70 cm (13%) or the wheelbase of such class of a car can be enlarged by approximately 40 cm (15%) while maintaining a minimum turning radius. In other words, a medium-sized car can feature a turning radius of a compact car or the passenger space of a larger car allowing designers more flexibility in consideration of layout and design.

References

- 1) Journal of Society of Automotive Engineers of Japan, vol.61 No.3 (2007)

Photos of authors



Manabu HOSHINO

C.V. Joint Engineering Dept.
 Automotive Sales
 Headquarters



Masashi FUNAHASHI

C.V. Joint Engineering Dept.
 Automotive Sales
 Headquarters

Measurement of the Internal Forces of Ball Fixed Constant Velocity Joints

Daiji OKAMOTO*

Hirokazu OOBA*



In recent years, the precise measurement of internal forces in constant velocity joints (CVJ) has become important in order to meet requirements for lightweight, reduced size, and high efficiency. The internal forces of a plunging-type CVJ have already been clarified both theoretically and experimentally. On the other hand, for fixed-type ball CVJs, the internal forces had been analyzed by employing a dynamic numerical simulation, but experimental verification had not yet been achieved. In this study, a new test rig

was developed in order to measure internal forces in a fixed-type ball CVJ. The measured results are in good agreement with those obtained from dynamic numerical simulations. In addition, we demonstrated the influence of the coefficient of friction, and the clearance between the cage and the surfaces of the inner and outer rings had on the internal forces.

1. Introduction

Constant velocity joints can be categorized into two groups, that is, fixed type and plunging type. NTN has so far established a method for simulating the force acting inside a plunging constant velocity joint through dynamic numerical simulation and experimental verification¹⁾⁻³⁾. For fixed constant velocity joints, NTN has also developed a dynamic numerical simulation technique for internally acting forces²⁾⁻⁵⁾. However, the spherical forms of the areas being measured including tracks make a measuring operation extremely difficult, and as a result, experimental verification for the internally acting forces has not yet been attempted.

To address this situation, we have fabricated a specially instrumented outer ring that permits, by means of piezoelectric devices, the forces acting inside a Rzeppa constant velocity joint (BJ) which is a fixed constant velocity joint, to be measured. Using this outer ring, we analyzed the forces acting on the loading side and non-loading side tracks and the balls. We were also able to analyze the forces acting on the contact areas between the inner spherical surfaces on the outer ring and the outer spherical surfaces on the

cage.

We also investigated the effects of the coefficient of friction of the lubricant, and the clearance across spherical surfaces onto each of these forces⁶⁾⁻⁷⁾. Furthermore, we have compared the simulation results from the already developed general-purpose mechanism analysis software ADAMS⁴⁾⁻⁵⁾ with the results of our experimental verification.

2. Conditions and parameters for measurement

The measurement conditions are summarized in **Table 1**, and the internal forces being measured (forces acting between the balls and tracks and a force acting between the cage and outer ring spherical surfaces) are illustrated in **Fig. 1**, while detailed data for the specimens used are given in **Table 2**. To determine the effect of a friction coefficient, we used two lubricants, each having a unique friction coefficient. To investigate the effect of clearance across spherical surfaces, we employed two cages, each having unique internal and external spherical diameters.

*New Product Development Dept. New Product Development R&D Center

Table 1 Measurement conditions

Test rig	Power circulating joint tester
Drive system	Driving inner ring (torque is transmitted from inner ring to balls and outer ring)
Running speed (min ⁻¹)	10
Load torque (Nm)	100
Working angle (deg)	10, 20, 30, 40
Test joint	BJ95L

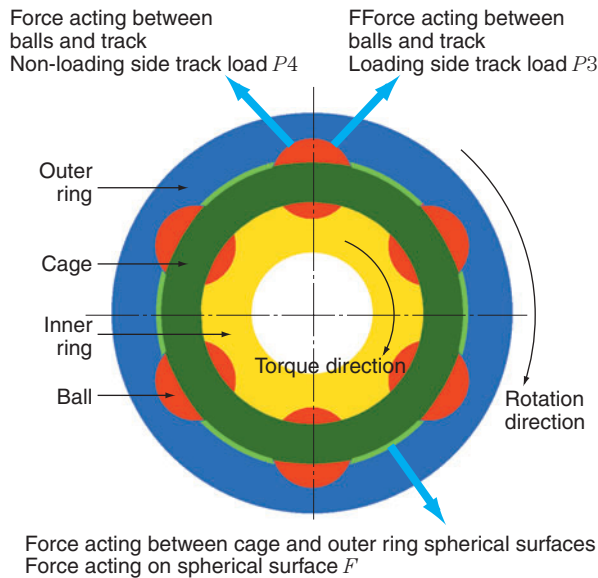


Fig. 1 Schematic illustration of internally acting forces

Table 2 Details of lubricants and cages used

Lubricant	Lubricant A ($\mu = 0.07$ NOTE) Lubricant B ($\mu = 0.10$ NOTE)
Cage	Cage A Ratio of inner spherical surface clearance to ball diameter : 0.0078 Ratio of outer spherical surface clearance to ball diameter : 0.0056 Cage B Ratio of inner spherical surface clearance to ball diameter : 0.0157 Ratio of outer spherical surface clearance to ball diameter : 0.0111

NOTE) Measurement values from SRV test

3. Measuring method

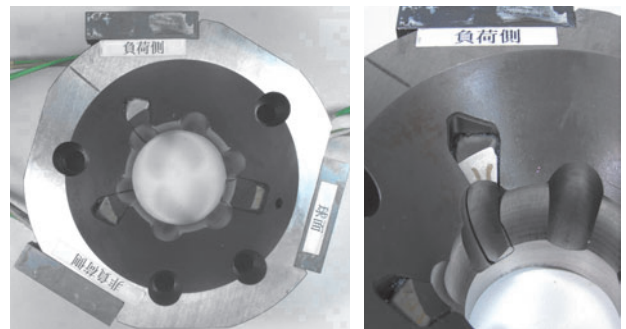
We have fabricated an instrumented outer ring that incorporates measuring terminals that allow us to be able to measure the forces acting between the balls and tracks on a fixed CVJ, and the forces acting between the cage and outer ring spherical surfaces on a fixed CVJ. The measuring terminals each comprise of separate sections in the outer ring track and spherical surfaces as well as tri-axial force sensors (piezoelectric devices).

3.1 Instrumented outer ring

A photograph of the fabricated BJ outer ring is given in Fig. 2. After incorporating the load measuring

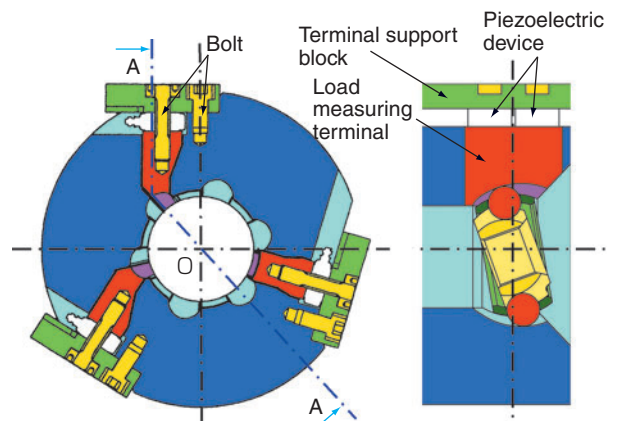
terminals, the tracks and spherical surfaces were precision finished to ensure good dimensional accuracy for this outer ring. In accordance with the measured outer ring dimensions, an appropriate inner ring, cage, and balls were then incorporated.

A cross-sectional view showing the installed piezoelectric devices is included in Fig. 3. Because a moment occurs on each load-measuring terminal, due to the shifting of contact areas between the balls and the cage, two piezoelectric devices (see Fig. 4) were arranged in the axial direction, and a load on each piezoelectric device was measured.



(a) Instrumented outer ring (b) Load measuring terminal of load-side track

Fig. 2 Overview photograph of instrumented outer ring



(a) Circumferential cross-sectional view (b) Axial cross-sectional view (A-O-A)
Fig. 3 Arrangement of piezoelectric devices

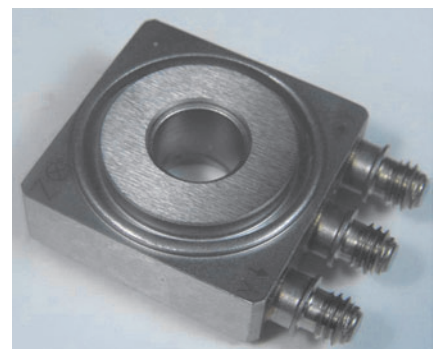


Fig. 4 Photograph of piezoelectric device

3.2 Measurement coordinates system and symbols

The measurement coordinate system used is illustrated in Fig. 5. The positive direction of a load in Fig. 5 is an arrow direction. The piezoelectric devices are arranged in accordance with this measurement coordinates system. The mounting angle for the piezoelectric devices to the tracks was allowed to coincide with the contact angle. At the same time, the mounting angle for the piezoelectric devices to the spherical surface was allowed to coincide with the normal direction. The resultant forces from the internally acting forces were calculated based on the triaxial forces being output from these piezoelectric devices (see Table 3).

3.3 Working angle and rotary phase angle

Working angle and rotary phase angle are defined in Fig. 6. A working angle is an inclination angle that occurs between the outer ring axis and the inner ring axis. The shift of the ball situated in the plane that includes the outer ring axis and inner ring axis is the greatest (situation in Fig. 6 (a)). At the rotary phase

angle $\phi = 0$ deg, the balls are pushed in the furthest side in the outer ring. At the rotary phase angle $\phi = 180$ deg, the balls are situated nearest to the outer ring inlet side. By referring to this coordinates system, we measured the loading side track loads, non-loading side track loads, and forces acting on the spherical surfaces, and compiled the resultant data.

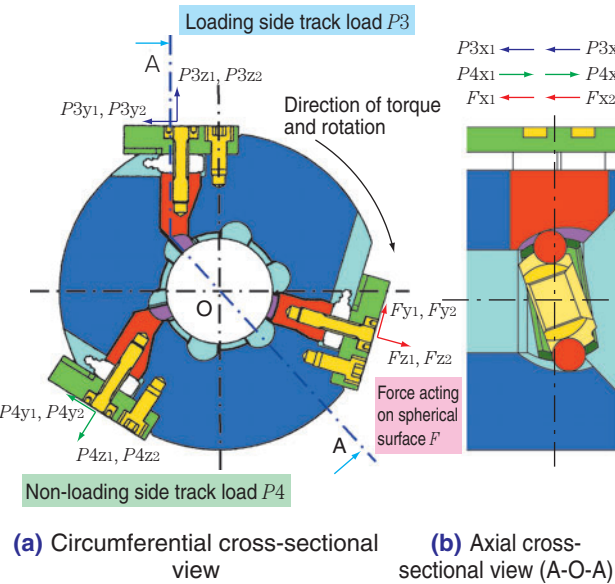
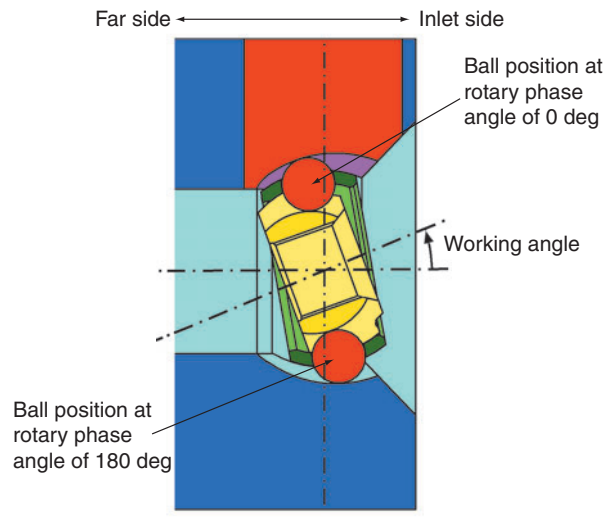
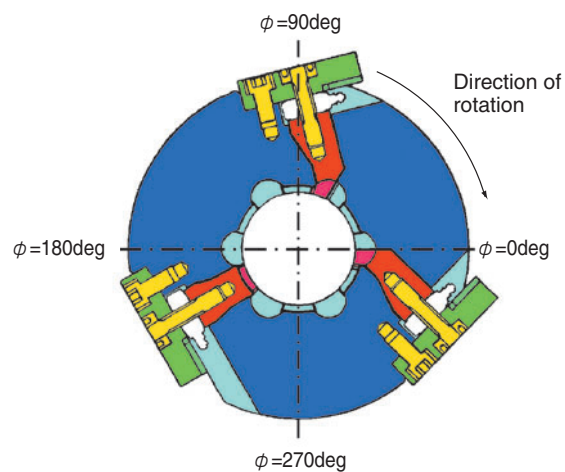


Fig. 5 Measurement coordinate system



(a) Working angle



(b) Rotary phase angle

Fig. 6 Working angle and rotary phase angle

Table 3 Classification and details of internally acting forces

Internally acting forces	Symbol	Calculation formulas for resultant forces
Loading side track load P3 Contact force between balls and outer ring loading side track	$P3x(P3x1 + P3x2)$ $P3y(P3y1 + P3y2)$ $P3z(P3z1 + P3z2)$	$P3 = \sqrt{P3x^2 + P3y^2 + P3z^2}$
Non-loading side track load P4 Contact force between balls and outer ring non-loading side track	$P4x(P4x1 + P4x2)$ $P4y(P4y1 + P4y2)$ $P4z(P4z1 + P4z2)$	$P4 = \sqrt{P4x^2 + P4y^2 + P4z^2}$
Force acting on spherical surface F Contact force between cage and outer ring spherical surface	$Fx(Fx1 + Fx2)$ $Fy(Fy1 + Fy2)$ $Fz(Fz1 + Fz2)$	$F = \sqrt{Fx^2 + Fy^2 + Fz^2}$

3.4 Measuring system

The measuring system that we used is illustrated in Fig. 7. An output from a piezoelectric device is amplified by an inline charge amplifier, transmitted via a slip-ring situated at the shaft end of the test rig, and is recorded by a memory high coder. After completion of the measuring operation, the obtained data is processed with a personal computer. With this measuring system, the output signal from the rotary encoder is input every 0.1 degree (3600 pulses per revolution), and acts as a trigger for the system to read the data. In our measuring operation, a BJ was used as a joint that constituted a pair together with the test outer ring. Usually, a plunging constant velocity joint having axial freedom constitutes a pair together with a fixed constant velocity joint such as the test outer ring. When compared with a fixed constant velocity joint, a plunging constant velocity joint does not have as large of a working angle. Therefore, for our measuring operation, the BJ was used so as to be able to obtain a working angle up to 40 degrees. Our measuring system is constructed such that the test rig to which the BJ is mounted, slides (white arrow in Fig. 7) to provide a working angle.

4. Analysis model

The dimensions of the test outer ring and samples used for the experiment were measured using a 3D measurement system. Based on the obtained shape dimensions and friction coefficients of the lubricants, simulation was performed by the already developed general-purpose mechanism analysis ADAMS⁴⁾⁻⁵⁾.

5. Results of measurement and analysis

5.1 Effect of friction coefficient of lubricant

5.1.1 Loading side track load P_3

The influence of different lubricant types and different friction coefficients resulting from different lubricant types on the loading side track load P_3 is illustrated in the measurement result and analysis result in Fig. 8. The resultant findings are described below:

- [1] Peak load was observed at around a rotary phase angle at which the balls are situated in the far side and inlet side of the outer ring.
- [2] With a greater friction coefficient, the peak of loading side track load shifts to a greater rotary

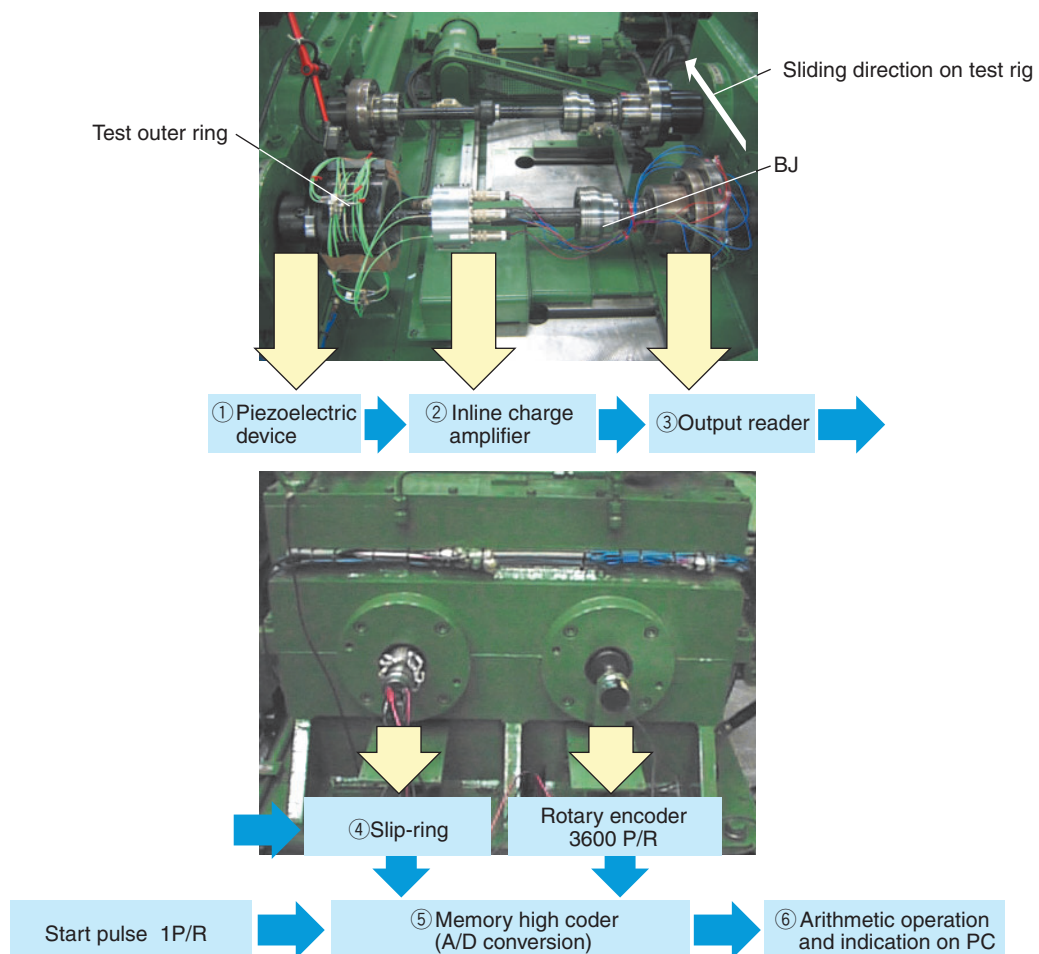


Fig. 7 Measurement system

phase angle under a low working angle situation.

[3] According to the analysis results too, the findings [1] and [2] remain true.

5.1.2 Non-loading side track load P_4

The influence of different lubricant types and different friction coefficients resulting from different lubricant types on the non-loading side track load P_4 is illustrated in the measurement result and analysis result in Fig. 9. The resultant findings are described

below:

[1] Peak load was observed at around a rotary phase angle at which the loading side track load decreases.

[2] With a greater friction coefficient, the peak of non-loading side track load shifts to a greater rotary phase angle under a low working angle situation.

[3] According to the analysis results too, the findings [1] and [2] remain true.

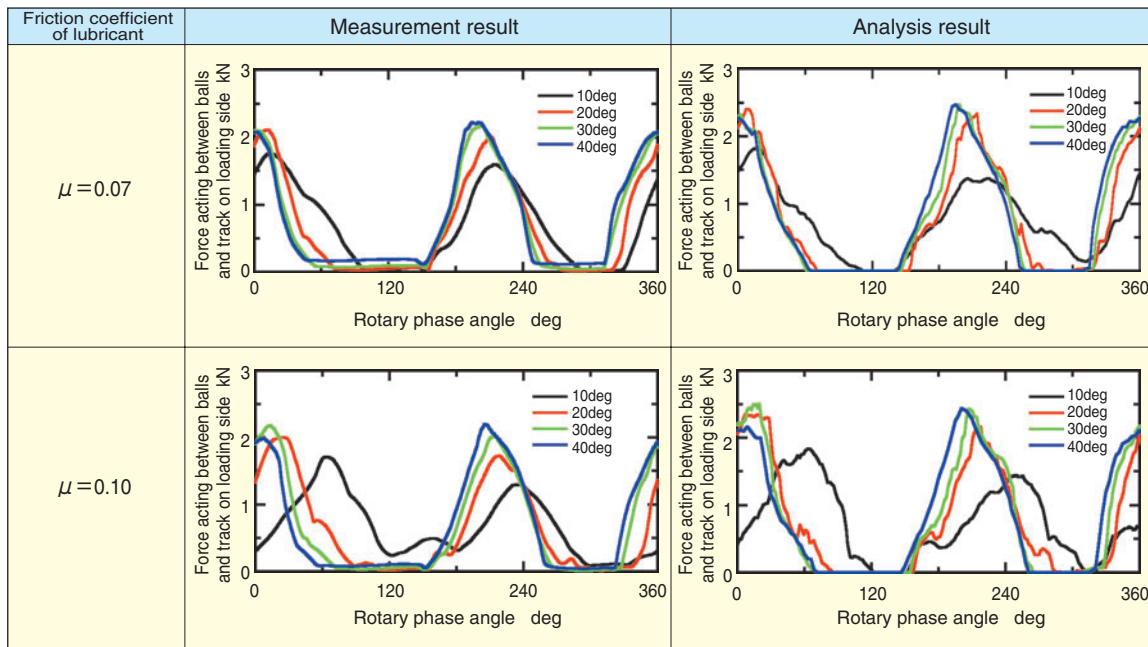


Fig. 8 The influence of coefficient of friction of lubricants on loading side track load P_3 (Lubricant: A and B, Cage: A)

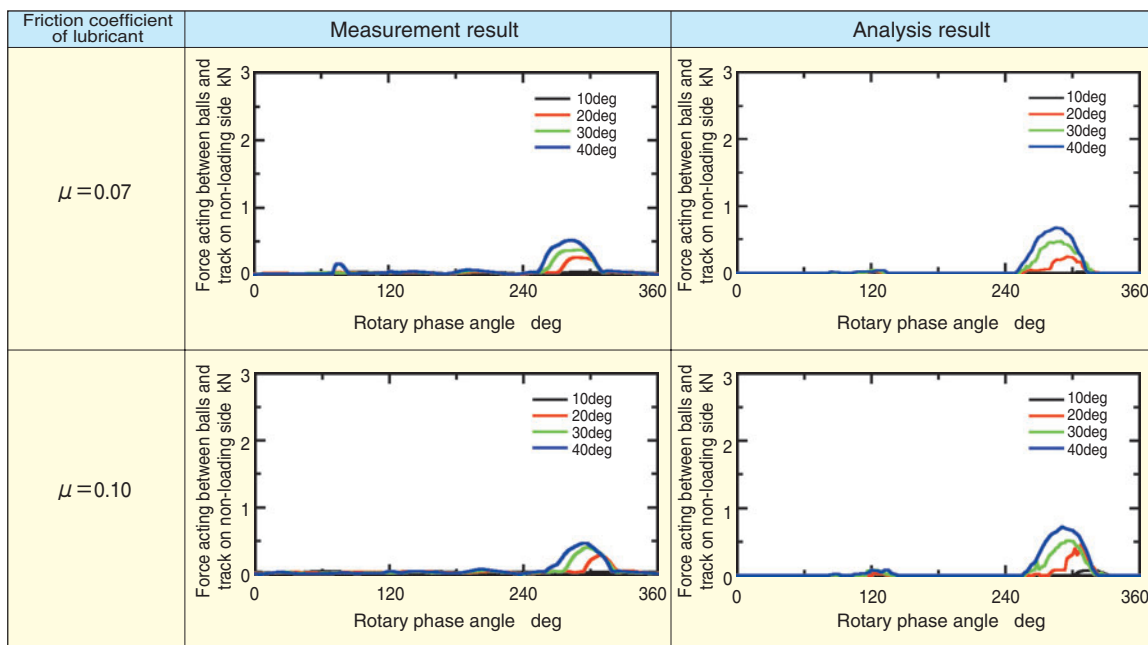


Fig. 9 The influence of coefficient of friction of lubricants on non-loading side track load P_4 (Lubricant: A and B, Cage: A)

5.1.3 Resultant force from spherical surfaces

The measured force (F) which acted on spherical surfaces is a load acting on one of the six spherical surfaces on the outer ring, and the resultant force mentioned here is a load acting from the entire cage onto the spherical surfaces on the outer ring. By determining the resultant from the spherical surfaces, it is possible to determine the load acting on the cage within a joint. The resultant force from the spherical surfaces can be calculated from the result of the force acting on the six spherical surfaces. The measurement results of the force acting on the spherical surfaces are graphically plotted in Fig. 10. A formula for calculating a resultant force from spherical surfaces is given in the expression (1) below:

$$\begin{aligned}
 \text{Resultant force from spherical surfaces} \\
 (\alpha \text{ deg}) = & (F(\alpha \text{ deg}))^2 + F(\alpha + 60 \text{ deg})^2 \\
 & + F(\alpha + 120 \text{ deg})^2 + F(\alpha + 180 \text{ deg})^2 \\
 & + F(\alpha + 240 \text{ deg})^2 + F(\alpha + 300 \text{ deg})^2)^{1/2} \quad (1)
 \end{aligned}$$

where, α : given rotary phase angle

From this measured force (F) acting on spherical surfaces, another measurement result (resultant force from spherical surfaces) was obtained with a different lubricant, and another analysis result (resultant force from spherical surfaces) was reached with another friction coefficient. These new results are graphically plotted in Fig. 11. The so-obtained results are summarized below:

[1] From the measurement result and analysis result, it is apparent that there are six peaks per

revolution.

[2] When the friction coefficient is 0.07, the load at the working angle of 30 deg is virtually same with that at the working angle of 40 deg. In contrast, when the friction coefficient is 0.10, the peak loads are greater with the working angle of 40 deg.

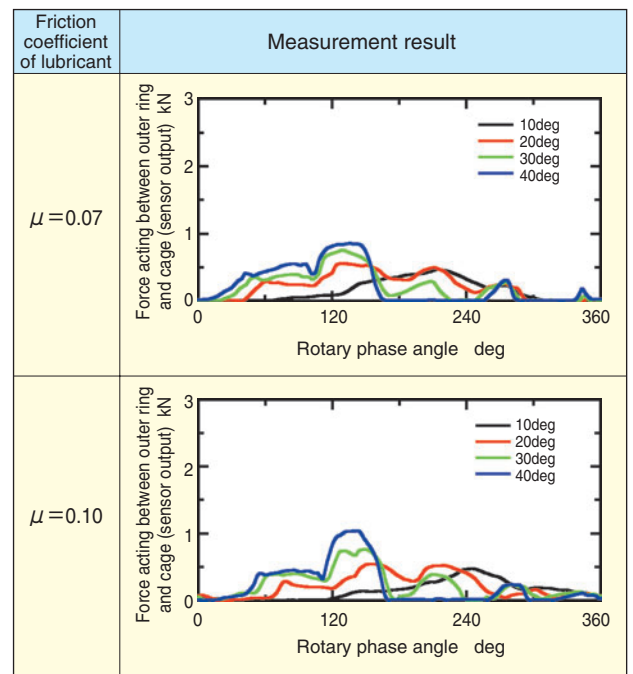


Fig. 10 Measurement results of forces F acting between outer spherical surface of cage and inner spherical surface of outer ring (Lubricant: A and B, Cage: A)

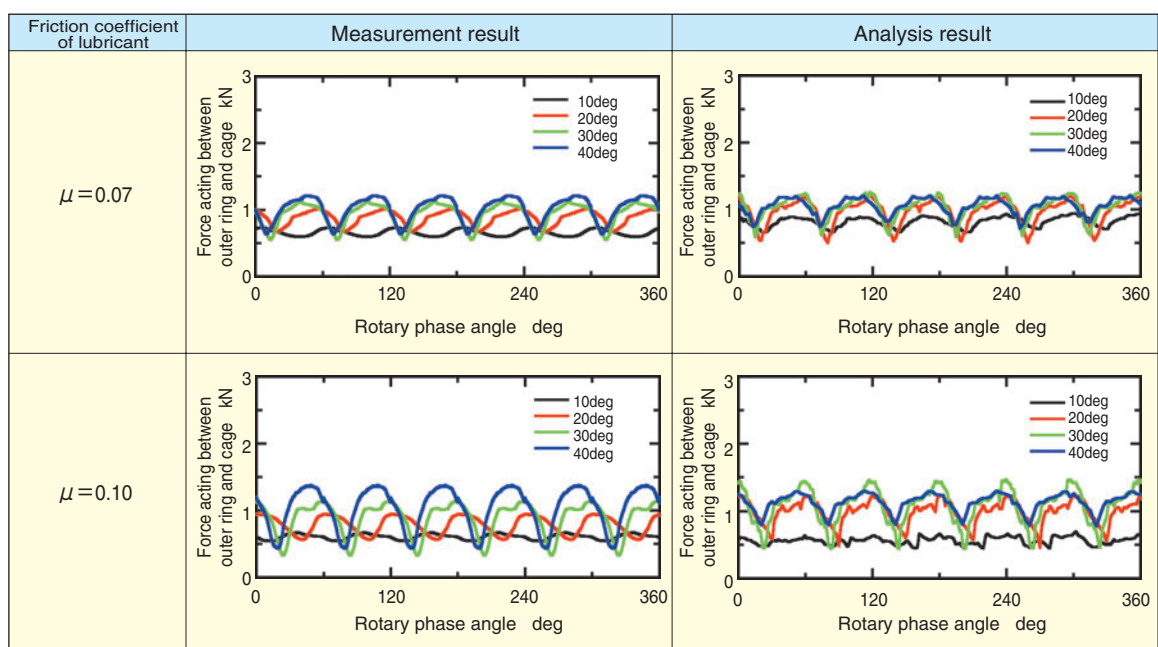


Fig. 11 The influence of coefficient of friction of lubricants on resultant forces acting between outer spherical surface of cage and inner spherical surface of outer ring (Lubricant: A and B, Cage: A)

5.2 Influence of clearance between spherical surfaces

5.2.1 Loading side track load P_3

Measurement results and analysis results were obtained with a plurality of cages each having a uniquely dimensioned clearance between spherical surfaces. The loading side track loads P_3 in these results are provided in Fig. 12. The so-obtained results are summarized below:

[1] With a greater dimension with clearance between spherical surfaces, the peak loads are greater.

[2] With a greater dimension with clearance between spherical surfaces, and when the working angle is smaller, the peak position (previously at around the rotary phase angle of 0 deg) shifts to a greater rotary phase angle region.

5.2.2 Non-load side track load P_4

Measurement results and analysis results were obtained for multiple cages, each having a uniquely dimensioned clearance between spherical surfaces. The non-loading side track loads P_4 in these results are provided in Fig. 13. The so-obtained results are

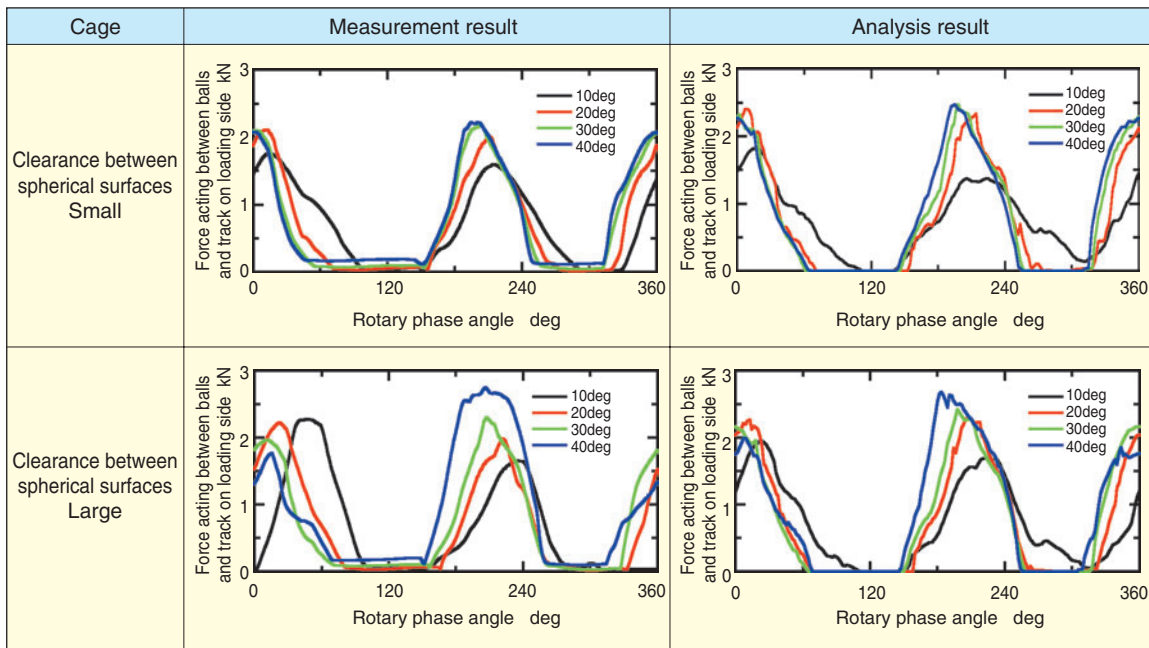


Fig. 12 The influence of clearance between spherical surfaces of cage and outer ring on loading side track load P_3 (Lubricant: A, Cage: A and B)

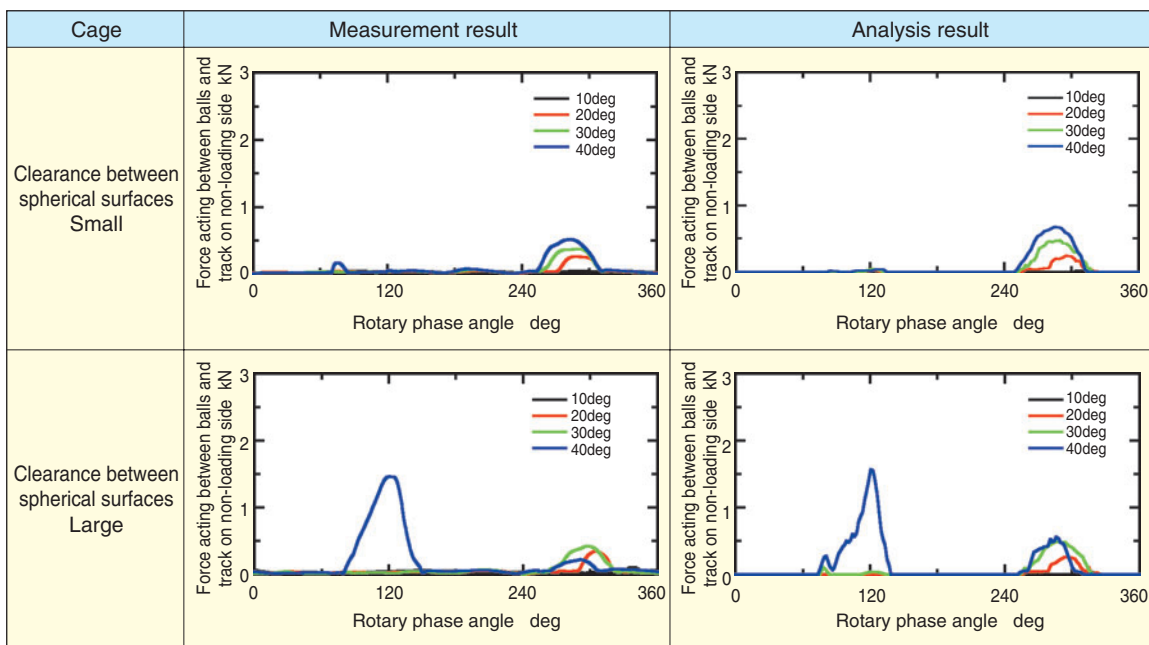


Fig. 13 The influence of clearance between spherical surfaces of cage and outer ring on non-loading side track P_4 (Lubricant: A, Cage: A and B)

summarized below.

Let us consider a situation with a greater clearance between the spherical surfaces. At a working angle of 40 deg and a rotary phase angle of 120 deg, a non-loading side track load is detected. The analysis result fairly well matches this finding.

5.2.3 Resultant force from spherical surfaces

A procedure similar to that described in Sec. 5.1.3 was performed. The resultant forces acting between the spherical surfaces (F) as well as the influence of resultant forces from the spherical surfaces are graphically plotted in Figs. 14 and 15. The so-obtained findings are summarized below:

With a greater clearance between the spherical surfaces, the resultant force from the spherical surfaces is lower and the vibration amplitude increases. The analysis result fairly well matches this finding.

6. Conclusion

We have not only developed a unique measuring technique for determining forces acting inside fixed constant velocity joints (previously extremely difficult task) but also verified reliability of analysis result that are obtained from the already developed dynamic general-purpose mechanism analysis software-ADAMS. In addition, we have clarified that the forces acting within any fixed constant velocity joint are affected and varied by the magnitude of the coefficient

of friction of the lubricant used, and the dimension of the clearance between spherical surfaces. As a result of our verification work, the optimized design for a fixed constant velocity joint can be now analyzed easily and accurately in a shorter time span.

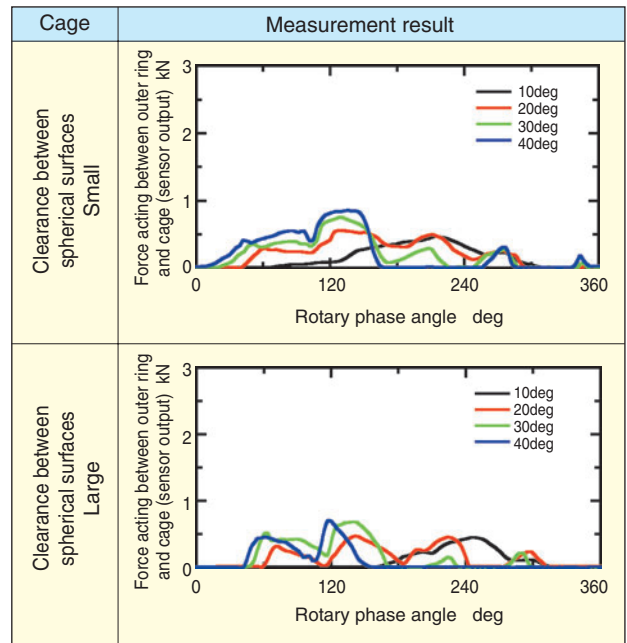


Fig. 14 Measurement results of forces F acting between outer spherical surface of cage and inner spherical surface of outer ring (Lubricant: A, Cage: A and B)

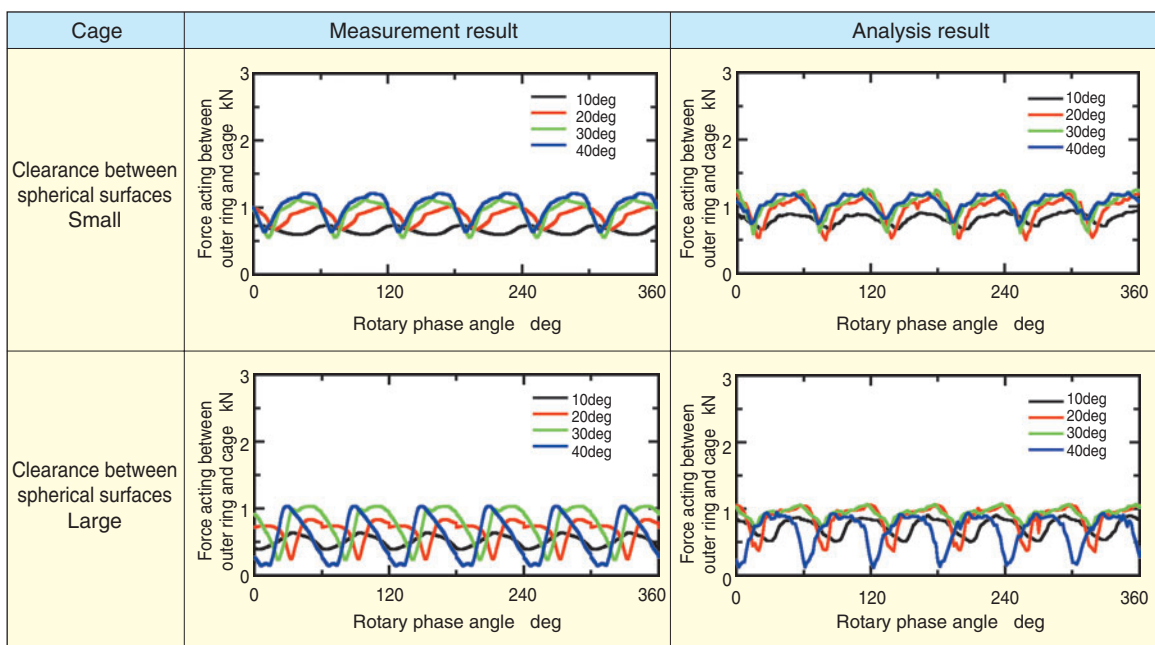
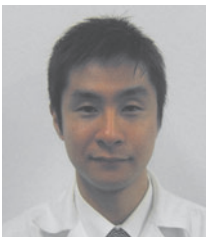


Fig. 15 The influence of clearance between spherical surfaces of cage and outer ring on resultant forces acting between outer spherical surface of cage and inner spherical surface of outer ring (Lubricant: A, Cage: A and B)

References

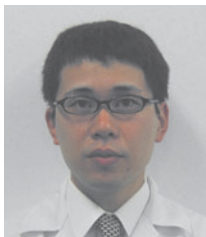
- 1) Kei Kimata: Friction and lubrication in constant velocity joints, Lubrication, vol.31 No.10 pp.697-702 (1986)
- 2) Kei Kimata, Haruo Nagatani, Masayuki Imoto, Takeshi Kohara: Numerical Analysis and Experiments on the Characteristics of Ball-Type Constant-Velocity Joints, Transactions of the Japan Society of Mechanical Engineers. C, vol.69, No.678 pp.487-495 (2003)
- 3) Nozaki, Kohara: Experimental determination of forces acting on tripod constant velocity joint housing, the Japan Society of Mechanical Engineers, 2003 annual meeting preceedings, pp.155-156 (2003)
- 4) Yoshihiko Hayama: Dynamic Analysis of Forces Generated on Internal Parts for Ball-Type Constant Velocity Universal Joint; Double-Offset-Type and Ball-Fixed-Type, JSAE Transactions vol.34, No.4 pp.154-162 (2003)
- 5) Yoshihiko Hayama: Dynamic Analysis of Forces Generated on Internal Components of a Double Offset Constant Velocity Universal Joint (DOJ) by Utilizing ADAMS software, NTN Technical Review, No.69, pp.97-102 (2001)
- 6) Okamoto, Hayama: Measurement of internal forces in fixed constant velocity joints (effects on friction), Japan Society of Mechanical Engineers Machine Design and Tribology Division Lecture Meeting, Meeting Proceeding, pp.151-152 (2006)
- 7) Okamoto, Akamatsu: Measurement of internal forces in fixed constant velocity joints (effects on friction), Tribology Conference Preprints, pp.139-140 (2007-5)

Photos of authors



Daiji OKAMOTO

New Product Development Dept.
New Product Development
R&D Center

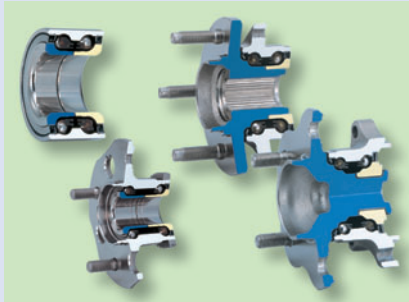


Hirokazu OOBA

New Product Development Dept.
New Product Development
R&D Center

Technical Trends in Axle Bearings and the Development of Related Products

Kiyotake SHIBATA*
Takayuki NORIMATSU*



Demand for lighter weight, more compact, and lower friction automotive parts is increasing rapidly with the purpose of improving fuel efficiency. NTN has developed various products in order to meet these demands. This report introduces these efforts for axle bearings.

1. Introduction

Among environmental issues, global warming seems to be responsible for the increased ambient air and seawater temperatures around the earth. Natural disasters seemingly resulting from global warming are occurring around the world. The Kyoto Protocol, which was passed in December 1997 and enacted in 2005, requires each member nation to reduce greenhouse gas emissions.

A major greenhouse gas is carbon dioxide (CO₂). To help reduce CO₂ emissions the automobile industry around the world has increased attempts to improve the fuel economy of their cars by employing lighter and lower-friction designs for their automotive components.

NTN has also been committed to this effort by offering lighter, lower-friction automotive components. This paper will discuss the following four points associated with the above-mentioned efforts:

- (1) **Topology technique-based super-light hub bearing**
- (2) **Positively sealed & low friction hub bearing w/ built-in seal**
- (3) **High load capacity tapered roller hub bearing**
- (4) **GEN4 (4th generation) hub joint**

2. Topology technique-based super-light hub bearing

Through the optimization of the hub flange shape we have minimized the weight of hub bearing design, thus leading to the successful development of a “super light-weight GEN3 hub bearing for economy vehicles” whose mass is only 1 kg (a 30% reduction compared to a conventional design).

We have applied our topology optimization technique to light-weight designs for GEN3 hub bearing products in an attempt to establish a technique that allows any person to obtain the optimal shape and succeeded in developing a significantly lighter hub bearing design.

2.1 Overview of topology optimization

Using the basic approach of topology optimization material is added to a key area while the thickness is reduced from less functional areas in order to attain a lean shape, while still maintaining mechanical strength and rigidity requirements.

The shape created using the topology optimization technique is usually a very complicated 3D shape. Consequently, a product with this shape cannot easily be produced with a standard industrial process and as a result it may be unjustifiably expensive. Therefore, we have to use a result of topology optimization as a starting point to develop a final and easy-to-machine shape.

*Axle Unit Engineering Dept. Automotive Sales Headquarters

2.2 Topology optimization

Through topology optimization, we are able to answer the question “what is an optimal structure for a given part so that the part can achieve its necessary functions?” This technique can assist in changing the structure of a mechanism dramatically.

(1) Analysis model

The analysis model used is illustrated in Fig. 1. Assuming that the hub spindle and inner ring are a single piece, a mesh topology was developed on this block to restrict the translation 3 degrees of freedom for the nodes at the bolt holes on the flange. As for the external load acting on the hub spindle, the load concentration was assumed to occur on the rolling surface by employing a rolling element load value that is obtained using a bearing internal force analysis program. At the same time we employed a rather larger region for a possible shape change (design region) and defined a region where shape change is impossible due to the mounting location on a counterpart member (non-design region), thereby

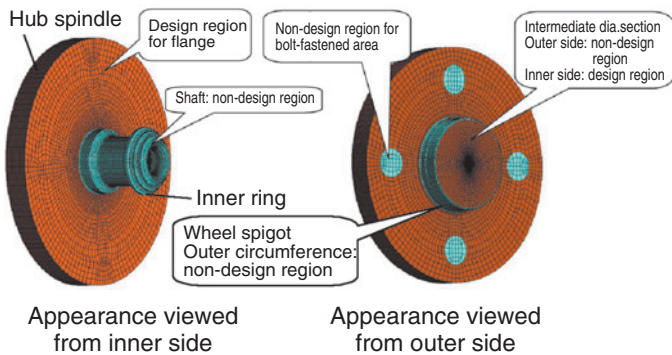


Fig. 1 Topology optimization model

executing an analysis operation (Fig. 1). The objective and constraint conditions applied are given below:

Objective: Strain energy minimization

Constraint conditions: 22.5%, 27.5% and 30% volumes relative to the volume, or mass, of the initial shape

(2) Analysis result

The shapes in Fig. 2 and the maximum stress data in Fig. 3 were obtained through the analysis operation. Fig. 3 shows how the stress greatly increases with an attempt for a lighter design. We have selected the shape at 27.5% (relative to the initial volume), which is closest to the threshold stress value as the basis for basic structure of the hub bearing.

2.3 New design

We also applied the above-mentioned technique for shape optimization of the outer ring. At the same time we achieved a light-weight arrangement to the bearing internal design by the development of materials and new grease, thereby finalizing the bearing

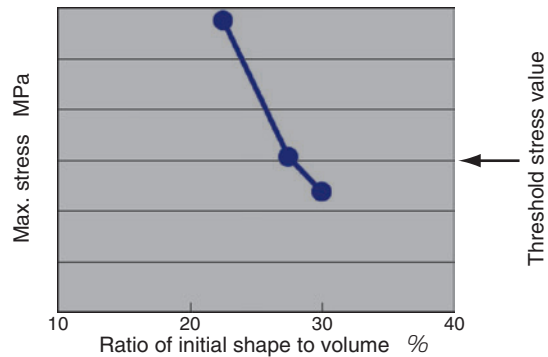


Fig. 3 Principal stress of each design

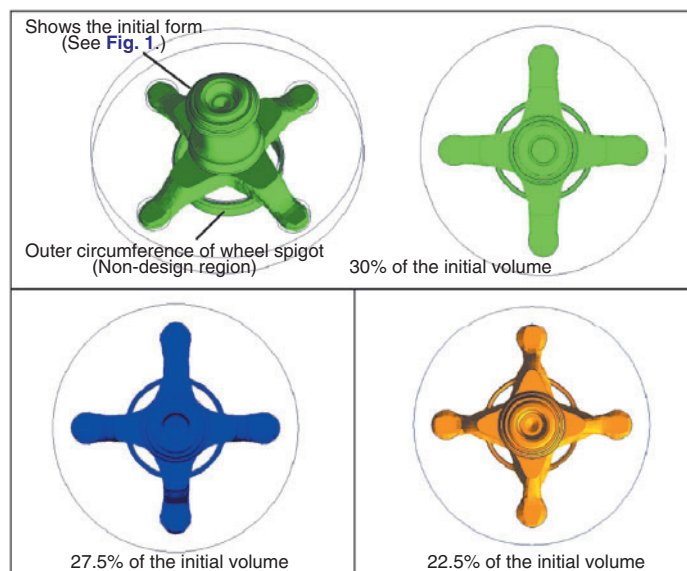


Fig. 2 Result of topology optimization

specification. The hub bearing we developed has the shape shown in Fig. 4. The final design attains the targeted mass of 1.0 kg while maintaining the desired strength, durability, and rigidity. The hub spindle and outer ring achieved weight reductions that are summarized in Fig. 5.

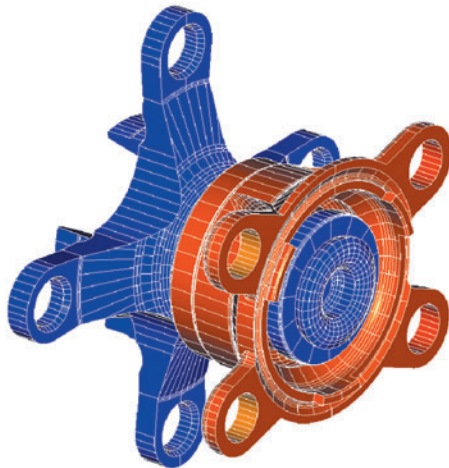


Fig. 4 Shape of final design

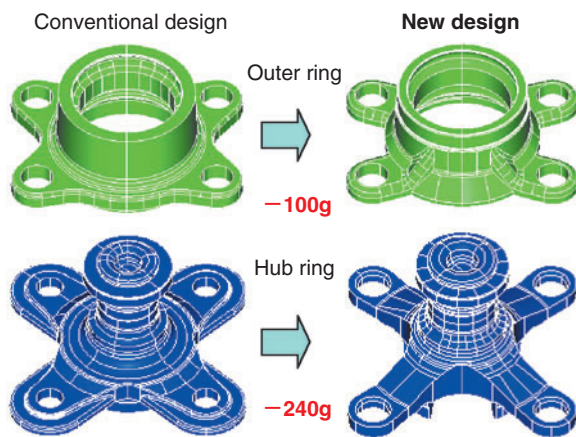


Fig. 5 Amount of each component lightening

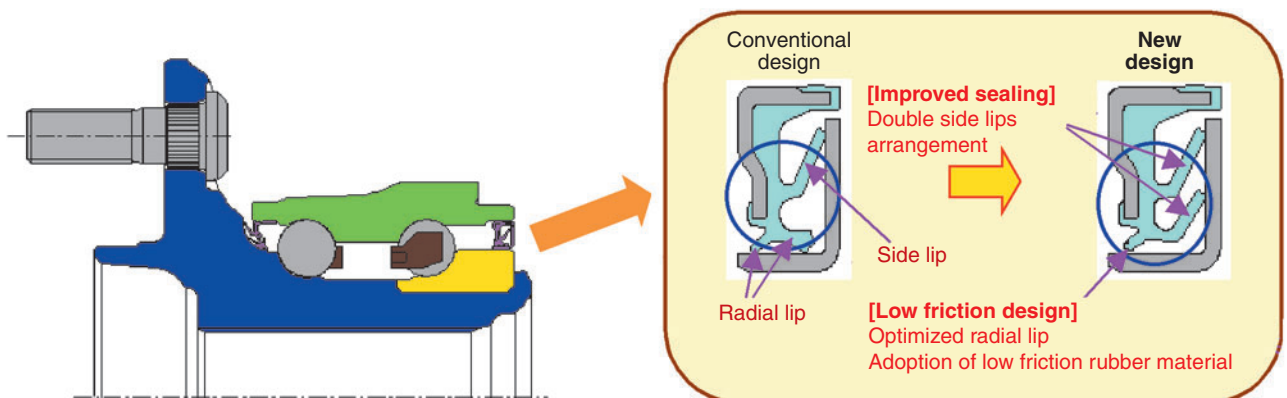


Fig. 6 High-sealing, low-torque hub bearing structure

3. Positively sealed & low friction hub bearing w/ built-in seal

Approximately half of rotational friction (rotational resistance) on a hub bearing is accounted for by sliding resistance of the seal. Reduction in sliding resistance of the seal contributes to greatly improved fuel economy of a given vehicle.

However, reduction in sliding resistance of the seal can also lead to poorer sealing performance. This creates a challenge for reducing rotational friction and improving seal performance.

NTN has created a seal that performs two times better than a conventional seal in regards to muddy water resistance and has a 15% reduction in rotational friction (30% reduction with seal alone) while maintaining the conventional seal space by: [1] adoption of low friction rubber material, [2] low friction design through optimization of the radial lip, and [3] improvement in muddy water resistance by incorporation of double side lips design.

3.1 Features

With a cross-sectional area same as that of the conventional seal:

- [1] Sealing performance (muddy water resistance): two times as great
- [2] Rotational friction of hub bearing: 15% reduction (30% with seal alone)

3.2 Structure

We adopted a low friction material with a unique rubber blend for the seals installed on the hub bearing in order to reduce rotational friction caused by the seal lips. We have also optimized the radial (grease) lip and introduced double side lips to satisfy the conflicting needs of improved sealing performance while reducing rotational friction (Fig. 6).

3.3 Performance

In **Figs. 7** and **8** the conventional design is compared with the new design by examining the results of muddy water resistance test and rotational friction test.

From the data in **Figs. 7** and **8** we can see that when comparing the conventional design with the new design, the muddy water resistance is improved two times and there is a 15% reduction in rotational friction within the entire bearing (30% reduction with seal alone).

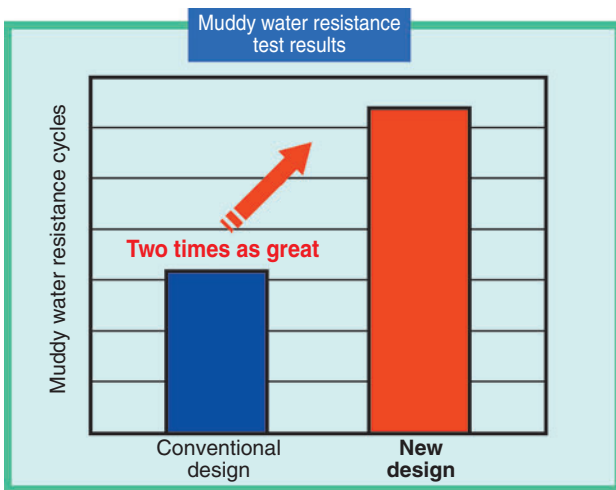


Fig. 7 Muddy water resistance test results

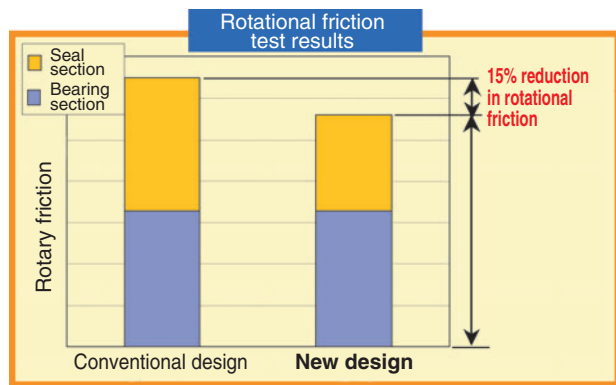
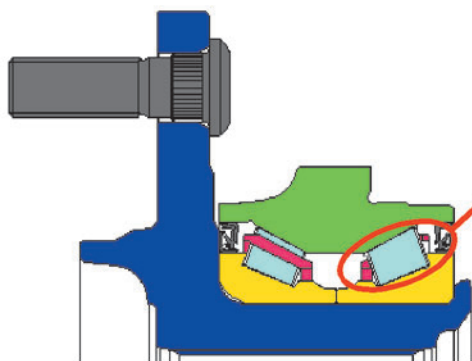


Fig. 8 Rotational friction test results



4. High load capacity tapered roller hub bearing

Passenger cars use hub bearings whose rolling elements are steel balls, while many pickup trucks and SUV's use tapered roller hub bearings whose rolling elements are tapered rollers. Tapered roller bearings have a greater load capacity and higher rigidity when compared to ball bearings.

NTN has thoroughly re-evaluated the previous internal design specification for its tapered roller hub bearings and has successfully developed a unique high load capacity tapered roller hub bearing. The number of the rollers can be maximized (approximately same as with a full complement roller bearing) without reducing the cage strength by situating the cage nearer to the outer ring in order to reduce the roller-to-roller clearances; this results in the size of the new tapered roller hub bearing being the same as the old design. This new design has helped increase the bearing life by 20% and the bearing rigidity by 7% without increasing the bearing size.

4.1 Features

- [1] Longer bearing life: 20% increase in life (calculated life)
- [2] Greater bearing rigidity: 7% increase in bearing rigidity (comparison to old design)

4.2 Structure

The cage diameter is increased towards the outer circumference in order to realize a smaller roller-to-roller clearance dimension. The result of this is that the number of rollers on the new design can be as great as that of a full complement roller bearing of a similar size (**Figs. 9** and **10**).

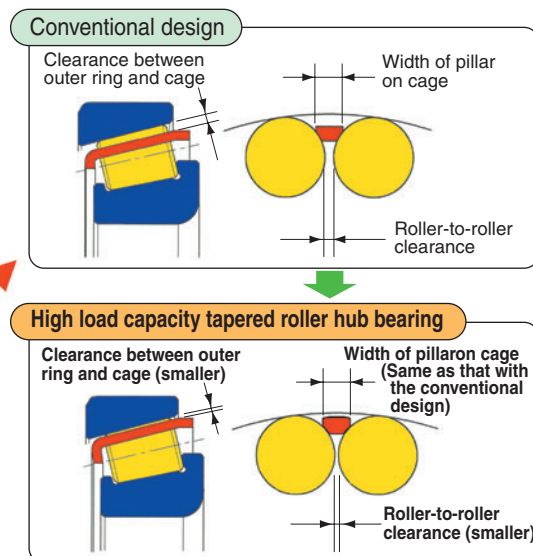


Fig. 9 High-load capacity tapered roller hub bearing structure

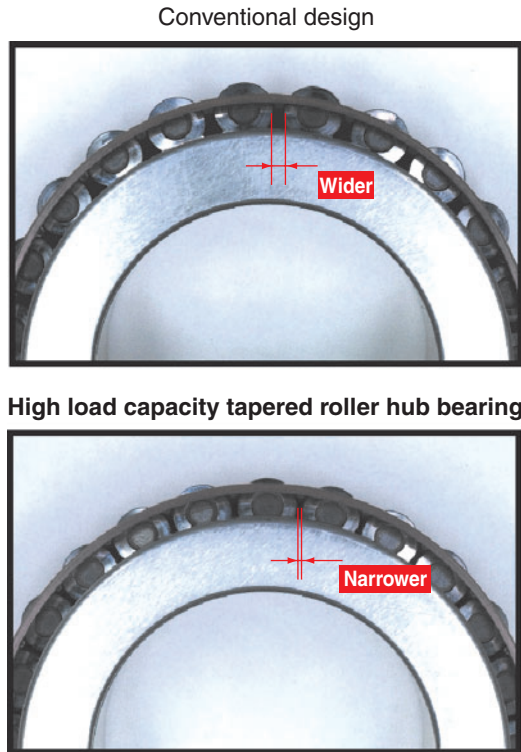


Fig. 10 Cage part appearance

4.3 Design study example

As described above, the new high load capacity tapered roller hub bearing will offer a longer life and a higher rigidity compared to that of a conventional design. The new bearing design can be more compact and light-weight without the need for an increase in the bearing diameter.

One design study example is shown in Fig. 11. The

outside diameter on the outer ring pilot section of the new design is 7 mm (6%) smaller and the resultant weight reduction is 400 g (6%).

5. GEN4 hub joint

NTN has developed a 4th generation hub joint product series (GEN4 H/J) by integrating a constant velocity joint (CVJ) with a hub bearing (H/B). This product line contributes to lighter weights, more compact sizes, higher rigidity and easy assembly procedure for axles. The structural features and basic characteristics of the GEN4 H/J products are described below.

5.1 Structure

NTN's newly developed tube forming method is applied to GEN4 H/J as a method for fastening the H/B to the CVJ outer ring. This tube forming method for the GEN4 H/J is described below:

- [1] By knurling, square pyramid shaped knurls are formed inside the bore surface of the hub.
- [2] The entire area containing the knurls is hardened through heat-treatment. The appearance of the knurled area including the knurls is shown in Fig. 12.
- [3] A punch is driven into the bore of the stem on the CVJ outer ring to expand the stem in the circumferential direction, so that the stem is formed to the knurls (Fig. 13).

The area where the stem is formed to the knurls is hereinafter referred to as the expansion-formed section.

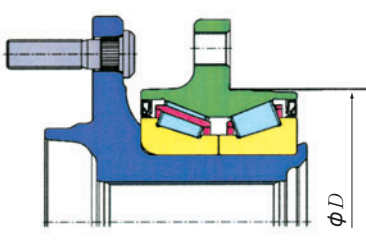
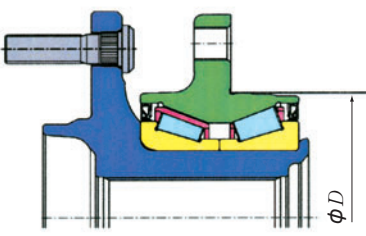
Specification	Scheme	Compactness (ϕD)	Lightness
Conventional design		Basic diameter	Basic weight
New design		-7mm (6%)	-400g (6%)

Fig.11 High-load capacity tapered roller hub bearing study

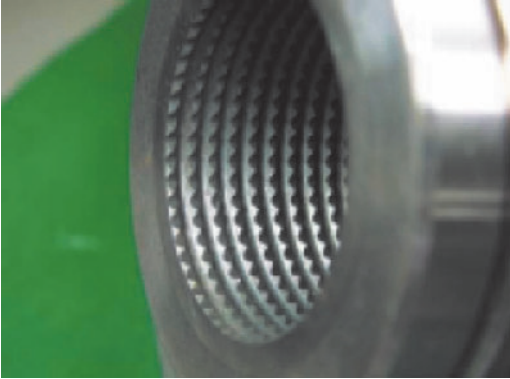


Fig. 12 Knurl appearance

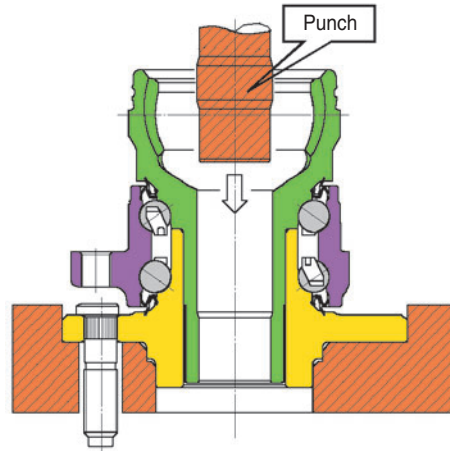


Fig. 13 Tube forming method

5.2 Advantages of new design

Another feature of the GEN4 H/J is that the raceway surface of the H/B is directly formed on the CVJ outer ring. At the same time, by adopting a high efficiency CVJ (EBJ), the GEN4 H/J offers the following advantages:

(1) Light-weight, compact design

The weight is reduced which in turn contributes to improved handling, stability of the vehicle, and better fuel economy.

(2) Improved degrees of freedom for suspension design

A shorter axial distance between the hub flange and the CVJ helps to increase the degrees of freedom for suspension design. The GEN4 hub joint can be applied to a suspension of a complicated structure to help improve handling and stability of the vehicle.

(3) Easy assembly and improved serviceability

The GEN4 H/J assembly (outboard-side fixed H/J, intermediate shaft and inboard-side plunging joint) is

structured so that the entire H/J assembly can pass through the bore of the knuckle (Fig. 14).

Consequently, component handling on the vehicle assembly line and serviceability in the market are improved.

5.3 Design study example

The structure and advantages of the GEN4 H/J have been presented so far. Concrete data for possible reduction in weight and size is described below, which refers to a study using a large-sized FF layout car with an engine displacement of 3 liters (Fig. 15).

As summarized in Fig. 15, compared with a configuration that is based on a conventional GEN3 H/B and CVJ the new design contributes to an 800 g (14%) weight reduction per wheel and a 22 mm (20%) size reduction per wheel.

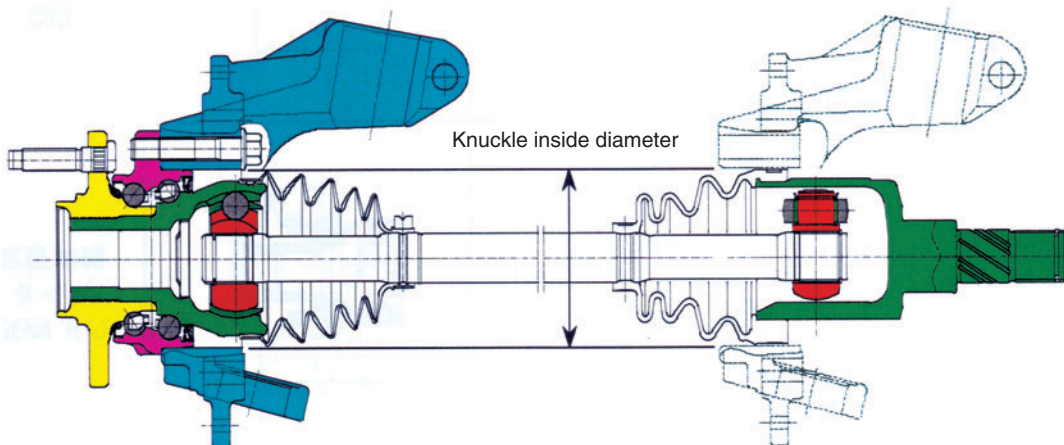
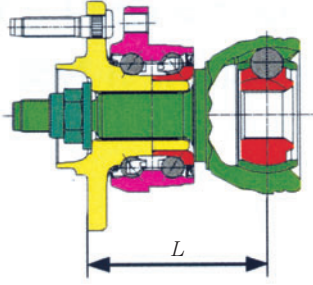
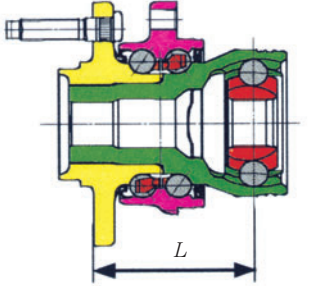


Fig. 14 Easy assembly and improved serviceability

Specification	Scheme	Lightness	Compactness**
Conventional design GEN3 H/B + CVJ		Basic weight	Basic length
Expansion-formed type GEN4 H/J		-800g (14%)	-22mm (20%)

*Comparison in terms of the axial distance between the hub flange and CVJ center.

Fig. 15 GEN4 H/J study

5.4 Evaluation test

The following bench tests were performed to verify that the strength and durability of the expansion-caulked section are at least equivalent to those of nut-fastened section and oscillation-formed section.

Bench tests

- (1) Pulling force measurement
- (2) Static torsional strength measurement
- (3) Torsional fatigue strength test
- (4) Rotary bending test

In addition, to evaluate the overall durability of the GEN4 H/J we have successfully tested this line of bearing products on actual cars (overturning moment test, full steering & violent start test, etc.) without any issues.

6. Conclusion

We have presented our efforts for reduction in weight and friction with axle bearings in order to improve fuel economy and to help reduce pollution. Though a lighter weight is an important requirement, the axle bearings must maintain their basic functions by supporting the axles and smoothly running.

To satisfy the ever mounting needs for better fuel economy, NTN will fully utilize the items mentioned above and commit to development a novel technology that ensures a highly reliable and robust design practice.

References

- 1) Haruo Nagatani, Tsuyoshi Niwa: NTN Technical Review, No.73 (2005)
- 2) Shigeaki Fukushima, Hiroyuki Ogura: NTN Technical Review, No.70 (2002)

Photos of authors



Kiyotake SHIBATA

Axle Unit Engineering Dept.
Automotive Sales Headquarters

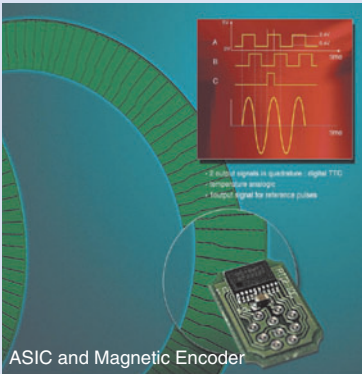


Takayuki NORIMATSU

Axle Unit Engineering Dept.
Automotive Sales Headquarters

Development of High Resolution Sensor Element MPS40S and Dual Track Magnetic Encoder for Rotational Speed and Position Measurement

Pascal DESBIOLLES*
Achim FRIZ*



Higher precision and resolution requirements for rotational speed and position sensors in automotive and other applications lead SNR to investigate in the potential of their ASB¹⁾®-Technology, where magnetic single track encoders have been integrated in wheel bearings and serve together with small active sensors for detecting the speed of each individual wheel of a car. Such information is used for ABS²⁾, ASR³⁾, ESC⁴⁾ and other car systems.

Based on this well proven technology, which is installed in over 50 million cars now, SNR has developed two new basic components to improve the performance of such sensing systems. The magnetic sensor ASIC⁵⁾ MPS40S in combination with a new dual track magnetic encoder provides high resolution speed and incremental position signals, with direction of rotation and additionally the possibility of reference or index signals for absolute position determination.

1. Introduction:

The industrial developments go more and more into electric devices and even traditional mechanical systems become electrically assisted, such as manual gearboxes, steering systems etc.... So the need for precise and reliable sensor is continuously increasing. At the same time the cost factor becomes more and more important. Since SNR has introduced the ASB[®] Technology for wheel speed detection in cars, which became a world standard now, the research efforts in that domain have lead SNR to develop not only magnetic encoders with better magnetic material and higher precision, but also sensing elements in order to implement more functionality in the Sensor Bearings. At the SNR Mechatronics Department in Annecy, France, basic developments and research programs are conducted especially for magnetic sensor devices as these are seen as robust and cost effective solutions, which can work even in harsh environment situations. The performance of the latest sensor development is presented in this paper as well as a short overview of the technology.

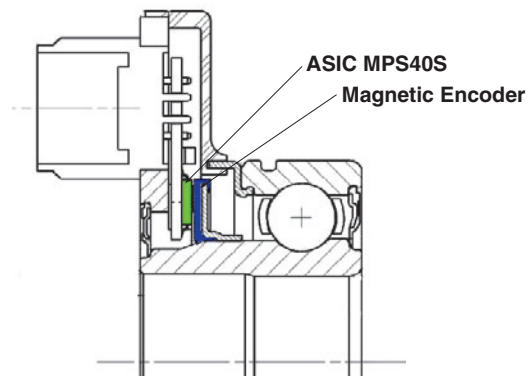


Fig. 1 Section of high resolution sensor bearing

- 1) Representing "Active Sensor Bearing" named by SNR.
- 2) "Anti-lock Brake System".
- 3) "Anti Slip Regulator" or "Anti Skating Regulation system".
- 4) "Electric Stability Control"
- 5) "Application Specific Integrated Circuit".

*SNR Mechatronics Research & Development

2. Sensor Components:

2.1. Magnetic Encoder

At the end of the eighties, SNR developed a first magnetic multi-pole encoder, which was integrated in a sensor bearing. Meanwhile such encoders are to be found in many different sensor bearings typically in combination with standard Hall or MR elements. This was one of the basic components of the ASB[®] system. The qualification program for the magnetic encoders especially for automotive wheel applications proved the robustness of the design; none of water, salt, mud or small metallic particles could disturb the quality of the signal. Today SNR is introducing a new generation of magnetic encoders with a second track in the same space of the single track encoders. With the second track it is possible to put one or more reference points on the encoder, which indicate an angular position of the encoder. The magnetisation process has been adapted for such dual track encoders, as the magnetic field has to be well controlled in order to minimise the influence from the magnetic poles of the reference track to the high resolution track. **Fig 2** shows the different types of magnetic encoders and the corresponding magnetic fields. Following the points ① to ⑥ show the variation of the magnetic field strength, which is seen by the sensor. Standard Hall or MR (magneto resistor) elements cannot interpret such field configurations and would lead to a false signal. Therefore SNR has developed a new sensing element which shall be described paragraph 2.2.

In **Fig 3** is shown how the magnetic poles look like on a real encoder. At the inner circle of the magnetic encoder the poles are all the same size. On the outer circle this is not the case; the red points indicate the positions where the reference pulse is generated. The poles are visualised with a special magnetic film, so that the two tracks with the phase shift change between the poles can be seen easily. Furthermore

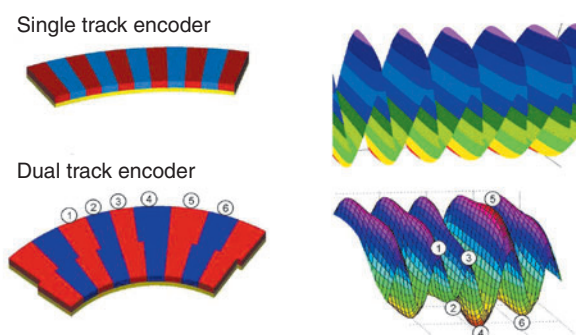


Fig. 2 Scheme of single and dual track encoder

it is shown that such phase shift changes, resulting in a reference pulse signal, can be put on every single pole pair of a north and a south pole. The poles are separated by a straight transition line, when a signal shift from 1 to 0 or from 0 to 1 is implemented. On this sample a special pattern of 65 pole pairs is implemented. The position of the reference pulses has been calculated according to the application specification. Theoretically it is possible to put as much reference pulses as pole pairs on a magnetic encoder of this type. SNR developed a special magnetisation process to improve the pitch error that is very important for such a device. The phase shift of the transitions over one pole pair in Y/Z direction is depending on the calculated nominal airgap (X direction) in order to get acceptable mounting tolerances. Field simulations helped to optimise the magnetisation tool, which is specific for different reading diameter and airgap. The standard magnetisation tools do not provide sufficient precision for the dual track encoder.

2.2. Magnetic Sensing Element MPS40S

The magnetic field sensor ASIC MPS40S integrates a first array of Hall elements for high resolution purposes and a second array which reads the second track of above described magnetic encoders in order to create reference pulses. On the MPS40S block diagram, **Fig 4**, some of the features are directly shown. In order to make this device as flexible as possible, some features have been implemented which are patented. The MPS40S can read a wide range of magnetic pole widths, which is new

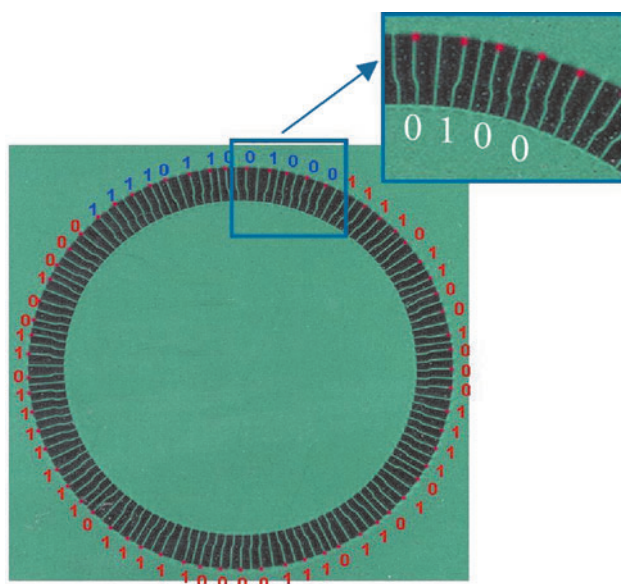


Fig. 3 Magnetic encoder with reference track and signal status

compared to magnetic wheel speed sensors, the pole size can be programmed which makes the reading even more precise. A very special interpolator block on the die of the MPS40S allows raising the resolution over one pole pair. The interpolation factor is also programmable as shown in **Table 1**. Furthermore the MPS40S provides the direction of rotation from 90° phase shifted signals A and B. In parallel such magnetic encoders, which may be integrated in a bearing seal, have been designed by adding a second magnetic track in the same envelope of the series

product. The second track is read by the MPS40S simultaneously and provides angular position information of the magnetic encoder. The magnetisation process is done in a way that even existing designs of magnetic encoder seals can be magnetised with the new dual track for existing product improvement. In this case only the sensor head has to be adapted for integrating the MPS40S. For a better understanding the signals are shown in **Fig 5**, where the analogue signals input from both tracks are compared to the digital signals. Reading

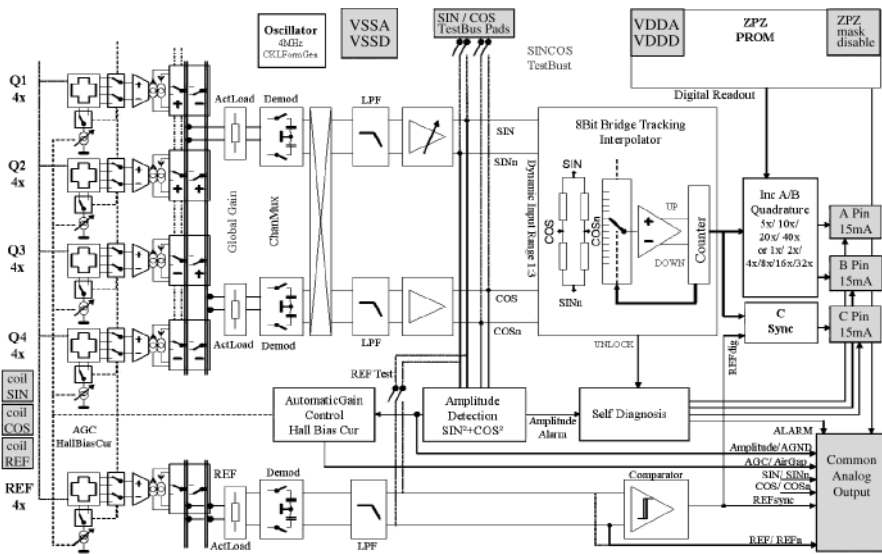


Fig. 4 MPS40S block diagram

Table 1 Interpolation factor programming table

Interpolation	1x	2x	4x	5x	8x	10x	16x	20x	32x	40x
Pulses ¹⁾	32	64	128	160	256	320	512	640	1024	1280
Edges ²⁾	128	256	512	640	1024	1280	2048	2560	4096	5120
Resolution ³⁾	2.8°	1.4°	0.7°	0.5°	0.35°	0.25°	0.18°	0.12°	0.08°	0.07°

1) Based on a 32 pole pair encoder 2) Number of raising and falling edges of the signal output lines
 3) Resolution, when using all edges of the signals

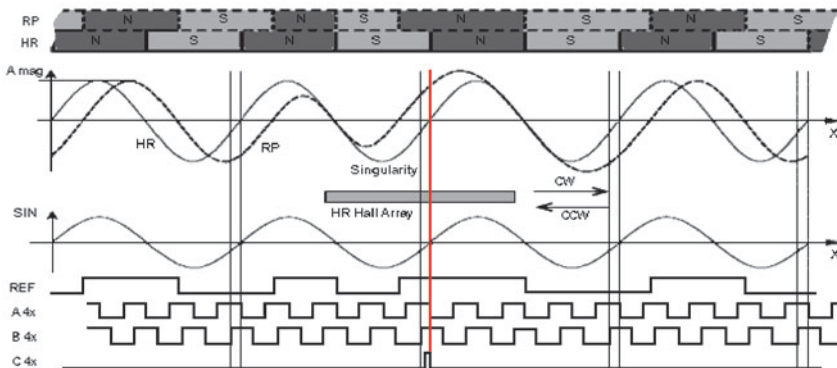


Fig. 5 MPS40S signals

from left to right is the clockwise direction and from right to left the counter clockwise direction of rotation, in any case the reference pulse comes at the same position by internal comparison of the high resolution input and the reference input.

Features of the MPS40S combined with Dual Track Magnetic Encoder:

- **Non contact sensor concept**
- **Compact design, smallest reading diameter:**
 ϕ 35mm
- **Temperature range: -40°C to +125°C**
- **Compatible with harsh environment, dust, mud, water, oil ...**
 A lot of tests have been done, when this encoder material has been qualified for automotive applications such as encoder for wheel bearings in cars. All car manufacturers have released our products for such application.
- **Wide range of magnetic pole width: 1.15mm to 6mm, with a pitch of 0.02mm**
 Over the pole width, combined with the interpolation factor, almost all resolutions can be achieved. The pole width is programmable.
- **Flexible design of magnetic encoders, number of pole pairs, ...**
- **Automatic Airgap Adjustment, within the detectable magnetic field ($\geq 5\text{mT}$)**
 In case the detectable magnetic field becomes too small, the MPS40S sets an alarm.
- **Programmable Interpolation Factor: 1x to 40x**
 The different interpolation factors are shown in [Table 1](#).
- **Direction of rotation information**
 By reading the A- and B-signal, which are 90° phase shifted. The raising edge which comes first, whether on A or B indicates the direction of rotation (shown in [Fig 5](#)).
- **Reference pulse information (1 or more on the magnetic encoder)**
 The MPS40S compares the magnetic fields of both tracks, shown in [Fig 5](#). On the C-signal line a pulse is sent, when at the Zero-crossing of the A-signal the positive field of the RP-track is above the threshold, as shown on the red line in [Fig 5](#). Obviously this can be repeated on every pole pair on the magnetic encoder.
- **Self diagnostic features integrated in the MPS40S**
 As already mentioned, the MPS40S can detect failures concerning the magnetic field out of the detectable range, but also internal failures. In this case the MPS40S sends a failure message via the three output lines.

- **Test bus, for application development purposes**

The output of the test bus is programmable for analogue and digital signal readings.

- **AEC Q100 qualification**

3. Applications and some examples:

Such a sensor concept can be used in many industrial applications, where speed and position have to be measured on hollow shafts or where the end of a rotating shaft cannot be accessed. As the sensor head is very small and the encoder can be integrated in any rotating part, such as a bearing, applications with reduced available space may be interesting as well.

Steering Angle Sensor, a joint development with Continental Automotive Systems:

Sensor and encoder may be separated or integrated, both designs are under development. First series production developments have been started. In [Fig 6a](#) the separated version of the steering angle sensor is integrated lower part of the steering system. This is the most effective design in terms of space and cost and it can be even improved if the magnetic encoder can be integrated in a bearing, which is shown in [Fig 7](#). Therefore the bearings must have a section, which is big enough to get the encoder, and there must be a "window" to this section where the sensor can read the two magnetic tracks.

For more conservative designs the angle sensor can be packaged in a plastic housing, where airgap is controlled by internal design, shown in [Fig 6b](#). The sensor is mounted with screws and the steering shaft goes through the sensor. This takes more space and makes replacement more complicated, as the steering shaft has to be disassembled. Compared to this, the separated design is more convenient as the electronic part of the systems can be taken out easily and the magnetic part, which is mounted to the steering shaft, is not affected. In each case the sensing concept is contactless and does not add any torque to the steering system, neither any noise. Both points are very important for such applications as noise and torque are directly felt by the driver.

EPS motor position sensor:

Sensor and encoder are separated; the encoder is integrated in a ball bearing

The same sensor concept can also be used in the rotor position sensor for electric motors and actuators, such as EPS motors. Because of the high resolution capability of the sensor, this application is

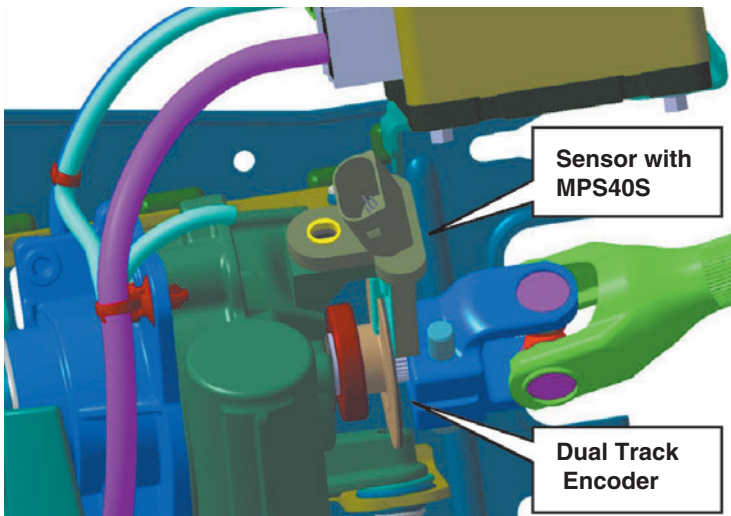


Fig. 6a Steering angle sensor SNR/Continental automotive systems

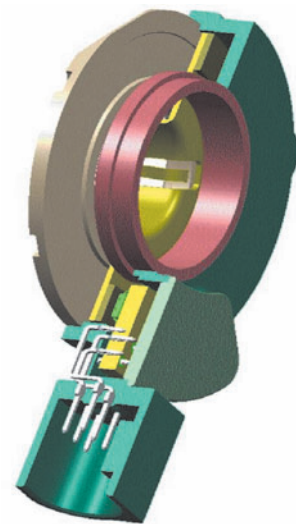


Fig. 6b Steering angle sensor

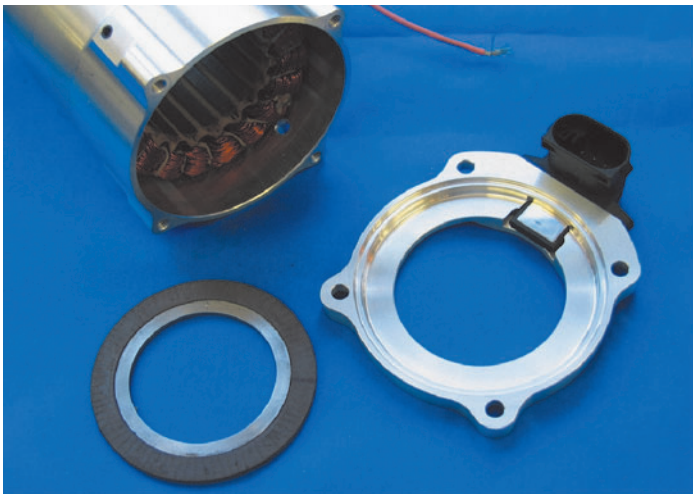
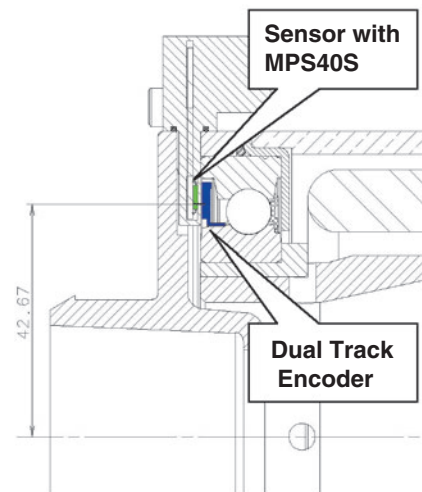


Fig. 7 EPS motor with sensor and encoder bearing



interesting, especially if no sensor can be placed at the end of the motor shaft. The magnetic encoder pattern on the second track is then designed to get absolute position over one electrical period and repeat this pattern for all pole pairs of the motor. Patents have been filed for the special way of the pattern layout for such applications. Even if the sensor is not absolute true power on, with the special pattern the absolute rotor position can be determined within a small angle at power on and from this point the sensor works like an absolute angle sensor. The enormous advantage is again space and weight saving compared to any resolver technology. Furthermore if the motor design has to be changed in terms of number of pole pairs on the rotor, the sensor design does not change, only the magnetic encoder gets a different magnetisation and the programming of the chip may be adapted.

The flexibility of the sensor with the MPS40S helps to accelerate the development of new motors as the programming is done through the Vdd pin. It is very easy to test new configurations without changing the mechanical environment.

High Resolution Sensor Bearing for Industrial Applications

The demand for sensor bearings in Industrial Applications is also increasing and the SNR technology can be applied easily in the same way. However the design should be more integrated to ease assembly and therefore SNR created a first sensor bearing design which uses all functions of the ASIC and fits into ISO dimensions regarding inner and outer diameter of a 6203 deep groove ball bearing. This bearing is available as a prototype as the engineering department at SNR prefers to

develop such type of bearing as an integral part of a complete system optimised for the final application in terms of environmental requirements, assembly, space and cost. Our experience shows that too often a standard design does not perfectly fit in the design of the application and we are forced to modify the "standard" product. Today SNR has all the necessary components in order to develop rapidly the product which fulfils the customer requirements at an attractive price.



Fig. 8 Sensor bearing

Radial Sensor – Incremental High Resolution Signals

Finally the last product developed as a standard sensor without bearing, SNR developed the Radial Sensor, which is also using the SNR ASIC. It delivers incremental speed and angle measurement signals. It is not foreseen that this encoder provides the Reference Pulse signal output; however full programming capabilities concerning pole width and resolution are implemented. This sensor works together with radial single track magnetic multi-pole encoders, which can be found on the market. The electrical interface is designed to work with different supply voltages from 5 to 8-30V and the output stages are realised as Push/Pull.

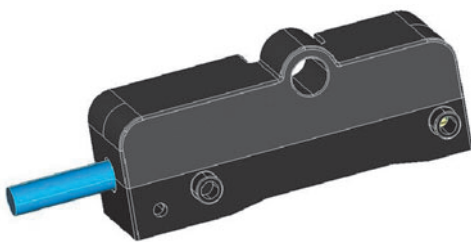


Fig. 9 Radial sensor

4. Conclusions

The newly developed technology by SNR is mainly designed for mass production systems, where the focus is on reliability in first place and seconds the cost. Hall Effect based sensor technology is proven in industry since a very long time and the improvements that SNR has integrated in the ASIC MPS40S make full profit of that background. Furthermore the very long experience in magnetic encoders for applications such as automotive wheel bearings, where water, mud, high and low temperatures are the normal environment, is the perfect base for SNR, who invented that technology and introduced it to the market in 1997, to make the next step in magnetic sensing technology. The very flexible combination of both components by programming of the MPS40S and adapting the magnetic encoders in terms of number of pole pairs, size etc makes it easy to find a solution. The engineering departments at SNR have all the tools to develop the integration of such sensor devices in many applications, even close to strong magnetic fields from electric motors or other harsh environment conditions. With all this benefits, this technology has a very good market potential in many industrial branches.

Photos of authors



Pascal Desbiolles

SNR Mechatronics
Research & Development



Achim Friz

SNR Mechatronics
Research & Development

Tube Forming Simulation in a Generation 4 Hub joint

Akitoshi IMOU*
Takehiro TAKANO*



Accurate CAE analysis is a very useful tool for shortening development timing and reducing the frequency of development trials. In this report, we introduce the process of improving CAE accuracy in plastic forming, which is an NTN original method of combining HUB and CVJ.

1. Introduction

The need for lighter automotive components has been ever mounting in order to realize more maneuverable, less energy-consuming cars. Improved functionality, lighter weight and reduced size have been required for wheel bearings. In this context, NTN developed the first generation hub bearing (GEN1 H/B) that combined two previously separate bearings. The GEN2 and GEN3 hub bearings (H/B) each incorporated not only a stem (hub ring), which is a peripheral component of a bearing, but also a portion of housing. The NTN GEN3 H/B products are widely used by car manufacturers today ¹⁾.

Aiming at lighter weight and more compact size, NTN has developed the fourth generation hub joint (GEN4 H/J) that combines a constant velocity joint (CVJ) and a GEN3 H/B with each being a bearing peripheral component ²⁾.

H/B product design requires strength analysis by a finite element method (FEM). This practice is very effective in decreasing the number of prototypes, shortening the development phase, and reducing the mass of the product ³⁾⁻⁴⁾.

For the GEN4 H/J, we have introduced a novel fastening technique called the "tube forming method". Without FEM analysis extensive prototyping would be necessary to verify reliability of this technique. FEM analysis work prior to the fabrication of actual

prototypes has allowed the development work to be greatly accelerated. In this paper, we present the content of a FEM-based analysis technique developed for the novel tube forming method used as a fastening work for GEN4 H/J.

2. Overview about the newly developed tubeforming method

The newly developed technique of tube forming is utilized by NTN to fasten the hub ring to the CVJ outer ring (Fig. 1). The basic process of the tube forming method can be summarized as follows:

- 1) Inside the hub bore, square pyramid shaped knurls are formed through a process known as 'knurling'.
- 2) The knurls are hardened by heat-treatment.
- 3) A punch is driven into the stem bore on the CVJ outer ring to expand the stem in the circumferential direction so that the outer circumference of the stem is engaged with the knurls (Fig. 2). As a result, the stem is fastened to the hub ring securely and the bearing is preloaded in an appropriate range.

The section where the knurls engage with the stem is hereinafter referred to as the "expansion-caulked section". The appearance of knurls formed inside the hub bore is shown in Fig. 3.

*Automotive Engineering Dept. Automotive Sales Headquarters

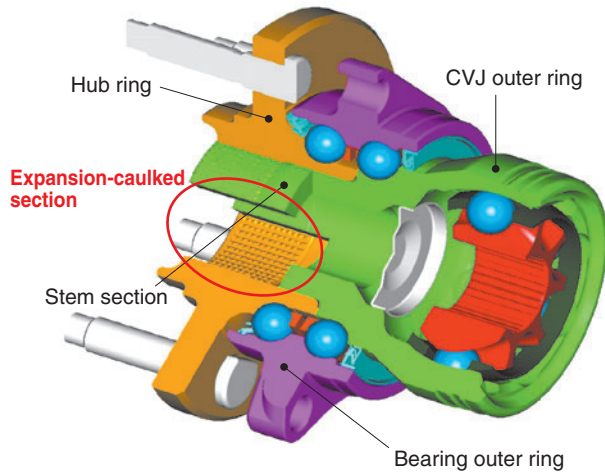


Fig. 1 Tube formed Gen4 H/J

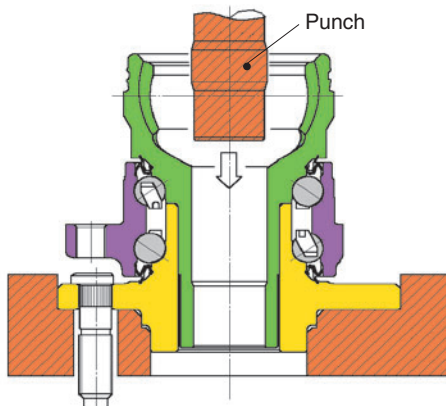


Fig. 2 Tube forming method

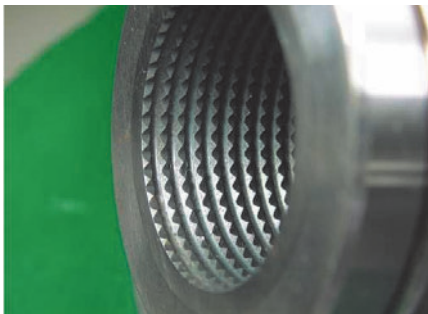


Fig. 3 Knurl appearance

- (a) Hub rings and CVJ outer rings are elasto-plastic solid (s).
- (b) The punch was treated as rigid due to its stiffness relative to the stem.
- (c) Nodes on the hub ring flange, hub ring itself, and CVJ outer ring surface were fixed in the axial direction.
- (d) Contact were defined at locations where the hub ring is in contact with the CVJ outer ring, and where the CVJ outer ring is in contact with the punch.

3.2 Results from the initial model

At first a static FEM analysis method was applied. A balancing condition was to be determined for each step in engagement process with the knurls. Consequently, an unjustifiably long calculation time was needed. To address this problem, we attempted to determine whether a dynamic explicit method could be used for the analysis. The result obtained from a dynamic explicit method on the analysis model in Fig. 4 is illustrated in Fig. 5.

The overall trend of the engaged knurls and stem bore deformation mode in the analysis results matched the measurement results:

- [1] The error in circumferential displacement on the stem bore relative to the measurement result is 5%.

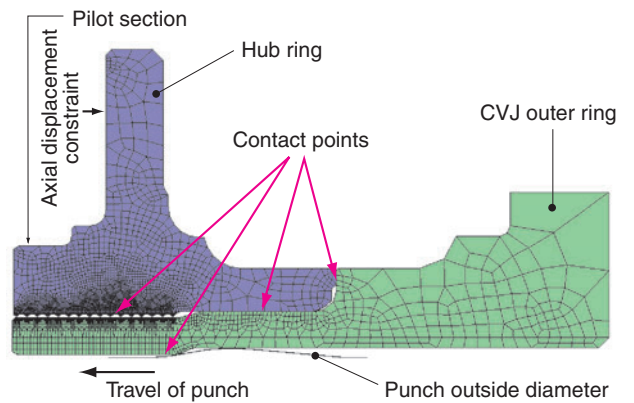


Fig. 4 Calculation model

3. FEM-based analysis for tube forming

3.1 Analysis model

As shown in Fig. 4, our analysis model comprised a hub ring, CVJ outer ring, and punch. The punch model consisted of its outer circumference surface that is in contact with the CVJ outer ring. Due to the symmetric structure, the expansion-caulked section was modeled according to the 1/2 pitch with the knurls on the circumference. The assumptions for the testing are as follows:

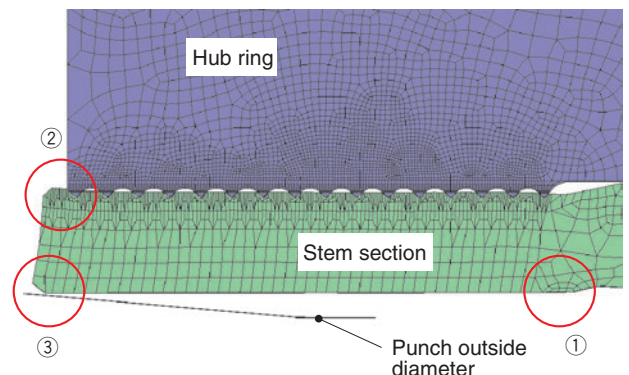


Fig. 5 Tube forming simulation result

[2] The expansion at the end of the expanded portion is outward.

[3] The axial elongation over the entire length of expanded portion, as well as the elongation at the end of expanded portion are greater in the bore side rather than in the outer circumference side.

The trends with the earlier models were consistent with the measurement result, and it was apparent that analysis for the tube forming process was possible. However, some factors in the analysis results, such as excessive punch load and depth of engagement with the knurls, did not match the measurement result. In order to correct this, and provide more accurate results, the model was modified.

3.3 STEP 1

To correct the aspects whose analysis results did not match the measurement results, we attempted to improve consistency of the punch load. If the punch load (which is a macro characteristic) in the analysis results does not coincide with the measurement results, then factors such as the stress in the analysis results would also not coincide with those in the measurement results. Since analysis for the tube forming process is elasto-plastic, the results can vary depending on factors such as the material data in the plastic regions. For this reason, we obtained deformation resistance curve for the hub ring. Incidentally, for the first model, the friction coefficient occurring between the punch and stem bore was assumed to be 0.2. However, for the tube forming process a lubricant is applied to the punch, and the assumed coefficient was greater than the actual coefficient. Therefore, we varied the friction coefficient to allow the analysis results to coincide with the measurement results (Fig. 6).

3.4 STEP 2

In a metal forming process such as our tube forming process, wherein projections (knurls) could be expected to engage with a surface, the projections may fail to engage with the surface when the mesh is too coarse. To address this problem, the previous coarse mesh was replaced with a finer mesh. This makes the projections more positively and deeply engaged with the surface (the stem side is deformed in accordance with the contour of these projections). However, at the same time, deeper engagement by projections can cause the elements to have too much deformation and the elements can be disrupted. In an attempt to improve the engagement situation we varied the contact parameters. This did improve the situation although it did not fully solve the problem.

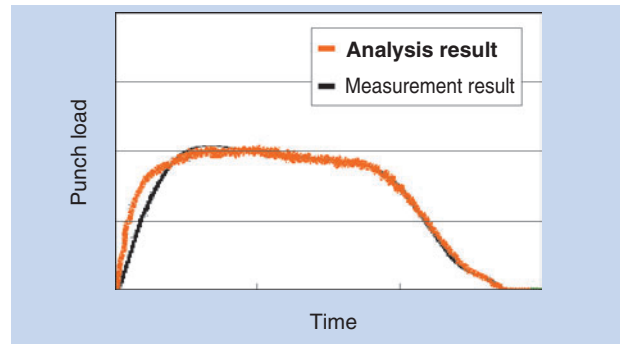


Fig. 6 Punch load

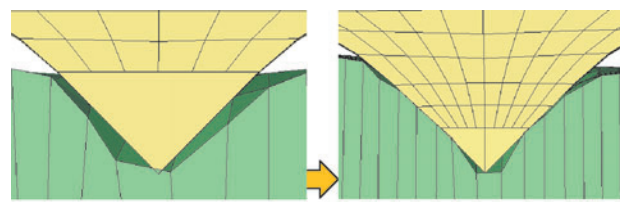


Fig. 7 Detail of tube expanding part

3.5 STEP 3

Next, let us compare the expansions on the outer circumference of the pilot section. The expansion value in the analysis results was about one half of that found in the actual measurement results making the value of circumferential stress occurring on the pilot section lower than expected. Therefore, to investigate the influences of unknown factors on the expansion of the outer circumference of the pilot section, we investigated the following:

[1] Finer mesh for the stem section:

In addition to the axial mesh in STEP 2, a mesh more finely divided in the circumferential direction on the CVJ stem was used to simulate the deformation on the stem section.

[2] Altered shape for the projection tips:

The tip shape of the knurls was measured, and the actual shape was reflected in the analysis model.

[3] Alteration to the initial clearance on the stem as well as to the expansion allowance:

The initial clearance between the stem outside diameter and the inside diameter of the knurled bore as well as the expansion allowance between the punch and the stem bore were converted into the measurement result.

[4] Alteration to the material characteristics for the stem section:

In addition to the deformation resistance curve for the hub ring obtained in STEP 1, data for a similar curve for the CVJ outer ring was obtained. The data was then translated into the characteristics of the material of the CVJ outer ring. As shown in

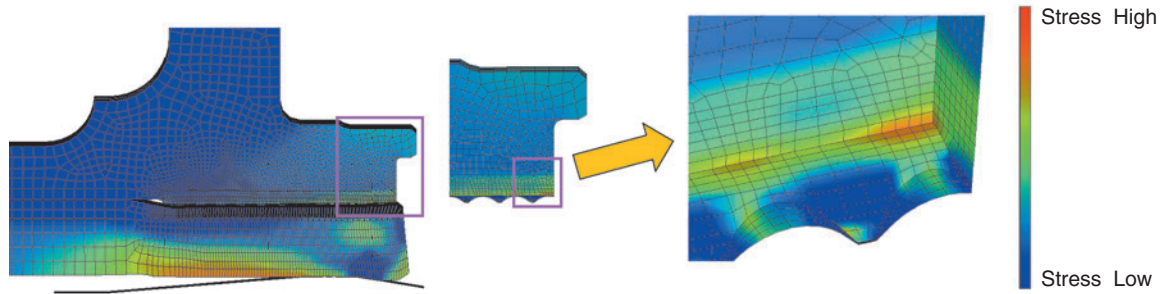


Fig. 10 Stress distribution at the time of tube forming simulation processing

Figures 8 and 9, after implementing the above factors, the outside diameter expansion on the pilot section in the analysis results now coincides with that found in the measurement results. and Similarly, the stress value has also improved. Our analysis technique can be now be utilized with confidence, and greatly reduce the number of test as well as the overall development time.

3.6 Stress value

With our analysis technique, we are now capable of determining the overall stress level on the stem section that results from the tube forming process, and we can now determine portions where a greater stress occurs from the tube forming process (Fig. 10).

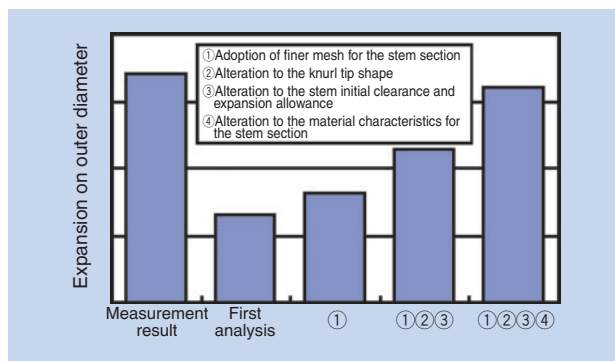


Fig. 8 Quantity of outer diameter expansion

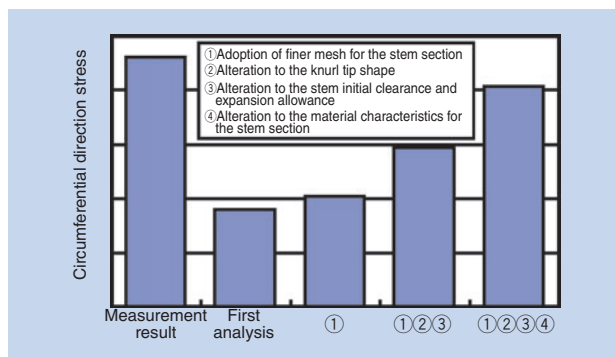


Fig. 9 Circumference direction stress

4. Conclusion

We have developed a new analysis technique for the tube forming process that is used as a fastening process for GEN4 hub joint products. The resultant improved accuracy of analysis is sufficiently high for a practical application. Through this newly developed analysis technique, it is now possible to define a combination of optimal forming conditions while at the same time accelerating the development of new hub joint designs.

The remaining challenges to be addressed will include the development of a technique for evaluating the mechanical strength of the joint resulting from the tube forming process, in terms of the necessary extraction power and torsional strength. We will address these challenges, and further improve our CAE technique, thus allowing it to be fully utilized in our design activities.

References

- 1) Eiji Funahashi: History of Hub Bearings and Recent Technology, NTN Technical Review, No.70 (2002)
- 2) Shigeaki Fukushima, Hiroyuki Ogura: Generation 4 Hub Joint, NTN Technical Review, No.70 (2002)
- 3) Akitoshi Imou: computer Analysis of Hub Bearings, NTN Technical Review, No.70 (2002)
- 4) Haruo Nagatani, Tsuyoshi Niwa: Application of Technology Optimization and Shape Optimization for Development of Hub-Bearing Lightening, NTN Technical Review, No.73 (2005)

Photos of authors



Akitoshi IMOU

Automotive Engineering Dept.
Automotive Sales Headquarters



Takehiro TAKANO

Automotive Engineering Dept.
Automotive Sales Headquarters

Development of an In-Wheel Motor Axle Unit

Minoru SUZUKI*

Koichi OKADA**

Kayo SAKAI*

Yusuke MAKINO**



In order to respond to the global demand for more energy efficient and environmentally friendly electric vehicles, NTN has developed an in-wheel motor axle unit for upcoming electric vehicles. This axle unit consists of a high-reduction cycloid and a high-speed axial gap motor to achieve a compact and lightweight design. In this paper, the initial design explanation is presented and the on-vehicle test results are shown.

1. Introduction

Recently in Japan, not only the car industry but also the government and private organizations have been putting much effort into addressing global warming issues and energy concerns. There have been breakthrough technologies in both electric motors and rechargeable batteries for fuel cell electric vehicles (FCEV) and electric vehicles (EV) that have dramatically improved the performance of these vehicle types ¹⁾.

The drive mechanisms for FCEV and EV can be broken down into two categories. The first category is a more conservative system where a single electric motor replaces a traditional internal combustion engine. The electric motor is mounted on the chassis and the power from the motor is transmitted to the tires via the drivetrain. The second category is an in-wheel motor axle system where a separate motor is installed in each wheel. In-wheel motored cars are capable of offering more passenger space than traditional engine-powered cars and have greater vehicle stability due to independently driven wheels. In-wheel type designs are currently being developed by various car manufacturers ²⁾⁻⁴⁾. NTN also has begun developing an in-wheel drive unit for electric vehicles ⁵⁾.

In this paper, we will explain the information learned from the bench testing of this design as well as the results from tests on an actual car that incorporated our prototype in-wheel motor axle units.

2. Specification and structure of the newly developed in-wheel motor axle unit

2.1 Target specification

The car that incorporated our prototype in-wheel motor axle unit was a 1500 cc class compact car. We desired that the car used for this testing (**Fig. 1**) have power-performance comparable to current gasoline powered cars. The targeted performance values of our in-wheel motor axle unit are summarized in **Table 1**.

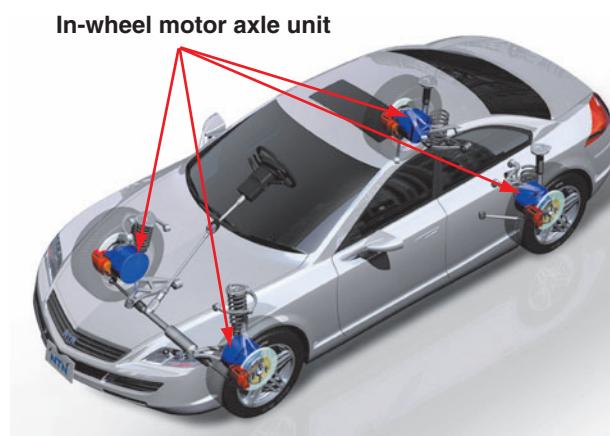


Fig. 1 Installation of the unit

*New Product Development Dept. New Product Development R&D Center

**Mechatronics Research Dept. New Product Development R&D Center

Table 1 Target specification of axle unit

Max. output	20kW
Max. torque	490Nm
Max. speed	150km/h
Mass	Approx. 25 kg
Reducer type	Cycloid reducing system
Reduction ratio	1/11
Motor type	Axial gap type permanent magnet synchronous motor
Max. motor speed	15000min ⁻¹

2. 2 Structure

Compared to other systems an in-wheel motor axle system can be disadvantageous because the four separate in-wheel motor axle units increases the unsprung weight, which can jeopardize driving stability and riding comfort in these vehicles. Therefore, in order for an in-wheel motor axle system to be effective and customer friendly, an in-wheel motor axle unit needs to be as lightweight and compact as possible.

The electric motor accounts for the largest amount of the total weight in an in-wheel motor axle unit.

Generally, a specified maximum torque output governs the motor size. Because of this specification and the desire for a lighter unit, we have introduced a reducer that will decrease the required maximum torque for the motor so that a lighter motor can be used. Our in-wheel motor axle unit schematic is illustrated in Fig. 2. The basic components of this design consist of a hub, a reducer, and a motor. Incidentally, the knuckle for installing the in-wheel motor axle unit to the vehicle is also the reducer housing.

2. 2. 1 Reducer Design

Instead of the commonly used 2K-H planetary gear reducer mechanism, we adopted a cycloid reducer mechanism⁶⁾. A cycloid reducer mechanism is a K-H-

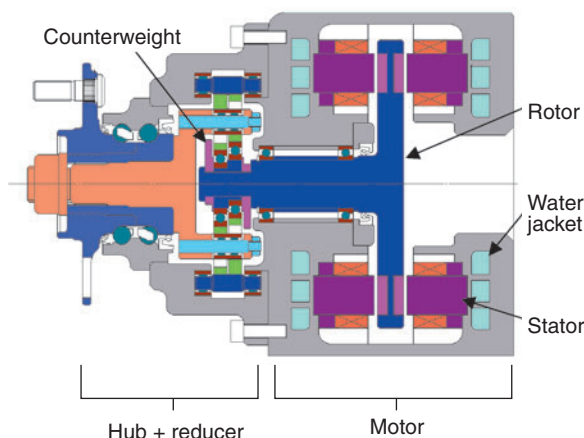


Fig. 2 Schematic of axle unit

V planetary gear reducing mechanism that is capable of a greater reducing ratio within a smaller space. As shown in Fig. 3, the cycloid reducer mechanism comprises an external gear with an epitrochoidal tooth profile, multiple internal gears each having a circular tooth profile, and internal pins situated in the smaller diameter portions of the external gear. The reduction ratio can be expressed through equation (1) assuming that the internal gears are locked in place and the internal pins cause the rotation of the external gear. The reduction ratio is governed by the ratio of the number of teeth of the external gear to that of the internal gears. The proposed design is multiple rowed gearing, but even single-row gearing can attain a higher reduction ratio. Use of this gearing mechanism causes a greater number of teeth to remain in contact, and therefore the torque transmission per unit volume of a reducer is greater and the reducer size can be decreased.

Generally, the transmission efficiency of a cycloid

$$\frac{N_{out}}{N_{in}} = - \frac{Z_i - Z_o}{Z_o} \dots\dots\dots (1)$$

- where, N_{out} : output shaft speed
- N_{in} : input shaft speed
- Z_o : number of teeth on external gear
- Z_i : number of teeth on internal gears

reducer mechanism is lower than that of a 2K-H planetary gear reducer. The lesser efficiency of the cycloid reducer seems to be due to the sliding contact between the inner and external gears and also between the internal pins and external gear. To address this issue, we have attempted to reduce the power loss by incorporating rolling bearings into these sliding contact areas⁵⁾.

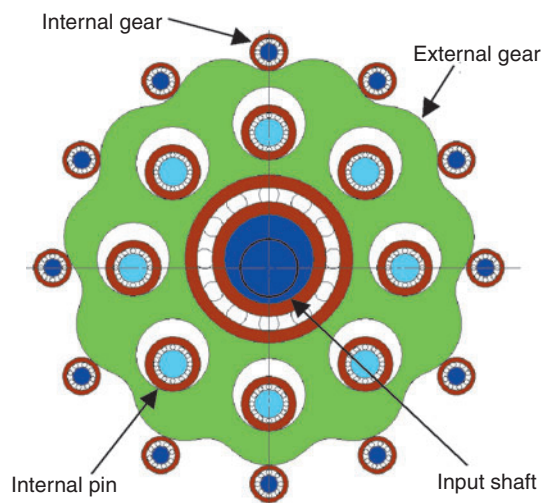


Fig. 3 Structure of reducer

On an ordinary cycloid reducer mechanism, two external gears (which constitute a pair) are allowed to run. The phase of one external gear is opposite that of the other external gear in order to compensate for the vibration of a component next to the rotational axis that is caused by the oscillation of the external gears. Furthermore, there is an unbalanced inertial couple that is next to the rotational axis of the two external gears. Because of this, we have incorporated a counterweight to dampen the vibration from this inertial couple⁵⁾.

2. 2. 2 Motor Design

To reduce the axial size of the unit, we employed axial gap type motors. Each motor is an SPM motor that has stators axially opposed to the rotor so that an axial attraction force is compensated for. The cooling system for the motor is comprised of a water-cooling arrangement consisting of a jacket situated at the rear of the stators, and an air-cooling arrangement that consists of radiator fins on the outer casing.

3. Bench test

The entire unit (including the hub, reducer, and motor section) was subjected to a bench test.

3. 1 Reducer section

3. 1. 1 Test rig

Fig. 4 shows a photo of the test rig used. An induction motor was used as a power source that transmitted power via a speed changer. An input side torque meter was used to drive the test reducer. The output rotation is transmitted through an output side torque meter and a belt driven reducer to the induction motor that will create the regenerative braking action.

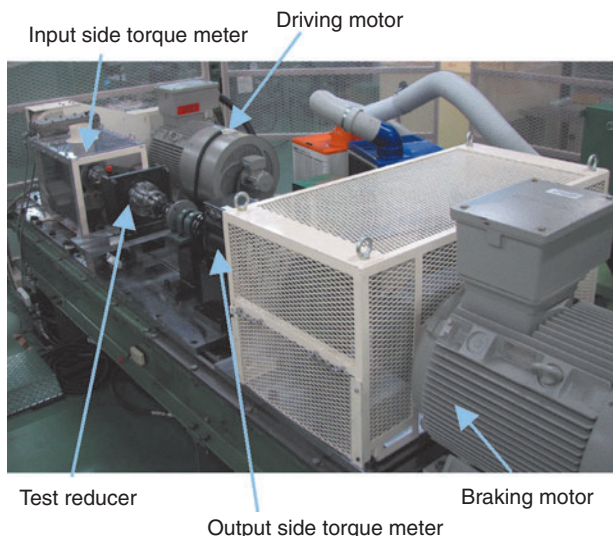


Fig. 4 Test machine

3. 1. 2 Test reducer and test conditions

The test sample illustrated in Fig. 5. is comprised of a hub and a reducer. The hub bearing is lubricated with grease while the reducer is lubricated with oil.

The test conditions applied are summarized in Table 2.

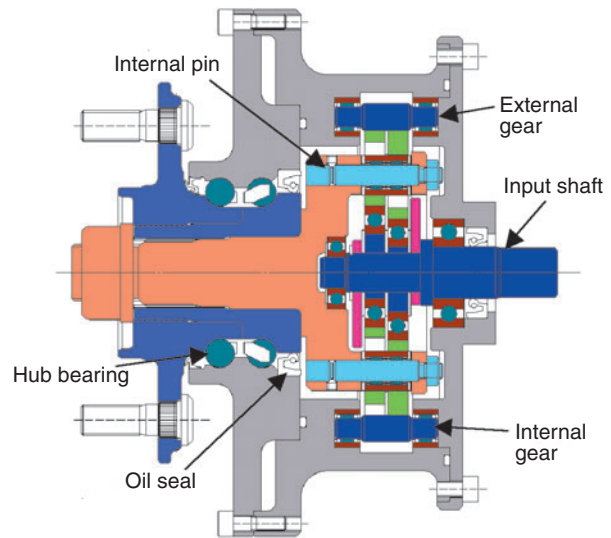


Fig. 5 Test reducer

Table 2 Test condition

Max. input speed	15000min ⁻¹
Max. input torque	45Nm
Lubricant oil grade	Industrial lubricant oil ISO VG150
Oil temperature	60~80°C
Lubrication system	Oil bath
Oil level (amount of oil)	Rotation center of input shaft (at 0 min ⁻¹)

3. 1. 3 Test result

The measurement results for the reducer efficiency are shown in Fig. 6. The maximum efficiency was approximately 95% and the efficiency in vehicle cruise mode up to 100 km/h is greater than 90%.

Another test was performed using the test condition in Table 2 with the only change being that the oil level was lowered by approximately 15 mm. The result of the second test is illustrated in Fig. 7. A third test was performed with a different lubricant whose viscosity grade was VG32 instead of VG150. The result of this test is shown in Fig. 8. Changing the lubricant amount and viscosity improved the efficiency in both the high speed and low torque regions. These two changes in lubricant condition proved to have higher efficiency.

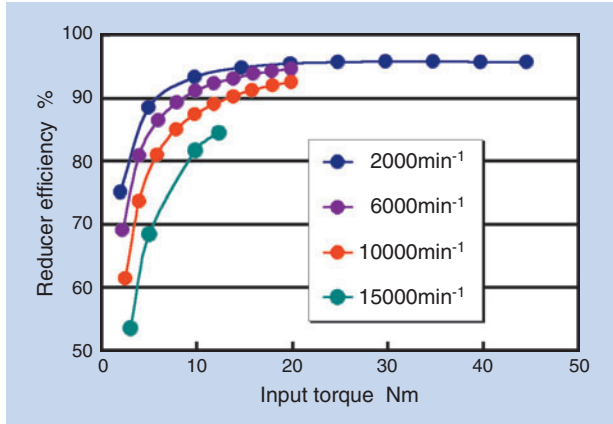


Fig. 6 Efficiency of reducer

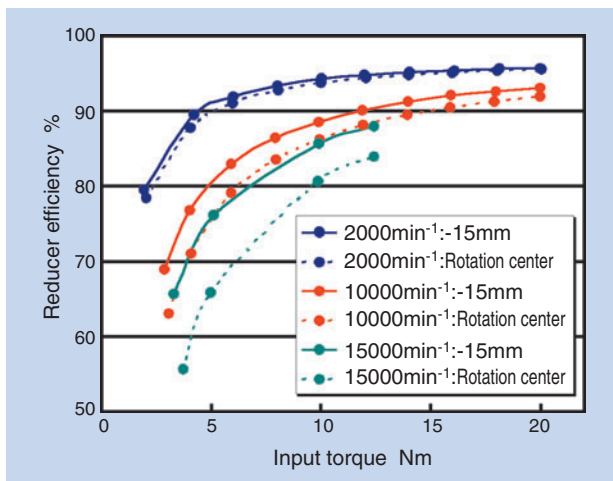


Fig. 7 Influence of oil level on reducer efficiency

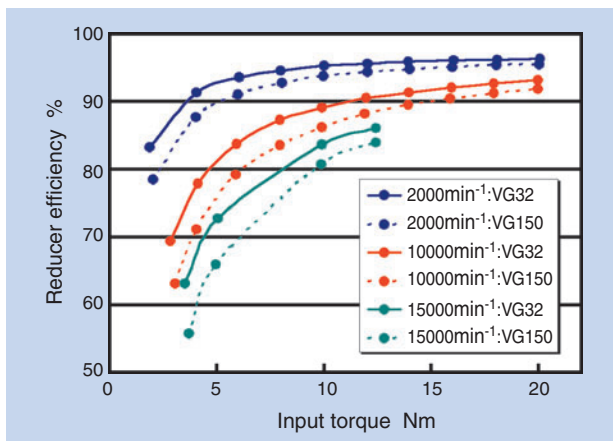


Fig. 8 Influence of viscosity on reducer efficiency

3. 2 Motor

3. 2. 1 Specification

The specification of the axial gap motor is summarized in **Table 3**.

To drive the motor, an inverter was used whose specification is given in **Table 4**.

Table 3 Target specification of axial gap motor

Max. output	20kW
Motor type	Axial gap type, Model SPM
Number of rotor poles	12 poles
Stator	9 slots
Permanent magnet	Nd-based
Cooling system	Water-cooling + air-cooling
Rotary sensor	Hall's IC

Table 4 Specification of inverter

Supply voltage	Max. 450 V
Output	30kW
Dimensions	W400×D500×H248mm
Carrier frequency	20kHz
Drive system	Rectangular wave PWM system
Cooling system	Forced cooling
Powering system	120–180°degrees switchover powering system

3. 2. 2 Shape Design Based on Magnetic Field Analysis

We used a magnetic field analysis technique to design the shapes of the stators and rotor. **Fig. 9** shows an example obtained from this analysis where the magnetic flux density distribution on the stator core is mapped out. To be able to efficiently generate torque relative to the level of input current, it is important to prevent the saturation of the magnetic flux density on the stators and rotor. Therefore, in an attempt to prevent the saturation of the magnetic flux

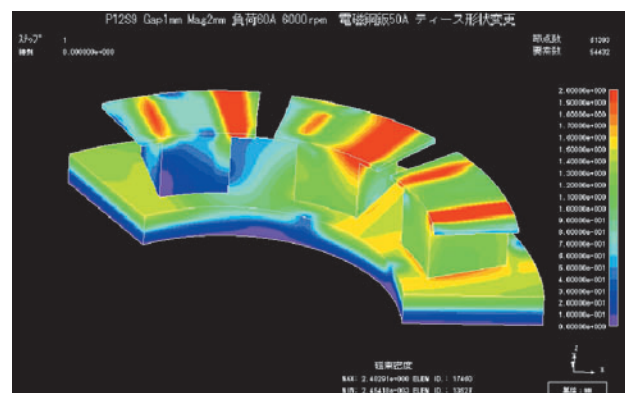


Fig. 9 Example of magnetic field analysis

density and keep a more compact size motor, we have redesigned the shapes and dimensions of the components. A prototype motor was fabricated based on this analysis. Fig. 10 provides a comparison of the design analysis values with the actual part test values in terms of the current vs. torque characteristics of the motor. The values of the design analysis closely match those of the actual part measurement result.

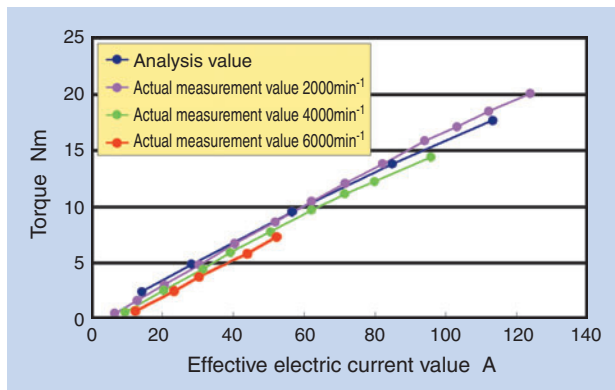


Fig. 10 Characteristic of electric current vs torque

3. 2. 3 Efficiency test

For ordinary radial gap motors, the rotor and stators are made by laminating silicon steel sheets (low core loss material) in the axial direction to decrease the loss of core material. However, for the rotor of an axial gap motor it is difficult to laminate the steel sheets that are used to effectively decrease core loss. The rotor used in our evaluation testing was made from a material other than silicon sheets because a much simpler fabrication of the rotor was used. The efficiency measured with this prototype motor is illustrated in Fig. 11 where the maximum efficiency was approximately 75%.

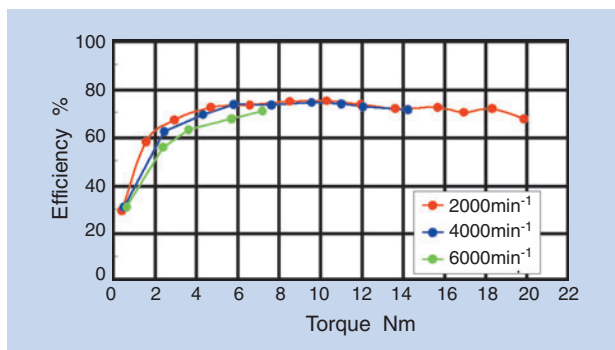


Fig. 11 Efficiency of motor

4. Actual Vehicle Testing

To verify the concept of our technology and detect any potential problems of our in-wheel motor type axle units in practical use, they were mounted a vehicle and then tested.

4. 1 Test Vehicle Configuration

The unit shown in Fig. 12 was mounted to a vehicle as shown in the photo in Fig. 13. A few modifications were made to a current market FF layout vehicle with the vehicle specifications summarized in Table 5. Our in-wheel motor type axle units were installed in the two rear wheels (with relative ease), so that the initial characteristics on an actual vehicle can be easily obtained.

In order to mount our axle units we modified the torsion beam suspension, replaced the shock absorber coil springs, and modified the vehicle-side mounting sections. Also, we removed the engine and transmission and installed the driving battery (lithium ion type) and inverter. We also installed electric auxiliaries in the engine compartment along side the auxiliary driving battery. In order to cool our axle units, we installed a water-cooling circuit that included the existing radiator and an electric water pump.

A schematic of the configured vehicle system can be seen in Fig. 14. The torque for each wheel is controlled separately for the two rear wheels, as shown in the vehicle information summarized in Table 6.

Table 5 Specification of test vehicle

Driving system	Two rear wheels
Suspension system	Torsion beam system
Vehicle weight	1350kg
Driving battery	Lithium ion battery (150V)
Brake	Two front wheels only (existing)
Unit cooling system	Water-cooling + air-cooling (wind by traveling)

Table 6 Control of vehicle

Vehicle information	<ul style="list-style-type: none"> · Speed on four wheels (vehicle speed) · Motor current · Steering angle · Throttle opening
Axle Unit Control	Separate Torque Control for Each Side

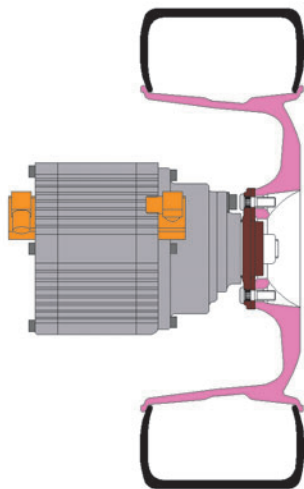


Fig.1 2 Unit

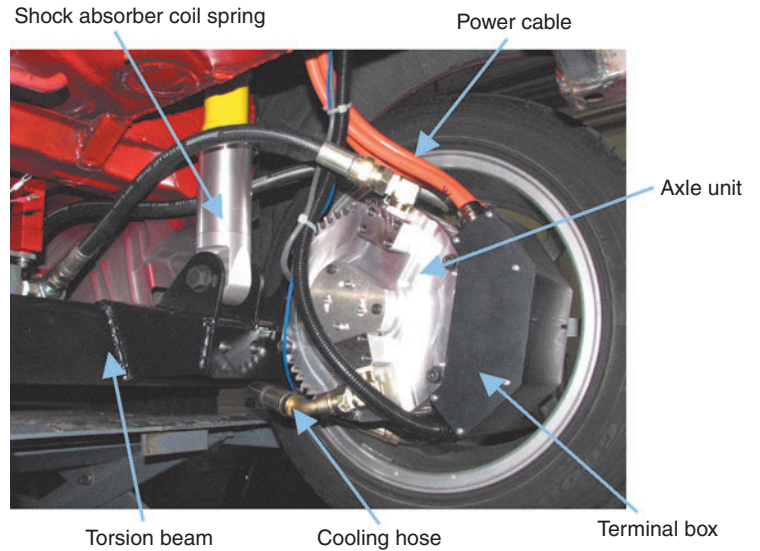


Fig. 13 Mounted unit

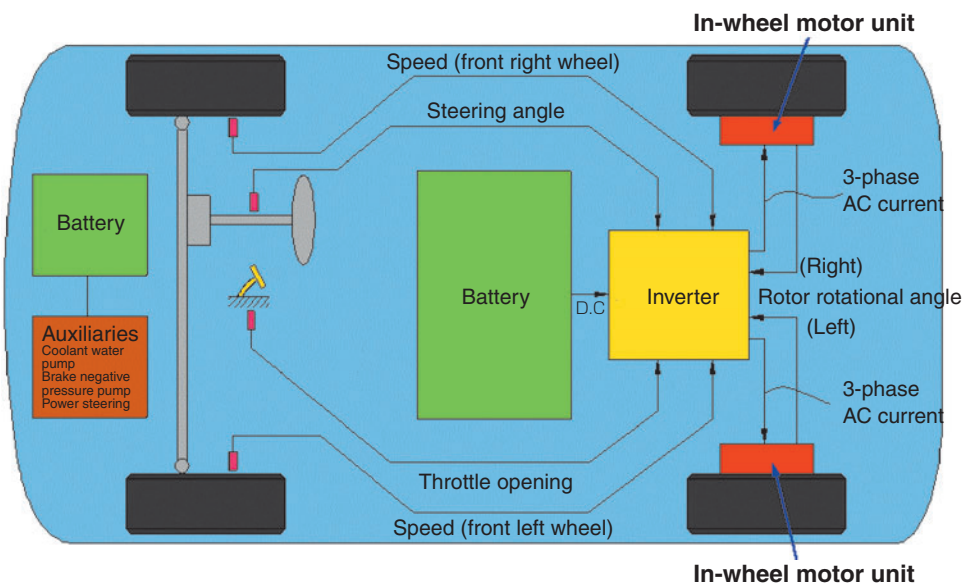


Fig.14 Structure of vehicle control system

4. 2 Vehicle Operating Test

The vehicle was run at speeds up to 40 km/h on a low friction, paved road that comprised of three different sections: a straight section, a curved section, and an inclined (hill) section.

To investigate the temperature characteristics of the axle unit, the test vehicle was run on a chassis dynamometer at a constant speed of 20 km/h and 40 km/h on a 0% gradient. The temperature was measured on various areas of the axle unit: the motor (stator coils), the reducer (lubricant temperature), and the motor cooling water. The result of the test is shown in Fig. 15.

Approximately 250 seconds after the start of operation, the temperature increase of the reducer was 6°C at 20 km/h and 8°C at 40 km/h. This temperature rise is relatively insignificant. During the same running period, the temperature increase of the motor stators was approximately 15°C at 20 km/h and 30°C at 40 km/h.

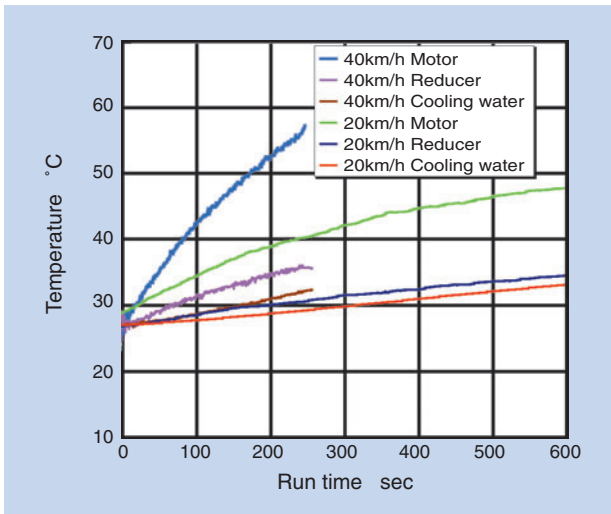


Fig. 15 Temperature characteristic of unit

5. Conclusion

Our cycloid reducer mechanism was found to have excellent power transmission performance (a maximum output of 20 kW, maximum input speed of 15000 min⁻¹, and maximum torque of 45 Nm). As well as excellent performance, this mechanism has a maximum efficiency of approximately 95%. For the motor section, we fabricated an axial gap motor and an inverter and then evaluated the characteristics of the motor. We mounted prototype axle units to a vehicle, each comprised of a reducer and an electric motor. We then tested the vehicle under constant velocity conditions on a chassis dynamometer. Lastly, we ran the vehicle along a paved road on straight and curved sections. Based on this vehicle test, we have verified trouble-free operation of our axle units.

References

- 1) Ministry of Economy, Trade and Industry, Agency for Natural Resources and Energy, Gathering on Next Generation Automobiles and Fuels: Next Generation Automobiles and Fuels Initiative Summary (2007).
- 2) Yasuki Tahara, Ryoji Mizutani, Yuki Tojima, Masafumi Sakuma: Development of In-Wheel Motor System, Society of Automotive Engineers of Japan, Lecture Session Preprints, No.131-06, 20065703 (2006)
- 3) Makoto Kamachi et al.: Improvement of Vehicle Dynamic Performance by Means of In-Wheel Electric Motors, Mitsubishi Motors Technical Review, No.18 (2006) 107-113
- 4) Rio S. Zhou, Fukuo Hashimoto: Highly Compact Electric Drive for Automotive Applications, SAE paper, 2006-01-3037
- 5) Minoru Suzuki, Dawei Wang: NTN Technical Review, No.73 pp.56-59 (2005)
- 6) Muneharu Morozumi: Theory and design calculation technique for planetary gears and differential gears, Nikkan Kogyo Shinbun, Ltd., pp.1-6 (1989)

Photos of authors



Minoru SUZUKI

New Product Development Dept.
New Product Development R&D Center



Kayo SAKAI

New Product Development Dept.
New Product Development R&D Center



Koichi OKADA

Mechatronics Research Dept.
New Product Development R&D Center



Yusuke MAKINO

Mechatronics Research Dept.
New Product Development R&D Center

Development of an Electromechanical Brake



Tatsuya YAMASAKI*
Masaaki EGUCHI*
Yusuke MAKINO**

The NTN electromechanical brake (EMB) system was designed and launched with the intention of improving overall performance of future automotive braking systems. NTN has designed and developed a new linear actuator that can be applied to this system. This paper reports on the configuration, design principles, efficiency calculation methods and related experiments.

1. Introduction

In the automotive industry there has been an increased emphasis on vehicle safety. Improvement in brake technology has greatly contributed to stable running of vehicles. Increased functionality has resulted in products like ABS, ESC, and brake assist¹⁾⁻²⁾. An example of the increased functionality of automotive brakes is improvement in control techniques for hydraulic brakes. Furthermore, in an effort to continue this improvement in functionality and reduction in environmental impact, automotive components manufacturers and car manufacturers are developing electromechanical brake (EMB) systems.

Many of newly developed electromechanical brake systems employ linear actuators such as ball-screws and ball-ramps (torque cams). However, when any of these linear actuators is used to develop the sufficient thrust required to brake a traveling vehicle, greater input torque is needed because the load conversion ratio with the linear actuator alone is insufficient. To design a more compact, lightweight electromechanical brake unit, the motor must be more compact. Therefore an independent reducer needs to be incorporated. Additionally, the electromechanical brake is situated in the “unsprung” section of the vehicle and will be subjected to violent vibration. Therefore it must be positively fretting-resistant.

Incidentally, when the electromechanical brake unit

is used as a parking brake without any modification, a separate mechanism will be needed to lock the revolution motion of the motor because a linear actuator such as a ball-screw lacks a thrust holding function. To address this issue and satisfy the functions required for such an electromechanical brake unit (high load conversion ratio, fretting-resistant quality, load-holding function), NTN has invented a unique linear actuator mechanism that doesn't require an accompanying mechanism and developed a unique electromechanical brake unit that includes an electric motor.

In this paper, we describe the constitution and operating principle of this electromechanical brake unit, the method for calculating the efficiency of the brake unit, as well as the evaluation tests we have performed.

Legends

- a, b : half width of Hertz contact ellipse on threaded surface
- D_S : sun roller outside dia.
- D_P : planetary roller outside dia.
- d_{BS} : ball center diameter on ball-screw
- d_O : outer ring inside dia.
- F : force acting on the piston
- k : number of effective thread ridges on each planetary roller = l_P/P
- L_P : thread lead on planetary roller

*New Product Development Dept. New Product Development R&D Center

**Mechatronics Research Dept. New Product Development R&D Center

- L_O : thread lead on outer ring
- l_P : effective length of threaded portion on each planetary roller
- n : number of planetary rollers
- p : thread pitch
- P_{SC} : load acting on one screw = $\frac{F}{nk \cos \beta}$
- P_N : radial circumferential load from one planetary roller, acting on sun roller = $\frac{F}{n} \cdot \tan \beta$
- P_r : circumferential tangential force from one planetary roller, acting on sun roller = $\frac{2T_s}{nD_s}$
- P_a : axial tangential force acting on sun roller
- T_s : sun roller torque
- x : axial displacement of piston
- x_{BS} : axial displacement of nut (threaded shaft) on ball-screw
- W_{IN} : input (workload)
- W_{OUT} : output (workload)
- W_{REV} : loss from frictional torque occurring on revolution supporting bearing
- W_{ROT} : loss from frictional torque occurring on rotation supporting bearing
- W_S : loss from frictional torque occurring on sun roller supporting bearing
- W_{SC} : loss from slipping on screw thread
- α : equivalent lead angle
- α_{BS} : thread lead angle on ball-screw
- α_P : thread lead angle on planetary roller
- α_O : thread lead angle on outer ring
- β : thread flank angle on planetary roller
- δ : amount of offset at contact point on screw thread
- η : efficiency
- μ : friction coefficient on circumferential contact surface
- μ_{SC} : friction coefficient on screw thread
- θ_{BS} : angular displacement of threaded shaft (nut) on ball-screw
- θ_S : angular displacement on sun roller
- θ_{REV} : angular displacement of revolution on planetary roller = $[D_s (d_o + D_s)] \cdot \theta_s$
- θ_{ROT} : angular displacement of rotation on planetary roller = $[-D_s (d_o - D_s)] \cdot \theta_s$
- θ'_{ROT} : angular displacement of rotation on planetary roller (relative to carrier) = $\theta_{ROT} - \theta_{REV}$

2. Linear actuator

2.1 Constituent Elements and Operating Principle

The constitution and operating principle of NTN's linear actuator are discussed below.

NTN's linear actuator comprises, as shown in Fig. 1, a sun roller, planetary rollers, an outer ring, a carrier, a piston and a threaded member which constitutes the screw of the outer ring. Several planetary rollers are shrink-fitted between the sun roller and the fixed outer ring; thereby the planetary rollers rotate and revolve as the sun roller rotates. Spiral threading is provided on the outer circumference of each of the planetary rollers as well as on the inner circumference of the outer ring, wherein these threads have an identical pitch so that they can be correctly meshed with each other.

As a result of this layout, while revolving and rotating, the planetary rollers will be axially shifted relative to the outer ring. The carrier and piston each support rotation and revolution of the planetary rollers; then, the rotary motion of the sun roller is finally converted into the linear motion of the piston.

Suppose that there is no slipping at the contact points between the outer circumference of sun roller, outer circumferences of planetary rollers and inner circumference of outer ring, the amount of axial displacement x of the piston relative to the rotary motion of the sun roller can be expressed with the formula (1). At the same time, the amount of axial displacement x_{BS} of the nut on the ball-screw can be expressed with the formula (2). The axial displacement x of the piston is dependent on the difference between the lead angle of the thread on the planetary rollers and that on the outer ring; thereby the axial displacement x of the piston (our linear actuator) can be smaller than the axial displacement x_{BS} of the nut on the ball-screw. In other words, compared with a value obtained with the ball-screw arrangement, the load conversion ratio, which can be defined as the thrust relative to the input torque, can be greater with our linear actuator.

$$x = \frac{d_o}{2} \cdot (\tan \alpha_O - \tan \alpha_P) \cdot \theta_{REV} \dots\dots\dots(1)$$

$$x_{BS} = \frac{d_{BS}}{2} \cdot \tan \alpha_{BS} \cdot \theta_{BS} \dots\dots\dots(2)$$

Also, we have attempted to improve fretting resistance of our electromechanical brake by applying a negative clearance preload in the radial direction among the sun roller, planetary rollers and outer ring. To achieve, at a lower cost, both adjustment of radial clearance and formation of thread, the thread is

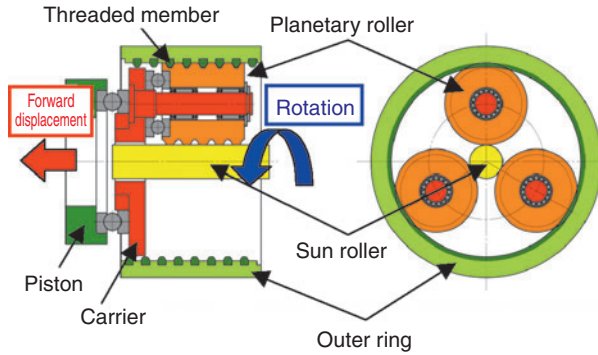


Fig. 1 Schematic of linear actuator

formed on the outer ring by adding a coil-shaped thread member in the spiral grooves formed on the bore surface of the outer ring.

2. 2 Efficiency

In order to be able to determine the efficiency of our linear actuator, we provided the following assumptions [1] through [4]:

- [1] The thrust occurring on the piston is uniformly carried by all the planetary rollers and threads.
- [2] Because of the smaller lead angle (not greater than 5 degrees), the circumferential component of the load occurring on the thread can be ignored.
- [3] No slipping occurs at the contact points between the outer circumference of the sun roller and the outer circumference of each planetary roller and between the inner circumference of the outer ring and the outer circumference of each planetary roller.
- [4] The areas where loss appears to occur are the revolution supporting bearing, rotation-supporting bearing, and sun roller supporting bearing and contact surfaces on threads.

In addition to these areas, the axial sliding at the contact areas between the planetary rollers and sun roller and between the planetary rollers and outer ring is regarded as a loss. However, this sliding accompanies rolling contact, and is considered to be fairly small.

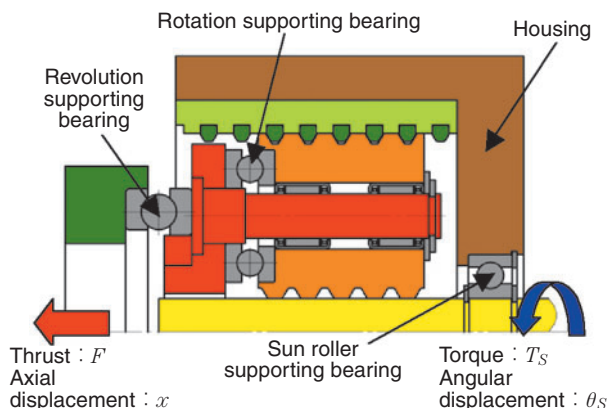


Fig. 2 Relation of input and output

By referring to Fig. 2, suppose that the torque being input from the sun roller causes the piston to move axially. Then, the efficiency of the linear actuator η and the relation between the work input and work output can be expressed with the formulas (3) and (4), respectively.

$$\eta = \frac{W_{OUT}}{W_{IN}} = \frac{F \cdot x}{T_s \cdot \theta_s} \dots\dots\dots(3)$$

$$W_{OUT} = W_{IN} - W_{REV} - W_{ROT} - W_S - W_{SC} \dots\dots\dots(4)$$

The torque loss from each bearing was calculated utilizing the Palmgren³⁾. experimental formula for friction torque.

Now, we would like to discuss the load acting on the sun roller supporting bearing. The normal force and tangential force from a planetary roller, shown in Fig. 3, act on the sun roller. From the relation with a frictional circle, we determined the axial tangential force P_a with the formula (5) below, and took the resultant force value as the axial load acting on the sun roller supporting bearing.

$$P_a = n \sqrt{(\mu P_N)^2 - P_r^2} \dots\dots\dots(5)$$

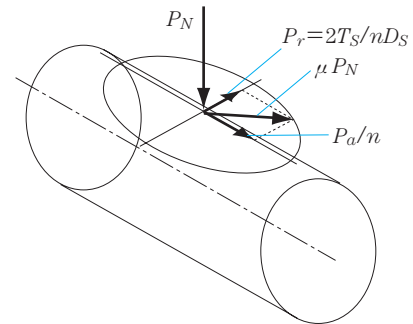


Fig. 3 Load on sun roller

Next, we would like to explain the losses arising from sliding on the screw thread. On the screw threads between the planetary rollers and outer ring, the Hertz contact ellipse shifts, as illustrated in Fig. 4, while the planetary rollers rotate. Suppose that each planetary roller moves along the inner circumference of the outer ring. Then, the contact ellipse on the screw thread shifts with the sliding motion that consists of the tangential displacement U of the center of ellipse (expressed with the formula (6)) and the rotational displacement θ on the center of ellipse (expressed with the formula (7)).

$$U = \left(\frac{d_o}{2} - \delta\right) \cdot \theta_{REV} + \left(\frac{D_p}{2} - \delta\right) \cdot (\theta_{ROT} - \theta_{REV}) = \delta \theta_{ROT} \dots\dots\dots(6)$$

$$\theta = (\theta_{ROT} - \theta_{REV}) \cdot \cos \beta = \theta'_{ROT} \cdot \cos \beta \dots\dots\dots(7)$$

Then, take the sliding-induced losses within the contact ellipse as the sum of losses within a miniature area such as a one given in Fig. 5. Then, from the amount of sliding $V(x, y)$, determined with the formula (8) and the normal load $f(x, y)$, determined with the formula (9), the sliding-induced loss W_{SC} on the screw thread can be expressed with the formula (10).

$$V(x, y) = \sqrt{(U + r\theta \sin \phi)^2 + r^2 \theta^2 \cos^2 \phi} \dots\dots\dots (8)$$

$$f(x, y) = \frac{3P_{SC}}{2\pi ab} \sqrt{1 - \frac{x^2}{a^2} - \frac{y^2}{b^2}} \cdot dx \cdot dy \dots\dots\dots (9)$$

$$W_{SC} = nk \int \mu_{SC} \cdot f(x, y) \cdot V(x, y) \dots\dots\dots (10)$$

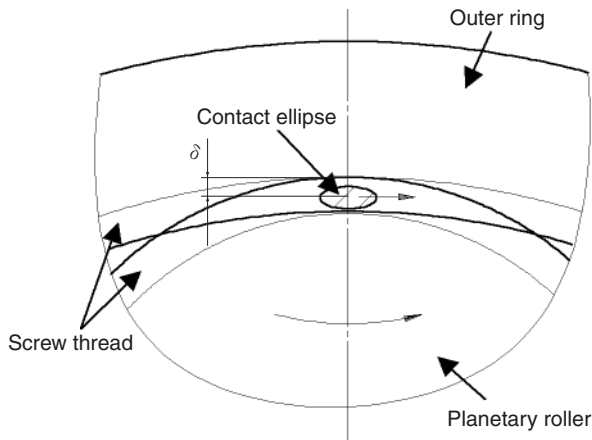


Fig. 4 Contact ellipse in thread of the screw

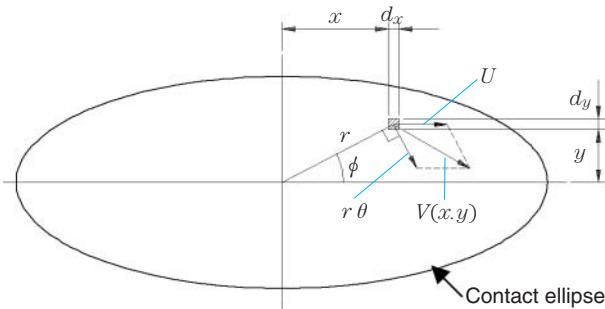


Fig. 5 Contact ellipse

Under the calculation conditions given in Table 1, the thrust F and efficiency η for the units No. 1 through 4 were calculated, and the result is plotted in Fig. 6; and the loss ratios relative to the inputs to the unit No. 1 are illustrated in Fig. 7. For these calculations, it was assumed that $\mu = \mu_{SC} = 0.1$. From Fig. 6, it should be understood that the thread can be variously specified and a variety of linear actuators each featuring unique efficiency can be designed. With Fig. 7, it is possible that the proportion of the loss resulting from sliding on the screw thread is large and increases as the torque increases.

Table 1 Calculation condition

Technical data	No.1	No.2	No.3	No.4
D_S , mm	12	←	←	←
D_P , mm	30	←	←	←
d_O , mm	72	←	←	←
n	3	←	←	←
L_P , mm	2	2	0	3
L_O , mm	4	2	2	6
p , mm	2	←	←	3
I_P , mm	16	←	←	←
δ , mm	0.3	←	←	←

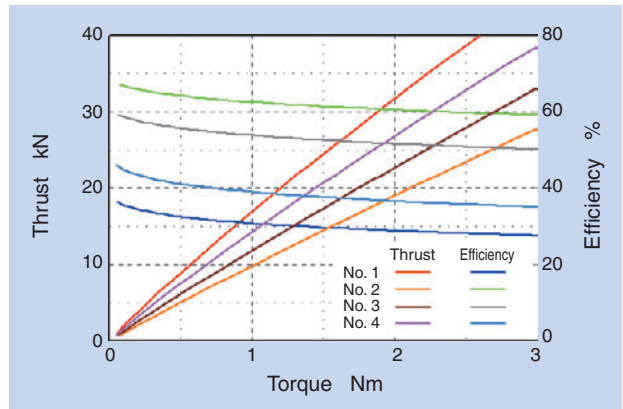


Fig. 6 Calculation results of thrust and efficiency

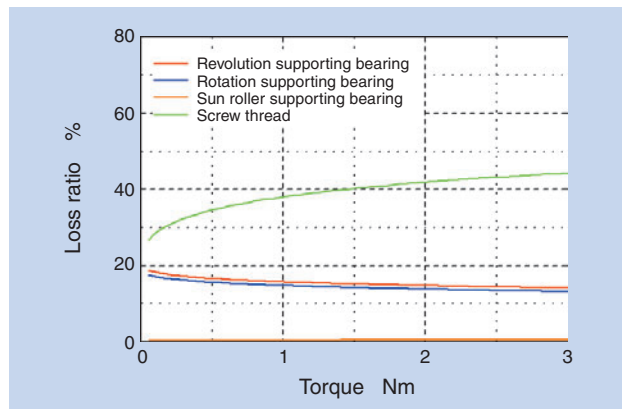


Fig. 7 Ratio of losses

3. Evaluation for characteristics of linear actuators

3.1 Units being tested and test method

We have evaluated the efficiency and thrust holding function of our linear actuator. The specifications of the linear actuator units tested are summarized in **Table 2**, and the configuration of the test rig is illustrated in **Fig. 8**. With the test rig, torque was applied to the linear actuator by, for example, applying a weight to the lever, thereby the efficiency of our linear actuator was determined based on the torque input to the sun roller and the thrust from the piston detected by the load cell.

Table 2 Specifications of linear actuator

Unit	A	B	C	D	E	F
D_S , mm	12	8	15	←	←	←
D_P , mm	30	26	28.5	←	←	←
d_O , mm	72	60	72	←	←	←
n	3	←	4	←	←	←
L_P , mm	2	0	2	0	2	3
L_O , mm	4	2	4	2	2	6
p , mm	2	←	←	←	←	3
α , deg	0.173	0.536	0.220	0.419	0.640	0.331

3.2 Efficiency and load holding function

The test results of thrust and efficiency for the units A and B are given in **Fig. 9**. These results coincide with the result of simulated calculation. This means our calculation practice is reliable.

The relation between the torque and thrust on the linear actuator in one cycle (a duration where the thrust is increased from a zero level to a particular level, and then is decreased to a zero level) is shown in **Fig. 10**. When the thrust is decreased, a negative torque is necessary on the unit A while a positive torque occurs on the unit B. This is because the sun roller rotates by the thrust and, consequently, its thrust holding function is lost.

To address this issue, we developed the relationship between the equivalent lead angle of the linear actuator defined with the formula (11), efficiency of the linear actuator when it develops 30 kN and availability of its thrust holding function, and this relation is plotted in **Fig. 11**. With a greater equivalent lead angle, the efficiency is better; when the equivalent lead angle is 0.331 deg or greater, the thrust holding function is not available. To sum up, it must be understood that the linear actuator needs to be designed to have an equivalent lead angle of approximately 0.3 deg so that it can have the thrust holding function.

$$\alpha = \tan^{-1} \left(\frac{2x}{D_S \cdot \theta_S} \right) \dots\dots\dots(11)$$

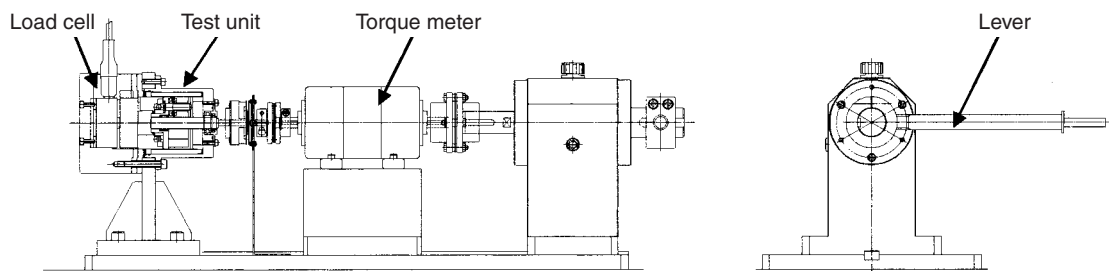


Fig. 8 Test rig for measuring efficiency

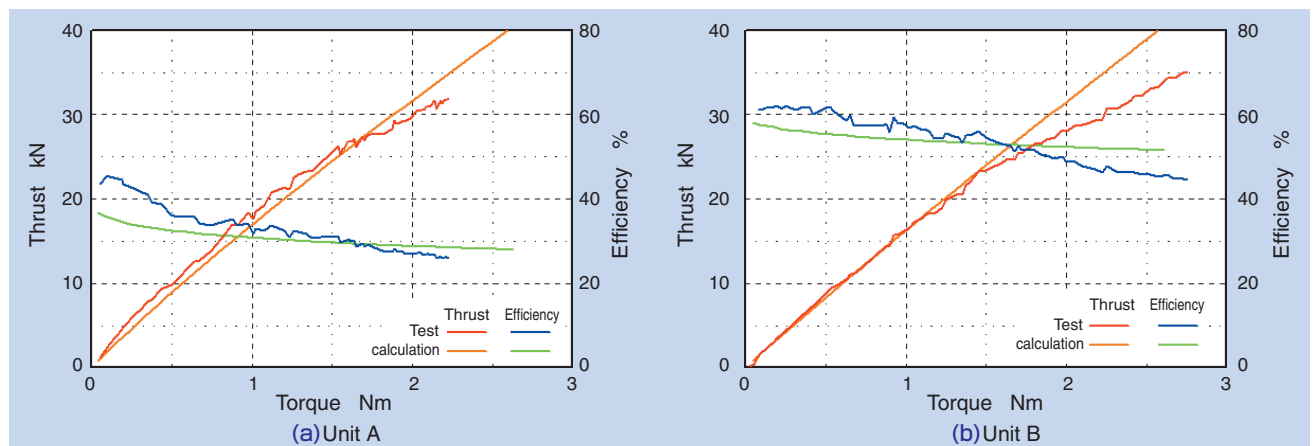


Fig. 9 Test results of thrust and efficiency

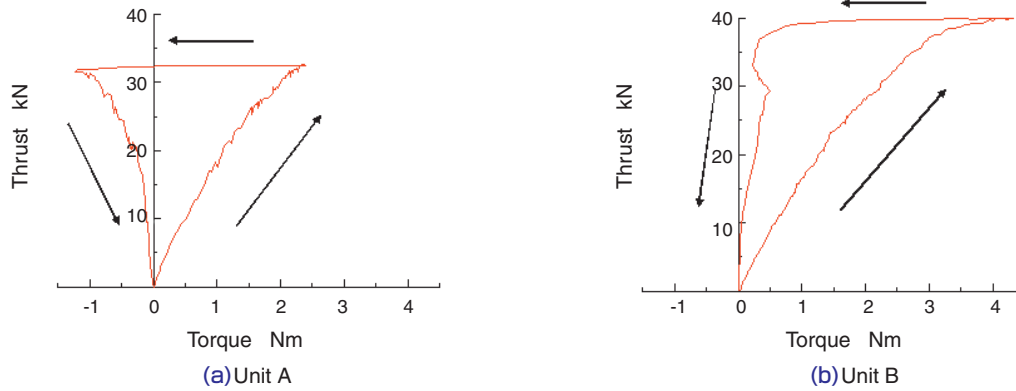


Fig. 10 Relation between torque and thrust

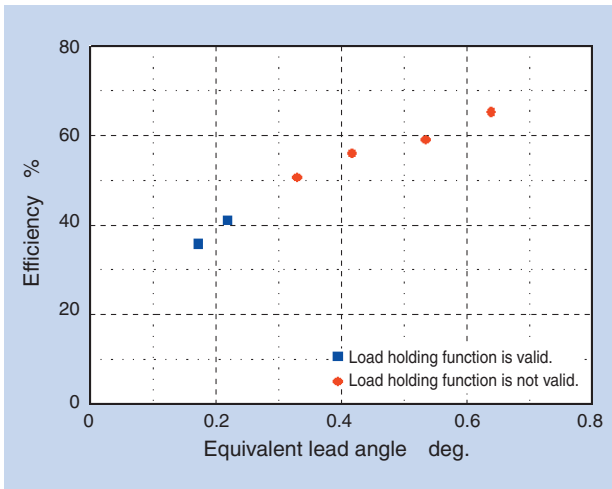


Fig. 11 Relationship between equivalent lead angle, efficiency and load holding

4. Evaluation for electromechanical brake units

4.1 Electromechanical brake units tested

We have manufactured a prototype electromechanical brake unit that can be incorporated into an actual car. It has been evaluated on a test rig and tested as mounted on an actual car. The specifications of the electromechanical brake units and motor used are summarized in [Tables 3 and 4](#), while the configuration of the electromechanical brake (EMB) unit is illustrated in [Fig. 12](#) and that of the motor is given in [Fig. 13](#). So that the axial length of EMB unit can be shorter, the motor is arranged parallel with the linear actuator and the motor itself is an axial clearance-type motor that has two stators. From this motor, the torque is transmitted via a gearing to the sun roller. For convenience of incorporation into an actual car, the linear actuator used is the type B unit described in [Sec. 3](#), which features a compact size.

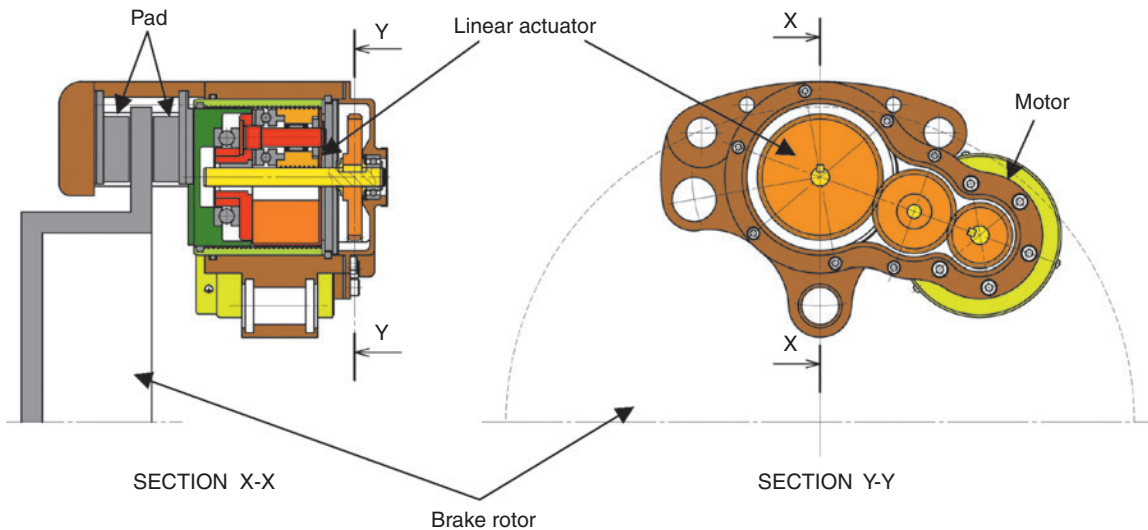


Fig. 12 Prototype EMB unit

Table 3 Specifications of EMB units

Characteristic	Specification
Max. thrust	30kN
Size (excluding caliper)	150mm × 82mm × 85mm
Mass (excluding caliper)	3.8kg

Table 4 Specifications of motor

Characteristic	Specification
Max. output	140W
Max. torque	2Nm
Max. speed	1500min ⁻¹

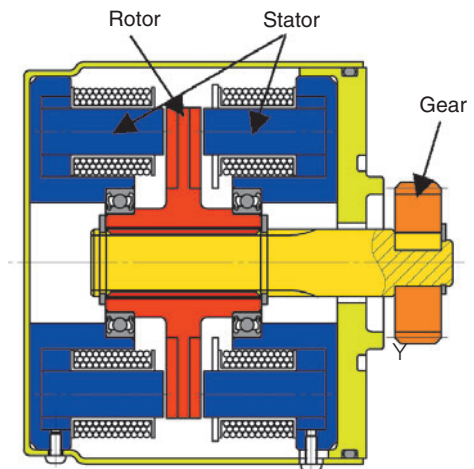


Fig. 13 Axial gap motor

4. 2 Evaluation about response

On the test rig illustrated in Fig. 14, we evaluated the response time relative to thrust on our EMB unit (increase and decrease characteristics). The thrust was measured with a load cell that was mounted in place of a brake rotor and pad. The test conditions are summarized in Table 5, and the test results are plotted in Figs. 15 and 16.

In our test project, a particular voltage was fed into the motor 0.1 sec. after the beginning of each measuring run, thereby the thrust increase/decrease characteristics were evaluated. Under any combination of test conditions, the time-dependent variation in the thrust is nearly constant in the region approximately 10 kN or greater. In the thrust range 10 kN or lower, this variation does not

appear to be linear. It is possible, by applying a greater voltage to the motor, to promote the variation in thrust, in either a thrust increase or decrease mode, to shorten the time needed to reach a targeted load.

This is because with a greater voltage applied, the maximum motor speed is greater.

Next, we want to discuss the effect of an initial clearance between the piston and load cell. Let us think of the cases where the initial clearance is set to 0.2 mm. When the voltage applied is 12 V, the time needed for a thrust to occur takes approximately 0.1 second while this time span is as short as approximately 0.05 second when the voltage is 20 V. Thus, the size of initial clearance significantly affects the response time.

Table 5 Test condition

Parameters	Thrust	
	Increase characteristic	Decrease characteristic
Voltage applied	12V, 20V	
Initial clearance	0mm, 0.2mm	—

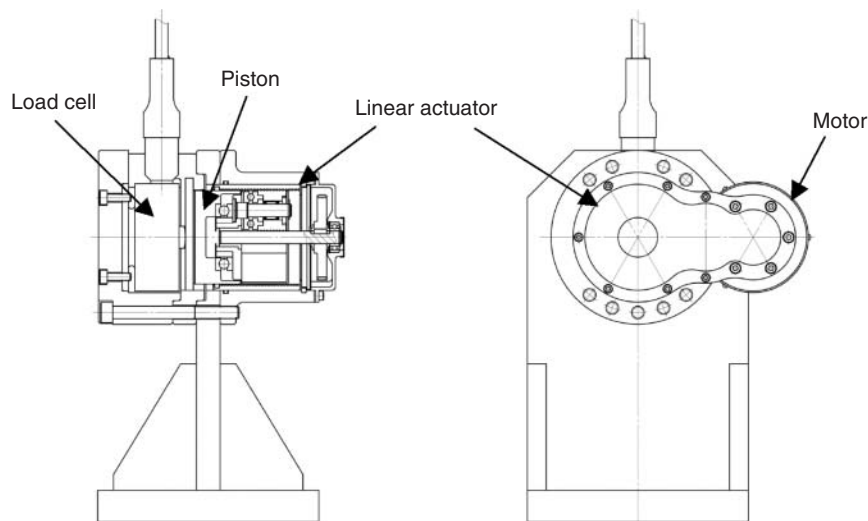


Fig. 14 Test rig for measuring the response time

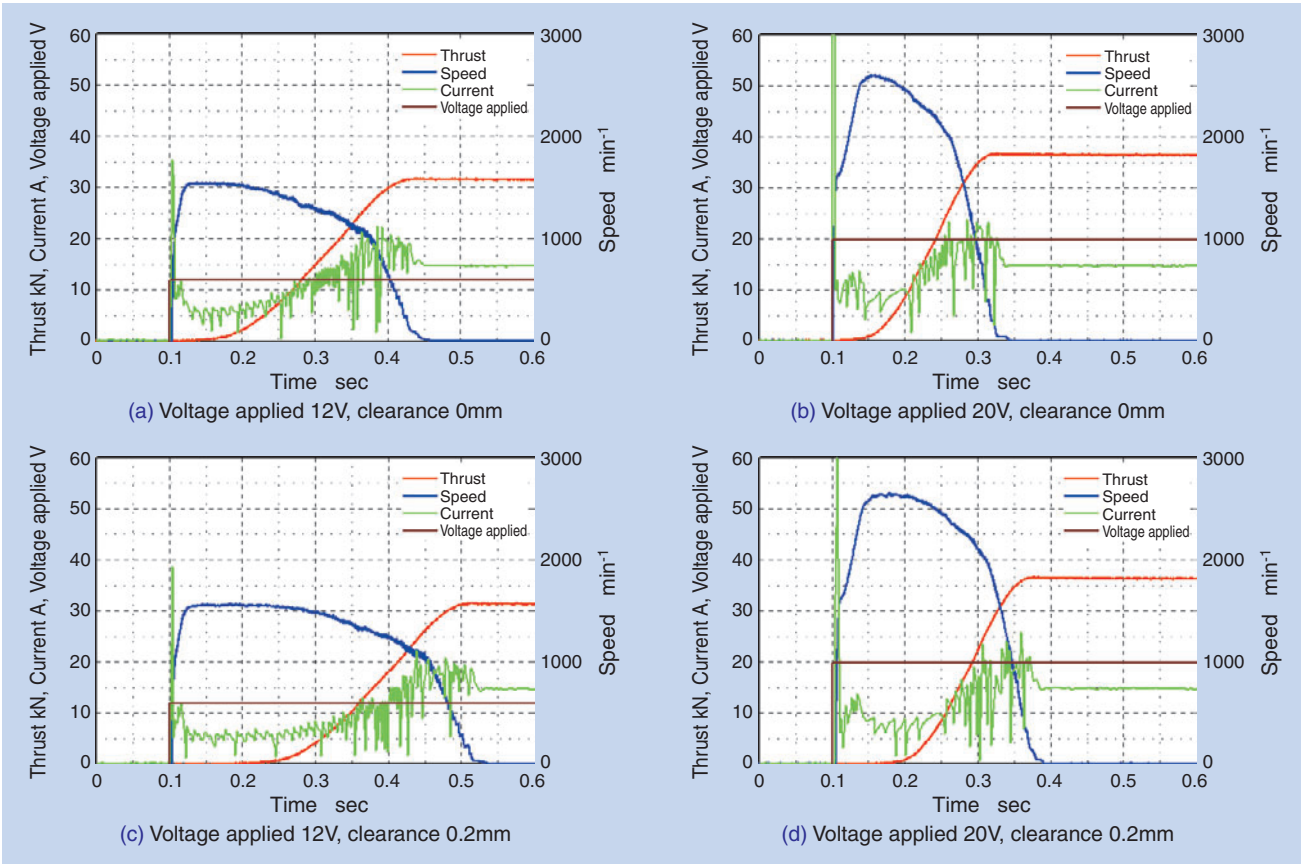


Fig. 15 Response time (increase characteristic)

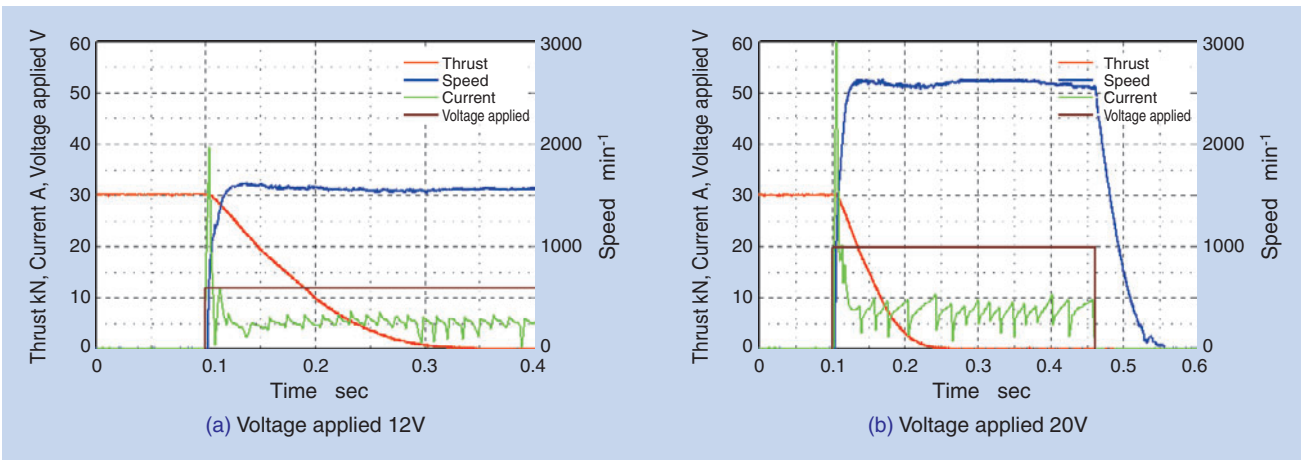


Fig. 16 Response time (decrease characteristic)

4.3 Test on actual car

As illustrated in Fig. 17, we incorporated our prototype EMB unit into each of rear wheels on the test car. Our EMB unit could be readily installed to the test car only with adjustment to the mounting position, and without modification to the area including the knuckle. Also, we have already verified that our EMB unit can be incorporated into the front wheels of the car without any significant modification. On the system

configuration shown in Fig. 18, a thrust value detected by the strain gage relative to a command value from the controller is fed back to the controller in order to control the motors. We attempted to brake the car traveling at a speed of approximately 30 km/h, by only actuating the EMB units on the rear wheels, and could reliably stop the car. For this test, we used a 12-V battery for automotive applications.



Fig. 17 Installation of the unit

5. Conclusion

NTN has invented a unique linear actuator for EMB units that will be marketed in the near future, wherein our linear actuator, though not having any additional mechanism, not only boasts a high level of load conversion ratio and high degree of fretting resistance but also features a unique load holding function. Then, we have evaluated an electromechanical brake

- (EMB) unit that includes our linear actuator and an electric motor, and obtained the following results:
- (1) We have developed an efficiency calculation technique for our linear actuator, and verified the validity of this technique through a series of tests.
 - (2) We have measured the thrust and efficiency of our linear actuator, thereby we have clarified the thread specifications for satisfying the thrust holding function.
 - (3) We have learned the characteristics of the EMB unit (a unit including an electric motor) through a response evaluation test and a braking test on an actual car.

References

- 1) Tomohiko ADACHI: The Electronic Stability Control System, Journal of Society of Automotive Engineers of Japan, Vol.60, No.12 pp.28-33 (2006)
- 2) Bo Cheng, Tetsuo Taniguchi, Tadashi Hatano, Toshiya Hirose: Effect of Brake Assistance System in Emergency Situation, Society of Automotive Engineers of Japan, Lecture Session Preprints, No.20065894
- 3) A. Palmgren : Ball and Roller Bearing Engineering, 3rd ed., Burbank, Philadelphia, (1959) 34.

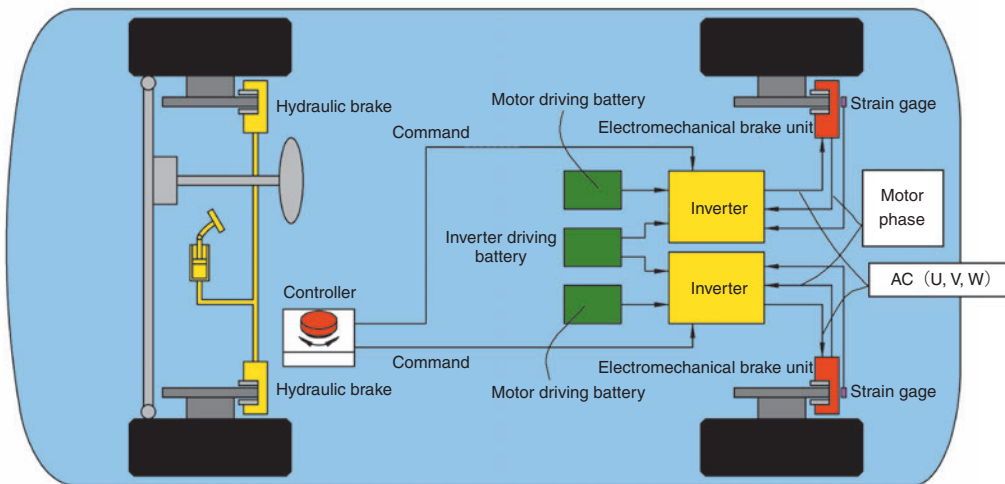


Fig. 18 Prototype EMB system diagram

Photos of authors



Tatsuya YAMASAKI

New Product Development Dept.
New Product Development R&D Center



Masaaki EGUCHI

New Product Development Dept.
New Product Development R&D Center



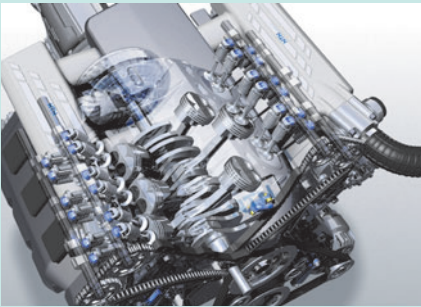
Yusuke MAKINO

Mechatronics Research Dept.
New Product Development R&D Center

Engine Part Technical Trends and New Engine Products

Yoshiaki RYOUNO*
Kouichi ONIMARU*

Kenichi KAWABATA**
Shinji OOISHI**



Engine specifications have been influenced by environmental and social conditions. Now, fuel-efficient engines are expected to reduce the emission of CO₂, a contributor to global warming. In particular, engine parts with extended lifespans, reduced frictional losses, and reduced weight are needed to meet the new 2015 fuel-efficiency standard targets. It goes without saying that all parts must be durable and reliable. This report discusses new engine part products, developed by NTN that, fulfill these requirements.

1. Introduction

EU released its new environmental regulation stipulating that by the end of 2012, the CO₂ emissions from new cars sold in EU have to be reduced to an average of 130 g/km; accomplished through improvement in engine performance. Also in the USA, there is a fuel efficiency improvement program according to which gasoline consumption has to be reduced by 20% in 10 years beginning in the year 2007.

In Japan, a regulation will be introduced, which will impose new fuel-efficiency standards (see [Table 1](#)) for small trucks, small buses and passenger cars and these standards must be satisfied by the end of the year 2015. In particular in terms of the fuel efficiency with passenger cars, the projected year 2015 level will be 23.5% better compared with the actual year 2004 level, and will be 29.2% better compared with the current fuel efficiency level (the target for FY2010).

Under such demanding circumstances, the

Table 1 2015 year fuel-efficient target (improvement rate compare with 2004)¹⁾

Car category	Actual year 2004 fuel efficiency	Projected year 2015 fuel efficiency	Improvement in fuel efficiency over year 2004 level
Passenger car	13.6(km/ℓ)	16.8(km/ℓ)	23.5%
Small bus	8.3(km/ℓ)	8.9(km/ℓ)	7.2%
Small truck	13.5(km/ℓ)	15.2(km/ℓ)	12.6%

automakers are committed to improvements in power performance of car engines, fuel economy and emissions performance, and in this context, they have been achieving novel technological developments. To help commercialize these new automotive technologies, NTN has developed a diverse group of new mechanical elements.

2. Power loss factors on cars—friction losses on automotive engines and requirements for NTN products for automotive engines

2.1 Power loss factors on cars

Typical factors contributing to power loss on cars are summarized in [Fig. 1](#).

The engine friction accounts for 27% of the entire power loss on an average car: therefore, we believe that a decrease in friction on an automotive engine will help improve the fuel efficiency of the car. We also believe that a lighter weight car will contribute to an improvement of fuel efficiency of the car.

2.2 Friction losses on automotive engines

A typical breakdown of friction ratios with an automotive engine is illustrated in [Fig. 2](#).

[1] The major friction losses on an automotive engine are derived from the valve system, crankshaft, oil pump system, valve drive system, and piston system.

*Automotive Engineering Dept. Automotive Sales Headquarters

**Needle Roller Bearing Engineering Dept. Automotive Sales Headquarters

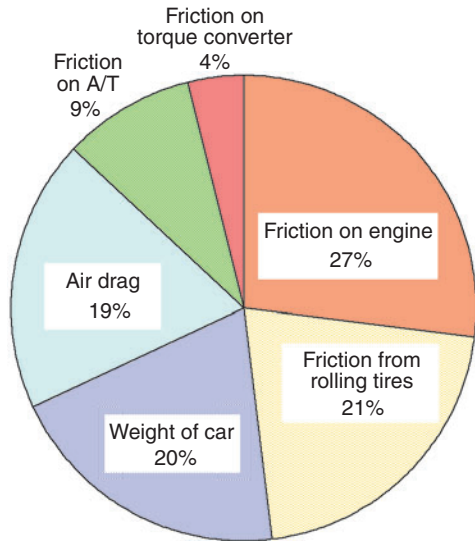


Fig. 1 Friction loss ratio at the car (HWY mode)²⁾

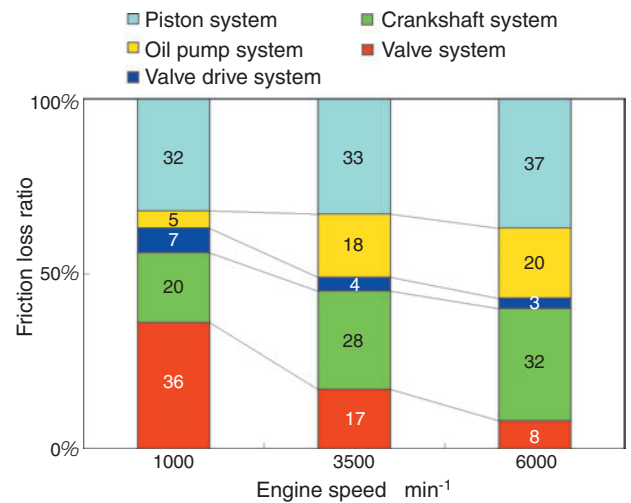


Fig. 2 Friction loss ratio of the engine³⁾

The proportions of friction loss ratios can vary from rotation to rotation of the engine. Notwithstanding, reduction in these friction losses will help improve the fuel economy of the car.

(Our present development program for the products intended for automotive engines does not cover the parts associated with pistons.)

[2] The friction loss derived from the oil pump is high at 3500 min⁻¹ and 6000 min⁻¹. There is a clear interrelation between the discharge amount and friction loss of the oil pump: by reducing the necessary discharge amount, the friction loss of the oil pump. By reducing the necessary discharge amount, the friction loss on of the oil pump can be decreased, and the necessary pump size can be smaller. Therefore, to reduce fuel consumption, reduction in the amount of oil fed by an oil pump appears to be important.

2.3 Requirements for NTN products for automotive engines

The requirements for NTN products for automotive

engines are summarized in Table 2. By reducing the friction losses with various parts for engines in order to reduce fuel consumption, we will be able to reduce CO₂ emissions and conserve energy resources.

2.4 Newly developed NTN products for automotive engines

The newly developed products for automotive engines described in this paper are illustrated in Fig. 3.

Among them, the following products are described in the sections below:

- (1) Oil-less chain tensioner
- (2) Rocker arm FA needle roller bearing
- (3) Low-friction capable needle roller bearings (for supporting crankshaft, for supporting camshaft)
- (4) Ball-screw unit for valve continuous variable mechanism

See the associated "New Product" section.

- (5) End-pivot type mechanical lash adjuster

See the associated "Technical Paper" section.

Table 2 Requirements for engine products

Portion on engine	Products for engines and requirements	Objective	Effects on the environment
Valve system	<ul style="list-style-type: none"> • Ball-screw unit for valve continuous variable mechanism (reduced pump loss) • FA needle roller bearing (smaller size, longer life) • End-pivot type mechanical lash adjuster (smaller oil pump) 	Lower fuel consumption	Reduction in CO ₂ emissions (prevention of global warming) Conservation of energy resources (wise utilization of resources)
Crank system	<ul style="list-style-type: none"> • Crankshaft supporting split needle roller bearing (lower frictional torque) 		
Valve drive system	<ul style="list-style-type: none"> • Camshaft supporting needle roller bearing (lower frictional torque) • Oilless chain tensioner (smaller oil pump) 		
Engine main body	<ul style="list-style-type: none"> • Each component (smaller size, lighter weight) 		

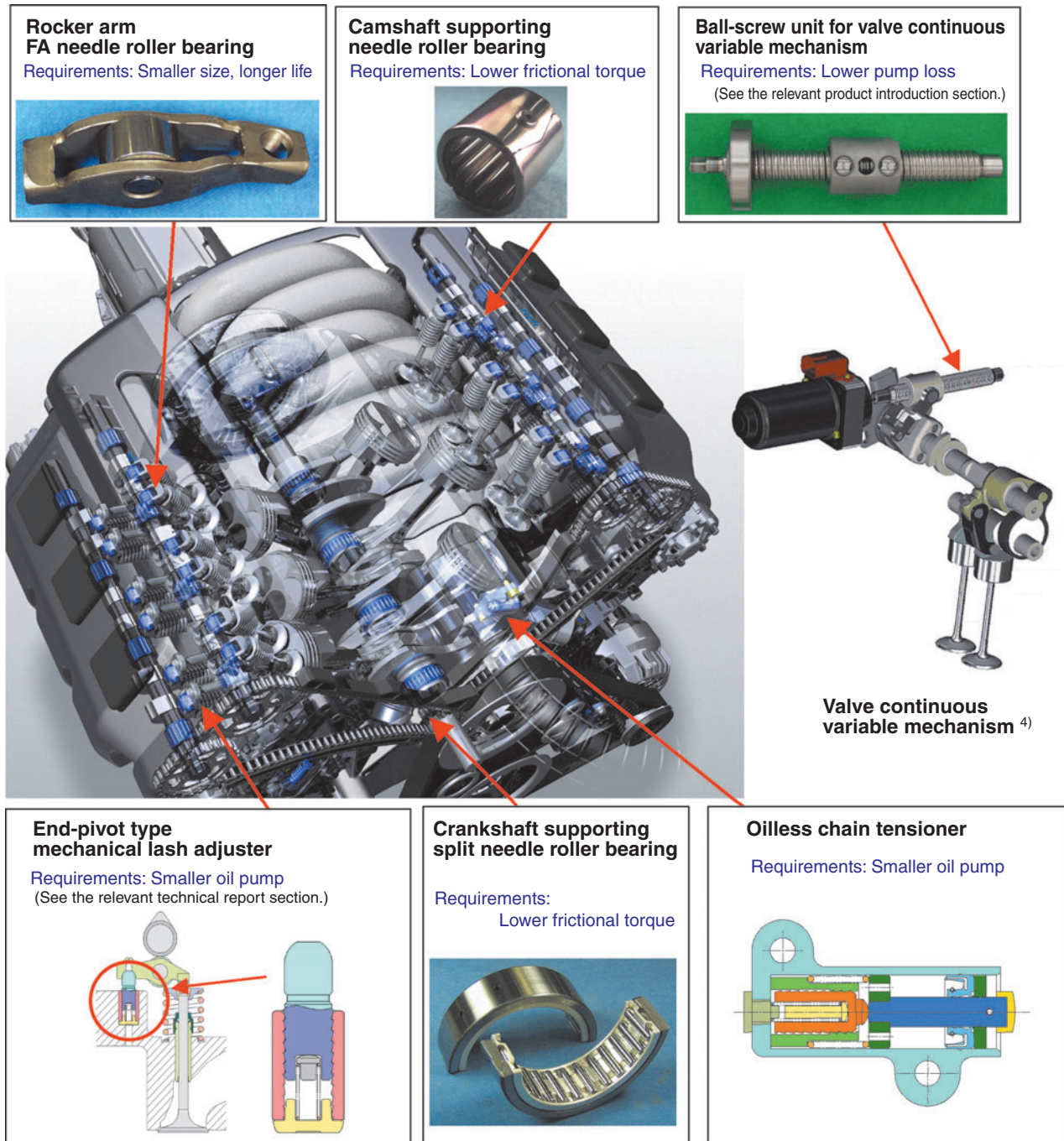


Fig. 3 Typical products for engine

3. Oil-less chain tensioner

Recently, the performance of automotive engines has been improving; and with this an increasing number of hydraulically actuated systems are incorporated into automotive engines.

As a result, oil pumps of larger size are used and the oil piping system is increasingly complicated. To address environmental issues, however, needs are for smaller, lighter oil pumps and reduced consumable lubrication needs.

NTN has been mass-producing two types of chain tensioners; – "buttress thread type" and "ring type", – each using the oil supplied from the engine as a damping means. To satisfy the current market need, we have developed an "oil-less type" chain tensioner that does not need oil supplied from the engine.

Our oil-less chain tensioner is described below.

3.1 Features

There are two representative functions required for the chain tensioner. They are the "damper mechanism"

and the "no-back mechanism".

[1] Damper mechanism

This mechanism is necessary to maintain constant tension on the timing chain. In an over – tensioned situation, the life of timing chain will be shorter and/or friction loss can occur on the timing chain. Not enough tension can cause the chain to wobble, possibly leading to excessive noise and teeth being skipped.

[2] No-back mechanism

While the engine is at a standstill, and depending on a phase relation between the camshaft and valve, a load may be applied to the tensioner even after the engine is turned off. When the engine is restarted in this position, the amplitude on the tensioner can be excessively large being in the forced-in position, which can result in noise. To solve this problem, a "no-back mechanism" will be integrated in the chain tensioner to prevent the plunger from ending up at the forced-in mode while the engine is at a standstill.

To provide a damper mechanism, NTN has adopted hydraulic damper types that utilize oil from the engine; namely, the buttress and ring types.

Our "no-back mechanism" employs a buttress thread structure (buttress thread type) or a wedge structure (ring type) consisting of a ring; causing the plunger to be forced in.

The damper mechanism on the oil-less chain tensioner consists of a buttress thread and a spring damper; while. The "no-back mechanism" on the tensioner relies on the frictional resistance of the buttress thread.

In summary, since our oil-less chain tensioner does not need oil supplied from the engine, the oil pump can be smaller and requires no oil piping system or pipe connections on the side of the engine.

Consequently, we can expect a lighter engine arrangement, lower fuel consumption, and a less expensive engine system.

3. 2 Construction and operation

Structures of the buttress thread and ring type chain tensioners are illustrated in [Fig. 4](#).

- [1] When the chain has slack, the plunger moves according to the force of the return spring, causing the chain to be adequately tensioned.
- [2] During this movement, the internal pressure of the pressure chamber drops, and the check valve opens allowing the oil to be supplied from the engine side.
- [3] While the chain is tensioned and the plunger is forced in, the oil in the pressure chamber is

gradually delivered to the outside through the leak gap defined by the cylinder and plunger. This causes the hydraulic damper to trip. Incidentally, depending on the engine characteristics, a relief valve may be integrated which releases oil to the outside when the internal pressure in the pressure chamber exceeds a particular threshold level.

The structure of our oil-less chain tensioner is illustrated in [Fig. 5](#).

- [1] When the chain has slack, the rod moves according to the force of the return spring, and follows the behavior of the chain. The buttress thread provides a mechanical damping force so that the chain is adequately tensioned.
- [2] When the chain is tensioned, the buttress thread is dynamically forced in from the operation of the lever guide and rod which protects the chain from over-tensioning.
- [3] The buttress thread is independent of the rod, so that the effect of rotating force on the buttress thread resulting from the sliding action relative to the lever guide is eliminated.
- [4] The oil prefilled in the tensioner lubricates the buttress thread. This arrangement means that the tensioner is not affected by the engine oil (type, viscosity, pressure, deterioration), and can perform stably.

3. 3 Evaluation of performance

The motor characteristics of an oil-less chain tensioner on an ordinary reciprocating engine are illustrated in [Fig. 6](#).

With specification A, the chain tensioner has a relief structure, and, therefore, runs stably over the entire range of running speeds, with minimal variation in chain tension. By adequately adjusting the relief setting, this chain tensioner can be used on engines with diverse running characteristics.

With specification B, the chain tensioner lacks a relief structure, and, as a result, the chain tension is high at higher running speeds. The drawback of this is that, the amplitude of the tensioner is very small, making this specification suitable for an engine that features smaller load variation.

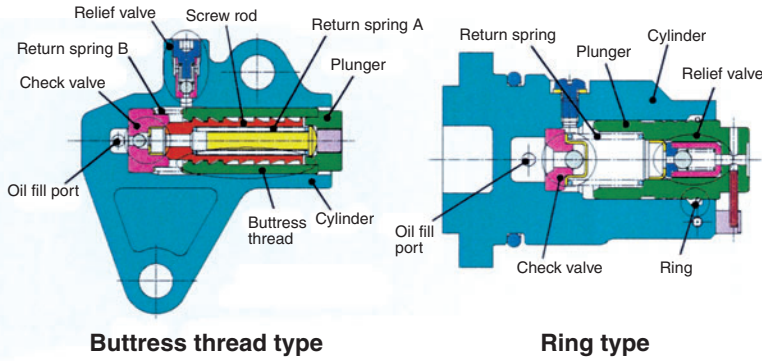


Fig. 4 Structure of butress thread type/ring type chain tensioner ^{5) 6)}

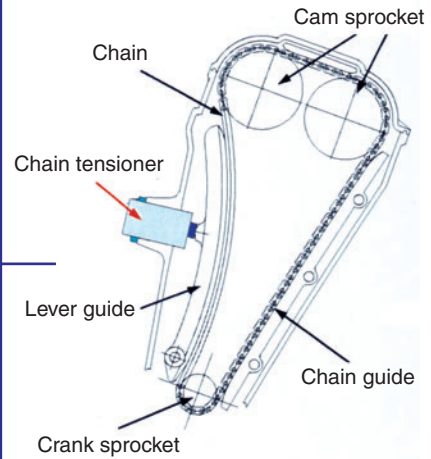
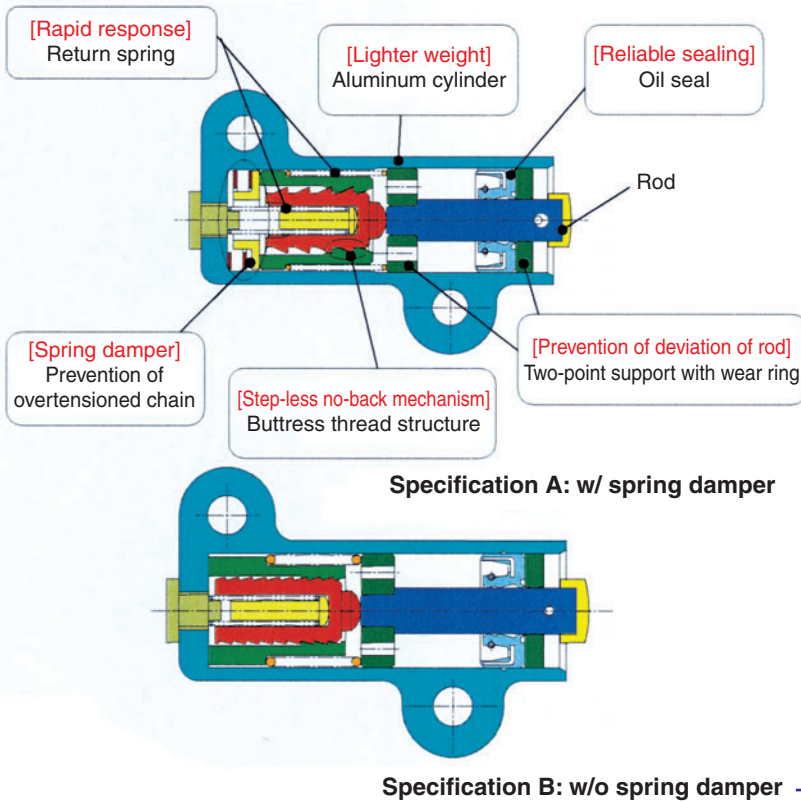


Fig. 5 Structure of chain tensioner without oil supply

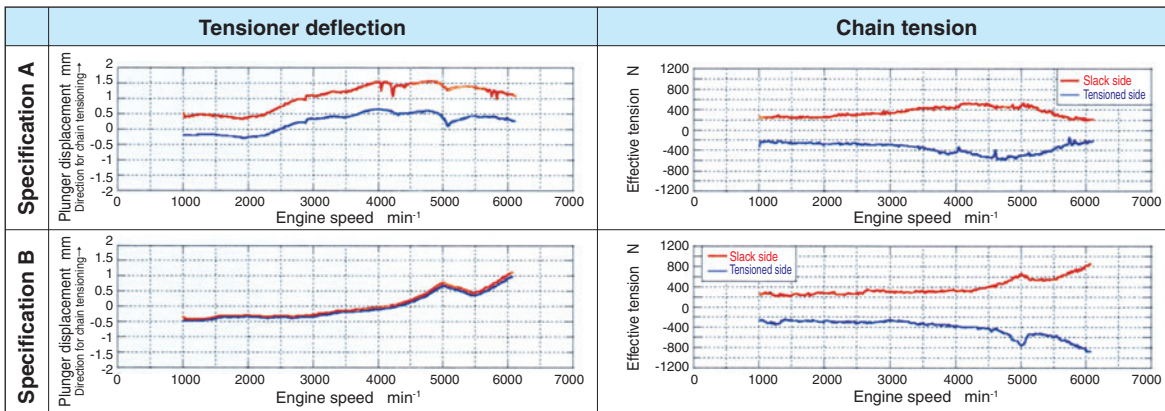


Fig. 6 Motoring characteristics of chain tensioner without oil supply

4. Rocker arm FA needle roller bearing

There is a steel making technology featuring finer crystal grain size for a given steel material in order to improve the fatigue strength. To use this advantage, NTN has developed a special heat treatment process (FA-treatment), wherein the crystal grain size on the bearing steel has been reduced to 1/2 or smaller compared with conventional bearing steel materials.

Because of this novel technology, the FA needle roller bearing for an engine rocker arm boasts a life at least 3.7 times as long as that of conventional rocker arm bearings. Consequently, for given operating conditions, the width and mass of our needle roller bearing can be as small as approximately 75% the size of a conventional needle roller bearings for the same application.

4.1 External appearance and microstructure of rocker arm bearing

[1] Photos of the rocker arm bearings are shown in **Photo 1**.

Each bearing is comprised of an outer ring,



Photo 1 Roller Rocker Bearing

rollers and shaft-each made of bearing steel.

[2] The austenite grain boundaries on a conventional standard heat-treated bearing steel material and those of an FA-treated bearing steel material are shown in **Photo 2**.

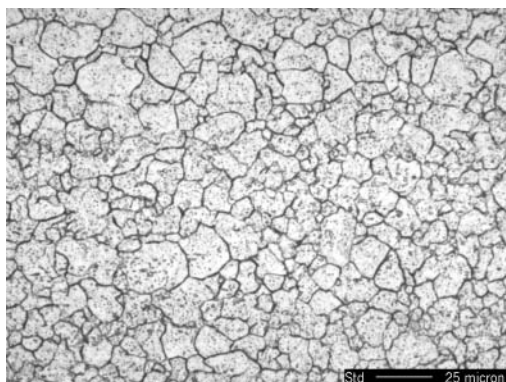
The size of the crystals from the FA-treatment are up to the size of those of standard heat-treated bearing steel.

4.2 Performance evaluation

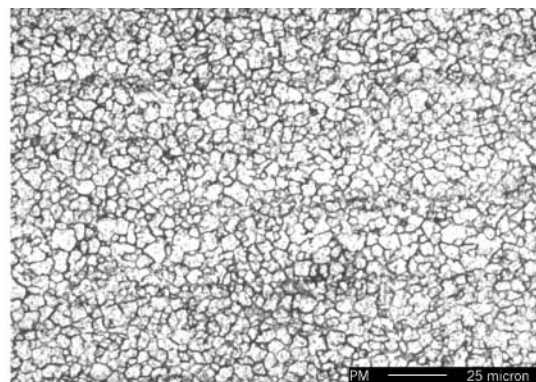
Comparisons between FA-treated bearings and conventional bearings, in terms of bearing life, are provided in **Fig. 7**. Comparisons between FA-treated bearings and conventional bearings, in terms of bearing life deriving from differences in face pressures are shown in **Fig. 8**.

Under a given set of operating conditions, the life of FA-treated bearings is 3.7 times greater than that of conventional bearings; The face pressure on the rollers and bearing with the FA-treated material can be 13% greater compared with those made with standard heat treatments. This advantage allows for a lightweight, compact needle roller bearing design.

A rocker arm bearing may be attached to the arm with one of two methods. One method is staking the arm with the shaft. The second method is to press-fit the bearing into the arm and locking it with a pin and/or retainer ring. For press-fitting, induction hardening is applied to ensure hardness for specific parts of the bearing. The FA-treatment technique can be applied to the latter method.



Bearing steel subjected to standard heat treatment



Bearing steel subjected to FA treatment

Photo 2 The prior austenite grain boundaries

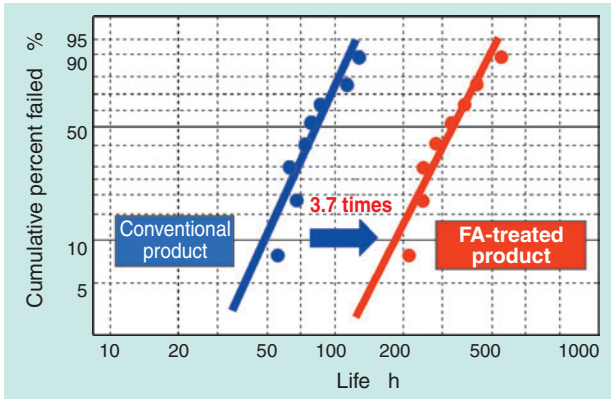


Fig. 7 Comparison of rolling contact fatigue of bearing

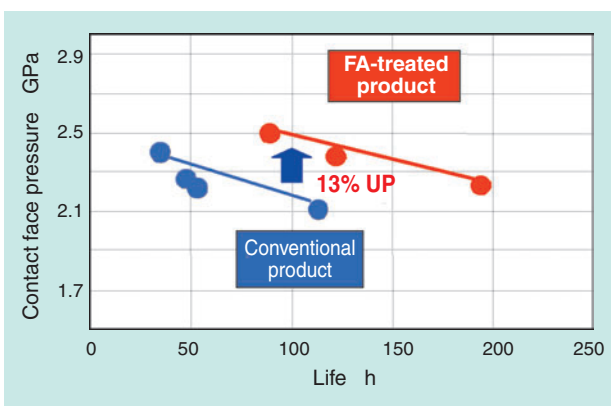


Fig. 8 Comparison of rolling contact fatigue of bearing by face pressure difference

5. Low-friction capable needle roller bearings (for supporting crankshaft and camshaft)

There is an increasing need for rolling bearings for supporting the shafts on automotive engines to reduce the friction possibly occurring between the shafts. Since crankshafts and camshafts have offset bearing journals, it is difficult to install an ordinary non-split bearing in the axial direction. At the same time, crankshafts and camshafts require a very low profile construction. Therefore, a split type sliding bearing can be used where the housing and shaft slide with each other.

In order for a crankshaft and a camshaft to readily incorporate a rolling bearing, we have developed a split needle roller bearing that provides easy installation and a low-profile structure. This unique needle roller bearing is described below.

5.1 Crankshaft supporting split needle roller bearing

Being a major component within a main motion system of any piston engine, the crankshaft converts the reciprocating motion of the pistons into the rotary motion via the connecting rod. Conventionally, a split type sliding bearing is used on the crank journal section. However, this arrangement leads to a need for much more oil supply compared with an arrangement that employs a rolling bearing. If a rolling bearing can be used in the crank journal section, a low-profile structure is necessary. Our crankshaft supporting split needle roller bearing is comprised of a two-piece outer ring and a set of needle rollers with a two-piece cage. The wall thickness of the outer ring can be as small as 2 mm since we have successfully developed a unique outer ring splitting scheme that can help inhibit deformation of the outer ring (Photo 3).

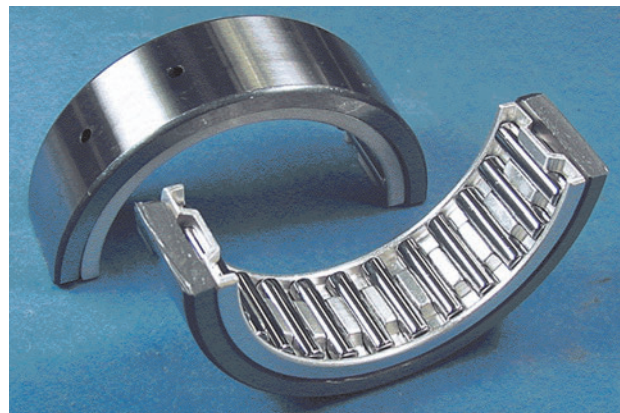


Photo 3 Split type needle roller bearing for crankshaft

5.1.1 Performance evaluation

Performance of our needle roller bearing was evaluated under the conditions that simulated those of an actual automotive engine. The torque of our product was compared with that of a split type sliding bearing. Also, our product was subjected to a bearing life test, acoustic measurement, and a measurement for correlation between oil level and torque. The result of the torque measurement is described below.

5.1.2 Bearing specification

Our needle roller bearing being tested measured 44 mm in inside diameter, 58 mm in outside diameter, 18 mm in width, with a roller diameter measuring 3.5 mm, roller length 14.8 mm with 26 rollers. This bearing was compared with a split type sliding bearing (inside dia. 46 mm, outside dia. 50 mm, width 14 mm).

5. 1. 3 Measuring conditions

The measurement was performed with the NTN high-speed outer ring run tester. The torque measuring conditions for our crankshaft supporting split needle roller bearing are summarized in **Table 3**.

5. 1. 4 Measurement result

The running torque measurement results are illustrated in **Fig. 9**, and the starting torque measurement results are shown in **Fig. 10**. A picture of the low-friction capable needle roller bearing evaluation test rig is shown in **Fig. 11**.

Compared with the split-type sliding bearing, the starting torque with our needle roller bearing is 90% to 92% lower and the running torque is 39% to 79% lower.

5. 2 Camshaft supporting split needle roller bearing

The camshaft, rotating in synchronization with the crankshaft, opens and closes valves by the motions of the tappets and rocker arms. Conventionally, the journal section on the camshaft uses a split type sliding bearing; and, generally, when the cylinder heads are made of aluminum, the camshaft is allowed to slide relative to the housing by utilizing the bearing metal function of aluminum itself.

Our camshaft supporting split needle roller bearing is comprised of a pair of outer rings and needle rollers with a single-split resin cage. The wall thickness of the outer ring can be as small as 0.6 mm because of a press-formed outer ring. (**Photo 4**).

Table 3 Split type needle roller bearing for camshaft torque measuring situations

	Running torque	Starting torque
Test rig	NTN high-speed outer ring run tester	
Applied load	9,150N	1,500N
Speed	1,000, 2,000, 3,000, 6,000min ⁻¹	Initial acceleration from 0 to 1,000 min ⁻¹ in 0.5 sec. period
Oil type	Engine oil 0W-20	
Lubricating condition	100°C, circulating lubrication at rate of 400 mL/min	Ordinary temperature, circulating lubrication at rate of 30 mL/min

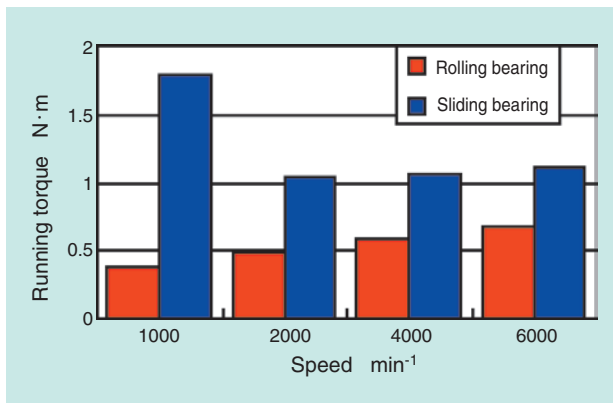


Fig. 9 Result of rotation torque measurement (Split type needle roller bearing for crankshaft)

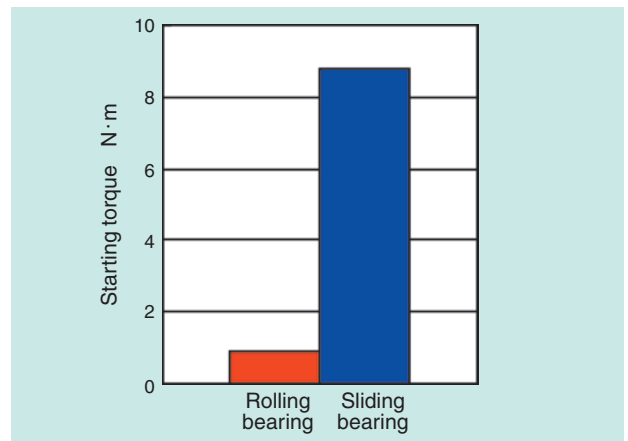


Fig. 10 Result of start torque measurement (Split type needle roller bearing for crankshaft)

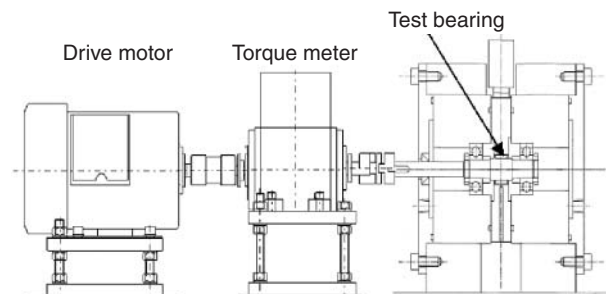


Fig. 11 Over view of test machine for “Low friction needle roller bearing”



Photo 4 Split type needle roller bearing for camshaft

5. 2. 1 Performance evaluation

Performance of our novel needle roller bearing was evaluated under the conditions that simulated those of an actual automotive engine. The torque of our product was compared with that of a sliding bearing of similar size. Also, our product was subjected to a bearing life test, acoustic measurement, and a measurement for mechanical strength of the outer ring positioning projection. The result of the torque measurement is described below.

5. 2. 2 Bearing specification

Our needle roller bearing being subjected to the evaluation measured 23 mm in inside diameter, 31.2 mm in outside diameter, 16 mm in width, with a roller diameter of 3.5 mm, roller length of 10.8 mm and the number of rollers was 16. This bearing was compared with a sliding bearing of similar size (inside dia. 23 mm, outside dia. 30 mm, width 25.8 mm).

5. 2. 3 Measuring conditions

The measurement was performed with the NTN high-speed outer ring run tester. The torque measuring conditions for our camshaft supporting split needle roller bearing is summarized in **Table 4**.

5. 2. 4 Measurement result

The running torque measurement result is illustrated in **Fig. 12**, and the starting torque measurement result is shown in **Fig. 13**.

Compared with the sliding bearing of a similar size, the starting torque with our needle roller bearing is 92% to 95% lower and the running torque is 35% to 62% lower.

6. Conclusion

Various development efforts have been made for better fuel efficiency with automotive engines, and the examples include hybrid engines, biofuel engines, compact powerful engine through downsizing; direct injection and lean-burn arrangements. To prepare for the 2015 fuel regulations, further attempts for more improved fuel economy are expected.

New auxiliary products for automotive engines featuring new functions will be needed while the conventional technologies are further improved (reduction in pump loss by utilization of valve continuous variable mechanism; reduction in friction, lighter, more compact arrangements for engine auxiliaries through use of roller rocker).

Table 4 Split type needle roller bearing for camshaft torque measuring situations

	Running torque	Starting torque
Test rig	NTN high-speed outer ring run tester	
Applied load	9,150N	1,500N
Speed	1,000, 2,000, 3,000, 6,000min ⁻¹	Initial acceleration from 0 to 750 min ⁻¹ in 0.5 sec. period
Oil type	Engine oil 0W-20	
Lubricating condition	100°C, circulating lubrication at rate of 400 mL/min	Ordinary temperature, circulating lubrication at rate of 200 mL/min

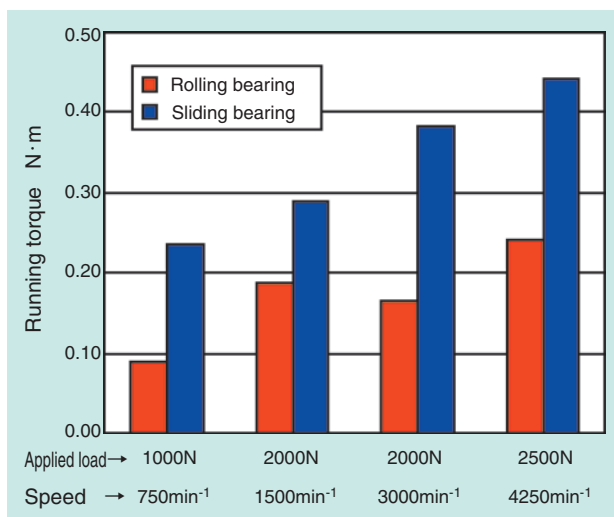


Fig. 12 Result of rotation torque measurement (Split type needle roller bearing for camshaft)

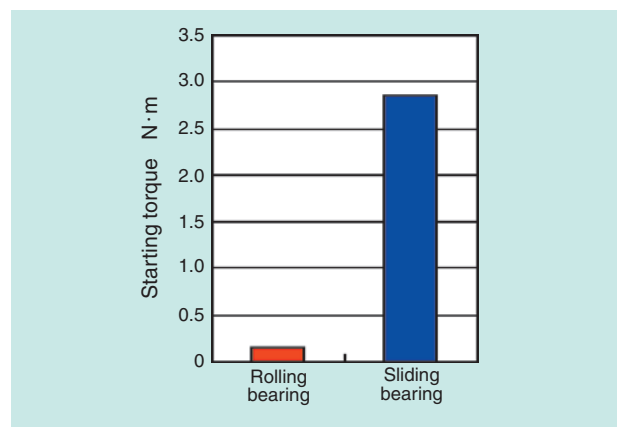


Fig. 13 Result of start torque measurement (Split type needle roller bearing for camshaft)

To remain compliant with any more demanding environmental regulation in the future, we will continually develop and market our versions of eco-friendly bearing products for automotive engines.

References

- 1) Website of Ministry of Land, Infrastructure and Transport Japan
- 2) Industry and Science Systems Co., Ltd., Engine friction reduction technology text, Engine Friction Reduction Technology, Nissan Motor Company, Powertrain Division Headquarters, Yoshinari Fujita
- 3) Tribology Monthly, Oct. 2003, Special Report II - Automobile Tribology: Engine Edition, About the reduction of engine friction, Suzuki Four-Wheel Drive Powertrain Design Group, Shun Kosugi, Ken Katagiri
- 4) Website of Nissan Motor Co., Ltd.
- 5) Satoshi KITANO, Tadahisa TANAKA, Tomokazu NAKAGAWA: The Auto-tensioner Market and Technical Trends, NTN Technical Review No.73 (2005)
- 6) Satoshi KITANO, Tadahisa TANAKA, Tomokazu NAKAGAWA: The Auto-tensioner Market and Technical Trends, Tribology Monthly, No.206 (2004)

Photos of authors



Yoshiaki RYOUNO
Automotive Engineering Dept.
Automotive Sales
Headquarters



Kouichi ONIMARU
Automotive Engineering Dept.
Automotive Sales Headquarters



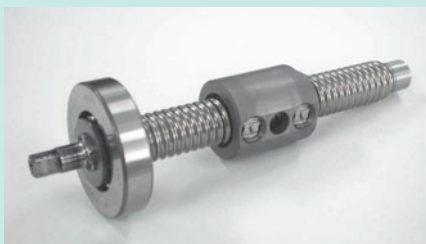
Kenichi KAWABATA
Needle Roller Bearing
Engineering Dept.
Automotive Sales Headquarters



Shinji OOISHI
Needle Roller Bearing
Engineering Dept.
Automotive Sales Headquarters

Ball-screw Unit for Variable Valve Event and Lift System

Keisuke KAZUNO*



Demand for improved fuel economy and cleaner exhaust emissions is increasing. One well-known technology to meet this demand is VTC, which makes it possible to change the timing between the crankshaft and engine valve opening. Recently, demand to continuously control the amount of valve lift has grown in order to further protect the environment. NTN has developed a new ball-screw unit, which reduces friction significantly while still having good durability. This ball-screw unit can control the electric actuator with higher efficiency and reaction time than current systems.

This article introduces the features of this ball-screw unit.

1. Introduction

Currently, most automotive gasoline engines are four-stroke cycle engines in which one cycle consists of four steps: induction of air-gasoline mixture into the engine, compression of the mixture, ignition of the compressed mixture, and emission of the resultant exhaust. Thus, this is how the gasoline engine develops power.

The valves situated at the top of the engine govern this operation. By varying the timing for opening and closing these valves, or by changing the lift in vertical motion of the valves, the fuel economy or output of the vehicle can be improved.

Recently, there has been mounting pressure for reduction in CO₂ emissions. Development work has been progressing for a continuously variable valve mechanism that is capable of the more delicate control that is necessary with the operating conditions of cars. In Europe, a worm-gear-based continuously variable valve mechanism has already been in the market for several years. Nissan Motor Co., Ltd. and Hitachi, Ltd., have succeeded in jointly developing the Variable Valve Event & Lift (VEL) system, which helps reduce electricity consumption and produces a quicker response. Utilizing the fact that a ball-screw is low friction and is highly efficient, this mechanism

achieves an overall smaller size, higher reliability (safety) and quicker response than conventional systems. Working together with Hitachi, Ltd., NTN has developed a unique ball-screw unit that operates the drive mechanism for the actuator that is responsible for the continuous variable control.

This paper hereunder describes this ball-screw unit.

2. Structure of VEL

2.1 Appearance of VEL

An illustration of the VEL is shown in **Fig. 1**.

Rotary motion of the driveshaft, which includes an eccentric cam, is translated into the vertical motion of the valve lifters by a plurality of links (link A—rocker arm—link B—output cam).

Based on this principle and by varying the phase of the control shaft coupled with the actuator section, the lift and operating angle of the valves are invariably controlled.

Incorporation of the VEL system will lead to improved output and response of automotive engines, improved fuel economy and cleaner emissions. In particular, the fuel economy appears to improve by approximately 10%.

*Automotive Engineering Dept. Automotive Sales Headquarters

2.2 Structure of actuator for VEL

The structure of the actuator section is illustrated in Fig. 2.

A ball-screw unit, as shown in Photo 1, is used on the actuator section in order to achieve a quicker response and lower electricity consumption. A DC motor is linked to the ball-screw shaft with a coupling. The rotating power of the motor is efficiently converted into the linear motion of the nut owing to a smaller rolling resistance, which is an advantage of the ball-screw unit, and accordingly varies the angular phase of the arm via the link connected to the middle point of the nut. Being engaged with the control shaft end, this arm invariably controls the lift and operating angle of the valves.

Incidentally, it is important to inhibit the noise and vibration that result from vibration loads occurring from the movement of the valves. To address this issue a high efficiency ball-screw is used, which features an optimized clearance. Also, the supporting bearing used is a four-point contact ball bearing that is capable of a compact, lightweight arrangement with a smaller clearance.

3. Features of ball-screw unit for VEL

An illustration of the ball-screw unit for the VEL system is shown in Photo 1.

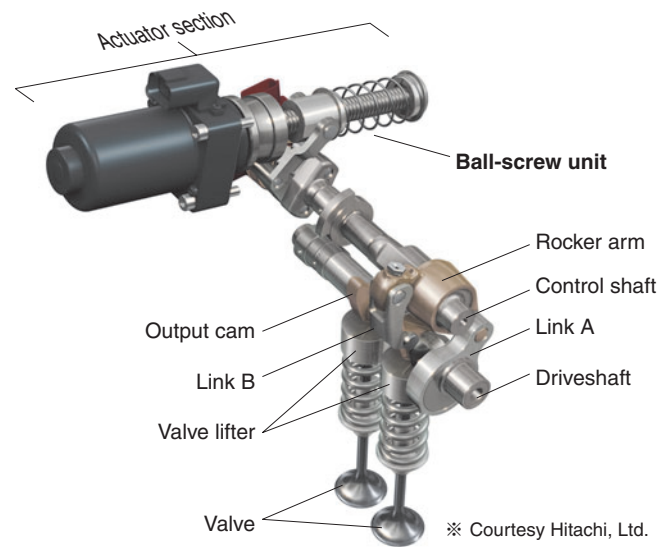


Fig. 1 Appearance of VEL system

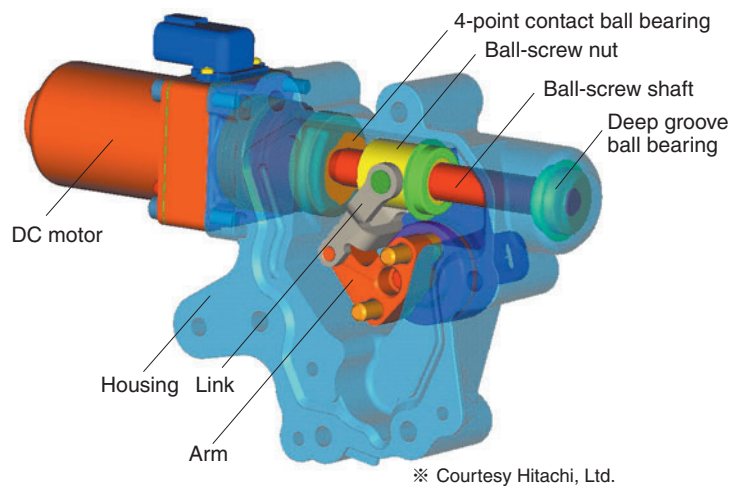


Fig. 2 Structure of actuator

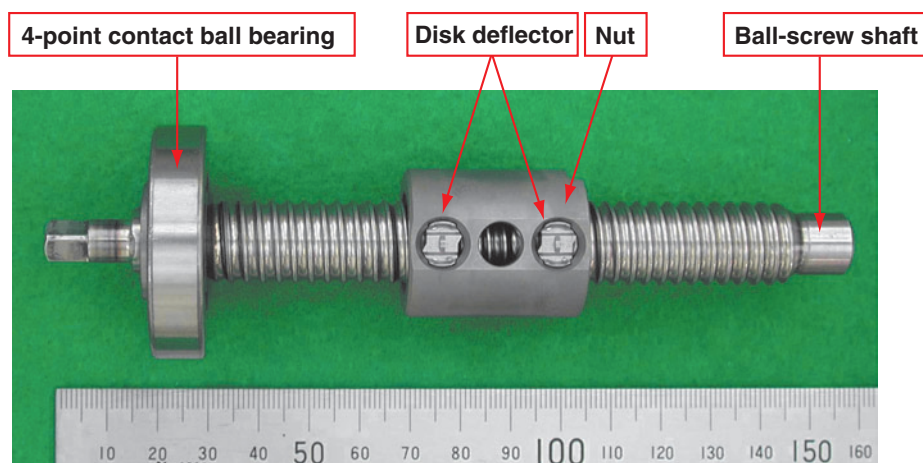


Photo 1 Ball screw unit for VEL system

The ball-screw unit on the VEL system can positively withstand the load application from the valves and still features a lower cost, as the result of incorporating the following unique features:

- (1) Use of disk deflector
- (2) Integration of supporting bearing by staking
- (3) Adoption of oil-immersed induction hardening technique for ball-screw shaft
- (4) Formation of nut thread groove without using grinding technique

Further detail on these features is given in the following sections:

3.1 Use of disk deflector

The ball-screw unit uses a deflector system for circulating the balls, wherein the deflector used is a disk type (improved shape) instead of a conventional oval type. An illustration of a conventional oval deflector is given in **Photo 2**, while the new disk type deflector is shown in **Photos 3** and **4**.

The new deflector is inserted into the round hole formed on the nut through the bore of nut, wherein the wing sections are allowed to remain seated in the thread groove where the balls do not roll, and several areas on the outer circumference of the nut are secured by staking.

Because the previous deflector was an oval type, it was necessary to open the deflector hole on the nut by moving an end-milling cutter sideways from the outer circumferential side of the nut in order to obtain the oval hole. In contrast, with our ball-screw unit, the deflector hole is round-shaped and can be easily machined with a standard tool; thereby the deflector hole is made at a lower machining cost.

Furthermore, the new deflector is made of a material boasting a sufficient mechanical strength so that the force needed to extract the deflector from the nut is sufficiently great relative to the load being exerted from the valve.

The result of the comparison between the conventional oval deflector and the new disk deflector, in terms of the force needed for extracting the deflector from the nut, is plotted in **Fig. 3**.

Oval (conventional) deflector



Photo 2 Appearance of past deflector

Compared with the conventional oval deflector, the extraction load for the disk deflector is approximately 1.8 times as great.

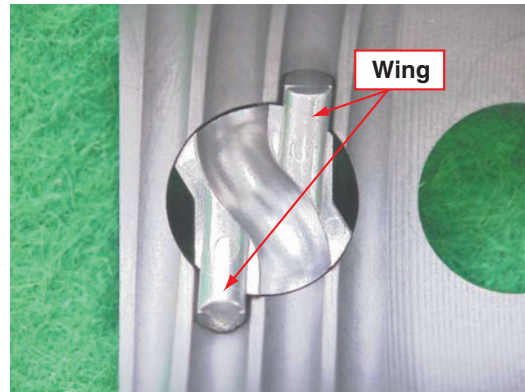


Photo 3 Appearance of new deflector

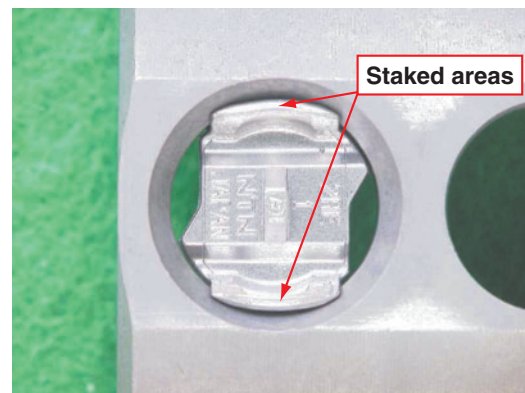


Photo 4 Appearance of new deflector staking

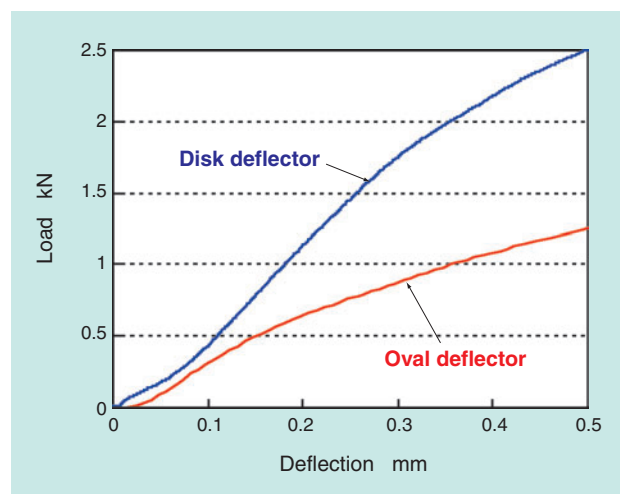


Fig. 3 Load-Displacement curve of deflector

3. 2 Integration of supporting bearing by staking

When being fixed along the axial direction on a ball-screw shaft, a bearing is usually secured with a lock nut or with a retainer ring. The locking arrangement with a lock nut means a necessity of an additional part (lock nut) and a procedure for forming the thread for the nut on the ball-screw shaft, which increases cost. This arrangement further needs an anti-loosening feature for the lock nut. Incidentally, a countermeasure against wear and tear will be needed for the retaining arrangement when using a retainer ring if a vibrating load acts on the retainer ring.

For the new ball-screw unit, the bearing is fixed to the shaft through plastic-deformation of a relevant portion of the ball-screw shaft by staking. Illustrations of the staked area are shown in Photos 5 and 6.

As shown in Photos 5, a portion of the shaft over which the bearing had been inserted was plastic-deformed so that it was brought into contact with the end face of the bearing, thereby integrating the bearing with the ball-screw shaft.

However, if the bearing is more strongly staked to ensure sufficient fastening strength, the circularity of the bearing inner ring could be adversely affected. To address this issue a spacer is inserted between the staked area and the bearing end face to decrease the load possibly occurring from radial deformation, which results from staking. Thereby, deformation of the bearing inner ring is avoided.

The result of the evaluation for the axial extraction force needed to remove the bearing secured by this staking method is plotted in Fig. 4. This evaluation was performed by applying a load to the bearing end face while the shaft was locked and then measuring the bearing displacement. The bearing extraction force needed was approximately 7 kN, which is

approximately 10 times as great as the maximum axial load acting on the ball-screw shaft.

Also, an extraction fatigue test was performed against the vibration load acting on the staked areas on the bearing.

The vibration load specified in Table 1 was applied to the ball-screw shaft, thereby verifying that the bearing did not come off the ball-screw shaft.

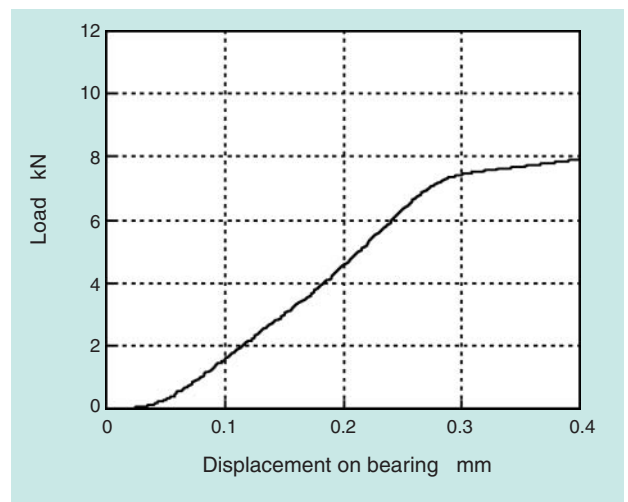


Fig. 4 Load-Displacement curve of bearing

Table 1 Table of fatigue test condition of bearing coming out

Load (kN)	Frequency (Hz)	Test duration (h)	Number of loading cycles ($\times 10^7$)
0.79 ± 0.77	30	103.5	1.11
1.57 ± 1.55		24	0.25
2.35 ± 2.33		24	0.25
3.13 ± 3.11	20	36	0.25

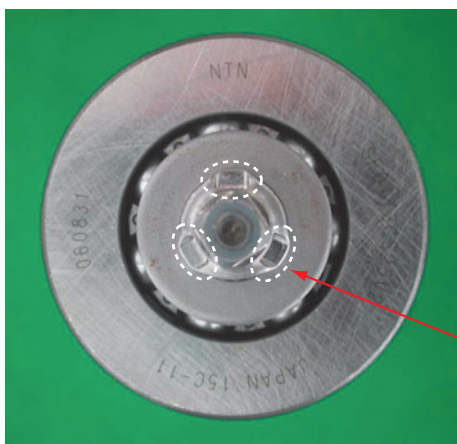


Photo 5 Appearance of bearing staking (view from axial side)

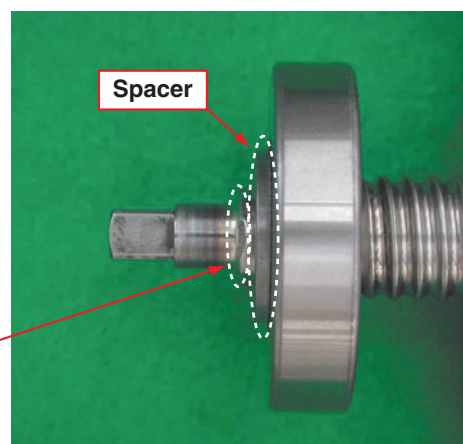


Photo 6 Appearance of bearing staking (view from radial side)

3.3 Adoption of oil-immersed induction hardening technique for ball-screw shaft

Previously, the ball-screw shaft was induction-hardened in air, which resulted in oxidation scale occurring on the rolling surface of the thread and so an additional process was necessary to remove this scale.

In the induction hardening process for the ball-screw shaft of the NTN ball-screw unit, the newly developed ball-screw shaft and induction-hardening coil are immersed in oil to isolate the rolling surface from the atmosphere. **Photo 7** shows the state of oxidation scale deposition on the ball-screw shaft subjected to conventional induction hardening in atmosphere and on the newly developed ball-screw shaft that has undergone induction hardening in oil.

Virtually no oxidation scale will occur from the oil-immersed induction hardening process and so an oxidation scale removal process can be deleted. Thus, the so-obtained ball-screw shaft boasts excellent surface quality and the ball-screw unit features a lower price.

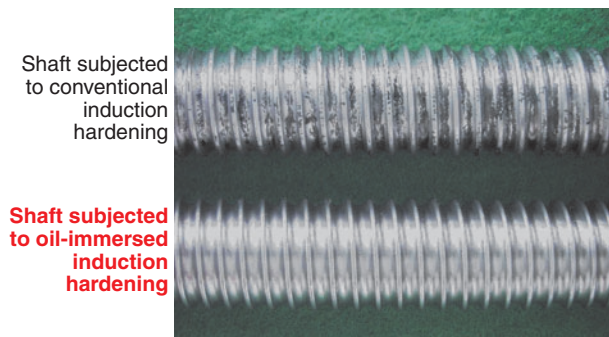


Photo 7 Comparison of Oxidation scale on the shaft

3.4 Formation of nut thread groove without using grinding technique

Previously, the machining process for the thread groove on the ball-screw nut consisted of a rough formation of the thread groove while leaving a sufficient grinding allowance. This was followed by a heat treatment process and then a grinding process to form the final thread groove profile.

Though positively capable of attaining an accurate thread profile, the thread grinding process necessitates an expensive plant and a longer processing time, leading to a cost issue.

The new ball-screw unit employs a novel thread groove machining process for the nut that offers sufficient durability and operability of the nut without involving grinding work. **Photo 8** shows the rolling surface of the nut machined without grinding.

NTN has realized this achievement through adoption of a NC-based, high-precision cutting process.

After the high-precision cutting work the nut is subjected to carburizing and quenching. As a result of this process, a grain boundary oxidized layer occurs on the thread groove surface owing to the oxygen in the furnace. If the groove is used as the ball-screw groove without any modification, then the thread groove will pose problems in terms of wear resistance and durability.

To overcome these problems the nut-rolling surface of the ball-screw unit, after undergoing the carburizing and quenching processes, is treated with a special shot-peening process to remove the boundary grain oxidized layer. This improves the wear resistance and durability of the thread groove.

NTN has performed a retaining & durability test in order to evaluate the wear resistance of the new ball-screw unit. In this test, we applied a vibrating load to the ball-screw shaft whose position was retained while the shaft was not allowed to rotate. Then the increase in the clearance on the ball-screw was evaluated relative to the clearance before the test. **Table 2** summarizes the comparison result in terms of wear resistance between samples that have undergone a special shot-peening process and those that have not undergone this process.

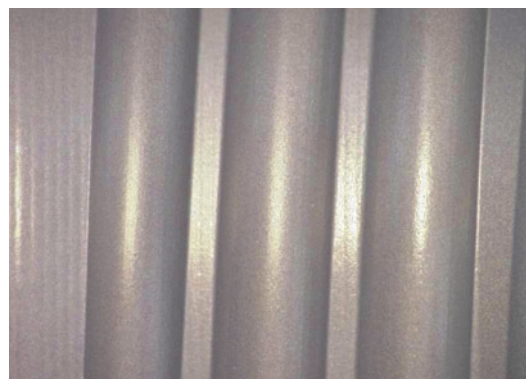


Photo 8 Surface of no-grinding nut groove

Table 2 Comparison of wear resistance

Test ball-screw	Specimen not undergone shot-peening	Specimen undergone special shot peening
Test load	Radial and axial loads combined 1032N, 40Hz	
Lubrication	Engine oil (5W-30) 1cc/5 min., drip	
Test duration (h)	68	
Increase in clearance on ball-screw (mm)	0.008	0.001

Samples that have undergone the special shot-peening process exhibit virtually no increase in clearance and have good wear resistance.

Next, we compared the durability of the ball-screw that has undergone the special shot-peening process with that of the ball-screw that has not undergone a similar process; the comparison result is graphically plotted in **Fig. 5**. In the durability test a constant load of 2400 N was applied to each specimen until flaking occurred and then a comparison was made of the life results.

The L_{10} life of the ball-screws that did not undergo the special shot-peening process stood at 9.4×10^6 rev., while the specimens that had undergone this process was 15.4×10^6 rev. This means that the life of the samples that had undergone the special shot-peening process are approximately 1.6 times as long compared with those that had not undergone this process.

On a bench test with an actual automotive engine, the new NTN ball-screw unit successfully withstood a durability test equivalent to 300,000 km of actual vehicle travel. This means that the ball-screw unit satisfies the requirements for both a high degree of durability and a lower cost.

4. Conclusion

The new NTN ball-screw unit incorporates various novel design techniques and machining processes has been described above.

Efforts have been mounting for electromechanical arrangements not only for variable valve mechanisms whose market seems to expand dramatically, but also for various car components. Under this situation more car developers are thinking of ball-screw based drive mechanisms. Therefore, the market size for improved ball-screw mechanisms for automobiles will continue to expand.

NTN has been promoting new developmental work for the ball-screw units that achieve a lower cost and improved durability and will remain committed to expanding the applicability of ball-screw units for automobiles.

In closing this document, I want to express my gratitude to the people of Automotive System Group, Hitachi, Ltd., who have kindly supported the development work for our ball-screw products and provided their invaluable engineering information.

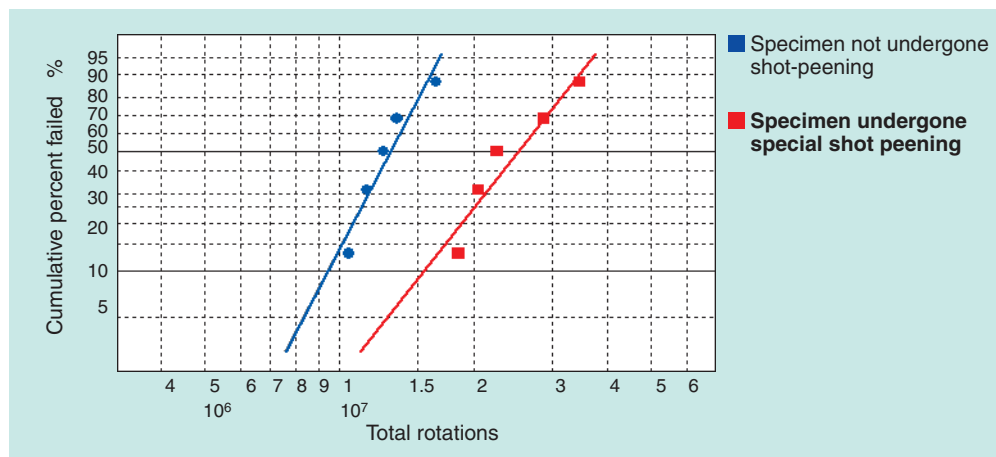


Fig. 5 Comparison of durability

Photo of author



Keisuke KAZUNO

Automotive Engineering Dept.
Automotive Sales Headquarters

Development of an End-Pivot Type Mechanical Lash Adjuster

Eiji MAENO*
Hiroshi BUNKO**
Katsuhisa YAMAGUCHI**



NTN has developed a Mechanical Lash Adjuster (MLA) that can replace conventional Hydraulic Lash Adjusters (HLA). This MLA, which applies buttress threads as the adjustment mechanism, shows excellent performance in fundamental function tests on valve-lift stability, valve-lash adjustment speed, and low-temperature characteristics. Durability tests confirmed that the MLA is capable of a 20% shorter axially design in comparison with conventional HLAs.

1. Foreword

Recently, an increasing number of car models are incorporating roller rocker arm type valve systems with one of the goals being better fuel economy. However, compared with a direct type valve system a rocker arm type valve system has a more complicated structure and a greater number of wear points. Therefore, a rocker arm type valve system needs a mechanism for adjusting the valve clearance ¹⁾.

Common examples of valve clearance adjustment mechanisms are a fixed type and a HLA. The fixed type valve clearance adjustment mechanism is manually adjusted with a screw and then tightened to lock the adjustment, whereas the HLA is an automatic adjustment system. However, these conventional valve clearance adjustment mechanisms have drawbacks. The fixed type needs to be adjusted manually when necessary. The drawback with the HLA is that when bubbles in the engine oil enter the high-pressure chamber a decrease in rigidity and noise can occur ²⁾. NTN has developed a unique mechanical lash adjuster (MLA) that supersedes these conventional mechanisms. This report describes the basic MLA functions and the result of their durability testing.

2. Structure

Fig. 1 shows a cross-sectional view of the MLA and **Fig. 2** gives a schematic view of the MLA incorporated into an automotive engine. Using buttress thread screw technology in conjunction with a return spring, the MLA is able to provide automatic adjustment of the valve clearance.

On the buttress thread screw system the male thread is formed beneath the pivot member that serves as the fulcrum for the rocker arm, while the female thread is in the inner circumference on the case that houses the pivot member. By operation of a compressed coil spring the pivot member is forced upward toward the rocker arm side, while a spring seat, whose top end is spherical, is inserted between the pivot member and the compressed coil spring to decrease the running resistance on the MLA.

*Automotive Engineering Dept. Automotive Sales Headquarters

**New Product Development Dept. New Product Development R&D Center

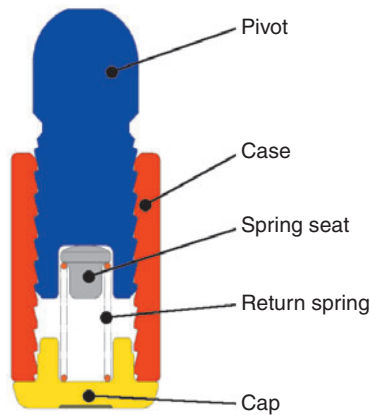


Fig. 1 Cross-section of MLA

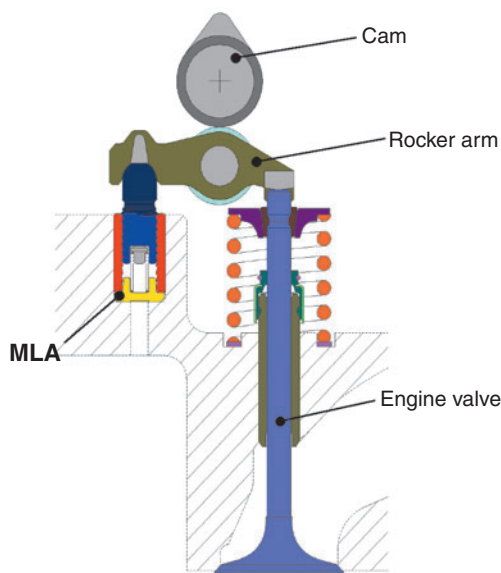


Fig. 2 Installation layout of MLA

3. Operating principle and functions

3.1 Operating principle (about buttress thread screw)

The static self-sustained (no occurrence of sliding rotation against the axial static load applied) condition of a screw is governed by the relation between the angles of the thread ridge (lead angle α and flank angle θ' on a cross-sectional plane square to the thread lead) and the inner-thread face friction coefficient. More specifically, if the actual friction coefficient μ is greater than the static self-sustaining friction coefficient μ_s defined by $\tan \alpha \cos \theta'$, then the screw will remain at a self-sustained state; and when the former is smaller than the latter, the screw will slide³⁾.

Because the two neighboring thread faces on a buttress thread are not symmetrical with each other, the self-sustaining coefficient μ_s of the buttress thread can vary depending on the orientation of the

axial load acting on the buttress thread screw. In other words, by appropriately adjusting the lead angle and two flank angles, it is possible to allow the buttress thread screw to remain at a self-sustained state against an axial load working from one side and to slide and rotate by an axial load acting from the opposite side. Utilizing this direction-dependency of a buttress thread screw, the NTN MLA realizes the automatic valve clearance adjustment function.

The shape of the buttress thread screw is illustrated in Fig. 3. The angles of the thread ridge are designed such that the screw slides in the projection direction for the pivot, and remains at a self-sustained state in the drive-in direction for the pivot, and that the screw does not develop wedge engagement-induced seizure against a drive-in load. The conditions required for the thread angles are summarized with the formula (1) below:

$$\left. \begin{aligned} \tan \alpha > \mu_{\max} \cdot \sec \theta_2' & \text{ (projecting condition)} \\ \tan \alpha > \mu_{\min} \cdot \sec \theta_1' & \text{ (self-sustaining condition)} \\ \cot \theta_1 > \mu_{\max} \cdot \cos \alpha & \text{ (wedge angle)} \end{aligned} \right\} \dots \dots \dots (1)$$

where,

- α : lead angle
- θ_1' : flank angle (self-sustaining side) on a cross-sectional plane A that is square to the thread lead
- θ_2' : flank angle (sliding side) on a cross-sectional plane A that is square to the thread lead
- μ_{\max} : maximum friction coefficient for friction between thread faces
- μ_{\min} : minimum friction coefficient for friction between thread faces

Formula (2) shows the relationship between the flank angle q' on the cross-sectional plane A square to the thread lead and the flank angle q on the cross-sectional plane B that includes the screw axis. However, note that the buttress thread screw used on the MLA features a sufficiently small α that permits an approximation of $\cos \alpha \doteq 1$.

$$\tan \theta_1 = \tan \theta \cos \alpha \dots \dots \dots (2)$$

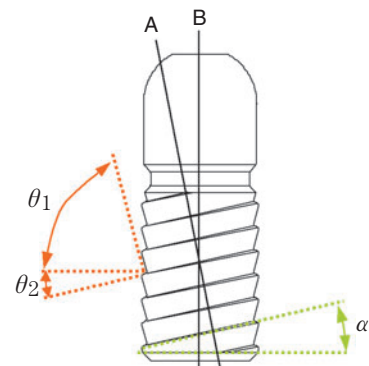


Fig. 3 Shape of the buttress threads

3. 2 Functions

In Fig. 4, typical factors that affect the valve clearance are illustrated. The lash adjuster is required to expand and/or contract in accordance with the variation in the valve clearance, which results from these factors, to maintain the valve clearance to a limited range.

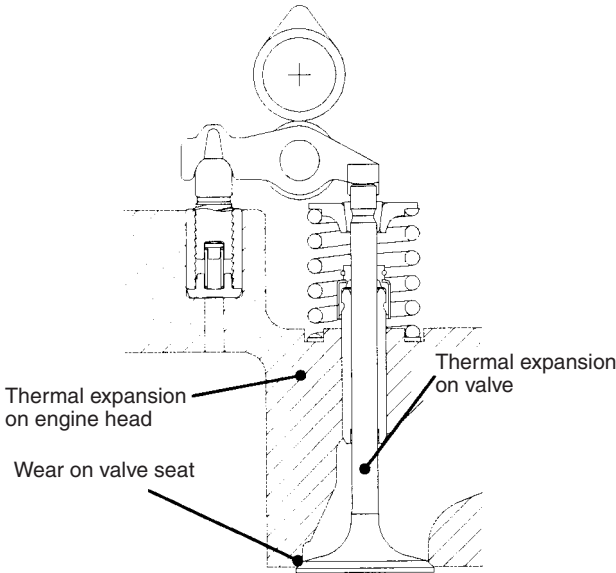


Fig. 4 Factor of changing valve clearance

3. 2. 1 Steady operation mode

When the valve opens as the thread faces on the self-sustaining side come into contact with each other due to the input from the cam load, which results in relative sliding occurs between the thread faces because of a squeeze film and elastic deformation of the thread faces⁴⁾. When the valve closes, the pivot is lifted by the reaction force of the return spring until the sliding side thread faces come into contact with each other, thereby maintaining the MLA at a constant height (Fig. 5).

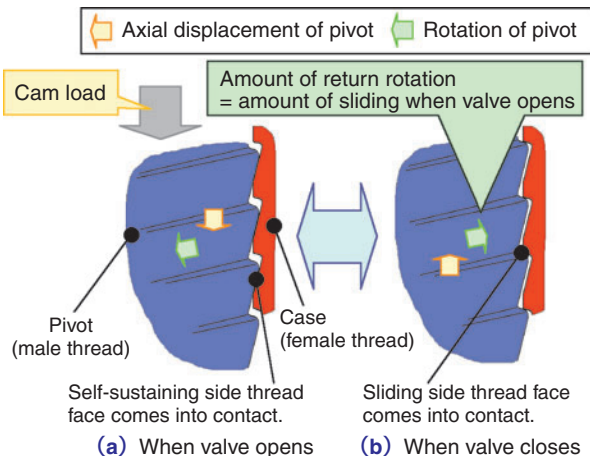


Fig. 5 Motion of buttress-thread (steady)

3. 2. 2 Adjustment against enlarged valve clearance

While the valve clearance increases due to factors including thermal expansion on the engine head and when the valve opens, the motion of the buttress thread screw is identical to that in the steady operation mode described in Sec. 3.2.1. On the other hand, when the valve closes, the pivot rotates in the return direction by a certain angle (an angle for slight sliding between the thread faces when the valve has opened plus an angle equivalent to a newly enlarged valve clearance), thereby the MLA expands causing the valve clearance to be maintained at an adequate level (Fig. 6).

3. 2. 3 Adjustment against decreased valve clearance

A worn valve seat will lead to reduced valve clearance. Since the valve clearance further decreases in such a situation due to the backlash on the screw; consequently, when the valve closes, the pivot cannot move upward to a position where the sliding side thread faces come into contact with each other and no return rotation occurs on the pivot.

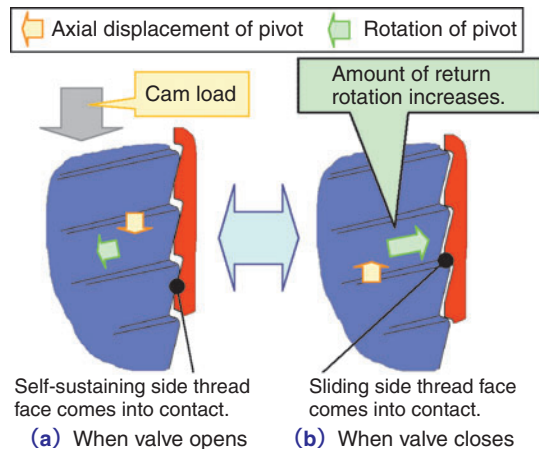


Fig. 6 Motion of buttress-thread (expansion)

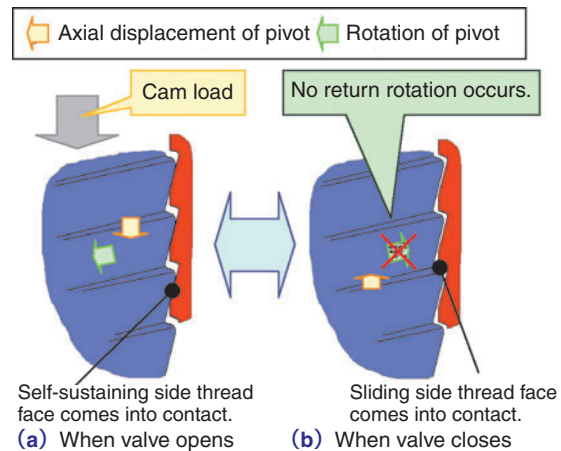


Fig. 7 Motion of buttress-thread (contraction)

Because of this, the slight sliding occurring when the valve opens will accumulate, thereby the MLA will gradually contract and as a result, the valve clearance will be maintained at an appropriate level (Fig. 7).

4. Evaluation result

4.1 Valve-lift stability

4.1.1 Analysis method

To investigate the valve-lift stability in steady operation mode, variation in the valve lift peak was measured while the engine speed was maintained at a constant level and by sweeping the engine speed (repeated variation). A picture of the engine bench test rig is shown in Fig. 8. The crankshaft of an automotive engine (1500 cc) was rotated with an electric motor and the valve position was detected with eddy current type gap sensors. Since the detection range of the compact gap sensor is limited two sensors were used to measure variation in the valve lift peak. One sensor

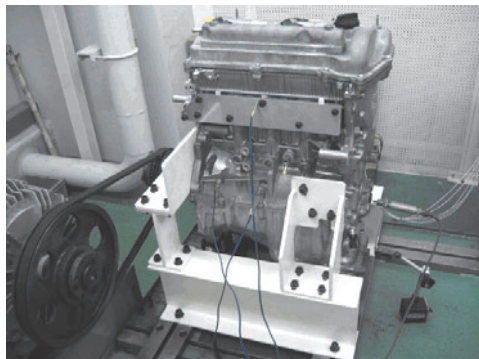


Fig. 8 Engine bench for functional tests

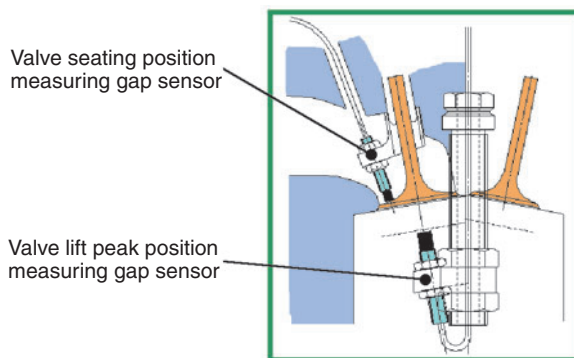


Fig. 9 Layout of gap-sensors

Table 1 Condition of valve-lift stability test

Oil viscosity	SAE OW-20
Oil temperature	Approx. 40-130°C (natural temperature increase)
Crank speed	① 6000 min ⁻¹ constant
	② 600-6000 min ⁻¹ sweeping
Run duration	6000 sec

was used to measure the area around the valve lift peak and the other for measuring the area around the valve seat. The sensor configuration is illustrated in Fig. 9 and the test conditions are summarized in Table 1.

4.1.2 Result

The valve lift peak positions are continuously plotted in Figs. 10 and 11. Fig. 10 represents a plotting obtained from an operation where the engine was run at a constant speed, while for the plot in Fig. 11, the engine speed was swept. For the test, the MLA (NTN's new product) and the HLA (conventional product) were both commonly incorporated into one automotive engine, thereby they were simultaneously analyzed. The absolute values of valve lift height are smaller with the MLA owing to the backlash on the screw in the MLA. However, the magnitude of variation in valve lift peak is the same with both the HLA and MLA. Thus, it was verified that the stability with a MLA is sufficiently high.

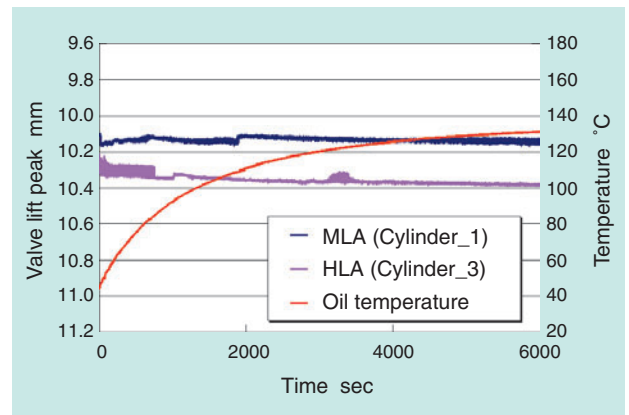


Fig. 10 Valve lift peak (constant-rotation)

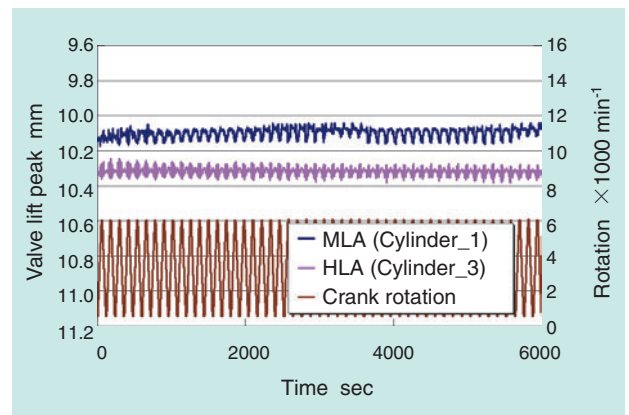


Fig. 11 Valve lift peak (cyclic-rotation)

4.2 Expansion/contraction follow-up quality

4.2.1 Analysis method

After the engine is started the exhaust valve, being exposed to hot exhaust gas, undergoes thermal expansion. When the exhaust valve expands, the valve clearance will decrease. In the case of a HLA, the original valve clearance on it is 0. If contraction of the lash adjuster is too slow the HLA can develop compression leakage. With the MLA the backlash on the buttress thread screw functions as a valve clearance, thereby the valve expansion is compensated for and a compression leak does not occur immediately. However, expansion-contraction follow-up quality is an important characteristic for the performance of the lash adjuster. The expansion-contraction follow-up performance of the MLA was compared with that of the HLA. An example of the test bench used is shown in Fig. 12. The engine head was placed on the test bench and the camshaft was driven by an electric motor via a timing belt. The position of the valve lift was detected from beneath the valve with a laser displacement meter. The test conditions are summarized in Table 2.

The displacement on the lash adjuster due to expansion/contraction was measured by inserting and removing a shim between the valve face and valve

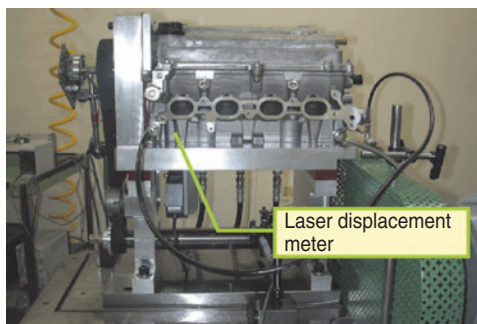


Fig. 12 Test bench for functional test

Table 2 Condition of adjustment speed test

Oil viscosity	SAE OW-20
Oil temperature	Approx. 40/80°C (temperature controller)
Crank speed	600, 1000, 2000 min ⁻¹
Run duration	30 sec

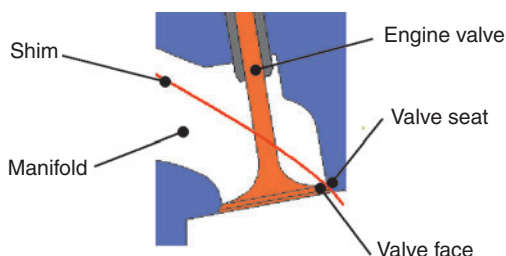


Fig. 13 Shim insertion diagram

seat (as shown in Fig. 13) and then by analyzing the resultant valve behavior (seating position and peak position of the valve).

4.2.2 Result

Valve behaviors in terms of the seating position and peak position, with a 0.3 mm shim inserted or removed, are illustrated in Figs. 14 and 15.

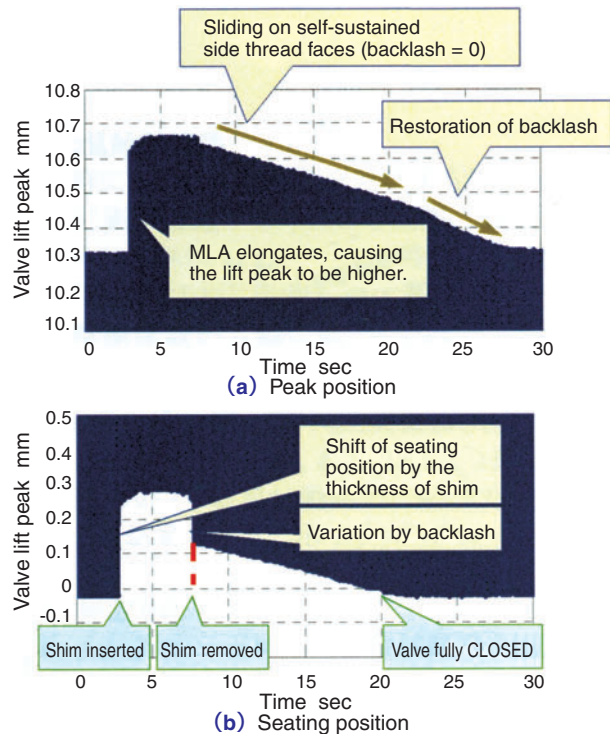


Fig. 14 Valve behavior in adjustment test (MLA)

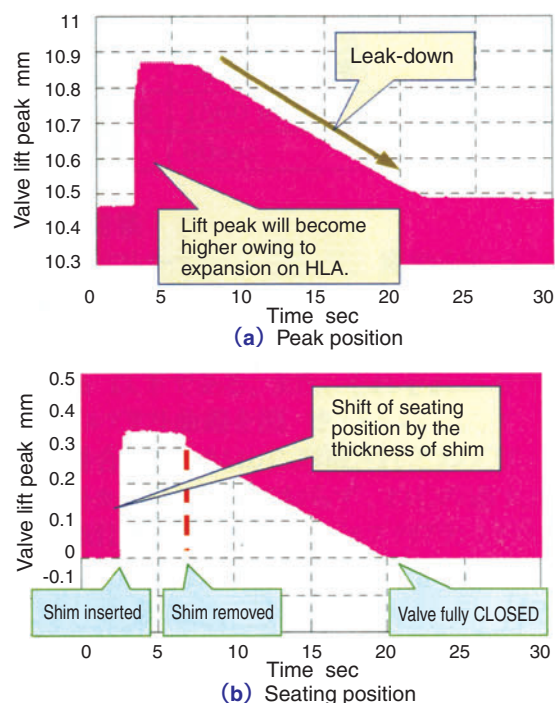


Fig. 15 Valve behavior in adjustment test (HLA)

For both the HLA and MLA with the shim inserted, the peak position varies at almost the same time as when the valve seating position varies. This means that an increase in valve clearance resulting from the inserted shim is compensated for as the lash adjuster instantaneously expands. In other words, the expansion speed of the lash adjuster is sufficiently high relative to the thermal expansion and wear speed.

After the shim is removed, the HLA gradually contracts and the seating and peak positions return to their original positions at a same speed. When the shim is removed with the MLA, the screw backlash is eliminated and the pivot is gradually driven in. Then, when the valve can be fully closed the pivot is further driven in by a distance equivalent to the screw backlash; thereby the MLA resumes its original state.

The contraction speed is relatively low and this fact sometimes leads to an occurrence of compression leakage. The HLA was compared with the MLA in terms of the time needed for the lash adjuster to sink by a particular stroke (contraction time) and the result is shown in Fig. 16. Since the HLA contracts due to the oil leakage from the high-pressure chamber, its contraction time varies depending on the temperature. In contrast, the contraction time of the MLA is dependent on the running speed rather than the temperature. This is because the contraction on the MLA derives from accumulation of slight sliding on the thread faces occurring in each cycle. The follow-up speed of the MLA is slowest in the idling mode. However, this slowest speed is still sufficiently high relative to the thermal expansion speed of the valve.

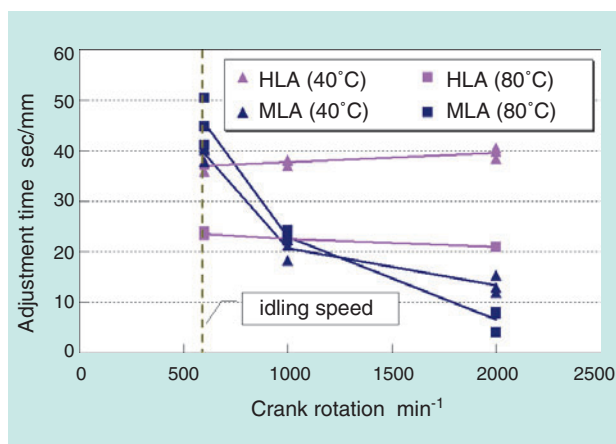


Fig. 16 Contraction speed of HLA and MLA

4. 3 Low temperature starting quality

At lower temperatures the viscosity of oil gets higher. Due to lower temperatures the female thread face is closely situated to the male thread face, which results in an oil film more readily occurring between these thread faces (squeeze effect). If the fluid lubrication state is present between the thread faces due to this oil film (squeeze film), the friction coefficient will greatly decrease and valve lift loss to over-rotation of the screw can occur. With the MLA the thread faces are provided with both oil drain grooves and fine concavities/convexities in order to be able to dissipate the squeeze film between the thread faces in a short time and attain a mixed lubrication mode where a relatively large frictional force is obtained. Valve lift behavior in low temperature starting operation was analyzed for samples that each featured a unique thread face specification. The analysis result is presented below.

4. 3. 1 Analysis method

The test bench for the engine head was cooled to a constant temperature of -30°C in a cryo-refrigerating chamber and the displacement in valve lift was measured. The two test pieces used (Samples A and B) each featured a unique thread face roughness and groove structure. The test conditions are summarized in Table 3.

Table 3 Condition of low temp. starting test

Oil viscosity	SAE 10W-30
Oil temperature	-30°C (constant temperature chamber)
Crank speed	1500 min^{-1}
Run duration	60 sec

4. 3. 2 Result

Variations in the peak positions in the valve lift curves are plotted in Figs. 17 and 18. With Sample A the valve lift loss of approximately 1 mm occurs immediately after the engine is started. In contrast, the valve lift loss with Sample B is 0.1 mm or smaller. The valve lift curve of seating position obtained from Sample A is given in Fig. 19, while the seating position obtained from Sample B is illustrated in Fig. 20. In Sample A the ramp section formed on the high point of the cam is not apparent in the valve lift curve; therefore, it should be understood that the MLA sinks due to excessive sliding of the screw and the valve clearance increases to a level higher than the ramp height. In contrast, with Sample B the evidence of the presence of the ramp section is apparent, which indicates that the amount of sliding on the screw is very small.

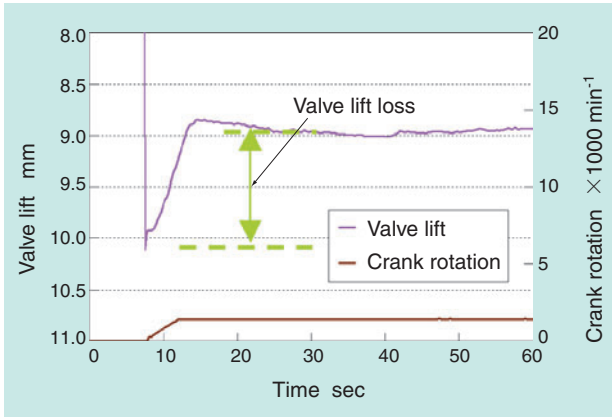


Fig. 17 Valve lift peak (Sample A)

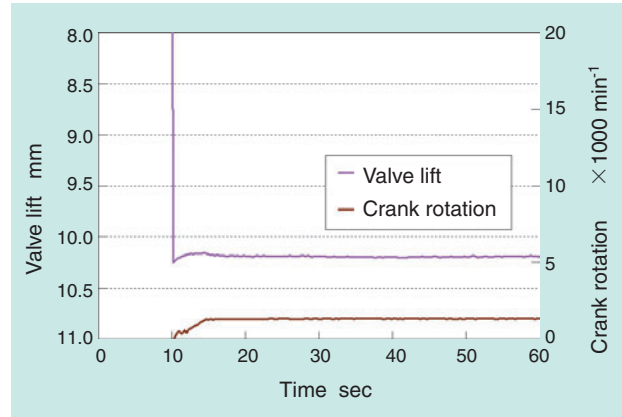


Fig. 18 Valve lift peak (Sample B)

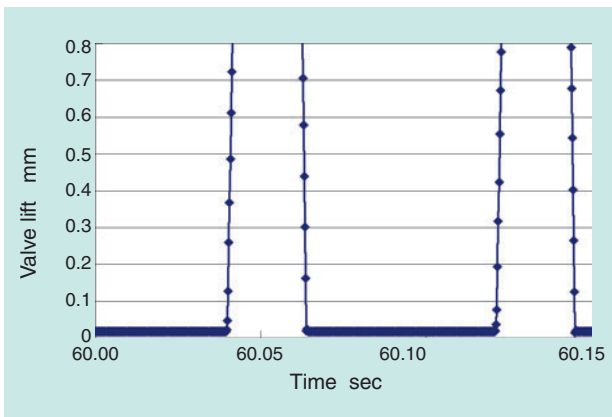


Fig. 19 Valve lift curve (Sample A)

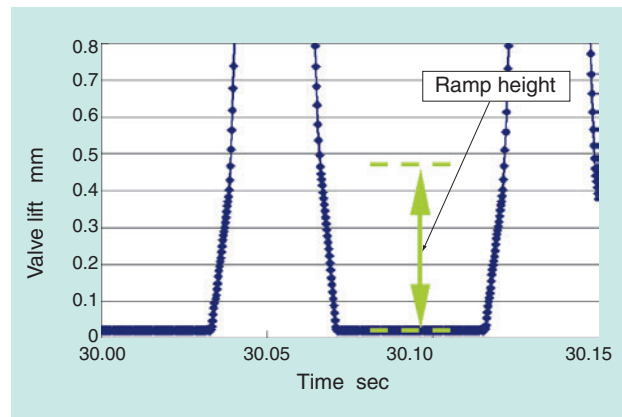


Fig. 20 Valve lift curve (Sample B)

In conclusion, by adequately designing the surface roughness of the thread faces and groove structure it is possible to inhibit excessive sliding between thread faces even at a very low temperature (-30°C) and attain a stable valve lift.

4. 4 Flank pressure dependency of wear on the thread faces

With the MLA the male and female thread faces are in contact with each other in a boundary lubrication or mixed lubrication state; therefore reducing wear on the thread faces poses an engineering challenge.

In an attempt to address this issue an automotive engine was subjected to a durability test in order to determine the allowance for thread face flank pressure. From the durability test the wear on the female thread face of the case member was measured.

4. 4. 1 Test method

As shown in Fig. 8, the crankshaft of an automotive engine was driven with an electric motor. The thread faces of each specimen were preconditioned such that

excessive sliding of the screw did not occur in the low temperature starting test. In addition, by varying the area of thread faces the flank pressures were sorted into several groups. The test conditions applied are summarized in Table 4.

Table 4 Condition of the endurance test

Oil viscosity	SAE 0W-20
Oil temperature	Approx. 110°C (natural temperature increase)
Crank speed	Engine maximum output speed

4. 4. 2 Result

The interrelation between the maximum flank pressure on the thread faces and the wear on the female thread face on the case member is illustrated in Fig. 21. Each maximum thread face flank pressure was calculated based on the maximum value of the load being an input to the MLA within one rotation of the camshaft. According to this result, it is possible to determine the minimum necessary mesh height with

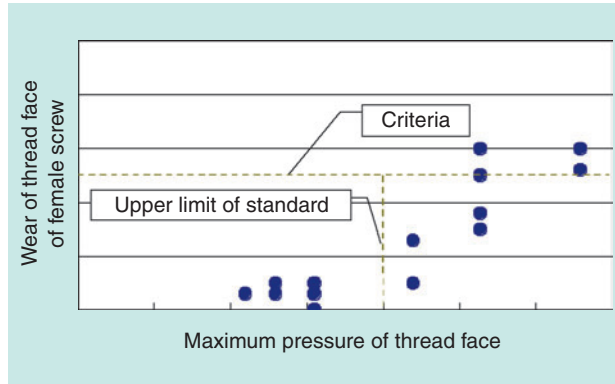


Fig. 21 Wear on the threaded flank of female screw with respect to maximum flank pressure

the threaded section and obtain a MLA design that is optimized for an automotive engine application. If NTN's MLA is applied to an automotive engine, for example a 1500 cc class engine, the axial dimension of the resultant package can be approximately 20% smaller compared with a package comprising of an HLA with the same outside diameter as our MLA.

5. Conclusion

We have evaluated the basic functions and durability of an automatic valve clearance adjuster (mechanical lash adjuster/MLA) that incorporates a buttress thread screw and obtained the following findings:

- 1) When the engine is running at a constant speed (6000 min^{-1}) or when the engine speed is swept ($600\text{-}6000 \text{ min}^{-1}$), the variation in valve lift peak with the MLA is comparable with that of the currently mass-produced hydraulic lash adjuster (HLA). Thus, we have verified that the MLA has attained

sufficiently high stability.

- 2) The contraction speed of the MLA is governed by the engine speed and is least dependent on the temperature. The contraction speed is lowest when the engine is idling; nevertheless, the lowest contraction speed is still sufficiently high compared with the thermal expansion speed of the valve.
- 3) It has been verified that by adequately designing the quality of thread faces the valve lift loss at -30°C is limited to 0.1 mm or smaller.
- 4) Based on the relation between the wear on the thread faces and the flank pressure on thread faces, the minimum necessary mesh height for the threaded faces is determined. With the mesh height known it is now possible to optimally design the MLA that best suits the intended automotive engine. For example, if our MLA is adopted for a 1500 cc-class engine the axial length needed is approximately 20% shorter compared with the HLA of the same outside diameter.

References

- 1) Kimihiko Todo, Yuji Yoshihara: Gasoline Engine: Roller Arm, Journal of Society of Automotive Engineers of Japan, No.59 p.29 (2005-2)
- 2) Noriyuki Miyamura, Syuji Nagano: Hydraulic Lash Adjuster, Journal of Society of Automotive Engineers of Japan, No.38 p.1110 (1984-9)
- 3) Akira Yamamoto: Principles and Design of Screw Fastening, Yokendo, p.30 (1970)
- 4) Bunko et al.: Fundamental analysis of the dynamic behavior of buttress-threaded screws, Japan Society of Mechanical Engineers, 2005 Annual Conference Proceedings (4), p.147 (2005)

Photos of authors



Eiji MAENO

Automotive Engineering Dept.
Automotive Sales
Headquarters



Hiroshi BUNKO

New Product Development Dept.
New Product Development
R&D Center



Katsuhisa YAMAGUCHI

New Product Development Dept.
New Product Development
R&D Center

Transmission Technology Trends and Product Developments

Takahiro KANAMOTO* Takashi UENO*
Akihiko KATAYAMA** Masanori SATOU**



The transmission is an important functional component that transmits the rotation power generated by the engine to the drive shaft and the drive wheel. Therefore, high reliability is demanded from the transmission bearings.

In addition, the market demands of –low fuel cost (low friction), reduced size, weight, and long life –have also increased in recent years along with concern for the environment. For this reason NTN introduces product developments that satisfy the market demands.

1. Introduction

Automotive transmissions have been generally categorized into manual transmissions (MT) and automatic transmissions (AT). However, continuously variable transmissions (CVT) are also used.

Though the market in Japan for MT seems to be shrinking, MT will remain favored for a while in the EU market owing to the better fuel economy associated with them. AT are most commonly used in the Japanese markets as well as other regions. Recently, 6- to 8- speed AT designs are becoming more common on large-sized vehicles because of their capabilities for better riding comfort and improved fuel economy. These AT systems of increased speed ranges will constitute a mainstream of the AT products. The most outstanding advantage of the CVT is fuel economy associated with CVT-equipped vehicles running within the city. Boasting better torque transmission efficiency, an increasing number of CVT products are used on compact and middle-sized vehicles. Recently, the DCT (Dual Clutch Transmission), which may be regarded as the third generation automatic transmission system following the AT and CVT, has been adopted by European car manufacturers.

The current trends common to these transmission types include use of low-viscosity transmission oil in

order to achieve low friction, and compact lightweight transmission designs to help decrease the vehicle's weight; in particular, a shorter transmissions so that a transmission can fit in a more compact engine compartment.

Thus, the requirements that newly developed automotive transmission products need to satisfy include reduced running friction (lower torque), more compact size, lighter weight and resultant longer life.

This paper reports newly developed transmission-related products that will satisfy these requirements.

2. FA (Fine Austenite Strengthening) technique

Ingress of foreign matters into a bearing in an automotive transmission is unavoidable, and bearings can develop premature flaking that starts at a foreign matter- derived dent.

By paying attention to grain refinement techniques it has been realized that a steel material of smaller grain size is essential in order to allow the steel material to feature improved wear strength. NTN has developed the "FA process", which is a heat treatment process capable of reducing the grain size of a bearing steel material to a level less than half of the previously possible level (**Photo 1**). NTN's FA process is unique in that the bearing steel, which has already undergone

*Automotive Engineering Dept. Automotive Sales Headquarters

**Needle Roller Bearing Engineering Dept. Automotive Sales Headquarters

a conventional carbonitriding process, is further subjected to a special heat treatment process so that the bearing steel material can more positively withstand surface damage.

Information about the result of test for NTN's new products is provided below.

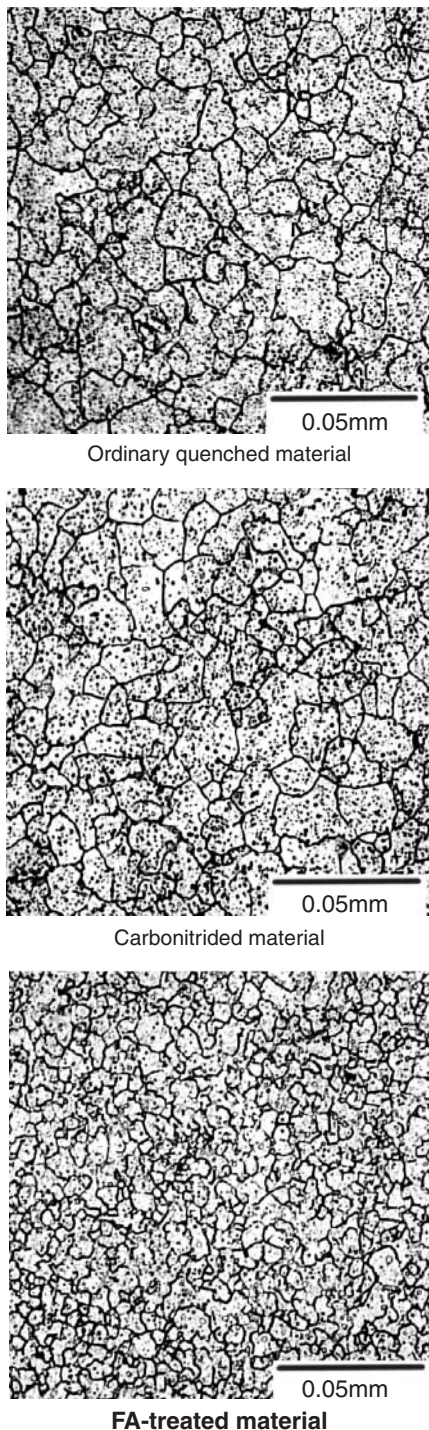


Photo 1 The prior austenite grain boundaries

2.1 Rolling contact fatigue life test for ball bearing under contaminated lubrication condition

The test rig used is schematically illustrated in **Fig. 1**, and the test conditions applied are summarized in **Table 1**. The grain size of the contaminant powder (hard material) falls in a range of 100-180 μm , which is a relatively large size.

The result of life test is summarized in **Table 2**. The L_{10} life of the bearing treated with the FA process is 3.7 times longer than that of the bearing treated with ordinary quenching and 2.1 times longer than that of the bearing having undergone carbonitriding. It was learned that grain refinement is effective against a failure mode that results from stress concentration such as flaking caused by dents.

So far, it has been reported that the life of a bearing steel material in a contaminated lubrication situation can last longer when the amount of residual austenite in the material is larger and the hardness of the material is greater. As summarized in **Table 3**, the amount of residual austenite is smaller with the FA-treated material when compared with the carbonitrided material; however, the life of the FA-treated material is longer. It appears that grain refinement is effective in compensating for the loss in bearing life resulting from a decrease in residual austenite.

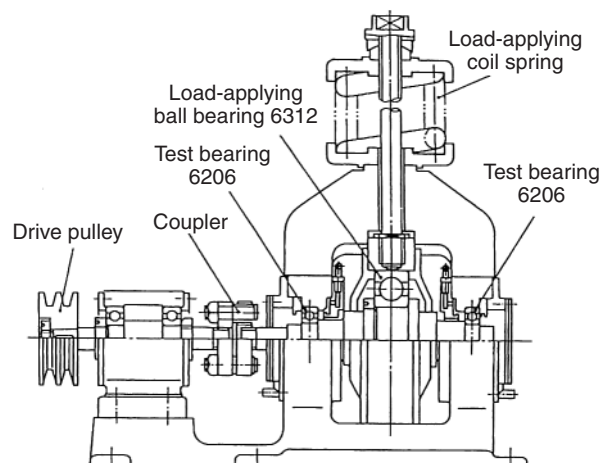


Fig. 1 NTN rolling contact fatigue test rig for ball bearing

Table 1 Test condition of ball bearing 6206 under contaminated lubrication

Load F_r (kN)	6.86
Contact pressure P_{max} (GPa)	3.2
Speed (min^{-1})	3000 (inner ring)
Lubrication system	Turbine 56 Oil bath lubrication, approx. 30 mL of oil
Concentration of contaminant	0.4g/L
Type of contaminant	Gas atomized powder Grain size: 100-180 μm Hardness: approx. HV800

Table 2 RCF (rolling contact fatigue) -life test results of 6206 under contaminated lubrication

Heat-treatment technique	L_{10} life (h)	L_{50} life (h)	L_{10} life ratio (taking the life of material having undergone ordinary quenching as 1.0)	L_{10} life ratio (taking the life of material having undergone carbonitriding as 1.0)
Ordinary quenching	13.1	19.4	1.0	0.6
Carbonitriding	23.0	45.5	1.8	1.0
FA process	48.0	87.2	3.7	2.1

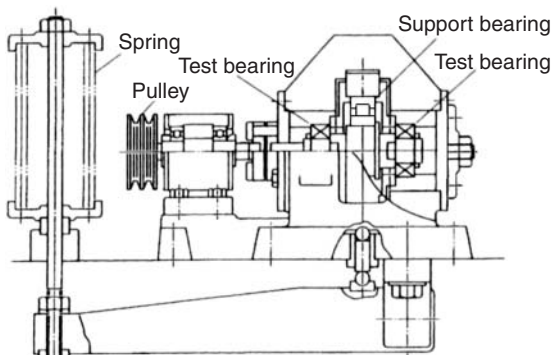
Table 3 Metallurgical properties of ball bearing 6206 (0.05mm depth from surface)

Heat-treatment technique	Mean grain size on conventional austenite boundary (μm)	HV hardness	Residual stress (MPa)	Residual austenite (%)
Ordinary quenching	10.5	746	-151	7.1
Carbonitriding	9.4	752	-211	25.5
FA process	4.4	733	-233	18.9

2.2 Rolling contact fatigue life test for tapered roller bearing 30206 under contaminated lubrication condition

The test rig used is schematically illustrated in Fig. 2, and the test conditions applied are summarized in Table 4. The contaminant powder (hard material) comprises 90wt% of smaller grains whose size measures 50 μm or smaller and 10wt% of larger grains whose size falls in a range of 100-180 μm .

The result of life test is summarized in Table 5. The


Fig. 2 NTN rolling contact fatigue test rig for tapered roller bearing

L_{10} life of the bearing treated with the FA process is 4.1 times longer than that of the bearing treated with ordinary quenching and 2.0 times longer than that of the bearing having undergone carbonitriding, in other words, the effect of grain refinement is apparent. Grain refinement can provide longer bearing life by making the bearing steel more robust against flaking caused by dents, regardless of size of the contaminant particles and bearing shape.

Table 4 Test condition of tapered roller bearing 30206 under contaminated lubrication

Load (kN)	F_r	17.64
	F_a	1.5
Contact pressure P_{max} (GPa)	2.5	
Running speed (min^{-1})	2000 (inner ring)	
Lubrication system	Turbine 56 Oil bath lubrication, approx. 30 mL of oil	
Concentration of contaminant	1.0 g/L	
Type of contaminant	Gas atomized powder 50 μm or smaller: 90wt% 100-180 μm : 10wt% Hardness: approx. HV800	

Table 5 The RCF (rolling contact fatigue)-life test results of 30206 tapered roller bearing under contaminated lubrication

Heat-treatment technique	L_{10} life (h)	L_{50} life (h)	L_{10} life ratio (taking the life of material having undergone ordinary quenching as 1.0)	L_{10} life ratio (taking the life of material having undergone carbonitriding as 1.0)
Ordinary quenching	101.2	117.3	1.0	0.5
Carbonitriding	211.6	284.5	2.1	1.0
FA process	415.6	464.3	4.1	2.0

Table 6 Metallurgical properties of tapered roller bearing 30206 (0.05mm depth from surface)

Heat-treatment technique	Mean grain size on conventional austenite boundary (μm)	HV hardness	Residual stress (MPa)	Residual austenite (%)
Ordinary quenching	11.8	792	-107	6.0
Carbonitriding	12.2	763	-265	32.4
FA process	5.2	748	-258	23.3

3. Up-graded tapered roller bearing

In order to achieve improved fuel economy the demands are increasing for compact, lightweight, low-torque designs of tapered roller bearings used in transmissions and differential gearings. To address this challenge, NTN has already achieved the following improvements for its tapered roller bearing products:

- [1] **FA process:** Compact, light-weight bearing design has been achieved by seeking longer bearing life through the adoption of metal material strengthening based on grain refinement.
- [2] **High load capacity design:** A larger pitch circle diameter for the cage allowed a maximum number of rollers to be incorporated, so as to increase the load rating and rigidity of the bearing. This feature has helped achieve a compact, lightweight bearing design.
- [3] **Low torque cage design:** By reducing the stirring-induced drag on the oil, the running torque of the bearing is decreased resulting in improved oil flow. Also, through a special shape of the cage pockets the shear resistance of the oil between the cage and rollers is reduced.

By combining these techniques, NTN has succeeded in developing the “high-rigidity, ultra-low torque tapered roller bearing” that boasts a lower running torque without a penalty of shorter life and lower rigidity. Since loss in rigidity on a bearing used in a transmission or differential adversely affects meshing of gears, a low-torque bearing not associated with loss in rigidity certainly satisfies the market needs.

Incidentally, to be able to improve fuel economy, lower viscosity lubricating oil is increasingly used in transmissions and differentials. However, use of low-viscosity oil can lead to poor lubrication can lead to surface damage failures such as seizure. To address this problem, NTN has already developed the “micro HL tapered roller bearing”.

This product is described in detail in the associated “Product Introduction” page.

3.1 Technique for achieving lower torque, while maintaining rigidity

A design technique that helps achieve a compact, low-torque bearing without developing loss in rigidity is possible only when a high load capacity design is adopted.

To be able to attain a low-torque bearing design, first we had to analyze the contribution of each design parameter for tapered roller bearing to a low-torque design. Therefore, we learned that a smaller pitch

circle diameter leads to a significantly lower torque though with a slight loss in rigidity. Usually, a smaller pitch circle diameter means a decreased number of rollers. However, by adopting a high load capacity design technique, it is possible to maintain the rigidity equivalent to that of conventional bearings without a decrease or increase the number of rollers. Furthermore, by adopting a low-torque cage design, it is possible to decrease the stirring drag of oil and shear resistance of the oil between the cage bars and rollers greatly reducing the torque on the bearing.

3.2 Design study for high-rigidity, ultra-low torque tapered roller bearing

An example of low-torque design study for 30306D, which is currently used for a differential pinion application, is illustrated in Fig. 3. The technical data for the conventional and low-torque bearing designs are summarized in Table 7.

AAs summarized in Table 7, in order to reduce the running torque while still maintaining the rigidity equivalent to that of the conventional design, the low-torque design has two additional rollers despite the smaller roller pitch circle diameter. By compensating for the loss in dynamic load rating with the life-extending effect derived from the FA process, the low-torque design boasts the life equivalent equal to or better than that of the conventional design.

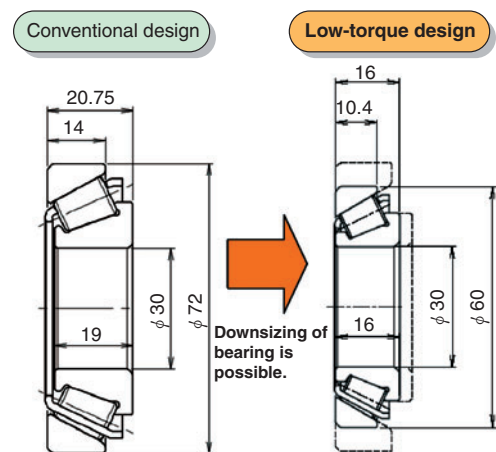


Fig. 3 The example of low torque bearing examination

Table 7 Bearing internal design

	Conventional design	Low-torque design
Dynamic load rating (kN)	$C_r = 49.0$	$C_r = 33.0$
Static load rating (kN)	$C_{0r} = 52.5$	$C_{0r} = 35.5$
Roller pitch circle diameter (mm)	$\phi 51.54$	$\phi 44.44$
Number of rollers	15	17
Mass (kg)	0.393	0.223

3. 3 Performance verification for high-rigidity, ultra-low torque tapered roller bearing

The running torque measurement results of the low-torque design and conventional design are plotted in Fig. 4. The results of the axial elastic displacement with these designs are shown in Fig. 5. As shown in Fig. 4, the new tapered roller bearing design attained a 50% torque reduction at a range of 2000-3000 min⁻¹ which is a normal speed range for differential pinions. Additionally, as can be noted from Fig. 5, the new design boasts rigidity virtually equivalent to that of the conventional design.

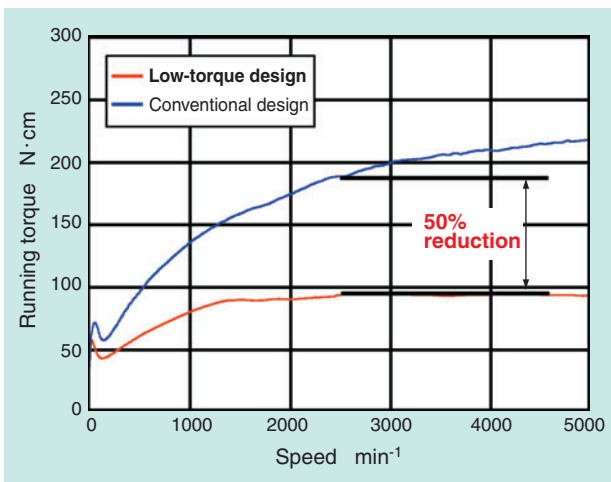


Fig. 4 Relationship between speed and torque of current bearing and low torque bearing

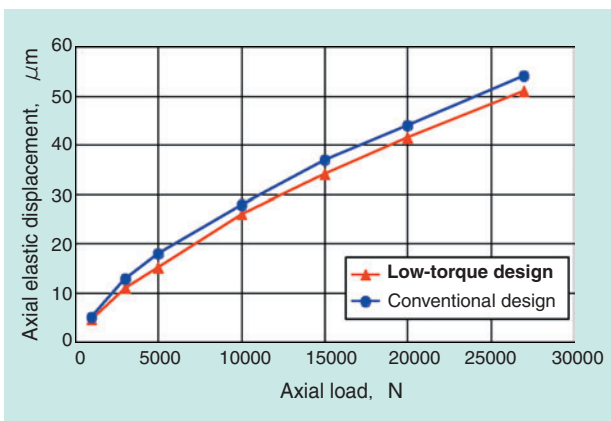


Fig. 5 Deformation of axial direction

4. Efforts for improved functions for planetary gearing

4. 1 Optimized high-speed bearing for planetary gearing

As the planetary gearing runs at a higher speed, stronger centrifugal forces will act on the planet gears and rollers; as a result, while the bearing is running the rollers can repeatedly hit the cage, possibly damaging the cage. To address this problem, NTN has performed FEM analysis for the bearing as well as dynamic behavior analysis with the bearing experiencing planetary motion, and then optimized the cage that is used in a high-speed application.

4. 1. 1 Stress analysis for cage (static analysis)

The most often failed points on cages used in planetary gearing are corner R sections on cage pockets. To prevent the damaged cage, it is necessary to mitigate the stress that may occur on such a corner. Therefore, fully utilizing our FEM analysis technique to optimize the shape of the cage, we have successfully reduced the stress that may occur at these points by 50% (see Table 8).

Table 8 Embodiment of FEM analysis

Conventional design	New design

4. 1. 2 Stress analysis for cage (dynamic analysis)

We have attempted a dynamic behavior analysis for the cage subjected to planetary motion that has been optimized through FEM analysis. The analysis result for the surface pressure acting between the outer race (planet gear bore) and rollers is plotted in Fig. 6, and the stress working on the cage is shown in Fig. 7. From these results it's apparent that the stress working on the cage peaks after the contact surface pressure between the outer race and rollers has peaked. As a result, we learned that the mechanical strength of the cage is most significantly affected by the roller exiting a loading region and hitting the cage. For detailed information about our dynamic analysis, refer to the Technical Paper "Dynamic Analysis for Needle Roller Bearings Under Planetary Motion" in this issue of NTN Technical Report.

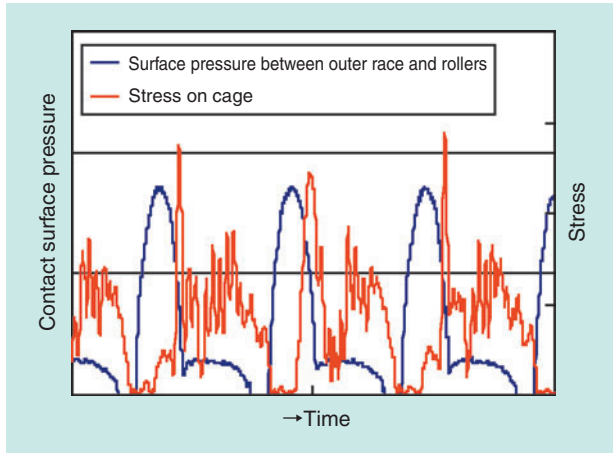


Fig. 6 Relation between outer race-roller surface pressure and cage stress

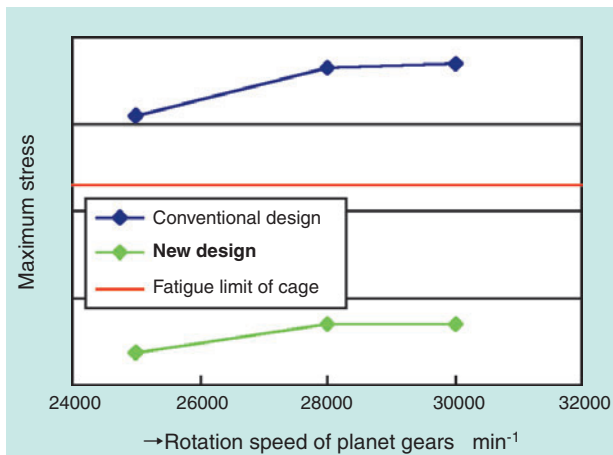


Fig. 7 The maximum value of cage stress

4. 1. 3 Function evaluation

To check relevance of our dynamic analysis, two types of cages were incorporated into a planetary transmission, and then the cages were tested under the conditions that are the same as those of the dynamic analysis. The result of evaluation is summarized in **Table 9**. As the stress applied during the analysis exceeded the fatigue limit of the conventional cage, all the test pieces of the conventional cage failed. In contrast, none of the test pieces of the new cage design failed, demonstrating reliability of our new cage design.

Table 9 Evaluation results of cage intensity

Condition		①	②	③
Rotation speed of pinion (min ⁻¹)		25000	28000	30000
State of cage having undergone the test	Conventional design	Failed		
	New design	No problem (further operation is possible)		

4. 2 Improved durability for gear tooth face

One typical example of a gear failure mode is pitting. When pitting arises abnormal noise and vibration will occur on the gearing and the efficiency in power transmission on the gearing will decrease. When a gear is running at a higher speed, oil film forming capability on the gear tooth can be jeopardized due to an increased temperature and metal-to-metal contact between the tooth face, possibly resulting in pitting.

NTN has adopted a special surface treatment technique to planetary gears, which can form an oil film to achieve longer life and be resistant to peeling (surface flaking failure). Pitting on a gear tooth face is a surface initiated flaking failure (comparable to peeling on bearings). To prevent gear tooth pitting and extend life, NTN has applied its special surface treatment to the gear tooth faces of its planetary gear products. An image of the surface having undergone the special surface treatment is shown in Fig. 8. As shown here, the specially treated surface has dimples (oil pots) that help improve oil film forming capability.

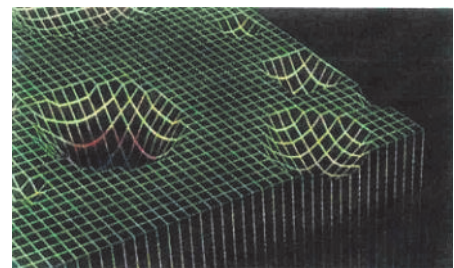


Fig. 8 Image of special surface treatment

4. 2. 1 Improved pitting resistance for gear tooth face

The combinations of the test gears used are specified in **Table 10**. Comparison was made in terms of the number of load cycles applied before pitting failure mode would occur. The example whose gear underwent the special surface treatment boasts pitting resistance four times greater than that of the other example. Thus, it has been verified that formation of oil film is effective to prevent pitting on gear tooth face (**Fig. 9**) as no pitting occurred on the gear that underwent the special surface treatment.

Incidentally, to achieve planetary gear improvement NTN has incorporated the above-mentioned elements into its planetary gear assembly (**Photo 2**).

Table 10 Combination of the gears for examination

	Gear I	Gear II
①	Not treated	Not treated
②	Not treated	Special surface treatment

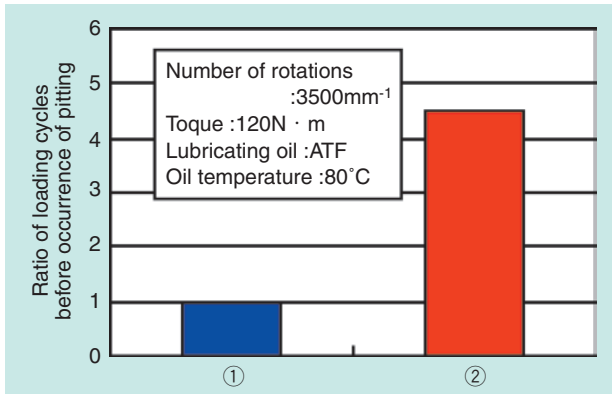


Fig. 9 Evaluation results of gear pitting

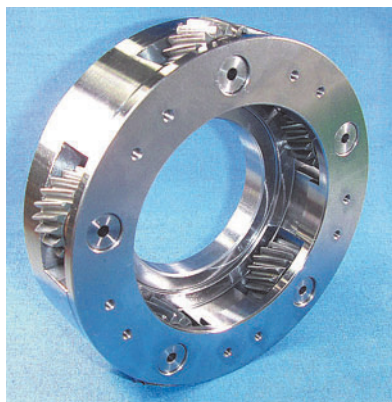


Photo 2 Planetary gear assembly

5. Triple unit 2 mm cross-section thrust needle roller bearing

To help improve fuel economy of automobiles by reducing the torque on AT, sliding bearings have been superseded with rolling bearings. At the same time, there has been a mounting need for a smaller cross-sectional height for thrust bearings in order to minimize increasing axial dimension of an AT that results from the demand of an increased number of gear sets. Furthermore, a need is also mounting for a triple unit type bearing having a bearing race that can be handled easily and is built into an automatic transmission through a smaller number of work steps.

To satisfy these needs, we have developed the “triple unit 2 mm cross-section thrust needle roller bearing” that, though having a bearing race, boasts a minimized cross-sectional height.

The NTN high-speed thrust needle roller bearing capable of higher speeds to cope with an increased

number of gear speeds on AT is described in detail in the relevant “Product Introduction” page.

5. 1 Features of the bearing–lower cross-section (compact design)

The bearing race consists of a thin sheet material whose thickness measures 0.5 mm. Its staked sections are shaped such that the thickness reduction is minimized while sufficient mechanical strength is maintained on these sections. The cage comprises of a single sheet metal piece formed by a pressing process that is capable of accepting a 1 mm diameter roller (Fig. 10).

This cage is held by the staking areas of the inner and outer races to achieve the triple unit design. Note that the NTN triple unit thrust needle roller bearing design with 2 mm cross-sectional height is the thinnest design of its kind in the world.

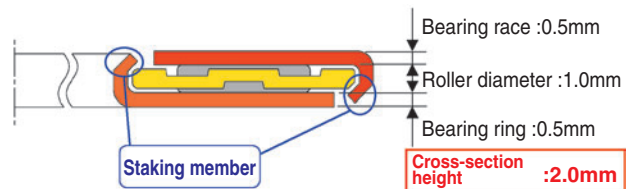


Fig. 10 Construction of triple-unit 2mm cross section thrust roller bearing

5. 2 Cage structure

We have invented a cage of a unique structure to hold 1 mm diameter needle rollers (Fig. 11). The single piece cage ensures a sufficient sheet thickness, while the rollers are retained with an ironing technique. The grooves are formed on the entire cage circumference in order to promote oil flow and simplify the ironing process.

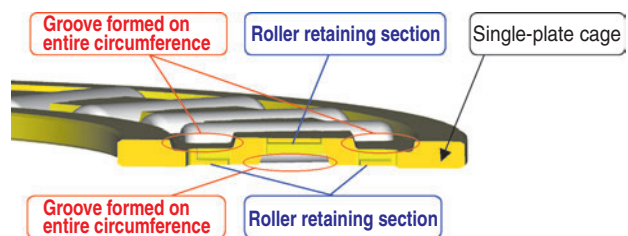


Fig. 11 Cross section of new shape pressed-cage

5. 3 Function evaluation

The needle rollers being built into the NTN low cross-section thrust needle roller bearing are optimally crowned. The functions (torque measurement, life evaluation) of the optimized needle rollers have been compared with those of the conventional needle rollers having standard crowning.

5.3.1 Torque measurement

The results of torque measurements with the conventional and new designs are illustrated in Fig. 12. The rotating torque of the new design, low cross-section, optimally crowned, thrust needle roller bearing is 37% lower compared with the conventional design.

5.3.2 Life evaluation

Life test results with the conventional and new bearing designs are plotted in Fig. 13.

The samples from conventional and new bearing designs were evaluated under misalignment conditions using assumptions for automotive transmissions. As a result, it has been found that our new design, a low cross-section thrust needle roller bearing whose rollers have been optimally crowned, boasts a bearing life 6.3 times longer when compared with the conventional design with needle rollers of standard crowning.

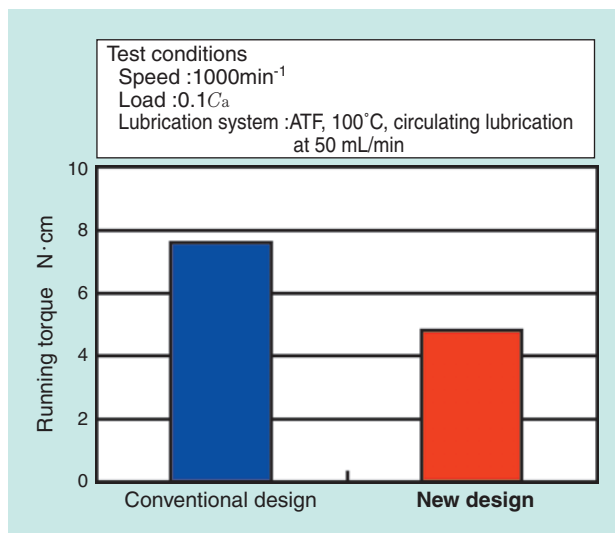


Fig. 12 Results of rotating torque

6. Conclusion

We are expecting that the working environments for bearings in an automotive transmission will become increasingly severe. NTN remains committed to the development and marketing of new automotive products that can cope with these working environments and market demands, positively contributing to mitigation of environmental impacts imposed by automobiles.

References

- 1) Chikara Ooki, Kikuo Maeda, Hirokazu Nakashima: NTN Technical Review, No.71 pp.2-7 (2003)
- 2) Takashi Tsujimoto, Jiro Mochizuki: NTN Technical Review, No.73 pp.30-39 (2005)

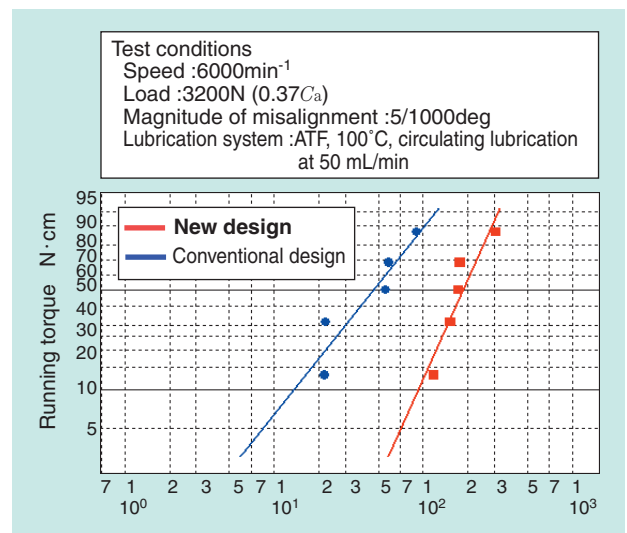


Fig. 13 Results of life test

Photos of authors



Takahiro KANAMOTO

Automotive Engineering Dept.
Automotive Sales Headquarters



Takashi UENO

Automotive Engineering Dept.
Automotive Sales Headquarters



Akihiko KATAYAMA

Needle Roller Bearing
Engineering Dept.
Automotive Sales Headquarters

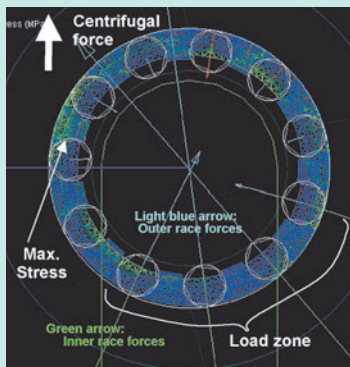


Masanori SATOU

Needle Roller Bearing
Engineering Dept.
Automotive Sales Headquarters

Dynamic Analysis for Needle Roller Bearings Under Planetary Motion

Tomoya SAKAGUCHI*



A dynamic analysis tool for needle roller bearings in planetary gear systems has been developed. This tool uses two-dimensional analysis, considering three degrees of freedom for both rollers and cage and two translational degrees of freedom for the planet gears on the radial plane. In addition, elastic deformation of the cage can be simulated using a Component-Mode-Synthesis method in order to evaluate cage stress.

Numerical results on the maximum principal stress of the cage using this dynamic analysis tool indicates that the effect of the planet gear orbital rotation speed on the cage stress is higher than that of the planet gear rotation speed and the maximum cage stress is in nearly proportional to the square of the orbital rotation speed. The reason is that stress on the base of the cage bar increases in the unloaded zone due to supporting the roller

centrifugal force induced by the orbital motion of the planet gear. In addition, relatively high stresses of the cage were observed in the two following cases: the roller just passing the load zone and accelerates due to centrifugal force and collides with the front bar, and cage bar contact force due to a roller in the load zone opposes the cage moments generated by rollers in the non-load zone.

1. Introduction

A rolling bearing consists of a pair of bearing rings, a number of rolling elements situated between the bearing rings, and a cage that separates the rolling elements at equal intervals. A cage will not fail in an ordinary application; however, a cage can fail in an application that accompanies a varying load or planetary motion. To prevent a failure, a cage must be provided with greater mechanical strength; unfortunately, determination of forces acting on a cage through a test is difficult. Therefore, a dynamic analysis technique for a rolling bearing which considers cage behavior will offer a useful solution to this challenge.

ADORE¹⁾ by Gupta is a known dynamic analysis technique for rolling bearings that positively reflects cage motions but, the cage assumed in this technique needs to be a simple-shaped solid body. Furthermore, this technique is not capable of directly determining a cage stress. If we attempt to determine a cage stress through FEM-based structural analysis, it will be difficult to rationally define the load and supporting conditions for the cage. To address this issue, the

author developed, on general-purpose mechanism analysis software, a dynamic analysis tool for a tapered roller bearing that is capable of considerations about six degrees of freedom of motion of the cage and rollers as well as elastic deformation of the cage²⁾. The author previously reported that the trajectory and stress output from this tool coincide well with the test result²⁾.

The above-mentioned dynamic analysis tool for tapered roller bearings has been applied to needle roller bearings under planetary motion. The stress acting on bearing cages was analyzed; wherein, the dynamic analysis was limited to three degrees of freedom on the radial plane of bearing in order to attain better analysis efficiency.

2. Dynamic analysis model

The planetary gear mechanism to be analyzed is schematically illustrated in Fig. 1. There are seven assumptions about his model, wherein, the model can be simplified as shown in Fig. 2 due to these assumptions.

*Elemental Technological R&D Center

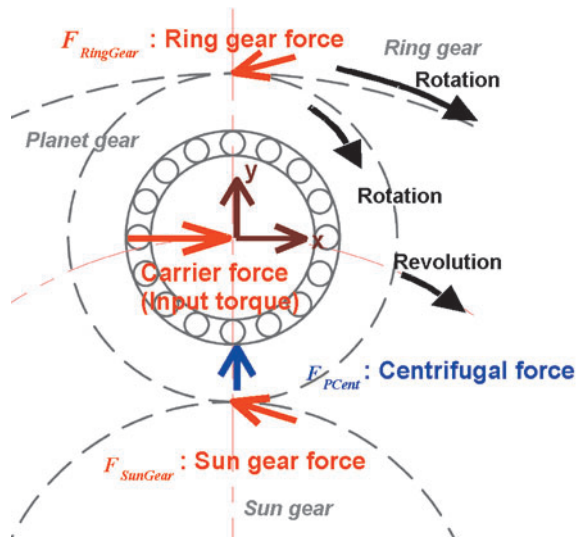


Fig. 1 Actual forces and motions on a planet gear

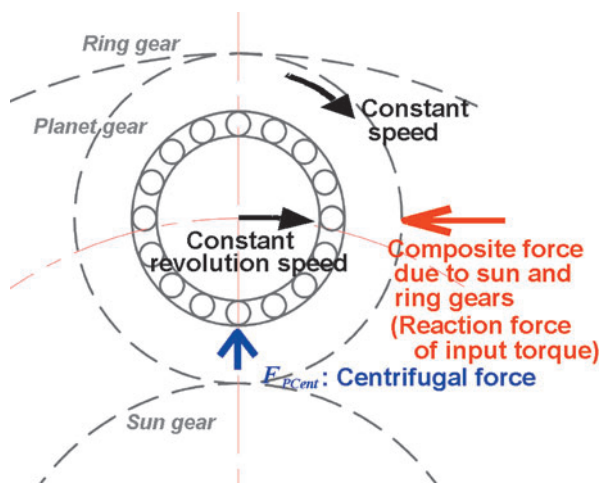


Fig. 2 Analyzed forces and motions on a planet gear

1. The analysis technique adopted is a two-dimensional dynamic analysis where degrees of freedom are limited only within a radial plane.
2. Apparent forces including the centrifugal force are taken into account.
3. The carrier rotates at a constant speed about a fixed axis.
4. The outer ring raceway (planet gears) has two translational degrees of freedom, provided that the rotation speed of the planet gears is known.
5. It is assumed that the radial internal clearance on the bearings is smaller than the mesh clearance on the gearing and all the centrifugal force on the planet gears acts on the rolling bearings. More specifically, it is assumed that the sum of interference forces from the sun gear and that from the ring gear each acting on the planet gears is equivalent only to the reaction force of the

transmission torque (Fig. 2).

6. The cage is assumed to be an elastic body based on the Component-Mode-Synthesis method⁴⁾ in order to take into account its elastic deformation. In other words, the elastic deformation of the cage is expressed as the sum of the elastic deformation in inherent deformation mode and that in restrained deformation mode. All other members are each assumed to be a solid member; and local elastic contact is considered for regions where interference can occur owing to their geometrical shapes.
7. Generally, three or more planet gears are situated on the carrier. Assuming that all the planet gears are equivalent with each other, one planet gear only is analyzed. For convenience of analysis, the weight of planet gears is ignored.

Based on these assumptions, it will be possible, like with a conventional dynamic analysis procedure for bearings²⁾, to analyze needle bearings in a dynamic planet gear. This analysis is done by describing the contact forces, frictional forces and rolling viscosity resistances occurring between the rollers and raceway and the rollers and cage on the general-purpose mechanism analysis software “MSC.Adams”⁵⁾.

To be able to assess these interference forces, the author has again used a model for the 2D dynamic analysis for cylindrical roller bearings³⁾. Despite change in the number of dimensions, the basic concept for tapered roller bearings²⁾ is same as that for the interference model in the present study.

The cage as an elastic body was treated in a manner essentially same as that for a cage in a tapered roller bearing²⁾. However, for the current analysis, a 2D cage model was developed: as illustrated in Fig. 3. A 3D geometrical cage model was cut at the middle cross-sectional plane of the bearing and constraints for the 2D plane were set up on this plane. Furthermore, the boundary point in the constraint deformation mode per the Component-Mode-Synthesis method⁴⁾ was situated at the midpoint of each bar of the cage on the above mentioned cross sectional plane. The cage mass on the general-purpose mechanism analysis software package is half as that of the actual cage. To cope with this situation, the other constituting elements were cut at their center in the axial direction so that the mass and inertial moment of each constituting element are half those on the actual cage. Accordingly, the magnitude of the interference force, such as a contact force or frictional force, acting between these elements was assumed to be a half the actual forces.

It was assumed that the interference force from a

roller acts on a corresponding pocket on the contact surface at the center of the rib. The maximum major cage stress often occurs at the base of a bar of cage pocket, and as a result, the above-mentioned assumption tends to slightly overestimate the stress.

Since the cage in question is guided by the outer ring raceway, the contact force and frictional force acting between the cage and the outer ring were evaluated. This contact force was calculated at three particular points along the cage outer surface, for each cage pocket, as shown in Fig. 4. Each contact force value was calculated based on the amount of geometrical indentation into the outer ring raceway.

The elastic deformation characteristics of the cage were calculated using the "I-deas NX Series"^{*1} (UGS)⁶, which is an FEM software package. For dynamic calculation, a mechanism analysis software package, "MSC.Adams"⁵, as well as an optional package, "ADAMS/Flex"⁵, which is an optional variant of MSC.Adams, were used. For stress evaluation, "ADAMS/Durability"⁵, which is another optional variant of MSC.Adams, was used.

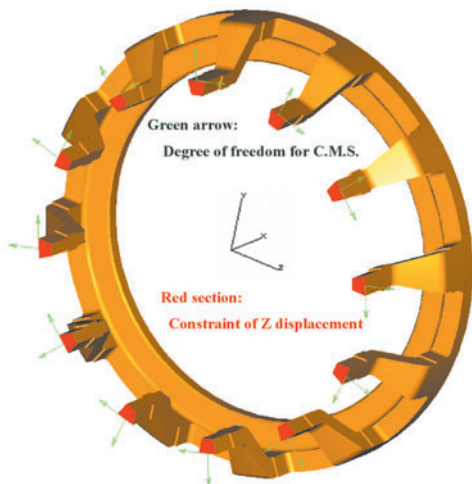


Fig. 3 Cage elastic model introduced into two-dimensional dynamic analysis

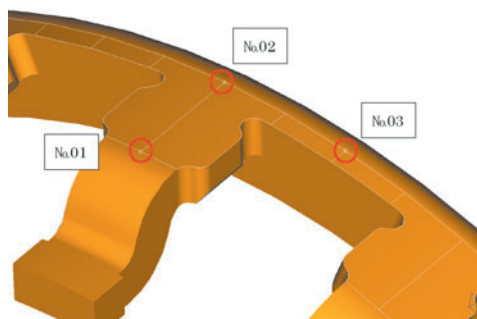


Fig. 4 Locations of interaction forces on cage outside

*1: The I-deas NX Series is a trademark or registered trademark of UGS Corp. or its subsidiary in USA and other nations.

3. Examples of analysis

The technical data for the planetary gear system and needle roller bearings used for the present study are summarized in Table 1. The cage used was an outer ring guided steel cage (model KMJ-S) fabricated through a press-forming and welding process.

Table 1 Specifications of needle roller bearing and planetary gear system

Planetary gear system		
	Pitch circle diameter of sun gear, mm	184.2
	Pitch circle diameter of planet gears, mm	57.4
	Pitch circle diameter of ring gear, mm	299.0
	Mass of planet gears, kg	0.045
Bearing technical data		
	Outer ring raceway dia., mm	19.85
	Inner ring raceway dia., mm	13.85
	Roller dia., mm	2.997
	Roller length, mm	13.8
	Number of rollers	11
Operating conditions		
	Orbital rotation speed of planet gears N_c , min^{-1}	5940
	Rotation speed of planet gears N_p , min^{-1}	25000
	Torque transmitted per planet gear T , N·m	16, 32
	Lubricating oil	ISO VG100
	Typical temperature of lubricating oil, °C	120

4. Stress generating mechanism of the cage

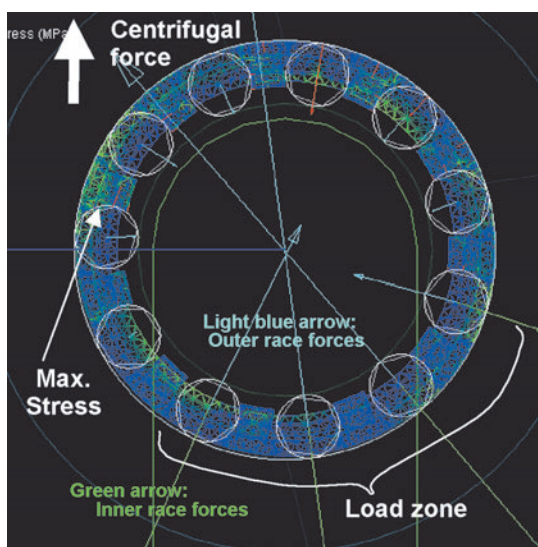
The analysis result shown in Fig. 5 was obtained at the instant where the orbital rotation speed of the planet gears was at 5940 min^{-1} and the major cage stress was at the maximum, wherein the direction of motion of the related components is same as that shown in Fig. 2. In Fig. 5, the centrifugal force is in the upward direction. The maximum major stress occurred at the base of pocket bar when a roller in the non-load zone came into contact with this bar. The contact force triggering this stress was induced by the centrifugal force on the roller.

To be able to review the state of contact between the rollers and cage on a running bearing, the maximum stress history is illustrated in Fig. 6. The stress values presented are non-dimensional values obtained by dividing by the fatigue strength of the cage material. To be able to locate the load zone, the displacements on the adjacent rollers along the radial direction of the planetary gear system are shown in this graphical representation. The above-mentioned maximum stress occurs because a cage bar exiting the load zone will be subjected to the centrifugal force of a roller in the non-load zone, thereby the a tensile stress and a compression stress sequentially occur in the right and left non-load zones as shown by ① and ② in Fig. 7. This maximum stress occurs at the .0173 point in Fig. 6. In the load zone, the frictional force

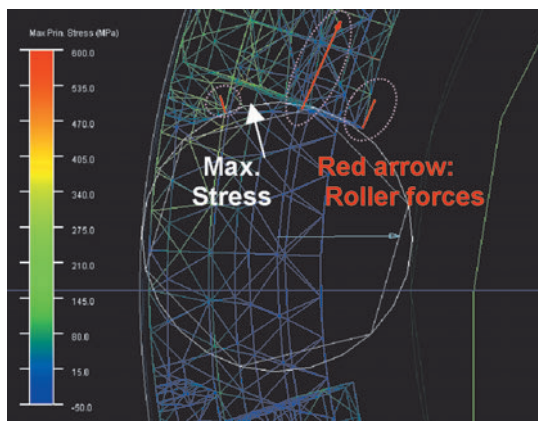
occurring from the raceway is greater than the centrifugal force occurring on the roller, thereby the centrifugal force on the roller does not act on the corresponding cage bar. At the 0.0212 s point in Fig. 6, a compressive force appears to be present. This means that in the latter half of the load zone, the bar is in contact with the roller in front of it (③ in Fig. 7), and as a result of this situation, a decelerating moment is exerted onto the cage. This decelerating moment occurs because an accelerating moment occurs in the non-load zone on the cage. The accelerating moment

on the cage is generated due to the frictional force between the cage outer surface and the outer ring raceway as well as the centrifugal force on the roller in the non-load zone.

In Fig. 6, a relatively large peak in tensile stress is present immediately after exiting the load zone. This is because around the end of the load zone, the roller is situated at the trailing end of the pocket and after exiting the load zone, the roller accelerates due to the centrifugal force acting on it and hits the bar in front of it (④ in Fig. 7).



a) all over the bearing



b) local view near the maximum principle stress point

Fig. 5 Analysis result of a needle roller bearing under planetary motion ($N_c: 5940 \text{ min}^{-1}$, $T = 32 \text{ N} \cdot \text{m}$)

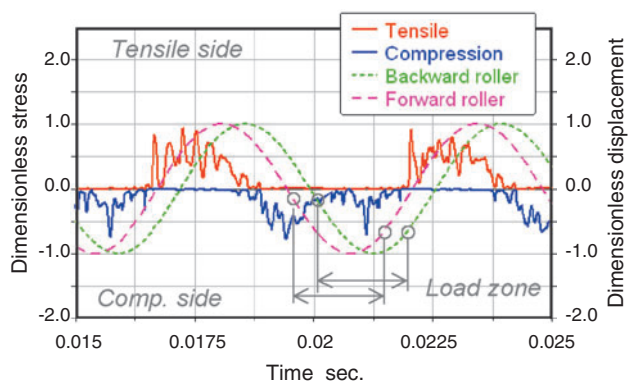


Fig. 6 Stress histories of a cage pocket bar and the adjacent rollers displacements along the radial direction of planetary gear system

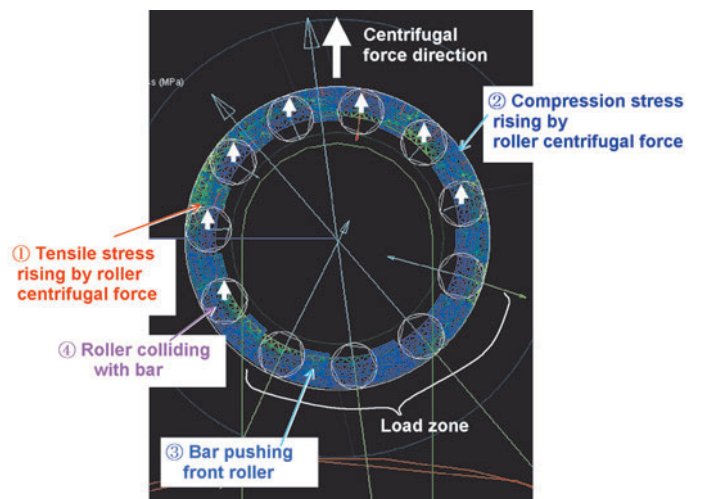


Fig. 7 Principal mechanisms to make cage stress rise under planetary motion

5. Effects of the operating conditions of the planetary gear system onto the cage stress

Fig. 8 plots the interrelation between the maximum cage stress and the orbital rotation speed of the planet gears. Assuming that the magnitude of the transmission torque T was 32 Nm or 16 Nm, the calculation result has been plotted. For transmission torques in the reverse direction, the calculation result has also been plotted. Though the stress varies depending on the magnitude and direction of transmission torques, the cage stress generally increases with a greater orbital rotation speed of the planet gears. As discussed in the previous section, there is a close interrelation between the centrifugal force on a roller and the cage stress. In **Fig. 8**, the stress is roughly in proportion with the square of an orbital rotation speed of planet gears.

A greater stress occurred when the transmission

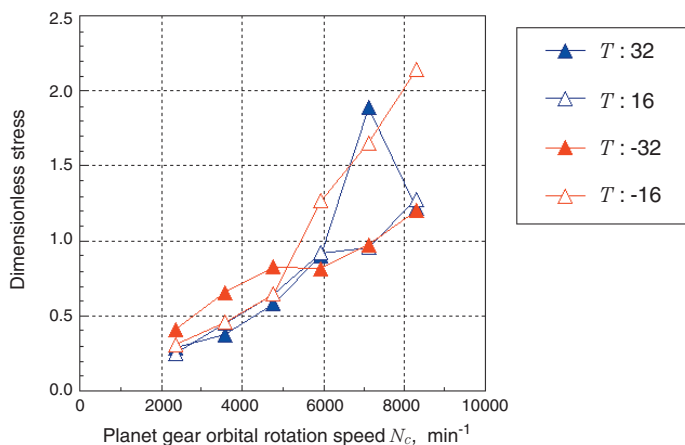


Fig. 8 Cage stress with various speeds of planet gear orbital rotation and transmitted torque

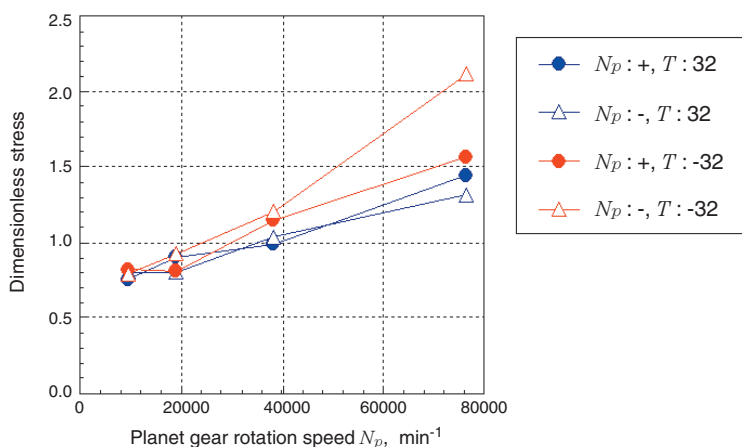


Fig. 9 Cage stress with various speeds of planet gear rotation and transmitted torque

torque T was 32 Nm and the orbital rotation speed was 7000 min^{-1} . This situation was true with the phenomenon ④ in **Fig. 7**. However, when the orbital rotation speed was 8000 min^{-1} , a different result was obtained as the collision shown in the phenomenon ④ in **Fig. 7** was less significant partly because the load zone position shifted due to an increase in the centrifugal force acting on the planet gears.

Next, the outcome from the reversed transmission torque direction was studied. Consequently, it has been found that, at the rotation speed range of 5000 min^{-1} or lower, the stress at $T = -32 \text{ Nm}$ is greater than that at $T = -16 \text{ Nm}$. Additionally, at the rotation speed range of 6000 min^{-1} or higher, the stress at $T = -32 \text{ Nm}$ is smaller than that at $T = -16 \text{ Nm}$. In a higher rotation speed range, and when $T = -16 \text{ Nm}$, a stress of greater magnitude occurred from collision in the situation ④ in **Fig. 7**. However, when $T = -32 \text{ Nm}$, the roller at the trailing end of the load zone has already begun to come into contact with the cage bar in front of it in the orbital rotation direction of the planet gears. As a result, the stress was relatively smaller (shown in

Fig. 8) due to a smaller difference in relative speed between the roller and cage car.

As can be derived from **Fig. 8**, the factor most apparently affecting the cage stress at a given planet gear orbital rotation speed is a collision phenomenon (④ in **Fig. 7**) between the roller immediately after exiting the load zone and the corresponding cage bar. Assuming that the magnitude of the transmission torque onto the maximum cage stress could be ignored, the result at approximately 7000 min^{-1} was considered. Consequently, it was learned that the stress at $T = 32$ where collision occurred is 100% greater compared with that at $T = 16$; and that the stress at $T = -16$ is 70% greater compared with that at $T = -32$. In other words, it may be concluded that the maximum cage stress when collision phenomenon has occurred is approximately 85% greater compared with that when collision phenomenon has not occurred.

The orbital rotational speed of the planet gears was fixed at 5940 min^{-1} and the non-dimensionalized maximum cage stress was measured while varying the speed and direction of rotation of the planet gears and the direction of transmission torques. The resultant maximum stress values are plotted in **Fig. 9**. Under all the conditions, the cage stress relative to the rotation speed of the

planet gears is proportional to the speed raised to the 0.34th power. The increase in the cage stress resulting from the increase in the rotation speed stems from the increase in the difference of the relative speed between the rollers and the cage.

From **Figs. 8** and **9**, it would be understood that the orbital rotation speed of the planet gears significantly affects the cage stress. This trend, as discussed in the previous section, stems from the centrifugal force on the rollers. At the same time, the cage stress will vary when the direction and magnitude of the transmission torque as well as the speed and direction of rotation of the planet gears are varied. The cage stress can rapidly increase particularly when the roller at the trailing end of the load zone is situated at the back of the cage pocket and this roller exits the load zone and is accelerated by the centrifugal force thereby hitting the cage bar in front of it. If this situation takes place, the cage stress can increase by approximately 85% as compared with a case where no collision has occurred.

The operating conditions under which the collision phenomenon discussed above appears to be determined by conditions including the angle of roller orbital motion at the load zone exit as well as the moment acting on the cage in the non-load zone. However, the affects of these operating conditions need to be detailed in the future.

6. Conclusion

A 2D dynamic analysis tool for needle roller bearings under a planetary motion has been developed. This tool allows its users to take into account the elastic deformation of a cage whose mechanical strength tends to be low relative to the constituting elements within a rolling bearing. The users can calculate the resultant cage stress based on the magnitude of this elastic deformation. Thus, this tool has been used to study the interference force

acting between the constituting elements of needle roller bearings as well as the resultant cage stress.

The orbital rotation speed of the planet gears had greater affect on the cage maximum stress compared with the rotation speed of the planet gears and is nearly proportional to the square of the orbital rotation speed. This is because the orbital rotational motion of the planet gears causes the centrifugal force to occur on the rollers. This centrifugal force acts on the corresponding cage bar, in the non-load zone, and the stress increases at the base of this cage bar. Furthermore, a relatively large cage stress was observed if the roller at the trailing end of the load zone is situated in the rear of the cage pocket opposite the direction of rotation when the roller exiting the load zone is accelerated by the centrifugal force hitting the cage bar in front of it. Large stresses also occur if the moment acting on the cage in the non-load zone is balanced by the moment resulting from the contact force between the roller and cage bar in the load zone.

References

- 1) Gupta, P. K.: *Advanced Dynamics of Rolling Elements*, Springer-Verlag, New York (1984).
- 2) Sakaguchi, T., and Harada, K.: "Dynamic Analysis of Cage Stress in Tapered Roller Bearings," Proc. ASIATRIB 2006 Kanazawa, Japan, (2006)649-650.
- 3) Tomoya Sakaguchi, Kaoru Ueno: *Dynamic Analysis of Cage Behavior in a Cylindrical Roller Bearing*, NTN Technical Review, No.71 pp.8-17 (2003)
- 4) Craig, R. R., and Bampton, M. C. C.: "Coupling substructures for dynamic analysis," *AIAA J.*, 6 (7), pp.1313-1319 (1986)
- 5) MSC.Adams (Registered trademark of MSC.Software Corporation)
<http://www.mscsoftware.co.jp/products/adams/>
- 6) I-DEAS: <http://www.ugs.jp/product/nx/l-deas.html>

Photo of author

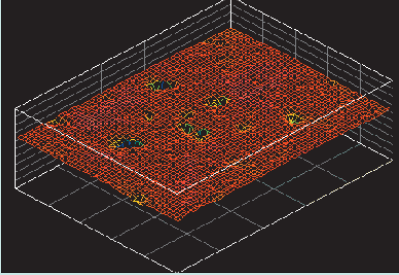


Tomoya SAKAGUCHI

Elemental Technological
R&D Center

Micro HL Tapered Roller Bearing

Takashi UENO*



With the viscosity of the oils being used in automotive transmissions and differentials becoming lower, oil film parameter λ is falling below 0.5 (VG10 oil used). In order to handle such increasingly severe lubrication conditions, NTN has developed Micro HL (high-lubrication) tapered roller bearings.

Micro HL treatment forms a finer dimple in the metal than conventional HL treatments and maintains surface roughness equal to a super-finish. Thanks to the micro oil pot effect, adequate oil films can form even under severe lubrication conditions of λ 0.2 to 0.5, conditions in which it's difficult for oil film to form. Therefore, this process maintains calculated service life by reducing lubrication limitations.

1. Introduction

Recently, lower viscosity oil use has increased in automotive transmissions and differentials in order to decrease fuel consumption (reduction in CO₂ emissions) and help reduce power needed for steering under low temperature conditions. Incidentally, the adoption of smaller and more powerful engines causes the oil temperature to be higher. This in turn leads to a decreased lubricant viscosity¹⁾.

In such circumstance, more bearings used in automotive transmissions and differentials will have increased failure due to surface damages such as peeling, smearing and seizure; each failure resulting from poor oil film formation, rather than internal flaking that may occur even when oil film is positively formed. A bearing that fails due to surface damage is short-lived, and does not satisfy the rolling fatigue life of 90% reliability. To address this problem, NTN has developed the "HL bearing" that is optimized for operation under low-viscosity lubrication conditions²⁾. The "HL bearing" is unique in that the surface of the tapered rollers has fine dimples to retain the oil; this arrangement helps improve oil film forming capability for the bearing. Regrettably, when the HL technique is applied to tapered roller bearings where sliding contact occurs on the rib portion, the seizure-immunity of the rib portion could be jeopardized.

To address the need for a much lower lubricant viscosity in the future, NTN has developed the "micro HL (High-Lubrication) tapered roller bearing" that is essentially a tapered roller bearing incorporating optimized HL treated rollers. Fig. 1 summarizes the relation between the oil film parameter (described later in the report) and the life ratio relative to the standard bearing. As shown in Fig. 1, when the oil film parameter is 0.2 or lower the life of the HL bearing samples are shorter than those of the standard bearing samples. In contrast, even when the oil film parameter is 0.5 or lower (a very severe lubricating condition), the micro HL tapered roller bearing samples boast better oil film forming capability and

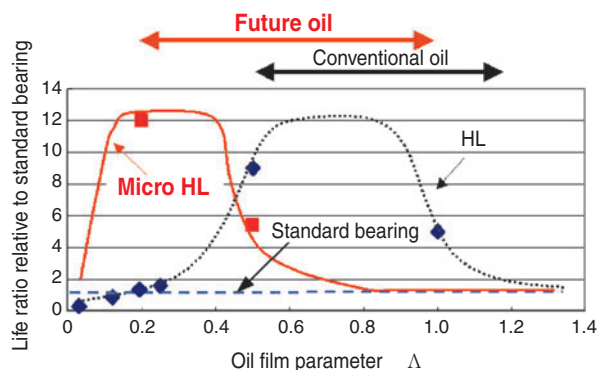


Fig. 1 Relationship between oil film parameter and life ratio compared to standard bearing

*Automotive Engineering Dept. Automotive Sales Headquarters

longer life when compared with the conventional HL bearing samples. The structure, advantages, and results of the evaluation test for the micro HL tapered roller bearing are hereunder described.

2. Facts about oil film parameter

It is widely known that the life of any bearing correlates with the oil film parameter that is determined by the elastic hydrodynamic lubrication theory (EHL theory), which is based on the ratio of the oil film thickness on the contact area of the bearing components to the combined roughness of these components³⁾. Therefore, a greater oil film parameter for the contact area appears to be effective in preventing various modes of surface damage on a rolling bearing. The oil film parameter formula is given below:

$$\text{Oil film parameter } \Lambda = \frac{h_{\min}}{\sqrt{\sigma_1^2 + \sigma_2^2}} \dots\dots\dots (1)$$

where:

- h_{\min} : minimum oil film thickness [mm]
- σ_1 : square mean roughness of bearing ring raceway surface [mm]
- σ_2 : square mean roughness of roller rolling surface [mm]

Typical measures for attaining a greater oil film parameter include: (1) maintenance of higher viscosity of the lubricant under actual operating conditions and (2) decrease in the combined roughness on the bearing's race and rollers. However, as previously described in Sec. 1, low-viscosity lubricants are increasingly being used in automotive applications and the lubricant viscosity will be further lowered owing to an increased lubricant temperature. Furthermore, the combined roughness on the bearing race and rollers cannot be further improved because the present-day bearing races and rollers mentioned in this report are already super-finished.

3. Basic principle of micro HL

As explained above, it is very difficult to obtain a greater oil film parameter. Therefore, NTN has addressed this problem by implementing the three approaches with its micro HL that are described below.

3.1 Approach based on lubricant flow model

By referring to the lubricant flow model in the contact area on a bearing⁴⁾ in Fig. 2, we describe NTN's basic way of addressing the challenges for both HL and micro HL. Pictures (a) through (c) in Fig. 2 show similar two-dimensional roughness, wherein each picture exhibits a unique directional path with the finished surface (note difference in three-dimensional surface roughness). The contact points in each picture are unique and these unique contact points affect the lubricant flow indicated with the broken lines. As also shown in Fig. 2, the degrees of smoothness of the lubricant flow can be arranged in the order of (a) smoothest flow, (b) and (c) slowest flow. In contrast, the longer the time during which the lubricant that has entered the contact area remains there, the greater the oil film forming ability of the lubricant. The degrees of ability for oil film forming can be arranged in the order of (c) greatest ability, (b) and (a) lowest ability. In other words, even with the same quality of the two-dimensional surface roughness, the directional path on the finished surface (that is, the quality of three-dimensional surface roughness) significantly affects the trend in oil film formation.

Now, let us think of the effect of the directional path of the finished surface onto the oil film forming capability of the this surface. NTN's dual cylinder tester and test specimen used for this purpose are illustrated in Fig. 3. Two types of specimens were used—, in which the direction of tool marks on one specimen type was in the circumferential direction (Fig. 2(a)) and the other type was in the axial direction (Fig. 2(c)). As shown in Fig. 4, the specimens having axial direction tool marks are capable of improved oil film formation and have better oil film parameter values.

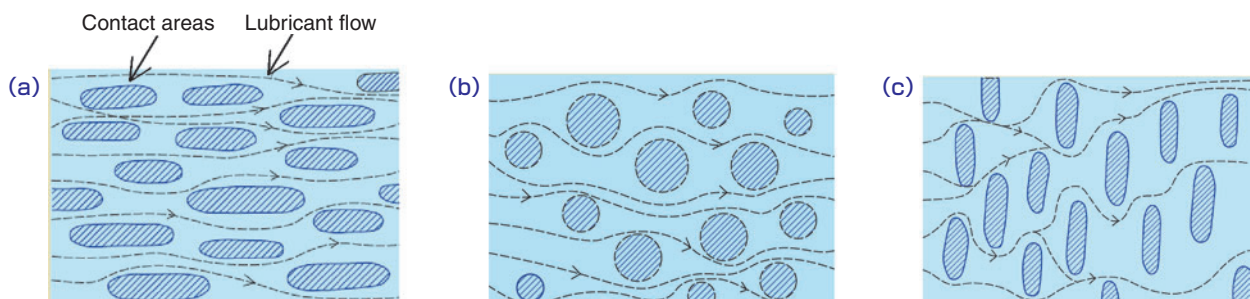


Fig. 2 Directional characteristics of finished surfaces and their effect on lubricant movement in a flow model

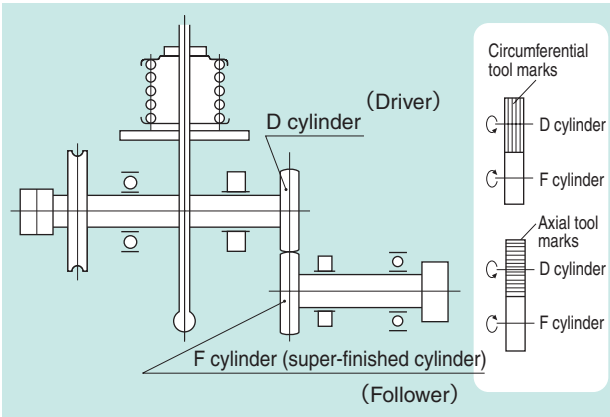


Fig. 3 NTN's dual cylinder tester and test specimen

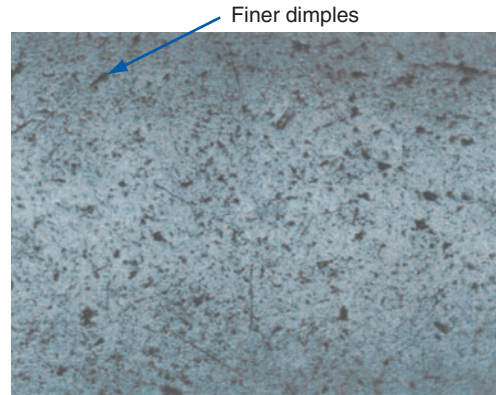


Fig. 5 Observation of roller surface with finer dimples

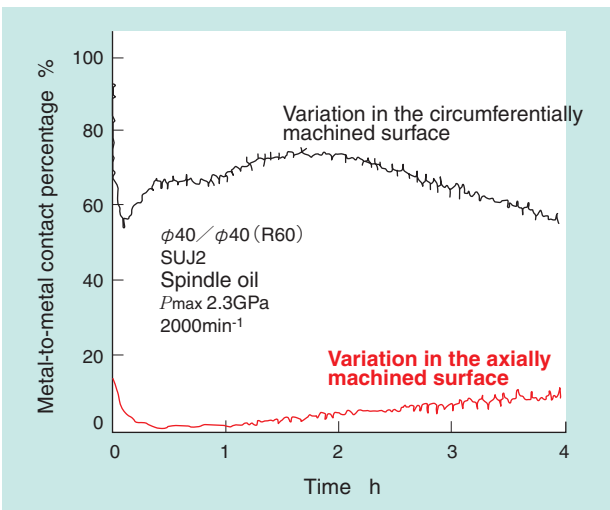


Fig. 4 The influence of finished surface directional characteristics on oil film formation

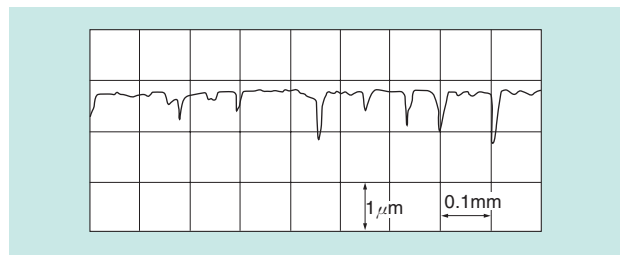


Fig. 6 Cross-sectional view of roller surface track with finer dimples

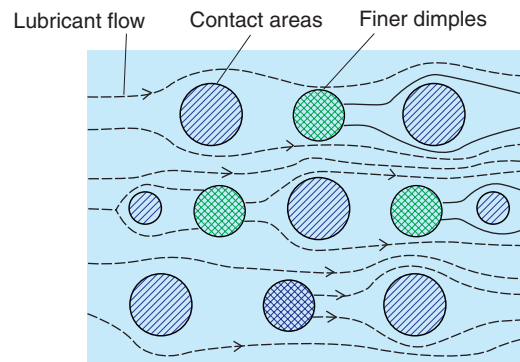


Fig. 7 A flow model showing fluid on finer dimples contact surface

3. 2 Approach based on form of dimples on roller surface

Fig. 5 shows a view of the surface of a tapered roller having the finer dimples, a unique feature on both HL and micro HL bearing products, which are represented by the black spots in this picture. A result of the measured surface of the rollers using a surface roughness tester is plotted in Fig. 6, where each finer dimple on the roller surface is represented on the plot as a valley.

The flow of lubricant over the roller surface can be modeled as shown in Fig. 7, which is in accordance to the author's flow model. The hatched round areas in Fig. 7 show the contact zones that occur from protrusions and deformations on the rough surface, while the cross-hatched round areas represent the zones containing finer dimples. The broken lines represent the direction of lubricant flow. The rolling direction is from the left side to the right side in the diagram and the lubricant fluid flow bypasses the contact point on the flat smooth surface. Furthermore,

the amount of fluid flowing increases around the finer dimples and this increased flow through the contact surface results in the surface having a better oil film forming capability, as compared with the conventional surface whose finish orientation (tool mark orientation) is in the circumferential direction.

3. 3 Optimal roughness for application to tapered roller bearing

There is sliding contact between the roller large end face and large end rib of the inner race on a tapered roller bearing. To better resist seizure -for a tapered roller bearing, the sliding contact surfaces on this type of bearing are super-finished. However, the quality of surface roughness on the HL treated tapered roller

bearing is inferior to that of the super-finished surface. As a result, metal-to-metal contact will occur on the HL treated tapered roller bearing due to the lack of oil film forming capability when subjected to an oil film parameter that is 0.5 or less. To cope with this problem, the quality of the surface roughness finish must be equivalent to that of super-finished process.

The micro HL tapered roller bearing is the result of an improvement based on the three above-mentioned approaches.

4. Structure of micro HL tapered roller bearing

Fig. 8 provides a comparison between standard rollers and micro HL treated rollers in terms of the quality in three-dimensional surface track. The surface of the rollers that underwent the micro HL treatment has finer dimples while still retaining the surface roughness equivalent to that obtainable from a super-finishing technique.

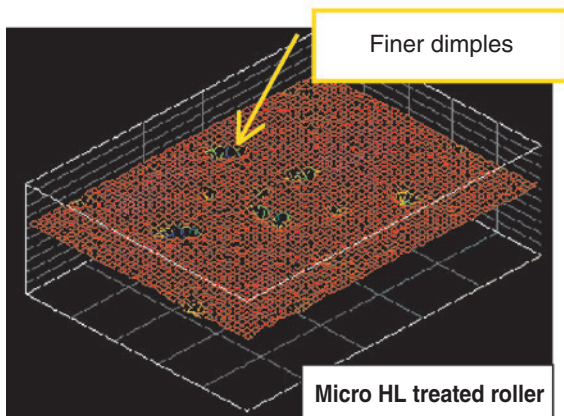
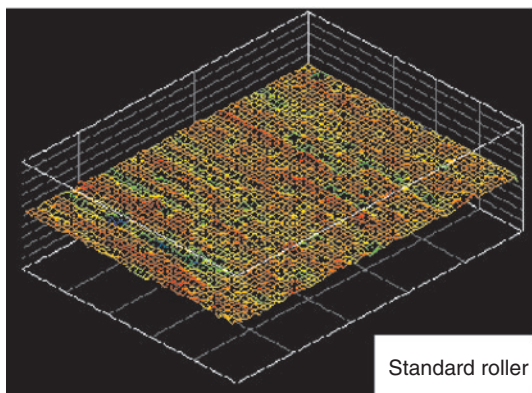


Fig. 8 Comparison of 3D surface track between micro HL treated roller and standard roller

5. Performance of micro HL tapered roller bearing

To assess the performance of the micro HL tapered roller bearing, a life test was performed under severe low viscosity lubrication conditions with an oil film parameter $\Lambda=0.2$ and $\Lambda=0.5$ (standard oil film parameter Λ =approx. 1.5).

The actual test conditions associated with the oil film parameter $\Lambda=0.2$ are summarized in Table 1, and the technical data for the bearing specimens tested are provided in Table 2. Also, the results of the bearing life test are graphically plotted in Fig. 9. These lubricating conditions are extremely demanding: as a result the specimens of the standard bearing failed owing to the damage starting at the raceway surface

Table 1 Test condition

Loading conditions	$F_r=19.1\text{kN}$, $F_a=6.4\text{kN}$ ($P/C=0.41$)
Running speed	$N_i=2500\text{ min}^{-1}$,
Lubricant	JOMO HIGH SPEED FLUID VG1.5 (clean oil)
Lubrication system	Oil bath (oil level is at the shaft center)
Calculated life	$L_{10}=92.2\text{h}$

Table 2 Comparison of test bearing spec

	Bearing ring	Rollers
Standard bearing	Raceway surface: super-finished Rib: super-finished	Rolling contact surface: super-finished Roller large end face: super-finished
HL	Raceway surface: super-finished Rib: super-finished	HL treated
Micro HL	Raceway surface: super-finished Rib: super-finished	Micro HL treated

Bearing size	$\phi 45 \times \phi 81 \times 16$ (mm)
Dynamic load rating	$C_r=42\text{kN}$
Static load rating	$C_{or}=52\text{kN}$

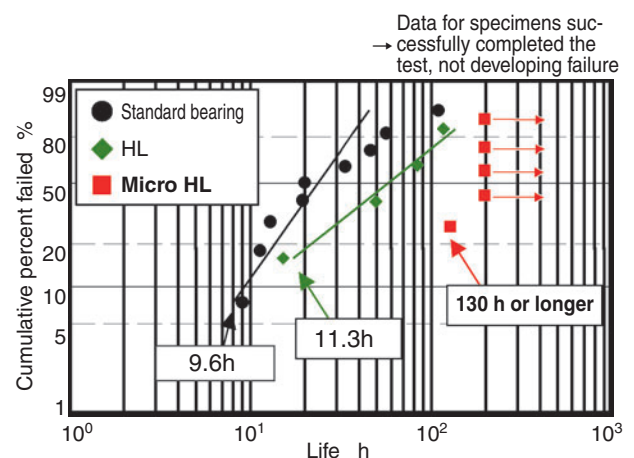


Fig. 9 Bearing life test results under severe lubrication conditions of lambda 0.2

only 9.6 h after the test began, which is much less than the calculated life of 92 h. In contrast, the micro HL tapered roller bearing specimens achieved a life of 130 h or longer which is higher than the calculated life. Thus, it has been verified that the life of the micro HL tapered roller bearing is at least 13 times longer than that of the standard bearing.

The actual test conditions associated with the oil film parameter $\Lambda=0.5$ are summarized in **Table 3**, and the technical data for the bearings tested is provided in **Table 4**. Also, the results of the bearing life test are graphically plotted in **Fig. 10**. The micro HL tapered roller bearing specimens achieved a life of 600 h or longer, which is much higher than the calculated life of 88 h. Thus, this verifies that the life of the micro HL tapered roller bearing is at least 5 times longer than that of the standard bearing.

Table 3 Test condition

Test conditions	$F_r=20\text{kN}$, $F_a=10\text{kN}$ ($P/C=0.49$)
Running speed	$N_i=2500 \text{ min}^{-1}$,
Lubricant	ENEOS Super Oil T10 (VG10 clean oil)
Lubrication system	Oil bath (oil level at the roller bottom end)
Calculated life	$L_{10}=88\text{h}$

Table 4 Comparison of test bearing spec

	Bearing ring	Rollers
Standard bearing	Raceway surface: super-finished Rib: super-finished	Rolling contact surface: super-finished Roller large end face: super-finished
Micro HL	Raceway surface: super-finished Rib: super-finished	Micro HL treated

Bearing size	$\phi 40 \times \phi 76.2 \times 17.5$ (mm)
Dynamic load rating	$C_r=46.5\text{kN}$
Static load rating	$C_{or}=56\text{kN}$

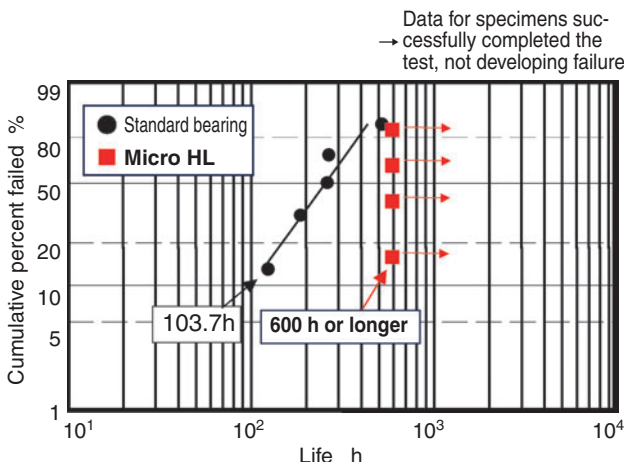


Fig. 10 Bearing life test results under severe lubrication conditions of lambda 0.5

6. Conclusion

The NTN micro HL tapered roller bearing boasts an improved oil film forming capability even under severe lubrication conditions, thanks to a unique fine surface modification technique. Thus, the author believes that the NTN micro HL tapered roller bearing products will operate reliably even if they are lubricated with less viscous oil.

The micro HL tapered roller bearings may be used in demanding situations including high-speed applications where poor lubrication can occur. They can run in poorly lubricated conditions, or in a specific area of an application where temperature increase should be avoided. Thus, the micro HL tapered roller bearing series will be a product that is positively accepted in the market.

References

- 1) Toshio Kunugi: Drive Lubricating Oil, Journal of Japanese Society of Tribologists Vol.39 No.10 p.845 (1994)
- 2) NTN Catalogue: HL Bearings, CAT. No.3020/J
- 3) Ryuki Yamashita: EHL in Rolling Bearings, Journal of Japanese Society of Tribologists Vol.49 No.4 p.330 (2004)
- 4) Patir N. & Cheng H.S., "An Average Flow Model for Determining Effects of Three-Dimensional Roughness on Partial Hydrodynamic Lubrication," Trans. ASME, J.Lub.Tech., 100(1978)12.

Photo of author



Takashi UENO

Automotive Engineering Dept.
Automotive Sales Headquarters

High Speed Thrust Needle Roller Bearings

Kosuke OBAYASHI*



NTN has developed a high-speed thrust needle roller bearing capable of 1.5-million $d_m n$ to meet the high-speed demand of high-powered electric motor units used in hybrid vehicles and multiple speed automatic transmissions.

In recent years, the demand for high-speed needle roller bearings has increased for high-powered electric motor units used in hybrid vehicles and multiple speed automatic transmissions in the pursuit of more fuel-efficient vehicles.

NTN's design features the following:

- Improved surface finish of the cage pocket contact with the roller end, while still maintaining a conventional cage configuration that has good oil flow.
- Special contact configuration of roller end and cage pocket which does not affect roller movement.
- Point contact of the roller end and cage pocket at the center point of the roller end with low circumferential velocity is made possible by the configuration of roller end curvature.

These features enable reduction of cage wear and seizure as well as improve the permissible rotational speed from the conventional 860,000 $d_m n$ to 1.5 million $d_m n$, which is the world's highest. In addition, the temperature rise at high-speed operation is reduced by 36% in comparison with conventional bearings while also improving lubrication reliability.

1. Introduction

Needs for vehicles that boast lower fuel consumption or better fuel economy have been ever increasing. As a result, smaller motors for use on hybrid vehicles and automatic transmission systems with increased number of gear speeds are more commonly being used in the automotive market, thus increasing the demand for thrust needle roller bearings capable of higher speeds.

NTN's newly developed high-speed thrust needle roller bearing (**Photo 1**) is based on the W-shaped NTN standard cage (**Photo 2**) that features better lubricant flow; and has been optimally designed. Thus, the new high-speed thrust needle roller bearing boasts an increased maximum allowable bearing speed, and has a $d_m n = 1.5$ million.

*1: $d_m n$ value = d_m (pitch circle dia. of bearing, mm) \times n (bearing speed, min^{-1})

Ex. : When a bearing of $d_m=100$ mm is run at $n=10,000 \text{ min}^{-1}$, the resultant $d_m n$ value is $100 \times 10,000 = 1$ million.

This paper hereunder describes the features and performance of this unique high-speed thrust needle roller bearing.

2. Structure of high-speed thrust needle roller bearing

By special treatment of the outside diameter of the pocket faces on the cage (**Table 2**) with which the roller end face contacts, we have improved the surface quality (surface roughness) of the contact surfaces of the NTN high-speed thrust needle roller bearing (**Tables 1 and 2**).

As a result of the special treatment, a larger contact surface occurs between the outer pocket face of the cage and the roller end face. Thus, a very stable cage pocket-roller end face contact state is maintained regardless of the motion of the cage or roller.

In addition, NTN employs special needle rollers each having a unique curved end face. Consequently, the center point of each needle roller, at which the roller circumferential velocity is low, can reliably keep a contact point relation with the cage pocket outside diameter resulting in an arrangement that has a lower

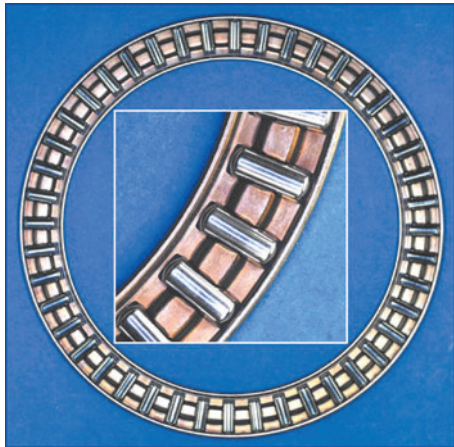


Photo 1 High-speed Thrust Needle Roller Bearings

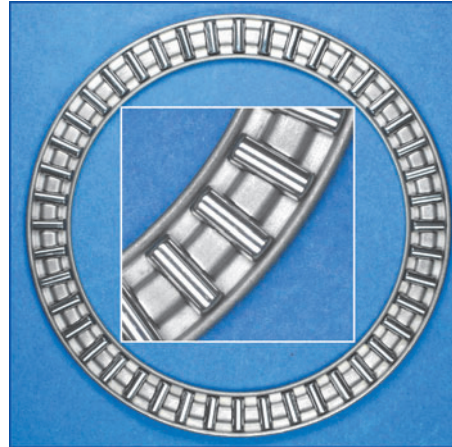


Photo 2 Current Bearings

Table 1 Diagrammatic illustration of development bearing and current bearing

Bearing specification	Cross section view
New design	<p>The cage pocket outside diameter is in contact with the curved roller end face.</p>
Conventional design	<p>The cage pocket outside diameter is in contact with a portion of the roller end face (flat face).</p>

Table 2 Enlarged illustration of development bearing and current bearing

Bearing specification	Cage pocket outside diameter
New design	<p>Contact surface (treated with new technique)</p>
Conventional design	<p>Contact surface</p>

PV value.

Furthermore, the cage riding clearance between the rollers and cage and also the riding position and the roller crowning form have all been optimized to provide a certain degree of freedom to the rollers, so that the cage least affects the behavior of each roller. Thus, we desire that each roller be independent of the motion of any other component. As a result of these efforts, premature wear and excessive temperature rise of the bearing have been minimized and the allowable running speed of the bearing has been increased, thereby attaining a d_{mN} value of 1.5 million.

3. Advantages of the new NTN high-speed thrust needle roller bearing

[1] Fastest in the world

d_{mN} value of 1.5 million (76% improvement over the conventional product)

[With a bearing that is run at a speed of 21,000 min⁻¹, where the bearing pitch circle diameter measures 72mm]

[2] Inhibition of temperature rise

36% decrease in bearing temperature rise (relative to the conventional design)

[Data obtained from the operation at an oil temperature of 80°C and a d_{mN} value of 86,000]

[3] Cage strength

1.3 times stronger (relative to the conventional design)

4. Performance evaluation

In evaluating the performance of the new NTN high-speed thrust needle roller bearing the conventional design was used as a benchmark. The conventional design and the new design have been subjected to a series of tests that included stress analysis, an allowable limiting speed test and a temperature rise test. A portion of the performance evaluation test result is presented below.

4.1 Technical data for test bearings

The test bearings used for performance evaluation measure 63mm in bore diameter, 80mm in outside diameter and 2.5mm in width.

The bearing technical data for the new design and conventional design are summarized in **Table 3**.

4.2 Analysis of cage stress

The cage stresses on the new design and conventional design have been analyzed through FEM analysis technique, and the resultant findings are summarized below.

(1) Analysis conditions

The analysis condition is summarized in **Fig. 1**.

For the analysis conditions, the outer circumference and bore circumference of the cage have been assumed to be fully constrained and a linear load has been assumed to be applied to the roller riding positions.

(2) Analysis result

The analysis result is summarized in **Table 4**.

The cage bar strength of the new design has been compared with that of the conventional design. As a result, it has been found that the ratio of the maximum

Table 3 Comparison of bearing specifications

Bearing specification	New design	Conventional design
Bearing size (mm)	Bore dia. 63×outside dia. 80×width 2.5	
Basic dynamic load rating C_a (N)	27800	
Basic static load rating C_{0a} (N)	143000	
Cage type	Cage of new form made of sheet steel	W-type cage made of sheet steel
PCD (mm)	72.0	71.5
Number of rollers	44	44

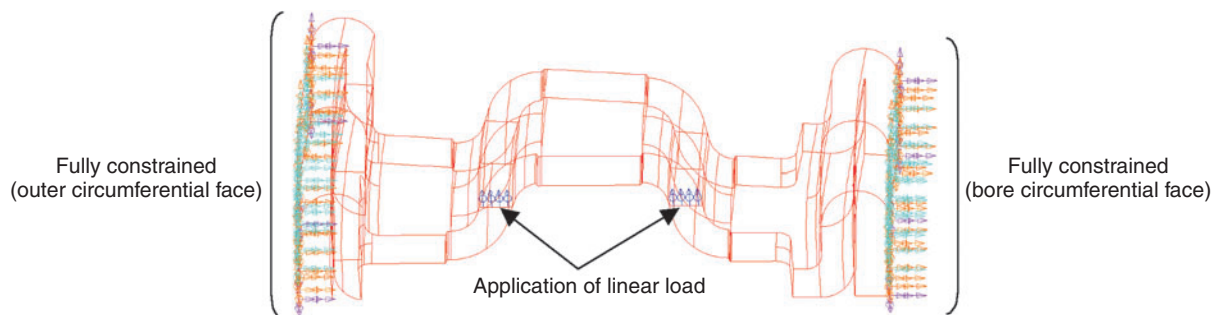


Fig 1 Analytical condition

Table 4 Analytical result

Bearing specification	Location of maximum principal stress occurrence/Corner R of the pocket inner diameter side		Maximum main stress ratio
New design			1
Conventional design			0.77

principal stress on the new design to that on the conventional design is 1:0.77. This in turn means that the cage bar strength of the new design is approximately 1.3 times stronger than that of the conventional design.

On the new design, the pocket position is closer to the outer circumference, as compared with that on the conventional design; thereby the cage bar width between the corner R portions at the inner diameter side of the neighboring cage pockets is greater, with each cage bar having greater strength. Furthermore, the width of the cage bar is again larger at the corner R area on the outside diameter side of the cage pocket, as not only the cage bars but also the cage outer circumference rib can be easily deformed. The resulting mechanical strength of the newly developed cage is approximately 1.5 times greater than that of the conventional design.

From these two facts, the newly developed NTN high-speed thrust needle roller bearing boasts a much-improved mechanical strength of the cage bars, compared with the conventional product.

4.3 Allowable limiting speed

For the allowable limiting speed test, an NTN horizontal-type thrust bearing test rig was used.

The NTN horizontal-type thrust bearing test rig used is schematically illustrated in Fig. 2.

(1) Test conditions

The conditions used for the allowable limiting speed test are summarized in Table 5.

(2) Test result

The bearing temperature on the new design is graphically plotted in Fig. 3. Table 6 provides appearances of the cage pocket outside diameter face and roller end face for the tested specimens.

The new design was tested at oil flow rates of 100 mL/min, 200 mL/min and 300 mL/min with no specimen developing a problem of roller drilling wear on the cage. Thus, it has been verified that our newly developed high-speed thrust needle roller bearing is capable of readily running at 21,000 min⁻¹ ($d_{m\Omega} = 1.51$ million), which is the maximum permissible speed of the test rig, regardless of the magnitude of oil flow rate. Thus, this speed was taken as the allowable limiting speed of this new bearing.

At an oil flow rate of 100 mL/min, the cage on the conventional design developed roller drilling wear and the end face of the roller exhibited wear when the conventional design was running at 13,000 min⁻¹ ($d_{m\Omega} = 93,000$). Therefore, the allowable limiting speed of the conventional design should be limited to 12,000

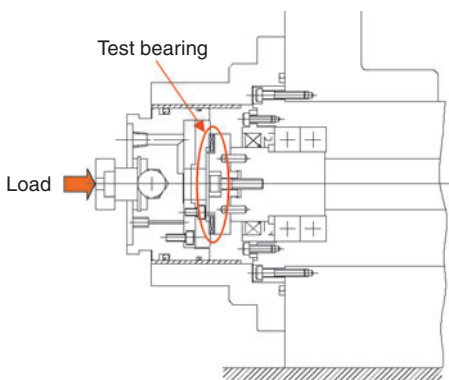


Fig. 2 Diagrammatic illustration of NTN horizontal type thrust bearing test rig

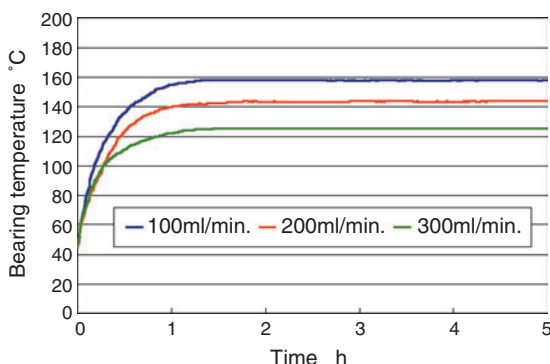


Fig. 3 Temperature-rise comparisons of each oil quantity

Table 5 Limiting speed test condition

Test rig	NTN horizontal-type thrust bearing test rig
Running speed	21000 rpm ($d_{m\Omega} = 1.51$ million)
Axial load	1961 N
Lubrication system	Apollo oil ATF-DX Circulating lubrication: 100, 200, 300 ml/min. Initial oil temperature: 80°C
Criteria for stopping the test	Detection of roller drilling wear ^{※2} , or occurrence of abnormal vibration
Run time	5 hours

※2 Roller Drilling Wear: The outer end face of each roller is forced into the outside diameter pocket face of the corresponding cage pocket owing to factors including the centrifugal force as well as roller rotation on its own axis. As a result, wear can occur on the cage pocket outside diameter face. This phenomenon is referred to as "roller drilling wear".

Table 6 Externals situation of cage and roller edge side

Oil flow rate	100ml/min.	200ml/min.	300ml/min.
Cage			
Roller			

min⁻¹ ($d_{m\Omega} = 86,000$).

The allowable limiting speeds of the new design and conventional design at an oil flow rate of 100 mL/min are graphically shown in Fig. 4.

The allowable limiting speed of the new design is at least approximately 1.7 times higher than that of the conventional design (76% improvement over the conventional design).

4. 4 Temperature rise test

For the temperature rise test, the NTN horizontal-type thrust bearing test rig shown in Fig. 2 was again used.

(1) Test conditions

The test conditions for the temperature rise test are summarized in Table 7.

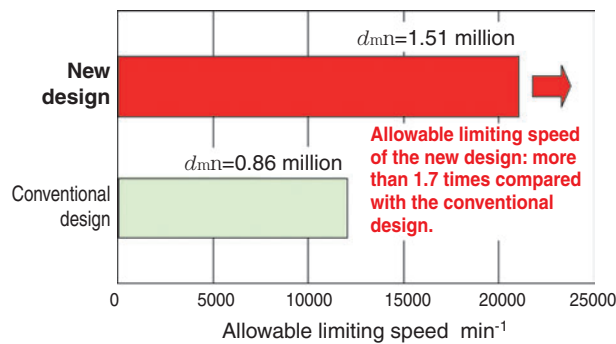


Fig. 4 Comparison of Limiting speed

Table 7 Temperature-rise test condition

Test rig	NTN horizontal-type thrust bearing test rig
Speed	Allowable limiting speed with the conventional design
Axial load	2780 N
Lubrication system	Apollo oil ATF-DX Circulating lubrication: 100, 200 ml/min. Initial oil temperature: 80°C
Criteria for stopping the test	At detection of occurrence of drilling wear, or occurrence of abnormal vibration
Run time	5 hours

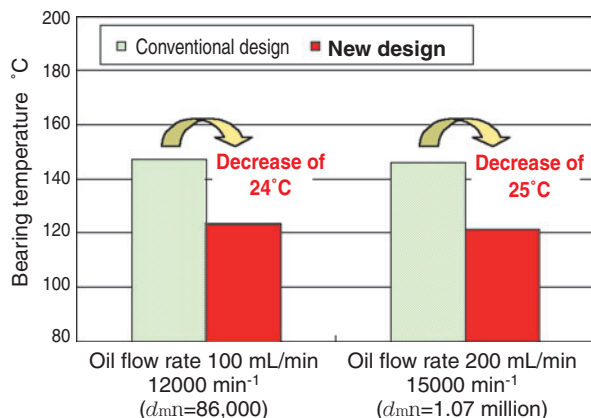


Fig. 5 Temperature-rise comparison between development bearing and current bearing by limiting speed for current bearing

(2) Test result

Under the test conditions in Table 7, the allowable limiting speeds of the new design are as follows: 12,000 min⁻¹ ($d_{m\Omega} = 86,000$) at oil flow rate of 100 mL/min; and 15000 min⁻¹ ($d_{m\Omega} = 1.07$ million) at oil flow rate of 200 mL/min.

In the temperature rise test, the bearing temperatures of the new design and conventional design were measured at the allowable limiting speed of the conventional design.

Fig. 5 illustrates the heat rise patterns for the new and conventional bearings at the allowable limiting speed of the conventional bearing.

The new and conventional bearings were run at a speed of 12,000 min⁻¹ ($d_{m\Omega} = 86,000$) at an oil flow rate of 100 mL/min. The temperature on the new design was approximately 24°C lower compared with the conventional design. In other words, the new design can limit the bearing temperature rise by 36%.

Also, the new and conventional bearings were run at a speed of 15,000 min⁻¹ ($d_{m\Omega} = 1.07$ million) at an oil flow rate of 200 mL/min. The temperature on the new design was approximately 25°C lower compared with the conventional design. In other words, the new design can limit the bearing temperature rise by 38%.

Compared with the conventional design, the newly developed high-speed thrust needle roller bearing can be characterized that the running temperature will be low, and its heat generation is limited.

5. Conclusion

The NTN innovative high-speed thrust needle roller bearing has been thus described.

This product will find a wide range of applications including motors for hybrid vehicles, automatic transmissions and CVT's on conventional vehicles, as well as general industrial machinery.

NTN's desire is to develop an optimized version of the new high-speed thrust needle roller bearing for each particular industrial field.

Photo of author

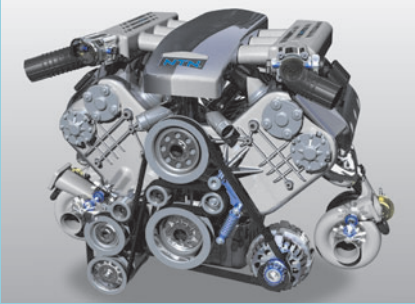


Kosuke OBAYASHI

Needle Roller Bearing
Engineering Dept.
Automotive Sales Headquarters

Accessory Technology Trends and Product Developments

Ikuo FUJINIWA*
 Makoto MURAMATSU*
 Tadahisa TANAKA*



In response to the demand for environmental compliance and high performance, in the automotive industry, NTN has developed accessory products that contribute to long-life, high performance, light weight, and compact design. In this paper we will introduce the design, features, and evaluation test results of these products.

1. Introduction

Automobiles have made a great deal of progress from the 20th to the 21st centuries with advances in safety, environment-friendliness (low fuel consumption), comfort, and cost. These advances have come about because factors such as the progress from passive to active safety, enhanced awareness of environmental protection, and requirements for enhanced convenience are all required from a single automobile.

At the same time, requirements for automotive parts, represented by electrical and auxiliary components, have become more and more severe in terms of elongation of life, improvement of reliability (safety), elimination of environment-burdening substances, weight reduction, downsizing (increased fuel economy), reduced vibration, enhanced quietness, and the transition from manual to motor-driven operation (comfort).

To respond to these requirements, NTN has developed lightweight, compact electromagnetic clutch bearings, alternator bearings responding to increased electrical loading, auxiliary-component-use auto-tensioners improving the quietness and life of belts, and pulley units with built-in clutches. It goes without saying that these products do not contain environment-burdening substances.

Fig. 1 shows a sketch of an engine with typical applications of the NTN products presented above. In

the following chapters, the authors will present how these NTN products are involved in, and contribute to, the evolution of automobiles.

The pulley with a built-in clutch mentioned above will be separately described in a product presentation featuring "alternator-use pulleys with a built-in small clutch."

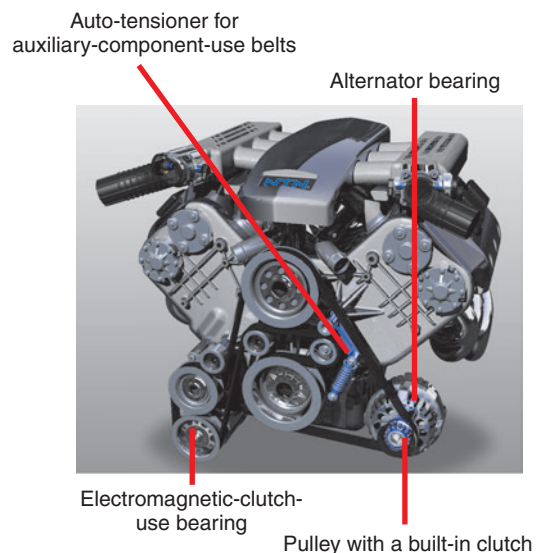


Fig. 1 Engine and accessory device

*Automotive Engineering Dept. Automotive Sales Headquarters

2. Double-row bearing for electromagnetic clutches

Electromagnetic clutches, for automotive air-conditioners, are used in environments allowing external moisture and dust to enter. For this reason, it is essential for such bearings to be provided with high sealing performance in order to ensure the service life of the bearings. In addition, the recent requirement of increased reliability makes the long life durability of grease under high temperature a problem that needs to be solved. Being successful in developing bearings responding to these requirements, we would like to present them in this commentary.

The seal developed by NTN was arrived at with FEM results and quality engineering; such as optimized seal lip contact angles, end shapes, and surface coarseness of the sliding surface, exhibiting stable sealing characteristics from low to high speed rotation. Fig. 2 shows the cross-section of a double-row bearing for an electromagnetic clutch, and Fig. 3 the seal lip shape of an existing product and the newly developed one. Regarding the elongation of grease life, we have developed a long-life grease with a life double that of the existing product by using a urea-

based thickening agent suitable for outer ring rotation.

Table 1 shows the characteristics of the existing grease and the newly developed product.

In addition to these, the features of the developed bearing are as follows:

- (1) Improvement in the resistance to muddy water**
 - Suppression of the invasion of muddy water to about 1/10 of the existing bearing design(Fig. 4)
 - Assurance of stable resistance to muddy water at high-speed rotation
 - Capable of accommodating thin bearings (with a cross-sectional height that is 70% of that of standard products)

Table 1 Grease properties

	Our existing product	Developed product
Thickening agent	Diurea	Diurea
Base oil	Ether oil + PAO	Ether oil
Base oil viscosity mm ² /s(40°C)	72.3	100
Rust development percentage %	10.2	0.8
Sodium nitrite	Contained	Not contained

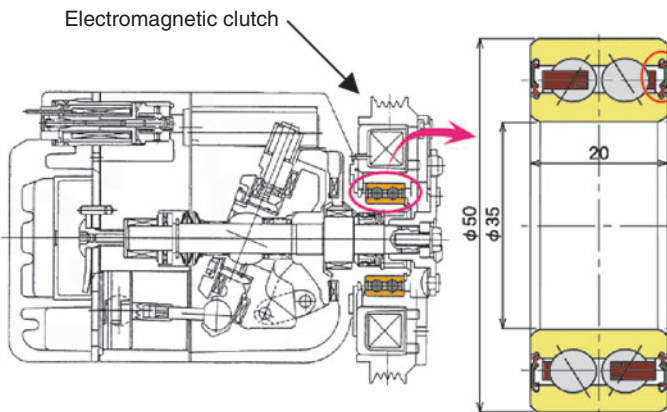


Fig. 2 Cross-section of double-row bearing for electromagnetic clutch

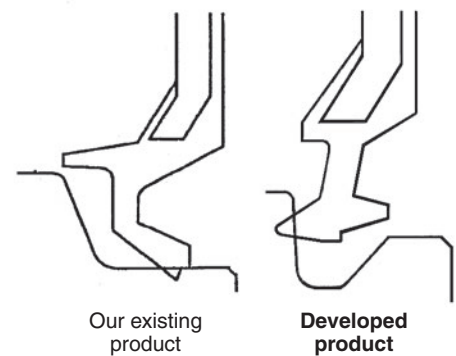


Fig. 3 Cross-section of seal lip

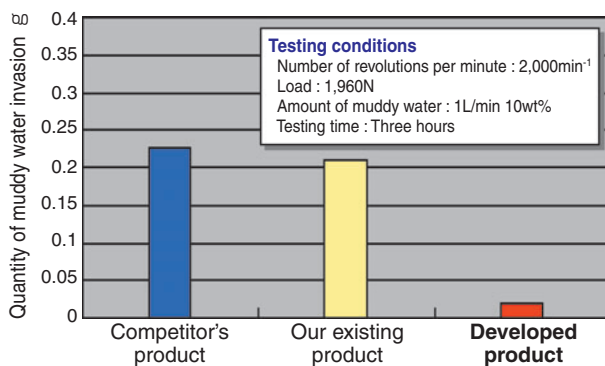


Fig. 4 The evaluation test result of seal nature

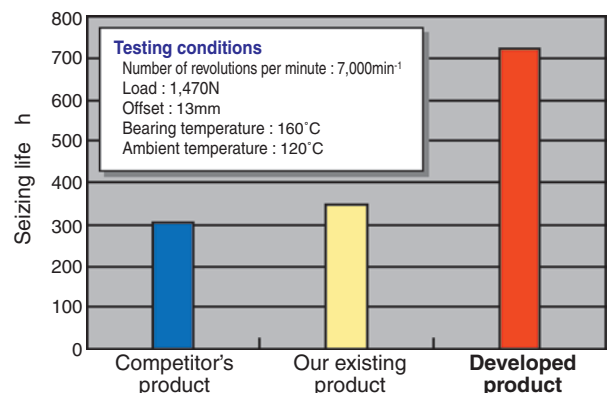


Fig. 5 The evaluation test result of durability

(2) Long life at elevated temperatures

- Assurance of a life about two times that of conventional products (Fig. 5)

(3) Environmental friendliness

- Grease does not containing sodium nitrite

3. Alternator-use high temperature, long-life ball bearings

Originally, direct current generators called dynamos were used as automotive generators. However, an increase in the placement of electrical components has lead to extensive use of alternators that are compact and yet capable of generating large power outputs. Two deep-groove ball bearings are commonly used on an alternator, contributing to reducing the size and weight of an alternator and increasing its output.

Presently, various on-board components have been made electronically operated to enhance comforts, safety, and fuel economy. A further increase in power generation of the alternator is then required. For this reason, it is foreseen that the temperature of a bearing in operation will rise from the current 150°C to 180°C. Bearings are needed that last long and are free from the flaking peculiar to alternator bearings (brittle flaking) under high temperatures. We have developed

alternator bearings that are capable of being continuously operated, even under a temperature of 180°C, which we would like to present below.

Fig. 6 shows the structural sketch of an alternator and Fig. 7 the schematic cross-section of the bearings. Attached to the housing, the bearings support shafts for the rotor, fan, and pulley. Mechanical load resistance is required of the front bearing that is close to a load point (the pulley), while heat resistance is required of the rear bearing that is placed in an environment with poor heat dissipation. The features of component parts forming the bearings are as follows:

(1) Bearing materials

High carbon chrome bearing steel (SUJ2) is used as the bearing material to achieve the goal of economy and long life. In addition, special heat treatment is applied to the material to secure dimensional stability at high temperature and to improve brittle flaking resistance. Fig. 8 shows the results of brittle flaking life tests.

(2) Cage

With loading due to lead and lag of the balls constantly applied to the cage, it need to be high strength. In addition, holding a ball in a stable

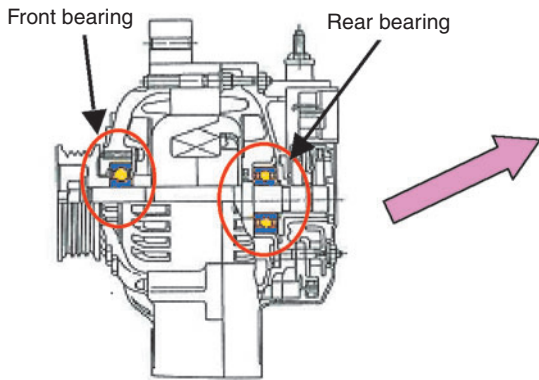


Fig. 6 Cross-section of alternator

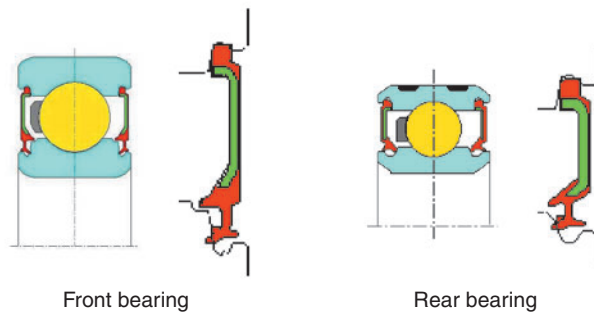


Fig. 7 Cross-section of bearing and seal

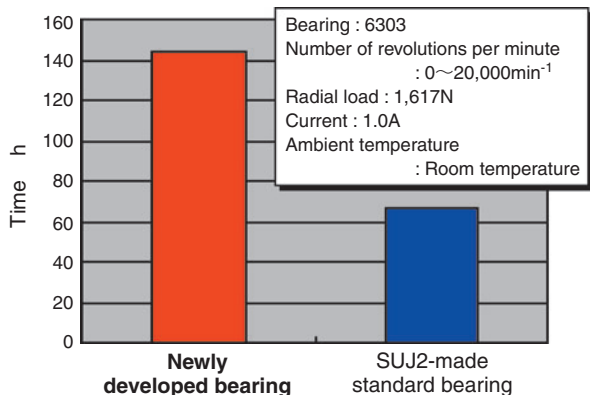


Fig. 8 Test result of brittle flaking life

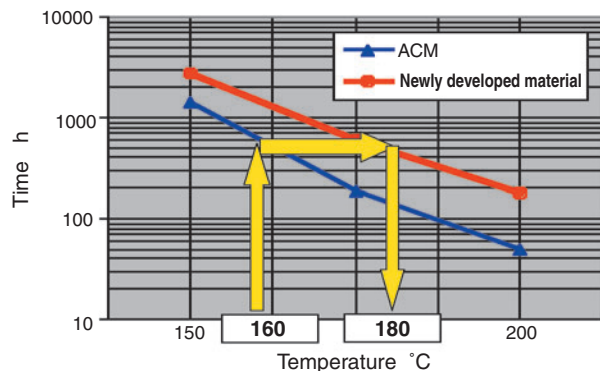


Fig. 9 Durability by seal material

condition requires the pocket gap to be stable in a wide temperature range. Made of aromatic polyamide resin material excellent in high temperature characteristics, the cage responds to these requirements.

(3) Seal

Newly developed heat-resistant acrylic rubber is used as the rubber material to make the seal operable at 180°C. Fig. 9 shows the heat-resistant life curve of the seal rubber material.

In addition, the seal tolerance is specified to always have interference contact; this allows a lip shape to be formed that requires low torque and prevents grease leakage and intrusion of dust.

(4) Grease

A urea-based thickening agent with reinforced hydrogen bonding strength is used. A newly invented additive helps increase high temperature life by 50% when compared with conventional products. Table 2 shows the characteristics of the newly developed grease and Fig. 10 the result of the life test for the grease capable of being used at 180°C. At the same time, the brittle flaking life has been increased by two times that of conventional products.

In addition, this grease is environment-friendly grease and does not contain sodium nitrite.

(5) Expansion-compensation bearing

In the rear bearing, a loose fit is usually used between the outer ring and the housing. Aluminum is

often used as housing material. If the creeping of a bearing while driving causes wear in the housing, the power generating performance is adversely affected.

To prevent housings from being worn, NTN has developed expansion-compensation bearings with a resin ring placed on the outside diameter of the outer ring. This ring has a large linear expansion coefficient and excellent heat resistance.

4. Auto-tensioners for auxiliary-component belts

In response to a recent trend of environmental friendliness, the serpentine scheme in which different auxiliary components are driven by a single belt to reduce engine size and weight is often adopted. This requires auto-tensioners to adjust belt elongation and tension.

Auto-tensioners for auxiliary component belts are classified into the friction type and the hydraulic type in terms of damper structures. NTN adopts the hydraulic type for the reasons of high damper force and high reliability.

The features of NTN auto-tensioners are described below, with the structure shown in Fig. 11.

(1) Lightweight

The cylinder, forming the casing for the hydraulic damper section, and the spring washers are made of die-cast aluminum, and they are combined with steel valve sleeves to achieve reduction in weight and wear resistance.

(2) High reliability

To seal the hydraulic fluid in the hydraulic damper section, an oil seal is adopted. The damper is formed in a gas-liquid two-layer structure to ensure the reliability against oil leakage.

High-strength rubber bushings are employed on the connecting section on both pulley arm and engine side to enhance wear resistance and usability under hostile environments.

(3) Tuning

In common reciprocating engines, auto-tensioners are subjected to sinusoidal load arising from the change in angular velocity of the engine crank (Fig. 12).

In addition, as shown in Fig. 13, variations in belt tension occur in the engine revolution range depending on the load on the engine and auxiliary components. Since large change in the belt tension occurs in the low revolution range (2000 min⁻¹ or lower), high damper force is often required.

The attenuation of a hydraulic damper is a one-direction damper as shown in Fig. 14. The damper force can be set at an optimum value such as a high damper or low damper specification depending on the

Table 2 Grease properties

		Newly developed grease	Conventional grease
Thickening agent		Aromatic urea	Aromatic urea
Base oil		Ether+PAO	Ether+PAO
Base oil dynamic viscosity mm ² /s	40°C	53.5	72.3
	100°C	8.5	10.1
Mixed consistency (60w)		286	300
Dropping point (°C)		>260	227

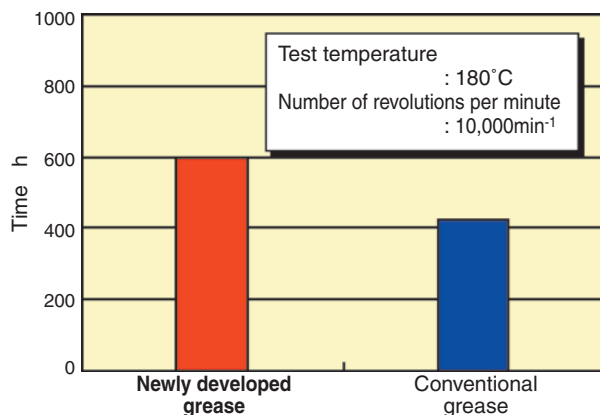


Fig. 10 Test result of grease life

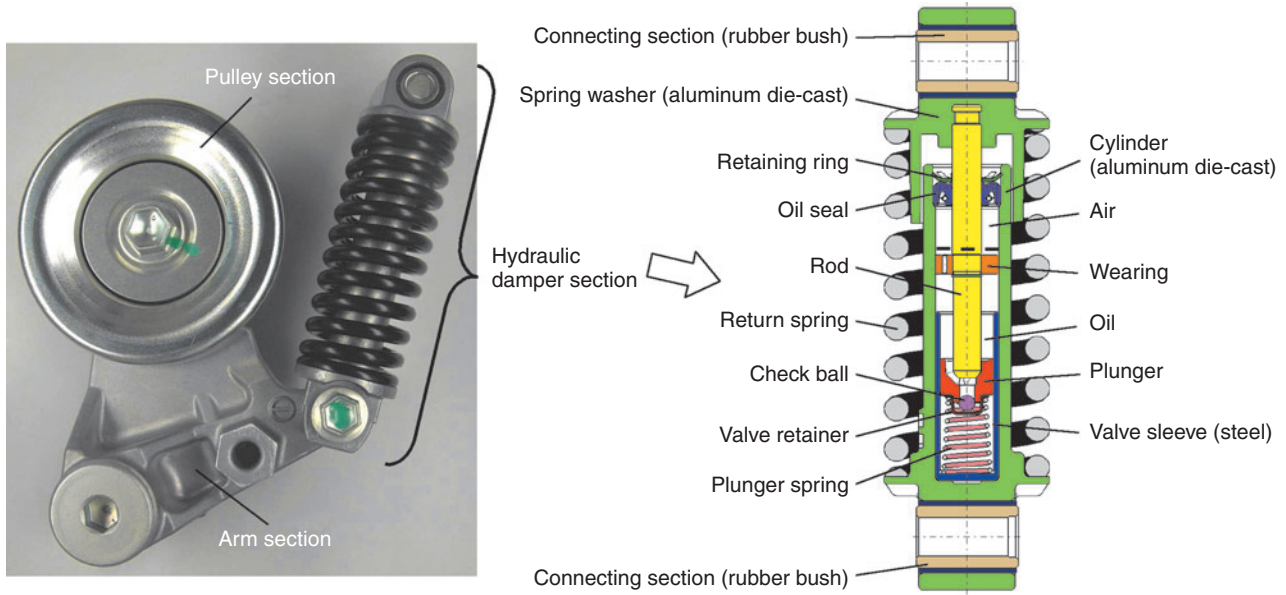


Fig. 11 Sectional view of auto-tensioner for accessory belt

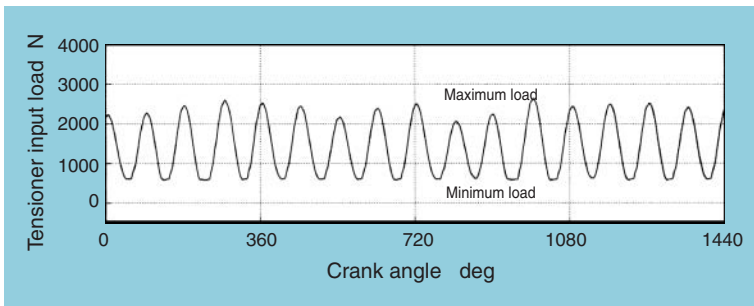


Fig. 12 Angular velocity of crank pulley

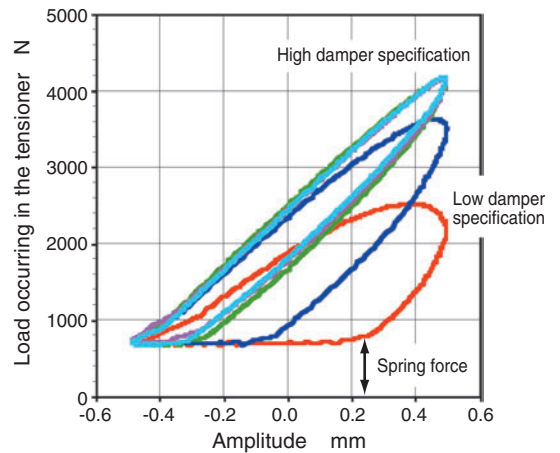


Fig. 14 Damping characteristics

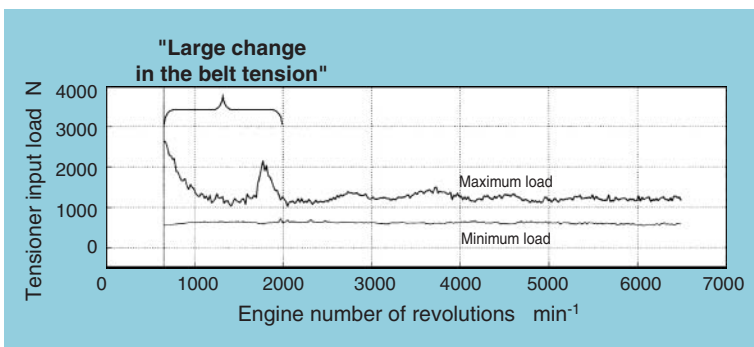


Fig. 13 Auto-tensioner input load variation depend on engine speed



Fig. 15 Compact auto-tensioner for accessory belt

characteristic of each engine. In addition, the return spring is arranged outside the case to be capable of accommodating various belt tension requirements.

Furthermore, we will develop auto-tensioners for small auxiliary-component belts (Fig. 15) seeking a further reduction in size, weight and cost.

5. Concluding remarks

In this commentary, we have described the recent trend in automotive electrical components and auxiliaries, along with NTN's approaches to these trends. We hope that these electrical components and auxiliaries will be spread in the market as products responding to requirements for automotive safety and environmental -friendliness.

Anticipating that requirements for automotive electrical components and auxiliaries will become increasingly sophisticated, we will push forward with the development of high-performance products capable of addressing required environmental conditions.

References

- 1) Satoshi Kitano, Tadahisa Tanaka, Tomokazu Nakagawa: NTN Technical Review, No.73 p.116 (2005)

Photos of authors



Ikuo FUJINIWA

Automotive Engineering Dept.
Automotive Sales Headquarters



Makoto MURAMATSU

Automotive Engineering Dept.
Automotive Sales Headquarters



Tadahisa TANAKA

Automotive Engineering Dept.
Automotive Sales Headquarters

Development of NA103A Long-life Grease for Automotive Components

Takayuki KAWAMURA*
Hidenobu MIKAMI*



Recently, as automotive components have become progressively more compact, ball bearings are required to operate at higher temperatures, rotational speeds and loads. In such cases, grease life and brittle flaking life have become more critical for determining the bearing's overall life than rolling contact fatigue life. This report presents a novel and unique method to generate brittle flaking in a short time, and also introduces the newly developed NA103A grease for automotive electrical instruments and auxiliary devices. NA103A is a great improvement over common greases, including enhanced

endurance under high temperatures and anti-brittle flaking performance. Moreover, this grease does not contain hazardous materials such as sodium nitrite and barium compounds. NA103A is expected to be useful in several types of automotive applications.

1. Introduction

To respond to recent requirements for the reduction in size, weight, and noise of automobiles, electrical components and auxiliaries (alternators, electromagnetic clutches, auxiliary component pulleys, and the like) are being downsized and slimmed. On the other hand, these devices require increased output and efficiency. As for electrical components and auxiliaries, the decrease in output resulting from downsizing must be overcome by increasing the rotational speed. For this reason, ball bearings tend to be increasingly exposed to high temperatures. Notably, bearings for alternators have required more and more power and it is estimated that the working temperature will be raised from the current 150°C to a level of 180°C. Since the life of grease is thought to be shortened substantially under high temperature conditions¹⁻³⁾, it is expected that conventional grease will not meet future service life requirements.

In the period from the latter half of the 80s to the former half of the 90s, V-belts were replaced by V-ribbed belts as driving belts for electrical components

and auxiliaries, distinct premature flaking (brittle flaking) occurred, which was accompanied by white structural change on the rolling surface of a ball bearing, posing a problem^{4) 5)}. Although the adoption of grease consisting of urea-ether base oil as a countermeasure has substantially reduced cases of nonconformance in the market⁶⁾, the trend toward increasingly severe working conditions threatens to pose this problem of brittle flaking again. However, since brittle flaking is difficult to reproduce in a short time, sufficient experimental verification has not been accomplished, thus hindering the possibility of taking effective counter measures.

This paper presents a unique method of reproducing brittle flaking in a short time that has been worked out from the viewpoint of friction. This paper also presents **NA103A** grease for electrical components and auxiliaries developed on the basis of the knowledge obtained through evaluation of this method. This grease has excellent durability at high temperatures, resistance to brittle flaking, cold hoot-noise suppression, and anti-rust resistance.

*Elemental Technological R&D Center

2. Method of reproducing brittle flaking in a short time

In bearings for automotive electrical components and auxiliaries, early stage flaking (brittle flaking) accompanied by white structural change occurs in some rare cases. NTN thinks that hydrogen embrittlement flaking is generated by the mechanism shown in Fig. 14-10). Although a number of countermeasures were taken, experimental

verification has been difficult to perform.

The authors conducted sliding tests in oil using a ball-on-disk testing device (Fig. 2) found the tests accompanied by heavy wear were coupled with a large amount of hydrogen intrusion into the steel (Fig. 3) 11-13). Paying attention to the fact that wear accelerates intrusion of hydrogen, we then operated the bearing with current passing through the bearing to accelerate wear and thereby reproduced brittle flaking in a short time 14-16).

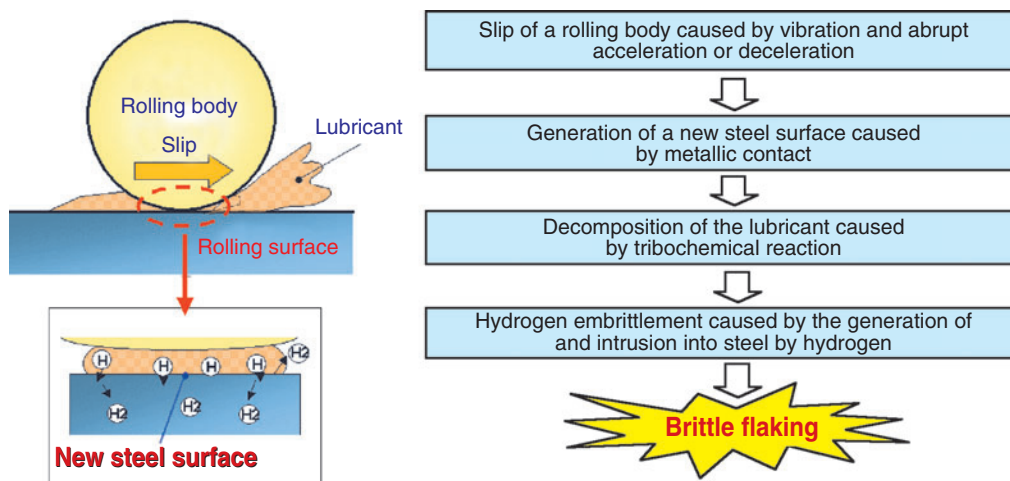


Fig. 1 Estimated mechanism for brittle flaking

Test condition
 Steel ball : Made of SUJ2
 Ring : Made of SUJ2 ($\phi 24.1\text{mm} \times \phi 17.3\text{mm} \times 1\text{mm}$)
 Oil temperature : 100°C
 Slip speed : 0.3m/s
 Bearing stress : 3.0GPa

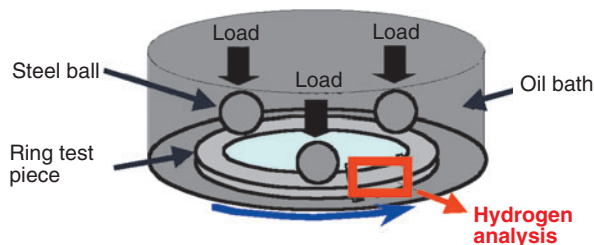


Fig. 2 Test apparatus for sliding test in oil

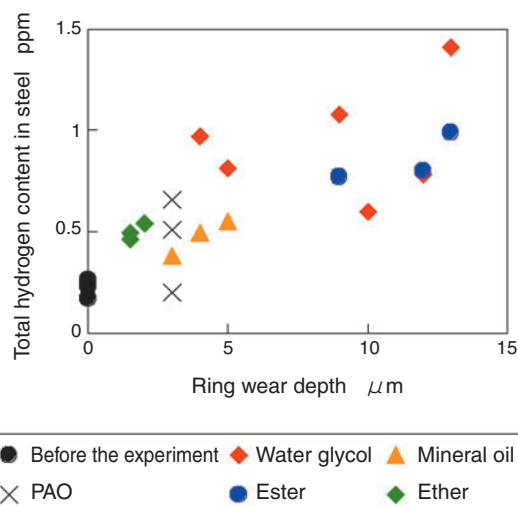


Fig. 3 Relationship between amount of hydrogen in steel and wear depth

2. 1 Experiment method

Fig. 4 shows a diagrammatic sketch of the testing machine. The specimen bearing and the support bearing support the rotation axis of this testing machine. With the housing divided into left and right halves with an insulating material inserted between them, the testing machine is structured so it allows current to flow from terminal A through the specimen bearing to the rotation axis, then through the support bearing, and finally to terminal B when electricity is applied between terminals A and B.

Tables 1 and 2 shows the characteristics of specimen greases and the experiment conditions. The experiment was conducted with a constant load current applied under the condition of abrupt acceleration and deceleration of a rotating inner ring. In another experiment, the direction of the current was reversed to study the effect of the reversing the current.

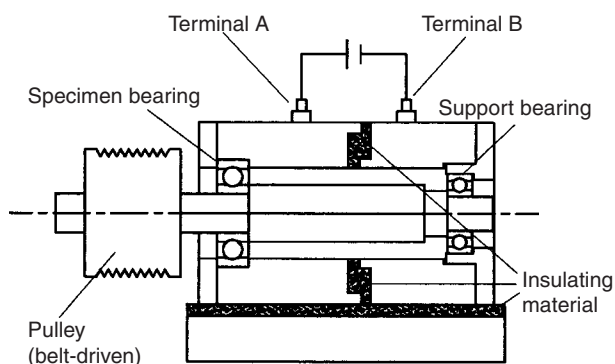


Fig. 4 Bearing test equipment

Table 1 Test greases

Grease	Grease A	Grease B
Thickening agent	Urea	Urea
Base oil	PAO + Ester	ADE + PAO
Dynamic viscosity mm ² /s (40°C)	40	72
Consistency	250	300

Table 2 Test conditions

Specimen bearing	Deep-groove ball bearing (6203)
Amount of enclosed grease (g)	0.86
Rotational speed (min ⁻¹)	Abrupt acceleration or deceleration between 0 and 20000
Atmosphere	Room temperature
Pulley load (N)	1,617
Bearing load (N)	2,332
Current (A)	0.1~3
Stopping condition	When vibration has become 10 times that at the beginning

2. 2 Results of the experiment and their consideration

Table 3 shows the results of the experiment. With no current flowing, both grease A and B allowed operation to continue over 300 hours. Under the electrically charged condition, both types of grease allowed flaking to occur in a short time. Flaking occurred in all of the inner rings, outer rings, and steel balls. Fig. 5 depicts where the flaking occurred along with a cross-sectional photo. The cross-section shows white structural change that is characteristic of brittle flaking.

Fig. 6 shows the relationship between current and brittle flaking life. Under electrically charged condition, the larger the magnitude of current, the earlier flaking occurs. When a current of 3-A flows, the flaking life is in the order of 10 hours. A current magnitude of 3-A does not reveal the difference in life between grease A and grease B. However, with smaller currents, the service life differs depending on the type of grease. With grease B, for which emphasis is placed has greater resistance against brittle flaking than grease A thus exhibiting a longer life.

As shown in Fig. 6, the bearing sealed with grease A allows flaking accompanied by white structural change to occur after having been operated for about 20 hours under an electrically charged condition with a current of 0.5 A. To study the correlation of flaking with hydrogen embrittlement, a bearing sealed with grease A was operated for 3 to 15 hours with a current

Table 3 Test results

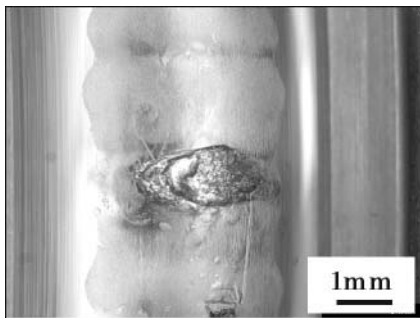
No.	Grease	Current A	Time to flaking h	Flaked portion	
				Direction of current	
				Inner ring to outer ring	Outer ring to inner ring
1	Grease A	0	>300	—	—
2		0.1	88.0	—	Steel ball
3		0.5	20.7	—	Steel ball
4			19.0	Steel ball	—
5		22.1	—	Steel ball	
6		2.0	8.6	—	Outer ring, Steel ball
7			12.4	Inner ring	—
8		3.0	13.1	Inner ring	—
9			13.6	Inner ring, Steel ball	—
10	Grease B	0	>300	—	—
11		0.1	>150	—	—
12		0.3	81.0	—	Steel ball
13		0.5	32.3	—	Steel ball
14			45.8	—	Outer ring
15		1.0	16.8	—	Steel ball
16		2.0	9.5	—	Outer ring

of 0.5 A. In addition, the quantity of hydrogen in the steel balls were measured 30 minutes after the stopping the test. Using a high temperature gas chromatograph apparatus, the quantity of hydrogen released while being heated up to 400°C at a rate of 180°C/h was used as measurement. Fig. 7 shows the relationship between the running time and the quantity of hydrogen. The longer the operating time, the greater the quantity of hydrogen in steel becomes. From the results described above, the flaking in a short time observed in this experiment can be said with a

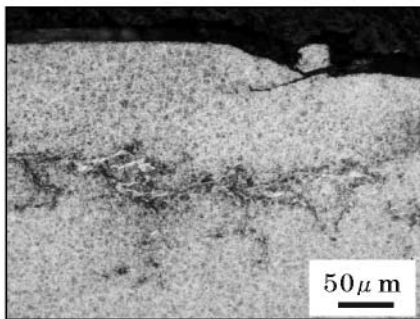
high probability be due to hydrogen embrittlement.

As shown in Table 3, flaking occurs in different portions depending on the direction of the current. When the current flows from the inner to the outer ring, flaking occurs on the inner ring or steel balls, while the current in the opposite direction causes flaking to occur on the outer ring or steel balls. In other words, flaking occurs only on the positive side. To explain the reason why flaking occurs on the positive side only, we ran a thrust ball bearing alternating the direction of the current; from this test, it turned out that portions on the positive side had been selectively worn¹⁵.

For the above reason, as shown in Fig. 8, allowing current to flow results in accelerated wearing on the positive side of the bearing, with the new surface produced by the wearing in turn causing grease to decompose with the generation of hydrogen. It is estimated that the intrusion of the hydrogen generated in this way leads to brittle flaking.



Flaking on a raceway



Cross-sectional view of tested bearing

Fig. 5 Flaking (outer ring)

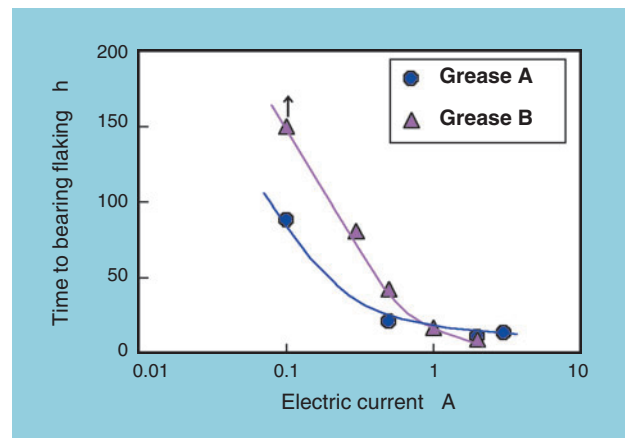


Fig. 6 Relationship between electric current and bearing life

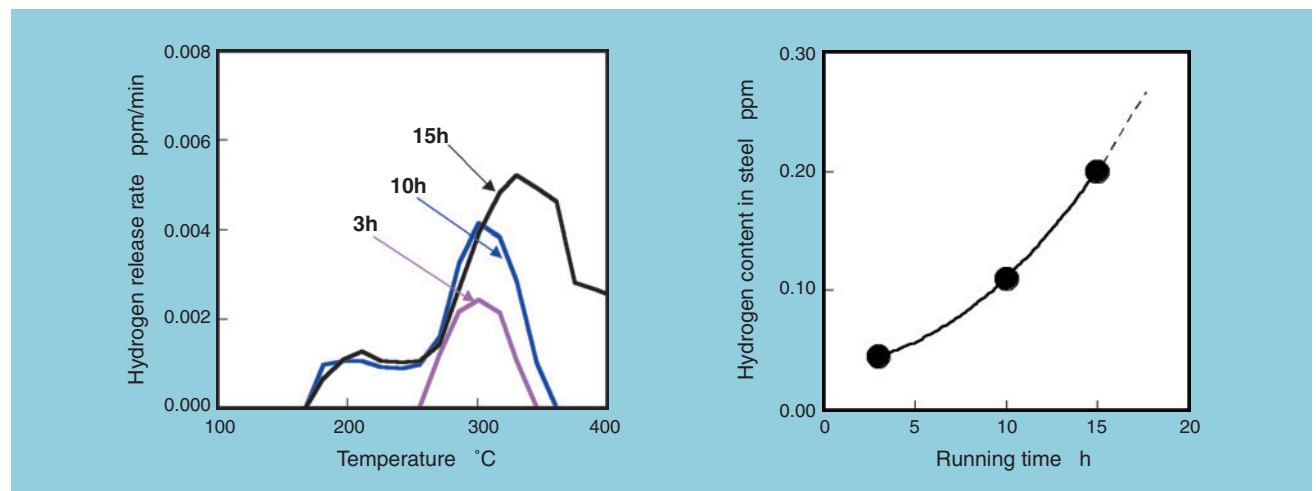


Fig. 7 Relationship between amount of hydrogen and running time

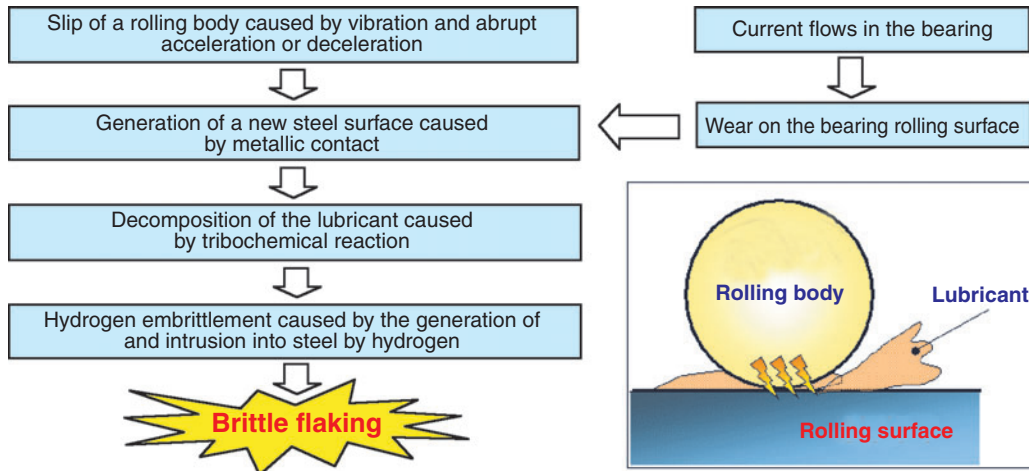


Fig. 8 Estimated mechanism for brittle flaking of bearing endurance test with electrical

3. Electrical component and auxiliary bearing grease "NA103A"

High temperature durability, resistance to brittle flaking, cold hoot-noise suppression, anti-rust resistance, and similar characteristics are required of grease for electrical components and auxiliaries. As shown in Table 4, all these type of greases consist of urea grease using synthetic oil as base oil; grease aiming at cold hoot noise suppression (conventional grease A) and grease aiming at resistance to brittle flaking (conventional grease B) are used. To replace these kinds of conventional grease, we have developed a new type of grease, NA103A that improves all characteristics required for use with bearings for electrical components and auxiliaries.

3.1 Composition and properties of NA103A grease

Like conventional grease B, grease NA103A uses urea compounds as the thickening agent and a

mixture of ether and PAO oil as the base oil. Provided with adequate dynamic viscosity, the new grease can be used in a wide range of temperatures including low to ultra-high temperatures by suppressing the self-heating of the grease at high speed rotation.

What distinguishes the new grease from conventional grease B is the passivation of newly produced steel surfaces with multiple additives to prevent brittle flaking and an improvement of high temperature endurance. This grease does not contain environment-burdening substances represented by sodium nitrite and barium compounds at all. Table 4 shows the properties of grease NA103A.

3.2 High temperature resistance

Grease NA103A underwent a high temperature endurance test (according to ASTM D3336) at 150°C and 180°C.

Fig. 9 compares the results obtained from conventional grease and NA103A. Grease NA103A exhibits durability 1.5 to 2 times that of conventional

Table 4 Greases for automotive components

Grease	NA103A	Conventional grease A	Conventional grease B	Test method
Thickening agent	Urea	Urea	Urea	
Base oil	Ether+PAO	PAO+Ester	Ether+PAO	
Dynamic viscosity mm ² /s (40°C)	54	40	72	JIS K2220.23
Worked penetration 60W 25°C	286	250	300	JIS K2220. 7
Dropping point °C	260<	250	240	JIS K2220. 8
Oil separation mass% 100°C 24h	3.0	0.2	1.7	JIS K2220.11
Oxidation stability kPa 99°C 100h	20	20	20	JIS K2220.12
Low temperature torque mN · m -30°C	Start	271	270	JIS K2220.18
	Rotation	63	78	

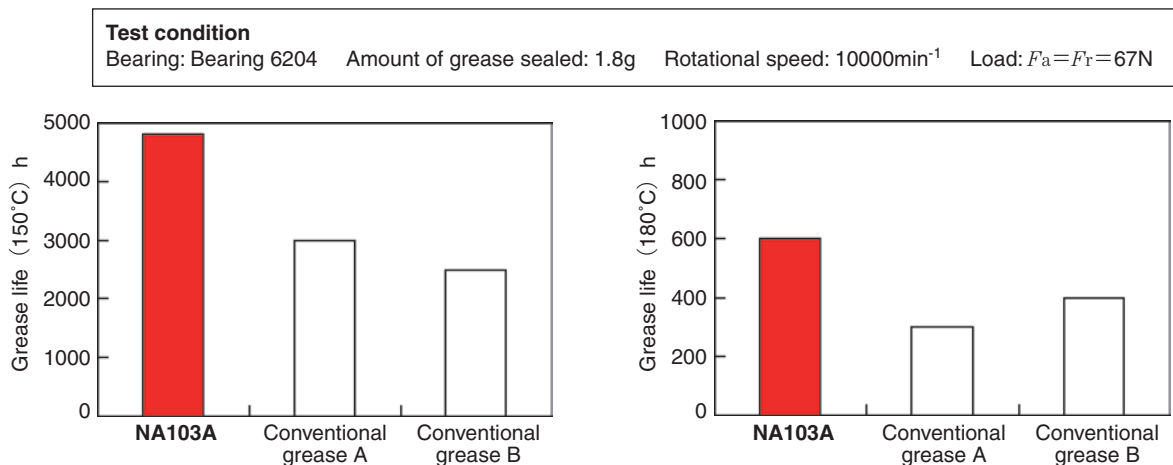


Fig. 9 Bearing endurance test results under high temperature

grease A and B under both of these temperature conditions. With an addition of optimum anti-oxidants, grease NA103A inhibits oxidation-based deterioration, exhibiting long life under high temperature conditions.

3.3 Resistance to brittle flaking

We evaluated the resistance to brittle flaking of grease NA103A by means of the current passage acceleration test method described in section 2.

As shown in Fig. 10, NA103A has resistance to brittle flaking more than twice that of conventional grease A and 1.5 times that of conventional grease B thanks to the effect of the additives passivating new surfaces on the steel.

3.4 Cold hoot-noise suppression characteristic

In belt pulleys equipped with deep-groove ball bearings, cold abnormal noise called hoot noise occurs occasionally at the time of starting in cold regions depending on the pulley specification and operating conditions. This abnormal noise has a frequency range between 500 and 1000 Hz, with the acoustic pressure exceeding 100dBA occasionally and thereby producing very grating noise. The cold abnormal noise is believed to be generated by the axial vibration of the outer ring (so-called translation motion) resulting from the resonance of the pulley system caused by the self-excited vibration of the rolling body. It is known that the type of grease affects the generation of noise greatly.

A specimen bearing incorporated into the test pulley, which is cooled at -60°C for five hours, is fastened to the testing machine shown in Fig. 11. The testing machine is started when the bearing temperature reaches -20°C, and is kept operating until the bearing temperature reaches +10°C with tensioning on the belt. The rate of occurrence of cold

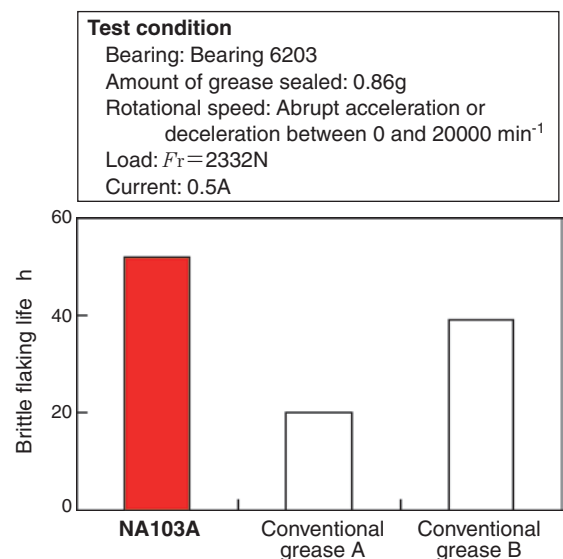


Fig. 10 Brittle flaking test results

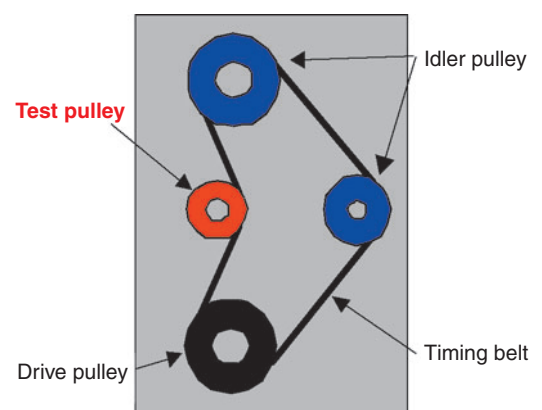


Fig. 11 Hoot noise measurement

hoot phenomena during this period was confirmed. As shown in Fig. 12, grease NA103A has a cold hoot suppression characteristic comparable to that of conventional product A that is excellent in low temperature properties.

3.5 Anti-rust resistance

Fig. 13 shows the result of an anti-rust resistance test on NA103A. To evaluate NA103A, we calculated the rate of occurrence of rust on a tapered roller bearing (30204). The bearing was coated with the grease under the test, immersed in a 1%-sodium-chloride aqueous solution and left alone in a 40°C, moist atmosphere for 48 hours. Then the outer ring's rolling surface was divided circumferentially into 32 equal sections. Then the number of sections that contained rust was divided by 32. We confirmed, thereby, that grease NA103A has anti-rust resistance equal or superior to that of conventional products.

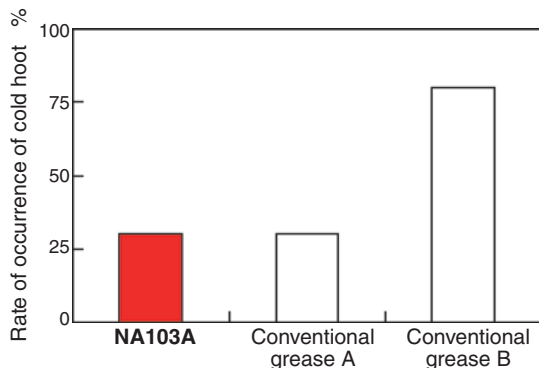


Fig. 12 Rate of hoot noise generation at low temperature

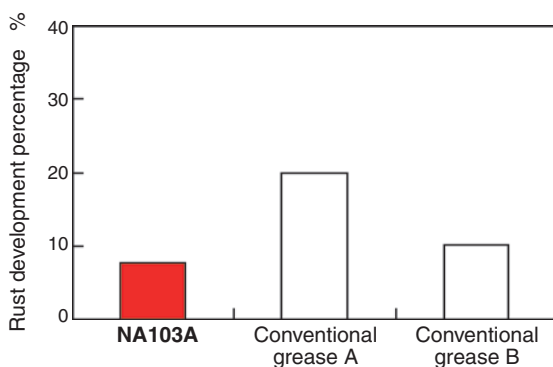


Fig. 13 Rust prevention ability of greases

4. Concluding remarks

Compared with conventional products, grease NA103A excels in all of high temperature durability, resistance to brittle flaking, cold hoot suppression characteristic, and anti-rust resistance, which are required of grease used with bearings for automotive electrical components and auxiliaries. In particular, provided with high temperature durability and resistance to brittle flaking, which are more than 1.5 times those of conventional products, the new grease is expected to be applied to bearings for alternators of which higher power generating capability is required and that are exposed to a high temperature environment.

In addition, composed of safer additives, base oil, and thickening agent, the new grease is expected to greatly contribute to the enhancement of performance of automotive electrical components and auxiliaries and the reduction in environment loading alike.

References

- Booser, E. R. (1974), "Grease Life Forecast for Ball Bearings", *Lubrication Engineering*, 30, pp 536-541.
- Kawamura, T., Minami, M. and Hirata, M. (2001), "Grease Life Prediction for Sealed Ball Bearings", *Tribology Transactions*, 44, 2, pp 256-262.
- Kawamura, T., Minami, M., Hirata, M. (2001). Projection of Life of Sealed Ball Bearing Grease, NTN TECHNICAL REVIEW No.69, pp76-81.
- Tamata, K., Maeda, K., Tsushima, N. (1992). New Type of Micro-structural Change Observed in Bearings for Electrical Components and Auxiliaries, NTN TECHNICAL REVIEW No.61, pp29-35.
- Nozaki, S., Fujimoto, K., Tamata, K. (1992). Brittle Flaking in Bearings for Electrical Components and Auxiliaries and Extension of the Life of Bearings, NTN TECHNICAL REVIEW No.61, pp36-39.
- Nozaki, S., Okasaka, M., Kubota, Y., Akabe, S. (1996). Technical Trend in Bearings for Electrical Components and Auxiliaries, NTN TECHNICAL REVIEW No.65, pp65-72.
- Tamada, K. and Tanaka, H. (1996), "Occurrence of Brittle Flaking on Bearings used for Automotive Electrical Instruments and Auxiliary Devices," *Wear*, 199, pp 245-252.
- Kino, N. and Otani, K. (2003), "The Influence of Hydrogen on Rolling Contact Fatigue Life and its Improvement," *JSAE Review*, 24, pp 289-294.
- Kino, N., Yamamoto, K., Otani, K., Uchiyama, N. (2004). Analysis of Factors of Hydrogen Embrittlement Type Early Flaking, *Proceedings of the Japan Society of Mechanical Engineers (Edition A)*, 70, 696, pp54-61.

- 10) Hamada, H., Matsubara, Y. (2006). Effects of Hydrogen on Tensile and Compression Fatigue and Rolling Fatigue of Bearing Steel, NTN TECHNICAL REVIEW No.74, pp50-57.
- 11) Kawamura, T., Ohara, M., Tamata, K. (2004). Measurement of the Amount of Intrusion of Hydrogen into Steel in a Ball-on-disk Test in Oil, Abstract for Tribology Conference, (Tokyo, May 2004), pp173-174.
- 12) Kawamura, T., Ohara, M., Tamata, K. (2004). Measurement of the Amount of Intrusion of Hydrogen into Steel in a Ball-on-disk Test in Oil (Second Report), Abstract for Tribology Conference, (Tottori, November 2004), pp593-594.
- 13) Kohara, M. Kawamura, T. and Egami, M. (2006), "Study on Mechanism of Hydrogen Generation from Lubricants", Tribology Transactions, 49, pp 53-60.
- 14) Mikami, H. and Kawamura, T. (2007), "Influence of Electrical Current on Bearing Flaking Life", SAE International, 2007-01-0113.
- 15) Kawamura, T., Mikami, H. (2007), Effect of Current Passage on Bearing Flaking, Abstract for Tribology Conference, (Tokyo, May 2007), pp267-268.
- 16) Kawamura, T., Mikami, H. (2007). Effects of Grease Additives on Brittle Flaking under Energized Condition, Abstract for Tribology Conference, (Saga, September 2007), pp57-58.

Photos of authors



Takayuki KAWAMURA

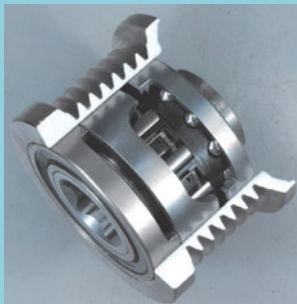
Elemental Technological
R&D Center



Hidenobu MIKAMI

Elemental Technological
R&D Center

Compact Clutch Integrated Pulley for Alternators



Koji SATO*
Isao MIKURIYA*

The demand for a Clutch Integrated Pulley (CIP) for alternators is increasing, as automakers try to reduce belt slip noise and fluctuation especially for engines with large torque vibration. NTN has developed a compact CIP with the same torque capacity as our standard type, making it possible to rotate at higher speeds.

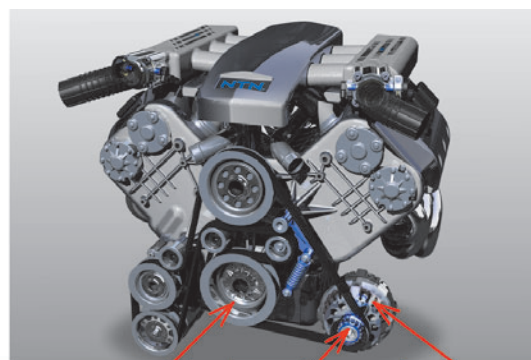
1. Introduction

Fuel-efficient diesel engines work on high compression ratios, which results in large fluctuations of engine torque. A clutch integrated pulley (abbreviated below as CIP) is mounted on the alternator of a diesel engine that has large torque fluctuation. The reduction in belt tension fluctuation improves the belt service life and prevents belt slip noise from occurring. In gasoline engines the adoption of direct injection fuel systems and the lowering of idling rotational speeds for better fuel efficiency tends to lead to an increased fluctuation in belt tension. These circumstances make the usage of CIP's a necessity. There is also a trend for reduced vehicle weight and downsized engine peripherals, which strengthens the need for downsizing and slimming engine auxiliaries. For diesel engines characterized by large torque fluctuation, high torque capacity is needed; while for gasoline engines that operate at high rotational speeds, responsiveness at high-speed rotation is required.

NTN has developed a small-sized CIP with improved high-speed idling performance, while still maintaining the same high torque capacity as the conventional product. This was accomplished by decreasing the shaft diameter, optimizing the design of the sprag clutch and support bearing, and adopting high-performance grease. This report presents this small-sized CIP.

2. Part to which a CIP is fastened

Fig. 1 shows the accessory component drive belt system to which the CIP is fastened. A belt conveying power from the crank pulley of the engine drives accessory components such as an alternator, a compressor for the air-conditioner, and a power steering pump. Among these components, the alternator has the largest moment of inertia. For this reason the CIP is fastened to the alternator in order to alleviate fluctuation in belt tension.



Crank pulley

CIP

Alternator

Fig. 1 Front end accessory drive system

*Automotive Engineering Dept. Automotive Sales Headquarters

3. Structure and Functions of a CIP

3.1 Structure of a CIP

Fig. 2 shows the cross section of a CIP. A sprag clutch is placed between the shaft and the pulley with the sides of the clutch supported by two bearings.

The clutch section consists of a cage with sprags and springs inserted into pockets of the cage, forming a one-way clutch between the outer ring that is press-fitted into the pulley and the shaft.

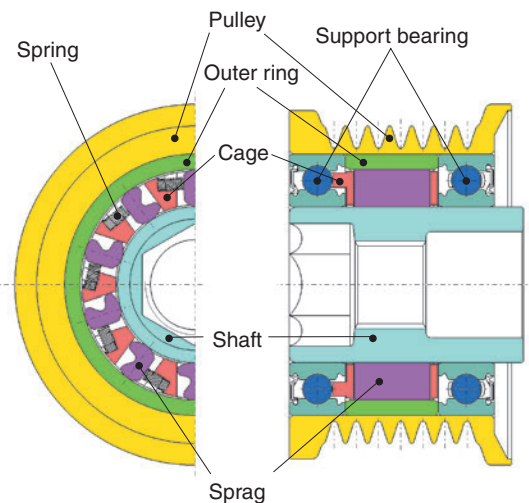


Fig. 2 CIP structure

3.2 Operating Principle of a Sprag Clutch

As shown in Fig. 3, a sprag is designed to change its height as its inclination changes. For example, when a sprag rolls counterclockwise, the height of the sprag decreases (H_1) and when it rolls clockwise, the height increases (H_2), with the relationship between H_1 and H_2 expressed as $H_1 < H_2$.

In contrast, the space formed between the inside diameter of the outer ring into which the sprags are inserted (D_o) and the outside diameter of the shaft (D_s) is constant (shown in Fig. 4). This is referred to in the following as the sprag space, $(D_o - D_s)/2$. When the outer ring turns faster than the shaft, that is, when a

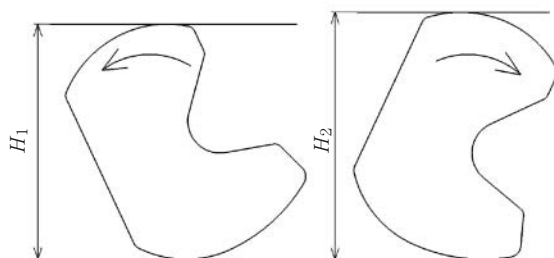


Fig. 3 Sprag Tilting

sprag is turned clockwise both by the outer ring and by the shaft the height of the sprag becomes higher than the height of the sprag space. This causes the outer ring and the shaft to come into engagement, as shown in Fig. 4. When the outer ring turns slower than the shaft, that is, when the sprag is turned counterclockwise both by the outer ring and by the shaft the height of the sprag becomes lower than the height of the sprag space. This causes the outer ring and the shaft to turn without engagement.

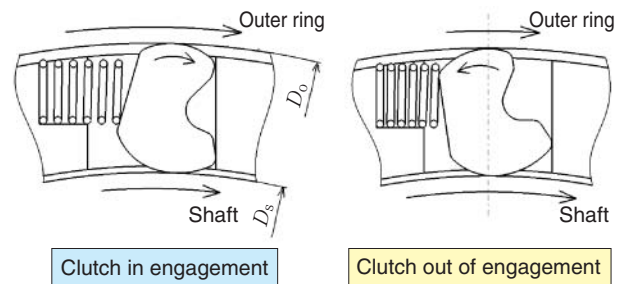


Fig. 4 Operational principle of sprag clutch

3.3 Functions of a CIP

When an engine that is greatly fluctuating in rotational speed drives an auxiliary component with a large moment of inertia, such as an alternator, fluctuation in torque occurs in the pulley and belt drive system. For this reason the belt undergoes large fluctuations in tension that can shorten its life. To solve this problem a one-way clutch is incorporated into the pulley to absorb the fluctuation in rotation caused by the fluctuation in torque. This reduces the fluctuation in tension acting on the belt, which results in increased belt life.

As shown in Fig. 5, when the engine speed (V_1) decreases due to fluctuation in rotation, the alternator, which has a large moment of inertia, acts to maintain its speed (V_3). When $V_2 < V_3$ the clutch runs without engagement to absorb the fluctuation in rotation; this in turn lowers fluctuation in belt tension, thus contributing to suppressing noise caused by the slipping belt when the engine is accelerated or decelerated harshly.

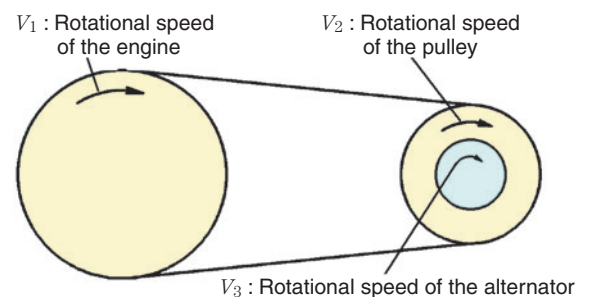


Fig. 5 CIP Operation

Fig. 6 data on fluctuation in rotational speed and in radial load for both a fixed pulley and the corresponding CIP. In this measurement the radial load acting on the pulley was measured as a substitute characteristic for belt tension. It can be seen from the figure that large fluctuations occur in radial load (belt tension) of the fixed pulley while the fluctuation in radial load is substantially reduced for the CIP.

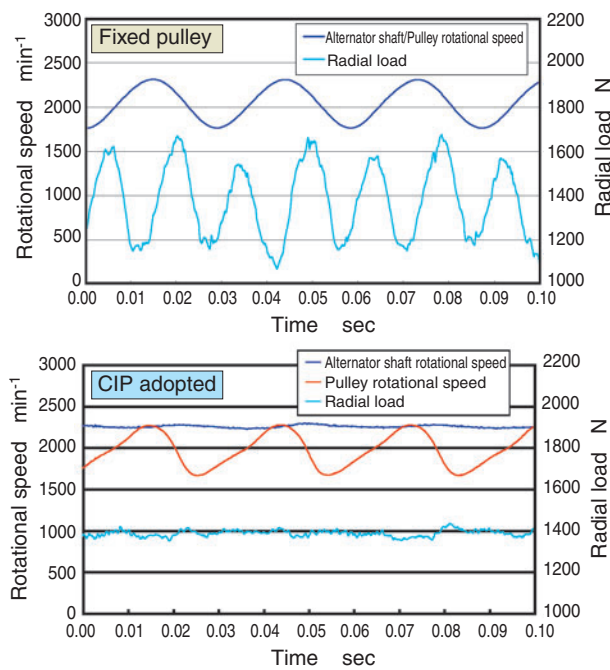


Fig. 6 Comparison of Idling test between solid pulley and CIP

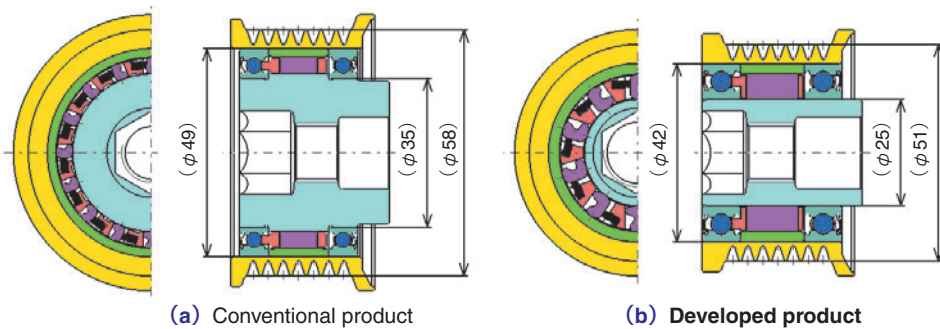
4. Features of a Small-sized CIP

We have successfully reduced pulley diameters without adversely affecting their high torque capacities for our conventional products, which have been in production since 2000 and are primarily used with diesel engines. In addition, we have developed CIP's capable of being used under the high rotational speed conditions of gasoline engines. Fig. 7 compares the developed compact and conventional products. The developed product incorporates an optimized design specification on the following points.

- (1) Reduction in the pulley diameter through the reduction in the shaft diameter and support bearing diameter
- (2) Securing of high torque capacities through the improvement of sprags (the enlargement of the cross section and curvature)
- (3) Improvement of high-speed idling performance through the adoption of high-performance grease
- (4) Improvement of ease of manufacturing through the straightening of the shaft

These efforts have provided the developed products with the following features:

- **High torque capacity: equivalent to that of a conventional product (rated torque: 90 Nm)**
- **Reduced size: reduction in the pulley diameter by 7 mm compared with that of a conventional product (51-mm diameter min.)**
- **Weight reduction: approximately 20% reduction in weight**
- **Improved high-speed idling performance**



Item	Conventional product	Developed product
Shaft	37-mm outside diameter, with steps	25-mm outside diameter, without steps
Pulley diameter	58-mm diameter min.	51-mm diameter min.
Support bearing	6807 with a special outer ring	6905 standard
Sprag	4 mm in height × 8.8 mm in length, 16 pieces	6 mm in height × 12.2 mm in length, 10 pieces
Spring	16 pieces	10 pieces
Weight	520g	400g

Fig. 7 Specifications of current CIP and compact CIP

5. Evaluation Test

Various single-unit tests were conducted to confirm functions of small-sized CIPs in a belt drive system. The following are results of three of the tests performed.

5.1 Functional Evaluation

5.1.1 Harsh Acceleration and Deceleration Test

In this test harsh acceleration and deceleration between low and high engine rotational speeds is reproduced to evaluate the idling characteristics of a clutch.

As shown in Fig. 8, this test allows one to confirm that a clutch has an adequate idling function under harsh acceleration and deceleration conditions.

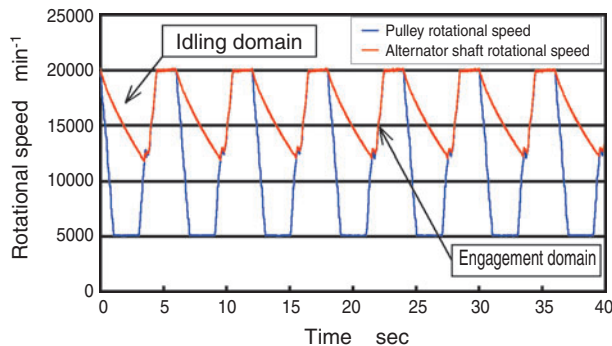


Fig. 8 Results of Cycled speed test

5.1.2 Rotation Fluctuation Test

In a rotation fluctuation test, a condition in which high frequency, large fluctuation in rotation (as in idling) is reproduced to evaluate clutch engagement characteristics.

As shown in Fig. 9, the test allows one to make sure that the engagement of the clutch poses no problems even under high frequency fluctuation in rotation.

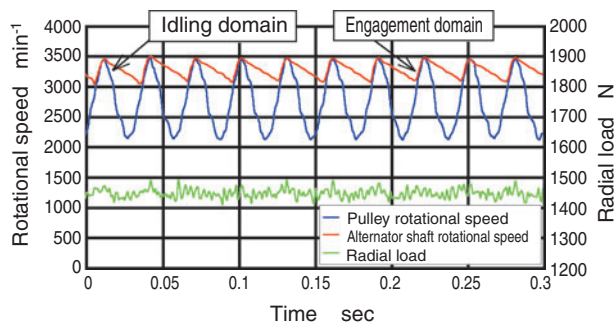


Fig. 9 Results of Idling test

5.2 Test for Selecting Grease

The selection of grease is important in order to improve high-speed idling performance. After comparing different types of greases, grease A was selected that is excellent in thermal stability and oil film forming capability and hence contributes to the improvement of wear resistance. Fig. 10 shows the results of the evaluation based on the comparison of grease A and grease B.

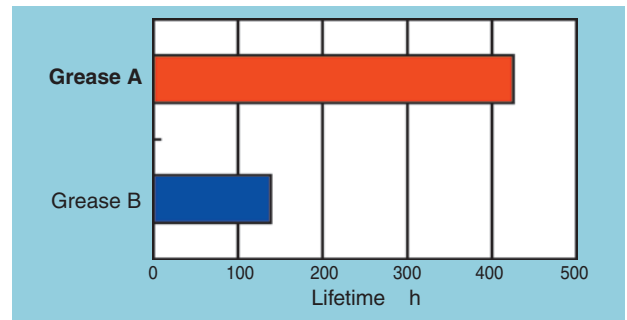


Fig. 10 Grease life comparison

5.3 Evaluation of Durability

To evaluate the durability of a CIP, tests were conducted for the following items to confirm sufficient durability.

- (1) Harsh acceleration and deceleration test: between 5000 and 20000 min⁻¹
- (2) Rotation fluctuation test: 2500 min⁻¹ 15%
- (3) High-speed durability test: 18000 min⁻¹

6. Summary

This report presented NTN's high-performance, small-sized clutch integrated pulley (CIP) that was made possible through a reduction in shaft diameter, improvement in sprags, and adoption of high-performance grease. Future market development for the CIP product will focus on diesel engines and low fuel consumption gasoline engine applications, where the addition of a CIP will enhance the reliability of auxiliary component drive belts.

Photos of authors



Koji SATO

Automotive Engineering Dept.
Automotive Sales Headquarters



Isao MIKURIYA

Automotive Engineering Dept.
Automotive Sales Headquarters

Society of Tribologists & Lubrication Engineers Captain Alfred E. Hunt Award

Crack Propagation of Rolling Contact Fatigue
in Ball Bearing Steel Due to Tensile Strain

Noriyuki TSUSHIMA**

Crack propagations or failure modes in rolling element bearings, which had been difficult to explain via conventional crack propagation mechanisms such as the orthogonal shear stress mechanism, were discussed from the viewpoint of a tensile strain mechanism. Contact stresses are compressive in three axes, whose values differ from each other, then strain can be tensile in one of these directions, acting at a right angle to the direction of the maximum compressive stress. A crack is considered to propagate by this tensile strain. When contact stress is small, a crack produced by some cause can propagate by this elastic tensile strain. When contact stress is large, residual tensile strain is produced by plastic deformation, which can also influence the crack propagation. Several failure modes of rolling element bearings, which had been difficult to explain, were explained by tensile strain.

1. Introduction

There are several theories for crack initiation and propagation mechanism in rolling contact fatigue. In the 1940s, Lundberg-Palmgren considered orthogonal shear stress to be the crack controlling stress because he observed arrested cracks lying parallel to the surface on a section of bearings after rolling contact fatigue. After that, the most commonly used theory was that the crack initiates and propagates by orthogonal shear stress.

However, as cited in the examples mentioned in the present article, there are failures that cannot be explained by the orthogonal shear stress: crack initiation and propagation under the existence of residual stress, through rolling element fracture or through inner ring fracture under fitting stress. These failures are closely related to the amount of residual stress or fitting stress, but the amount of orthogonal stress is not influenced by the existence of residual stress or fitting stress. Therefore, they cannot be explained by orthogonal stress.

After 1980, various theories emerged. Zwirlein and Schlicht¹⁾ proposed a concept of relative tensile stress—that is, the stress in a certain direction subtracted by hydrostatic pressure—discussing its influence on crack initiation and propagation under the three principal compressive stress states. In rolling contact, the three

principal stresses are all compressive, but a stress subtracted by hydrostatic pressure can be tensile and this stress is called relative tensile stress by Schlicht. Voskamp and Hollox²⁾ and Voskamp³⁾ discussed the influence of tensile residual stress that has been created by plastic deformation under large contact stress on crack initiation and propagation. Recently, Harris and McCool⁴⁾ considered von Mises equivalent stress and Zaretsky et al.⁵⁾ considered von Mises equivalent stress or maximum shear stress to be appropriate because the orthogonal shear stress cannot be used to evaluate the influence of residual stress on rolling contact fatigue.

On the other hand, in 1967, Lyman⁶⁾ discussed the role of tensile strain as the rolling contact fatigue mechanism, and in 1996, Muro and Yamamoto^{7), 8)} tried to explain the mechanisms of rolling contact fatigue, such as flaking, pitting, and spalling, by tensile strain as a unified theory for crack propagation under three principal compressive stresses.

Succeeding Muro's study, the present article explains the crack propagation of rolling contact fatigue by tensile strain, using stress and strain calculation programs developed by Muro⁹⁾. As examples for the clarifying explanation, rolling element bearing failures, whose involvement in the crack propagation mechanism has been difficult to explain, are mentioned.

*Former Bearing Engineering R&D Center

2. Calculation Program

Programs used for stress and strain calculations are those developed by Muro. The source codes have already been published (Muro ⁹⁾), and the summary of the code is described in the Appendix. These programs were changed for their language (Basic to Fortran) but were not revised in content. The program calculates the stress at a given point by using the Boussinesq equation for the concentrated force and sums the stresses due to every distributed force composing Hertzian contact stress. A strain calculation is done, using the stress obtained as mentioned earlier, in accordance with the method of Merwin and Johnson ¹⁰⁾. Their method is as follows. The stress at a given point of calculation increases as the loading point moves and, when the stress surpasses the elastic limit of the material, the deviatoric stress changes according to the Prandtl-Reuss strain incremental relation. The difference between elastic and plastic deviatoric stresses is the resulting residual stress. After unloading, the residual stress in the depth direction is eliminated by transforming it to residual stresses in the rolling and axial directions, keeping the strains in the rolling and axial directions as they are, because residual stress in the depth direction is assumed to be zero. However, in Muro's program, the residual stress in the depth direction is not transformed into residual stresses in the rolling and axial directions for the next loading, while making the residual stress in depth direction zero. This procedure was said to stabilize the calculation. Furthermore, Muro's program assumes that plastic deformation occurs when von Mises equivalent stress σ_M divided by the yield shear stress k exceeds $\sqrt{3}$ and simply calculates plastic deviatoric

stress by multiplying the elastic deviatoric stress by a factor of $\sqrt{3} / \sigma_M$. This modification for residual stress calculation was made to stabilize the calculation, which otherwise had scattered between a given loading cycle and the next loading cycle, making saturation difficult (Muro ⁹⁾).

The rolling direction is defined as the x -axis direction, the axial direction is defined as the y -axis direction, and the depth direction is defined as the z -axis direction, and for example the xy plane is the plane made by x and y axes. The half-radius of the major axis of contact ellipse is a and the half-radius of the minor axis is b . Load movement is from $x = -2b$ to $+2b$.

Stress values obtained are normalized by dividing them by the yield shear stress k . Strains obtained are multiplied by Young's modulus to express it in stress units for the convenience of comparison with the material strength, because stress values for the material strength are usually available in the literature and strain values are not. Because the yield shear stress k of hardened ball bearing steel is about 1 GPa (derived from the fact that one-dimensional yield shear stress k is one-dimensional tensile yield stress 1.7 GPa divided by $\sqrt{3}$), then the expressed values in the following tables can be considered values in GPa.

3. Examples of Crack Propagation by Tensile Strain

In this section, four rolling contact fatigue failures were cited for the explanation of crack propagation by tensile strain. They were thus far difficult to explain by ordinary mechanisms such as orthogonal shear stress. Specimen types, materials, dimensions, and lubricants are shown in **Table 1**.

Table 1 Test or running conditions for the examples of crack propagation analysis by tensile strain in this article

Example	Specimen, dimensions (Material)	Matching specimen, dimensions (Material)	a/b	P_{max} (GPa)	Slip	Lubricant	Related figure (Reference)
A	Ring (SUJ2) OD : 50mm AC : 50R	Ring (SUJ2) OD : 53mm AC : 50R	1.6	3.0 4.6	No	Turbin oil pad supply	Fig. 1, Fig. 2 (Muro et al. ¹¹⁾)
B	Ring (SUJ2) OD : 50mm AC : 25.0R	Ring (SUJ2) OD : 53mm AC : 26.5R	1.0	5.0	No	Turbin oil pad supply	Fig. 3, Fig. 4 (Muro et al. ¹¹⁾)
C	Ball bearing 6303 Outer ring (SUJ2)	9/32 in. Ball (SUJ2)	5.5	2.9	No	Grease	Fig. 6 (Tamada and Tanaka et al. ¹²⁾)
D	Spherical roller bearing 23160 Inner ring (SUJ3)	Spherical roller (SUJ3)	54.0	2.0	No	Grease	Fig. 7 (Tsushima et al. ¹³⁾)

OD: Outer diameter, AC: Radius of curvature in axial direction, SUJ2: AISI 52100 Equivalent in JIS

Fracture and Flaking of the Ring Specimen

The failure mode of the ring specimen (Muro et al.¹¹⁾ with 50 mm in diameter after rolling contact fatigue was flaking irrespective of load values when the specimen was not given residual tensile stress at the subsurface beforehand. However, when the specimen was given tensile residual stress before the test, the failure mode was fracture when the load was small, and flaking when the load was large. Fig. 1 shows the ring specimen fractured without flaking.

As the explanations for these different failure modes, the following was given by X-ray residual stress measurement shown in Figs. 2(a) and 2(b). When the load is small (Fig. 2(a)), the creation of residual compressive stress is small and the crack can propagate in the depth direction. When the load is large (Fig. 2(b)), compressive residual stress is created and the crack propagation into the depth direction is thus inhibited; then flaking occurs. However, a quantitative explanation for the crack propagation was difficult at that time. In the following, an explanation via tensile strain is attempted.

Tables 2 and 3 show calculated stresses σ_x , σ_y , σ_z in x-, y- and z-axis directions and maximum shear stress τ_{45} , orthogonal shear stress τ_o , and von Mises equivalent stress σ_M divided by $\sqrt{3}$ at the center of contact track ($x = 0, y = 0$) for the ring specimens at the first loading of rolling contact with $P_{max} = 3.0k$ (that is, 3.0 GPa).

In the test, ring specimens were subjected to standard heat treatment and some of them were previously given tensile residual stress after heat treatment by induction heating of the subsurface. Table 2 shows the stresses for the standard heat treatment specimen. Table 3 shows stresses for the specimen previously given residual tensile stress of

$RS1 = 0.4k$ (that is, 0.4 GPa) in the rolling direction and $RS2 = 0.2k$ (= 0.2 GPa) in the axial direction. The values of $RS1$ and $RS2$ were estimated from X-ray measurement in Figs. 2(a) and 2(b). In this test, the ellipticity of the contact surface is $a/b=1.6$. Therefore, calculation was made with $a/b=1.6$. The depth was normalized by b , the half-radius of the minor axis of the contact ellipse.

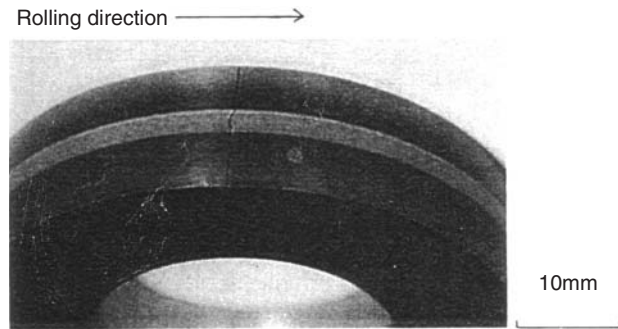


Fig. 1 Fracture of ring specimen tested at $P_{max}=3GPa^{11)}$

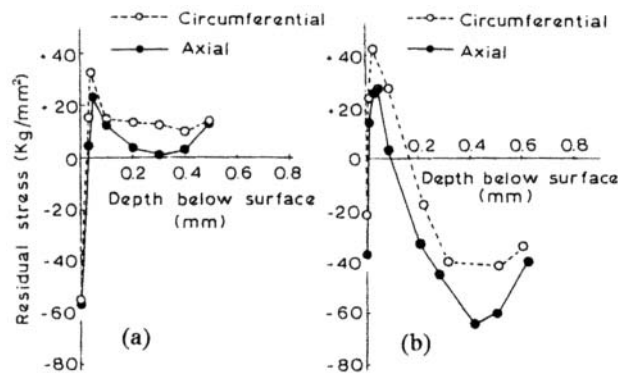


Fig. 2 Residual stress distributions of ring specimen measured by X-ray after testing at (a) $P_{max}= 3 GPa$ and (b) $P_{max} = 4.6 GPa$ (Muro et al.¹¹⁾)

Table 2 Calculated stresses under contact surface at initial stage of loading for ring specimen not given residual stress before test
(Calculating condition : $P_{max}=3.0GPa, RS1= 0GPa, RS2=0GPa, a/b=1.6$)

z/b	σ_x	σ_y	σ_z	τ_o	τ_{45}	$\sigma_M/\sqrt{3}$
0.01	-2.52	-2.26	-3.18	0.14	0.33	0.48
0.1	-1.99	-1.88	-2.98	0.46	0.50	0.61
0.2	-1.54	-1.54	-2.92	0.62	0.69	0.80
0.3	-1.17	-1.26	-2.82	0.68	0.83	0.93
0.4	-0.88	-1.02	-2.70	0.69	0.91	1.02
0.5	-0.65	-0.82	-2.56	0.68	0.95	1.06
0.6	-0.48	-0.66	-2.41	0.66	0.96	1.07
0.7	-0.35	-0.53	-2.25	0.63	0.95	1.05
0.8	-0.25	-0.42	-2.10	0.59	0.92	1.02
0.9	-0.18	-0.33	-1.94	0.56	0.88	0.98
1.0	-0.12	-0.26	-1.80	0.52	0.84	0.93

Table 3 Calculated stresses under contact surface at initial stage of loading for ring specimen given residual stress before test
(Calculating condition : $P_{max}=3.0GPa, RS1= 0.4GPa, RS2=0.2GPa, a/b=1.6$)

z/b	σ_x	σ_y	σ_z	τ_o	τ_{45}	$\sigma_M/\sqrt{3}$
0.01	-2.12	-2.06	-3.18	0.14	0.53	0.49
0.1	-1.59	-1.68	-2.98	0.46	0.69	0.62
0.2	-1.14	-1.34	-2.92	0.62	0.89	0.80
0.3	-0.77	-1.06	-2.82	0.68	1.03	0.93
0.4	-0.48	-0.82	-2.70	0.69	1.11	1.10
0.5	-0.25	-0.62	-2.56	0.68	1.15	1.05
0.6	-0.08	-0.46	-2.41	0.66	1.16	1.06
0.7	0.05	-0.33	-2.25	0.63	1.15	1.05
0.8	0.15	-0.22	-2.10	0.59	1.12	1.02
0.9	0.22	-0.13	-1.94	0.56	1.08	0.98
1.0	0.28	-0.06	-1.80	0.52	1.04	0.93

Comparison between **Tables 2** and **3** shows that the orthogonal shear stress τ_o is the same for the same depth despite other stresses being different. Although the orthogonal shear stress is the same irrespective of the existence of residual stress, the failure modes are different as mentioned earlier. Then it is clear that the orthogonal shear stress does not control crack propagation.

Tables 4(a) and **4(b)** show the residual stress calculations when rolling contact is done with $P_{max}=3.0k$ and $4.6k$, respectively. Since residual stress values would be different with the axial position (that is, the y coordinate), the calculation was made at $y = 0.5a$ to be able to compare the results with the X-ray measurement in **Fig. 2**, which will produce the average value over the contact track. RR_x is the residual stress in the rolling direction (x direction) and RR_y is the residual stress in axial direction (y direction); both are normalized by yield shear stress k in the tables. These are values at the loading cycle when plastic deformation reached or almost reached the saturation so that the plastic deformation lessened. Residual stresses in **Tables 4(a)** and **4(b)** would be almost similar, respectively, to the residual stress values in **Figs. 2(a)** and **2(b)** measured by X-ray.

Table 5 shows calculated "residual" tensile strain E_{1zxr} at each depth and the maximum value of "elastic" tensile strain E_{1zx} for $x = -2b$ to $+2b$, at $y = 0.5a$. (Note that E_{1zxr} and E_{1zx} are the principal tensile strains on the zx plane made by z and x axes.) This maximum elastic tensile strain exists outside of the contact surface (that is, at $x < -1.0b$ or $x > +1.0b$) and the value (for example, $0.45 \pm 30x$) in the table means that the elastic tensile strain changes its value during the movement of loading and the maximum strain 0.45 inclines by $+30^\circ$ clockwise from the x axis for the

range $x < 0$ and by -30° for $x > 0$. As mentioned earlier, the value of the strain is the value multiplied by Young's modulus to transform it to the stress unit.

Table 5(a) shows that, in the case of $P_{max} = 3.0k$, the residual tensile strain E_{1zxr} becomes extremely small (that is, about $0.02k$ or 0.02 GPa) for a depth larger than $z=0.22$ mm as the crack propagates into the depth. Because the critical value of the stress intensity factor range ΔK_{Ith} for the crack propagation by fatigue is assumed to be $5 \text{ MPa} \sqrt{m}$ (Muro ⁹⁾, the stress for the crack to propagate in this case is $5 \div \sqrt{\pi \cdot 0.0002} = 0.2 \text{ GPa}$ ($\because \Delta K_I = \Delta \sigma \sqrt{\pi a}$), much larger than the 0.02 GPa mentioned earlier. Then the crack cannot propagate by residual tensile strain. On the other hand, since elastic tensile strain E_{1zx} is large enough (over 0.30 GPa), the crack can propagate into the depth direction by this elastic tensile strain. The direction of elastic tensile strain changes from -30° to $+30^\circ$ after $z = 0.11$ mm as the contact point moves; then the crack is thought to propagate macroscopically in a zigzag with changing directions.

On the contrary, in the case of $P_{max} = 4.6k$ in **Table 5(b)** even around $z = 0.25$ mm, residual tensile strain E_{1zxr} is large, about 0.30 GPa, and a crack can propagate by this strain. In this case, residual tensile strain directs in the z direction (denoted by $0z$ in the table), and then the crack propagates at a right angle to this; namely, parallel to the surface or xy plane, finally resulting in flaking. Cracks can also propagate by elastic tensile strain E_{1zx} because it is about 0.5 GPa, but the direction changes variably as the loading point moves; then its contribution would be small. Therefore, it is considered that the crack propagates parallel to the surface mainly by residual tensile strain E_{1zxr} .

Table 4 Calculated residual stresses at $y=0.5a$ of ring specimen given residual stress before calculation

(a) $P_{max}=3k,$ $RS1=0.2k, RS2=0.2k$				(b) $P_{max}=4.6k,$ $RS1=0.4k, RS2=0.2k$			
z/b	$z, \text{ mm}$	RR_x/k	RR_y/k	z/b	$z, \text{ mm}$	RR_x/k	RR_y/k
0.01	0.005	0.40	0.20	0.01	0.008	0.40	0.20
0.1	0.05	0.40	0.20	0.1	0.08	0.35	0.15
0.2	0.11	0.40	0.20	0.2	0.17	-0.23	-0.25
0.3	0.16	0.30	0.14	0.3	0.25	-0.59	-0.58
0.4	0.22	0.02	-0.02	0.4	0.33	-0.59	-0.59
0.5	0.27	-0.08	-0.06	0.5	0.42	-0.65	-0.63
0.6	0.32	-0.05	-0.03	0.6	0.50	-0.63	-0.63
0.7	0.38	0.07	0.03	0.7	0.58	-0.91	-0.68
0.8	0.43	0.22	0.11	0.8	0.66	-0.60	-0.46
0.9	0.49	0.35	0.18	0.9	0.75	-0.34	-0.27
1.0	0.54	0.40	0.20	1.0	0.83	-0.35	-0.25

Table 5 Calculated residual E_{1zxr} , and elastic principal strains E_{1zx} at $y=0.5a$ of ring specimen given residual stress before calculation (Note: E_{1zxr} , and E_{1zx} are principal tensile strains on zx plane.)

(a) $P_{max}=3k,$ $RS1=0.4k, RS2=0.2k$				(b) $P_{max}=4.6k,$ $RS1=0.4k, RS2=0.2k$			
z/b	$z, \text{ mm}$	E_{1zxr}/k	E_{1zx}/k	z/b	$z, \text{ mm}$	E_{1zxr}/k	E_{1zx}/k
0.01	0.005	0.35 0x	0.53 0x	0.01	0.008	0.35 0x	0.63 0x
0.1	0.05	0.35 0x	0.42 0x	0.1	0.08	0.31 0x	0.43 $\pm 45x$
0.2	0.11	0.35 0x	0.45 $\pm 30x$	0.2	0.17	0.12 0z	0.45 $\mp 36z$
0.3	0.16	0.26 0x	0.44 $\pm 31x$	0.3	0.25	0.29 0z	0.50 $\mp 27z$
0.4	0.22	0.02 0x	0.33 $\pm 36x$	0.4	0.33	0.30 0z	0.48 $\mp 25z$
0.5	0.27	0.04 0z	0.29 $\pm 36x$	0.5	0.42	0.32 0z	0.46 $\mp 24z$
0.6	0.32	0.02 0z	0.30 $\pm 29x$	0.6	0.50	0.31 0z	0.42 $\mp 27z$
0.7	0.38	0.06 0x	0.38 $\pm 18x$	0.7	0.58	0.40 0z	0.45 $\mp 12z$
0.8	0.43	0.19 0x	0.52 0x	0.8	0.66	0.26 0z	0.33 $\mp 22z$
0.9	0.49	0.31 0x	0.64 0x	0.9	0.75	0.16 0z	0.31 $\pm 42x$
1.0	0.54	0.35 0x	0.68 0x	1.0	0.83	0.14 0z	0.29 $\pm 36x$

Crack Propagation for Circular Contact

In the rolling contact test of the ring specimen (Muro, et al.¹¹⁾ with 50 mm diameter and with certain curvature in the axial direction, when the contact surface is circular (that is, $a/b = 1$), the crack initiates not at the center of the contact track but at $2a/3$ away from the center of the contact track. Fig. 3 shows this situation: A crack initiated $2a/3$ away from the center of the contact track and then propagated at about 45° to the rolling direction. The crack propagating toward the center of the contact track turned its direction to the rolling direction after reaching the center. The crack also propagated parallel to the surface and resulted in flaking. In the following, the crack initiation at $2a/3$ away from the center of the contact track is discussed from the viewpoint of tensile strain.

Fig. 4 shows the result of X-ray measurement on the contact track after the test with $P_{max} = 5.0$ GPa. Residual tensile stress is created in the surface layer, balancing the created residual compressive stress inside. The calculation program used in the present article cannot calculate this kind of tensile residual stress, which is created in a plastically nondeformed shallower zone for the balance of created compressive residual stress at a plastically deformed deeper zone, because calculation at a given depth is independent of other upper or lower depths (that is, it does not influence the residual stress of other depths). The residual tensile stress of this kind was given beforehand in the calculation. Since this kind of residual tensile stress of the surface layer is considered to be different along the axial position y , depending on the residual compressive stress created in the neighbor inside (or, in other words, since the larger the residual compressive stress in deeper depth, the larger this kind of residual tensile stress),

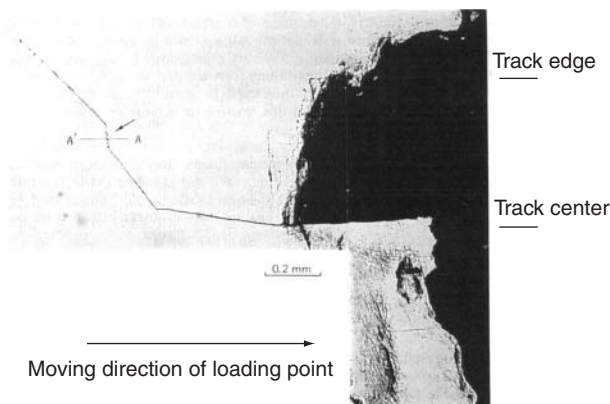


Fig. 3 Crack initiation and propagation on the surface in circular contact; arrow shows origin of cracking (Muro et al.¹¹⁾.

the residual compressive stress at the depth of $z = 0.15b$ was calculated at first for each y value, then this kind of residual tensile stress at the depth of $z = 0.05b$ was assumed by giving the opposite sign to the residual compressive stress value at the depth of $z = 0.15b$.

Table 6 shows the elastic principal maximum and minimum strains E_{1xy} , E_{2xy} and residual principal maximum and minimum strains E_{1xyr} , E_{2xyr} at $z = 0.05b$ on the xy plane parallel to the surface after plastic deformation reaches saturation. Some representative values in Table 6 are plotted in Fig. 5. The maximum elastic tensile strain exists at $y = 0.7a (= 2a/3)$ and $x = \pm 1.2b$. Then we can understand that the crack initiates at the position $y = 2a/3$. Namely, in the case of circular contact, the crack initiation site is not at the center of the contact track but at $y = 2a/3$. On the other hand, this elastic tensile strain inclines by $+36^\circ$ or -36° to the x axis at $y = 0.7a$ and $x = \pm 1.2b$. Namely, the crack can propagate at a right angle to this strain direction in both directions, $\pm 54^\circ$ to the x axis. In Fig. 3, the crack propagates nearly with this angle but in one direction. The crack propagation direction is considered to be influenced by other factors, for example, the tangential force. It has been confirmed that the crack propagation directions were opposite each other between the upper and lower specimens when there was a small slip (Muro et al.¹¹⁾).

Abnormal Flaking of Alternator Bearing

An alternator bearing outer ring flakes as shown in Fig. 6. It is a small flaking in appearance but a sectional view reveals many long cracks running in the depth direction (Tamada and Tanaka¹²⁾). Compared to

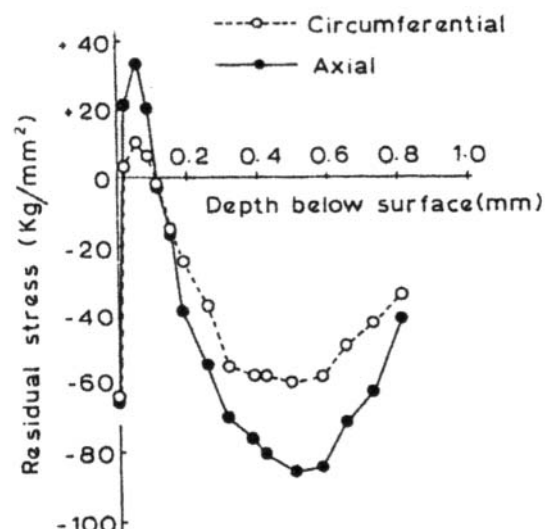


Fig. 4 Residual stress distribution of ring specimen measured by X-ray (Muro et al.¹¹⁾

Table 6 Residual and elastic principal strains E_{1xyr} , E_{1xy} and their directions on xy -plane at $z=0.05b$ for circular contact, E_1 and E_2 mean maximum and minimum principal strains, respectively (Calculating condition: $P_{max}=5.0k$, $a/b=1$)

x \ y	0a		0.3a		0.7a		1.0a	
	E_{1xy}/k	E_{2xy}/k	E_{1xy}/k	E_{2xy}/k	E_{1xy}/k	E_{2xy}/k	E_{1xy}/k	E_{2xy}/k
-2.0b	0.14 0x	-0.18	0.31 7x	-0.05	0.43 29x	0.19	0.14 27x	-0.15
-1.8b	0.16 0x	-0.22	0.34 8x	-0.09	0.46 30x	0.16	0.16 29x	-0.18
-1.6b	0.20 0x	-0.28	0.37 10x	-0.14	0.49 31x	0.11	0.18 32x	-0.21
-1.4b	0.23 0x	-0.36	0.40 11x	-0.22	0.52 33x	0.06	0.21 36x	-0.25
-1.2b	0.21 0x	-0.47	0.39 13x	-0.32	0.56 36x	-0.02	0.23 40x	-0.30
-1.0b	-0.20 0x	-0.64	0.06 16x	-0.46	0.55 40x	-0.13	0.26 -45y	-0.36
-0.8b	-0.52 0x	-0.96	-0.19 20x	-0.76	0.31 -42y	-0.26	0.26 -39y	-0.43
-0.6b	-0.96 0x	-1.17	-0.66 25x	-0.98	0.20 -35y	-0.49	0.21 -31y	-0.50
-0.4b	-1.23 0x	-1.29	-0.94 34x	-1.01	-0.11 -24y	-0.68	0.04 -22y	-0.57
-0.2b	-1.36 0y	-1.37	-1.10 -38y	-1.17	-0.29 -12y	-0.79	-0.17 -11y	-0.63
0b	-1.38 0y	-1.42	-1.15 8y	-1.19	-0.35 0y	-0.83	-0.18 0y	-0.66
0.2b	-1.36 0y	-1.37	-1.09 40y	-1.18	-0.29 12y	-0.79	-0.17 11y	-0.63
0.4b	-1.23 0x	-1.29	-0.93 -35x	-1.11	-0.11 24y	-0.68	0.04 22y	-0.57
0.6b	-0.96 0x	-1.17	-0.65 -26x	-0.98	0.20 35y	-0.49	0.21 31y	-0.50
0.8b	-0.52 0x	-0.96	-0.18 -21x	-0.77	0.31 42y	-0.26	0.26 39y	-0.43
1.0b	-0.20 0x	-0.64	0.06 -17x	-0.47	0.55 -40x	-0.13	0.26 45y	-0.36
1.2b	0.21 0x	-0.47	0.40 -14x	-0.32	0.56 -36x	-0.02	0.23 -40x	-0.30
1.4b	0.23 0x	-0.36	0.40 -12x	-0.22	0.52 -33x	0.06	0.21 -36x	-0.25
1.6b	0.20 0x	-0.28	0.37 -11x	-0.15	0.49 -31x	0.11	0.18 -32x	-0.21
1.8b	0.16 0x	-0.22	0.34 -10x	-0.09	0.46 -30x	0.16	0.16 -29x	-0.18
2.0b	0.14 0x	-0.18	0.31 -9x	-0.05	0.43 -29x	0.19	0.14 -27x	-0.15
	E_{1xyr}/k	E_{2xyr}/k	E_{1xyr}/k	E_{2xyr}/k	E_{1xyr}/k	E_{2xyr}/k	E_{1xyr}/k	E_{2xyr}/k
	0.01 0y	-0.03	0.15 -19y	0.13	0.39 0y	0.26	0 45y	0

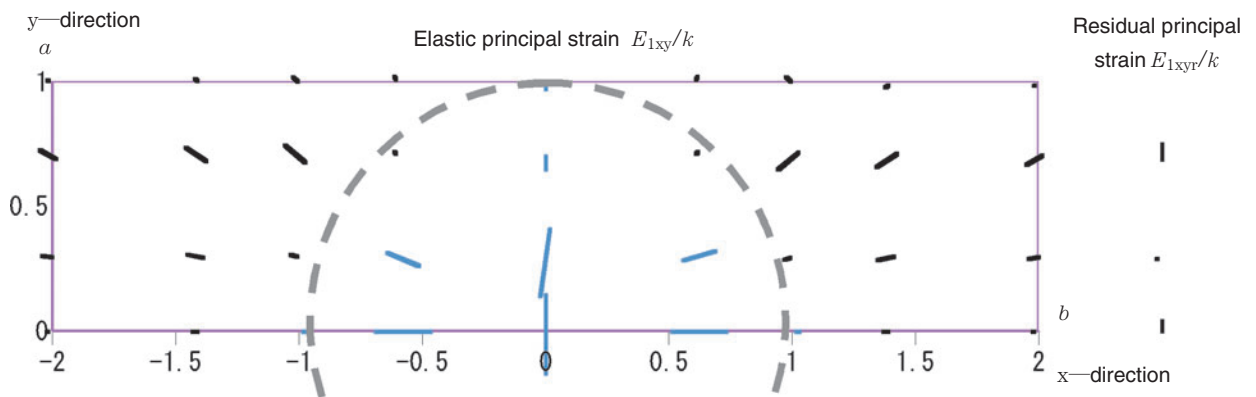


Fig. 5 Residual and elastic principal strains and their directions on xy plane at $z = 0.05b$ shown in **Table 6**. (Large dotted circle is circular contact surface. Dense dark lines mean elastic principal maximum strain E_{1xy}/k or residual principal maximum strain E_{1xyr}/k , which are tensile, and faint blue lines mean elastic principal maximum strain E_{1xy}/k , which are compressive.)



Fig. 6 Cracking on circumferential section of an alternator bearing outer ring (Tamada and Tanaka¹²⁾)

Table 7 Calculated principal strains and their directions for alternator outer ring
(calculation condition : $P_{max}=2.9k$, $y=0$, $a/b=5.5$)

$z \backslash x$	$0b$	$-0.2b$ $+0.2b$	$-0.6b$ $+0.6b$	$-1.0b$ $+1.0b$
0.1b	$-1.04 \pm 0x$	$-1.00 \pm 5x$	$-0.7 \pm 17x$	$0.26 \mp 37z$
0.2b	$-0.65 \pm 0x$	$-0.61 \pm 6x$	$-0.3 \pm 20x$	$0.32 \mp 40z$
0.3b	$-0.34 \pm 0x$	$-0.30 \pm 6x$	$-0.0 \pm 21x$	$0.36 \mp 43z$
0.4b	$-0.09 \pm 0x$	$-0.07 \pm 7x$	$0.16 \pm 22x$	$0.38 \pm 44x$
0.5b	$0.09 \pm 0x$	$0.11 \pm 7x$	$0.28 \pm 22x$	$0.40 \pm 42x$
0.6b	$0.22 \pm 0x$	$0.24 \pm 7x$	$0.35 \pm 22x$	$0.41 \pm 40x$
0.7b	$0.31 \pm 0x$	$0.33 \pm 7x$	$0.40 \pm 22x$	$0.42 \pm 38x$
0.8b	$0.38 \pm 0x$	$0.39 \pm 7x$	$0.43 \pm 21x$	$0.42 \pm 36x$
0.9b	$0.42 \pm 0x$	$0.42 \pm 7x$	$0.44 \pm 20x$	$0.42 \pm 34x$
1.0b	$0.45 \pm 0x$	$0.45 \pm 6x$	$0.45 \pm 20x$	$0.42 \pm 33x$
1.2b	$0.46 \pm 0x$	$0.46 \pm 6x$	$0.45 \pm 18x$	$0.41 \pm 30x$
1.4b	$0.46 \pm 0x$	$0.45 \pm 6x$	$0.44 \pm 17x$	$0.39 \pm 28x$
1.6b	$0.44 \pm 0x$	$0.43 \pm 5x$	$0.41 \pm 16x$	$0.37 \pm 25x$
1.8b	$0.41 \pm 0x$	$0.41 \pm 5x$	$0.39 \pm 14x$	$0.35 \pm 24x$
2.0b	$0.38 \pm 0x$	$0.38 \pm 5x$	$0.37 \pm 13x$	$0.33 \pm 22x$
2.5b	$0.32 \pm 0x$	$0.32 \pm 4x$	$0.31 \pm 11x$	$0.28 \pm 19x$
3.0b	$0.27 \pm 0x$	$0.26 \pm 3x$	$0.26 \pm 10x$	$0.24 \pm 16x$
4.0b	$0.19 \pm 0x$	$0.19 \pm 3x$	$0.18 \pm 8x$	$0.18 \pm 13x$
5.0b	$0.14 \pm 0x$	$0.14 \pm 2x$	$0.13 \pm 6x$	$0.13 \pm 10x$

Table 8 Calculated shear stress τ_0 acting at right angle to the surface for the alternator outer ring
(calculation condition : $P_{max}=2.9k$, $y=0$, $a/b=5.5$)

$z \backslash x$	$0b$	$-0.2b$ $+0.2b$	$-0.6b$ $+0.6b$	$-1.0b$ $+1.0b$	$-1.2b$ $+1.2b$	$-1.6b$ $+1.6b$
0.1b	± 0	± 0.06	± 0.21	± 0.42	± 0.08	± 0.01
0.2b	± 0	± 0.11	± 0.38	± 0.55	± 0.24	± 0.05
0.3b	± 0	± 0.15	± 0.50	± 0.62	± 0.37	± 0.11
0.4b	± 0	± 0.19	± 0.56	± 0.66	± 0.46	± 0.17
0.5b	± 0	± 0.21	± 0.60	± 0.68	± 0.52	± 0.23
0.6b	± 0	± 0.22	± 0.60	± 0.68	± 0.55	± 0.28
0.7b	± 0	± 0.22	± 0.59	± 0.67	± 0.57	± 0.32
0.8b	± 0	± 0.22	± 0.57	± 0.66	± 0.58	± 0.36
0.9b	± 0	± 0.21	± 0.55	± 0.64	± 0.58	± 0.39
1.0b	± 0	± 0.20	± 0.52	± 0.61	± 0.57	± 0.41
1.2b	± 0	± 0.18	± 0.46	± 0.56	± 0.54	± 0.42
1.4b	± 0	± 0.15	± 0.40	± 0.51	± 0.50	± 0.42
1.6b	± 0	± 0.13	± 0.35	± 0.45	± 0.46	± 0.41
1.8b	± 0	± 0.11	± 0.30	± 0.40	± 0.42	± 0.39
2.0b	± 0	± 0.10	± 0.26	± 0.36	± 0.38	± 0.37
2.5b	± 0	± 0.07	± 0.19	± 0.27	± 0.29	± 0.31
3.0b	± 0	± 0.05	± 0.14	± 0.20	± 0.22	± 0.25
4.0b	± 0	± 0.03	± 0.08	± 0.12	± 0.14	± 0.16
5.0b	± 0	± 0.02	± 0.05	± 0.07	± 0.09	± 0.11

Table 9 Calculated principal strains and their directions for spherical roller bearing inner ring
(calculation condition : $P_{max}=2.0k$, $RS1=0.1k$, $y=0$, $a/b=54$)

$z \backslash x$	$0b$	$-0.2b$ $+0.2b$	$-0.6b$ $+0.6b$	$-1.0b$ $+1.0b$
0.1b	$-0.73 \pm 0x$	$-0.71 \pm 5x$	$-0.5 \pm 17x$	$0.16 \mp 37z$
0.2b	$-0.46 \pm 0x$	$-0.43 \pm 6x$	$-0.2 \pm 20x$	$0.21 \mp 40z$
0.4b	$-0.06 \pm 0x$	$-0.04 \pm 7x$	$0.12 \pm 22x$	$0.26 \pm 44x$
0.6b	$0.17 \pm 0x$	$0.18 \pm 7x$	$0.26 \pm 22x$	$0.30 \pm 39x$
0.8b	$0.29 \pm 0x$	$0.30 \pm 7x$	$0.33 \pm 21x$	$0.32 \pm 35x$
1.0b	$0.35 \pm 0x$	$0.35 \pm 6x$	$0.35 \pm 19x$	$0.33 \pm 32x$
1.5b	$0.38 \pm 0x$	$0.38 \pm 5x$	$0.36 \pm 16x$	$0.33 \pm 25x$
2.0b	$0.36 \pm 0x$	$0.36 \pm 4x$	$0.34 \pm 13x$	$0.31 \pm 21x$
2.5b	$0.33 \pm 0x$	$0.33 \pm 4x$	$0.32 \pm 11x$	$0.30 \pm 17x$
3.0b	$0.30 \pm 0x$	$0.30 \pm 3x$	$0.29 \pm 9x$	$0.28 \pm 14x$
3.5b	$0.28 \pm 0x$	$0.28 \pm 3x$	$0.27 \pm 8x$	$0.26 \pm 12x$
4.0b	$0.26 \pm 0x$	$0.26 \pm 2x$	$0.26 \pm 7x$	$0.25 \pm 11x$
5.0b	$0.23 \pm 0x$	$0.23 \pm 2x$	$0.23 \pm 5x$	$0.23 \pm 9x$
6.0b	$0.21 \pm 0x$	$0.21 \pm 1x$	$0.21 \pm 4x$	$0.21 \pm 7x$
8.0b	$0.19 \pm 0x$	$0.19 \pm 1x$	$0.19 \pm 3x$	$0.19 \pm 5x$
10.0b	$0.17 \pm 0x$	$0.17 \pm 1x$	$0.17 \pm 2x$	$0.17 \pm 4x$
12.0b	$0.16 \pm 0x$	$0.16 \pm 1x$	$0.16 \pm 2x$	$0.16 \pm 3x$
14.0b	$0.15 \pm 0x$	$0.15 \pm 0x$	$0.15 \pm 1x$	$0.15 \pm 2x$
16.0b	$0.14 \pm 0x$	$0.14 \pm 0x$	$0.14 \pm 1x$	$0.14 \pm 2x$
20.0b	$0.13 \pm 0x$	$0.13 \pm 0x$	$0.13 \pm 1x$	$0.13 \pm 1x$

Table 10 Calculated shear stress τ_0 acting at right angle to the surface for spherical roller bearing inner ring
(calculation condition : $P_{max}=2.0k$, $RS1=0.1k$, $y=0$, $a/b=54$)

$z \backslash x$	$0b$	$-0.2b$ $+0.2b$	$-0.6b$ $+0.6b$	$-1.0b$ $+1.0b$	$-1.2b$ $+1.2b$	$-1.6b$ $+1.6b$
0.1b	± 0	± 0.04	± 0.14	± 0.29	± 0.06	± 0.01
0.2b	± 0	± 0.08	± 0.26	± 0.38	± 0.17	± 0.04
0.4b	± 0	± 0.13	± 0.39	± 0.46	± 0.32	± 0.12
0.6b	± 0	± 0.15	± 0.42	± 0.48	± 0.39	± 0.20
0.8b	± 0	± 0.15	± 0.40	± 0.46	± 0.41	± 0.26
1.0b	± 0	± 0.14	± 0.36	± 0.43	± 0.41	± 0.29
1.5b	± 0	± 0.10	± 0.27	± 0.35	± 0.35	± 0.31
2.0b	± 0	± 0.07	± 0.19	± 0.27	± 0.28	± 0.28
2.5b	± 0	± 0.05	± 0.14	± 0.20	± 0.22	± 0.24
3.0b	± 0	± 0.04	± 0.11	± 0.16	± 0.18	± 0.20
3.5b	± 0	± 0.03	± 0.08	± 0.13	± 0.14	± 0.17
4.0b	± 0	± 0.02	± 0.07	± 0.10	± 0.12	± 0.14
5.0b	± 0	± 0.01	± 0.04	± 0.07	± 0.08	± 0.10
6.0b	± 0	± 0.01	± 0.03	± 0.05	± 0.06	± 0.07
8.0b	± 0	± 0.01	± 0.02	± 0.03	± 0.03	± 0.04
10.0b	± 0	± 0.00	± 0.01	± 0.02	± 0.02	± 0.03
12.0b	± 0	± 0.00	± 0.01	± 0.01	± 0.02	± 0.02
14.0b	± 0	± 0.00	± 0.01	± 0.01	± 0.01	± 0.02
16.0b	± 0	± 0.00	± 0.00	± 0.01	± 0.01	± 0.01
20.0b	± 0	± 0.00	± 0.00	± 0.00	± 0.01	± 0.01

ordinary flaking, it is characterized by cracking into the depth direction, sometimes deeper than 0.6 mm ($z=2.5b$) or rarely deeper than 0.8 mm ($z=3b$), and the mechanism has not been clear. This crack propagation into the depth direction is discussed later from the viewpoint of tensile strain. In this case, the cause of the failure has been clarified: the hydrogen produced by the decomposition of the lubricant influenced this kind of failure (Tamada and Tanaka¹²).

Ellipticity of the contact surface between the outer ring and the ball is $a/b=5.5$. A test was conducted with $P_{\max}=2.9$ GPa. Elastic tensile strains and their direction angles calculated for each depth at $P_{\max}=2.9k$ are shown in **Table 7**. In **Tables 7** to **10**, for example, a value such as $-1.00 \pm 5x$ at $x=-0.2b$ and $+0.2b$ for $z=0.1b$ in **Table 7** shows that at $x=-0.2b$ the principal strain is $-1.00k$ with clockwise inclination of $+5^\circ$ to the x axis and at $x=+0.2b$ the principal strain is $-1.00k$ with clockwise inclination of -5° to the x axis. It is considered that, below the depth $z=1.0b$ ($=0.25$ mm), tensile strain in the x direction, namely parallel to the surface, is a maximum and the value transformed to stress unit is $0.45k$ ($=0.45$ GPa). Even at $z=2.5b$ ($=0.6$ mm), there exists tensile strain corresponding to 0.32 GPa. Due to material deterioration by hydrogen, it will be possible for the crack to initiate and propagate at a right angle to the x axis, namely into the depth direction, by this strain value.

On the other hand, orthogonal shear stress acting at a right angle to the surface is shown in **Table 8**. The orthogonal shear stress around the depth $z=1.0b$ ($=0.25$ mm) is about 0.6 GPa at $x=-1.0b$ and $+1.0b$ but it decreases rapidly as the depth increases. Below $z=2.5b$ ($=0.6$ mm), it is smaller than 0.3 GPa. In the case of high-hardness steels, for the crack to propagate it is said that the shear stress value must be three times larger than the tensile stress value. Then it would be difficult for the crack to initiate and propagate by this shear stress value. It will be reasonable to consider that the crack propagated by tensile strain.

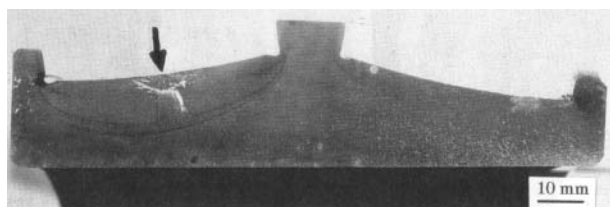


Fig. 7 Fracture of a spherical roller bearing inner ring (Tsushima et al.¹³). The arrow shows the origin of the cracking

Fracture of Spherical Roller Bearing Inner Ring

Some type of spherical roller bearing inner ring is used under some value of fitting stress. When the fitting stress is larger than 0.1 GPa, fracture of the inner ring rarely happens during service. It is considered that the fracture is caused by the repetition of small tensions due to fitting stress and large compression due to contact stress (Tsushima, et al.¹³). **Fig. 7** shows the fracture surface. The crack initiated near the surface of $z=0.05b$ ($=0.04$ mm) and propagated macroscopically in zigzag formation into the depth until $z=4b$ ($=3$ mm); then it propagated gradually, creating a smooth fracture surface and rapidly from $z=20b$ ($=16$ mm). Macroscopically zigzag crack propagations to a depth of 3 mm and smooth crack propagation from 3 to 16 mm have not yet been clarified. In the following, this crack propagation mechanism is discussed from the tensile strain viewpoint.

The ellipticity of the contact surface between the inner ring and roller is $a/b=54$. We assume $P_{\max}=2.0k$ (that is, 2.0 GPa) as the Hertzian contact stress during service. Calculation of tensile strain and its direction is shown in **Table 9**. Here, stress of $0.1k$ ($=0.1$ GPa) was given as the fitting stress $RS1$ in the circumferential direction (x direction). At certain depths, for example, at $z=0.6b$ ($=0.45$ mm) or deeper, as the loading point moves (x increases from $x=-1b$ to $+1b$), tensile strain changes its direction continuously from over $+10^\circ$ to below -10° against the x axis up to the depth $z=4b$ ($=3$ mm). Then, in this depth range, the crack is considered to propagate, sometimes changing its direction, which creates the macroscopic zigzag appearance of the fracture surface. Below the depth $z=4b$ ($=3$ mm), tensile strain is within 10° against the x axis and the crack is considered to propagate into the depth, creating a smooth fracture surface. Shear stress acting parallel to the depth direction, shown in **Table 10**, became significantly small below $z=4b$ ($=3$ mm) and would not be able to propagate the crack.

According to fracture mechanics, a crack can propagate by fatigue when the stress intensity factor range ΔK_I at the crack tip exceeds the critical value of the material ΔK_{Ith} . For a hardened ball bearing steel, DK_{Ith} is 5 MPa \sqrt{m} (Tsushima et al.¹³). The stress intensity factor range ΔK_I is roughly $\Delta \sigma \sqrt{\pi a}$ (a is crack depth); here $\Delta \sigma$ is stress range. In this case, stress changes from a value in **Table 9** during loading to the value of fitting stress 0.1 GPa during unloading. Then $\Delta \sigma$ is the value in **Table 9** subtracted by 0.1 GPa.

Now we examine whether the crack can propagate from 3 mm ($z=4b$) to 16 mm ($z=20b$). From **Table 9**,

we know that tensile stress at $z=4b$ converted from strain is about 0.26 GPa. Therefore, the stress range $\Delta\sigma$ at $z=4b$ is 0.16 GPa = 160 MPa. Then at $z=4b$ or 0.003 m depth, ΔK_I is $160\sqrt{\pi \cdot 0.003} = 15.5 \text{ MPa}\sqrt{m}$, which is larger than the critical value of $5 \text{ MPa}\sqrt{m}$. Then the crack can propagate by fatigue. Similarly, at $z=20$ or 0.016 m, the stress range is 0.03 GPa = 30 MPa. Then $\Delta K_I = \sqrt{\pi \cdot 0.016} = 6.7 \text{ MPa}\sqrt{m}$, which is larger than the critical value of $5 \text{ MPa}\sqrt{m}$. Then a crack can propagate by fatigue at least until this depth. At 0.016 m depth, however, stress intensity factor K_I due to fitting stress $\sigma\sqrt{\pi a} = 100\sqrt{\pi \times 0.016} = 22.4 \text{ MPa}\sqrt{m}$, reaching the fracture toughness value K_{IC} of this material (estimated as $21 \text{ MPa}\sqrt{m}$ by Tsushima et al.¹³⁾), then rapid fracture occurred.

4. Discussion

So far, the authors have reported the influence of heat treatment stress (Maeda and Tsushima¹⁴⁾), fitting stress (Maeda and Tsushima¹⁴⁾), and residual stress due to mechanical treatment on rolling contact fatigue life (Maeda et al.¹⁵⁾). It has been proved that, if small tensile stress such as 0.2 GPa exists, a crack can initiate during rolling contact fatigue due to this tensile stress and compressive stress due to contact stress—that is, by the repetition of small tension and large compression (Muro et al.¹¹⁾). However, as mentioned in the present article, there are some phenomena where cracks are propagated without such tensile stress. In these cases, however, by considering that the tensile strain is equivalent to tensile stress, the explanation of crack initiation and propagation is possible. The contact stress is compressive in three axis directions, but their values are not the same; then tensile strain can be produced in any of the three directions. This tensile strain can have enough value for crack propagation. Noticing this tensile strain, we can explain these phenomena that have been difficult to explain.

As fracture phenomena of hard and brittle materials by compression, there are some papers that reported crack initiation parallel to the direction of compression. For example, a cylinder specimen made from ball bearing steel rarely fractures vertically by compression (Muro¹⁶⁾), or a cylinder specimen made from marble fractures circumferentially by lateral compression (Sato et al.¹⁷⁾). Vertical fracture of a knock pin of a cold forging tool by fatigue was also reported (Hamatani¹⁸⁾). In these papers, the mechanism of crack propagation was not mentioned, but it may be considered that the cracking is due to tensile strain, as pointed out by Muro⁹⁾. Since papers are few that reported fatigue crack propagation by tensile strain using a method

other than rolling contact fatigue, such experiments are expected at present.

5. Conclusion

So far, as the mechanism of rolling contact fatigue, orthogonal shear stress acting parallel to the surface is considered to be the controlling stress for crack initiation and propagation. However, in failure analyses of rolling element bearings, there are some cases that cannot be explained by the orthogonal shear stress. In particular, they are phenomena in which a crack propagates deeply into the depth direction, such as through fracture of an inner ring under fitting stress. Contact stress is compressive in three axes, but the values are different; then strain can be tensile in the direction at a right angle to the maximum-compression stress direction. We consider that the crack propagates by this tensile strain. When contact stress is small, a crack, produced by some cause, can propagate by this elastic tensile strain. When contact stress is large, residual tensile strain is produced by plastic deformation and this residual tensile strain can also influence the crack propagation.

REFERENCES

- 1) Zwirlein, O. and Schlicht, H. (1982), "Rolling Contact Fatigue Mechanism-Accelerated Testing Versus Field Performance," ASTM STP 771, p 358.
- 2) Voskamp, A. P. and Hollox, G. E. (1988), "Failsafe Rating of Ball Bearing Components," ASTM STP 987, p 102.
- 3) Voskamp, A. P. (1997), "Microstructural Changes during Rolling Contact Fatigue," Ph. D. Thesis, Delft University of Technology, Delft, p 184.
- 4) Harris, T. A. and McCool, J. I. (1995), "On the Accuracy of Rolling Bearing Fatigue Life Prediction," ASME 95-TRIB-31.
- 5) Zaretsky, E. V., Poplawski, J. V. and Peters, S. M. (1996), "Comparison of Life Theories for Rolling-Element Bearings," STLE, 39, p 237.
- 6) Lyman, J. (1967), "Reversing Normal Strains Produced by Rolling Contact Load," ASME J. Lubr. Technol., 89, p 76.
- 7) Muro, H. and Yamamoto, T. (1996), "Tensile Strain Theory as a Unified Hypothesis for Various Rolling Contact Fatigue Failures such as Flaking, Edge Flaking, Pitting and Spalling (in Japanese)," in Proc. of JAST Tribology Conference, Kitakyushu, p 25.
- 8) Muro, H. and Yamamoto, T. (1995), "Simulation of Pitting and Spalling in Rolling Contact Fatigue Based

- upon Tensile Strain Theory for Crack Propagation," in Proc. International Tribology Conference, Yokohama, p 1327.
- 9) Muro, H. (1993), "Another View for Crack Growth in Rolling Contact Fatigue-Residual Tensile Strain Theory (in Japanese)," Preprint of Symposium on Rolling Contact Fatigue, p 31.
- 10) Merwin, J. E. and Johnson, K. L. (1963), "An Analysis of Plastic Deformation in Rolling Contact," Proc. IMechE, 177, p 676.
- 11) Muro, H., Tsushima, N. and Nagafuchi, M. (1975), "Initiation and Propagation of Surface Cracks in Rolling Fatigue of High Hardness Steel," Wear, 35, p 261.
- 12) Tamada, K., Tanaka, H. (1996), "Occurrence of Brittle Flaking on Bearings Used for Automotive Electrical Instrument and Auxiliary Devices," Wear, 199, p 245.
- 13) Tsushima, N., Nakashima, H. and Muro, H. (1970), "Fracture Toughness of Ball Bearing Steel and Its Application to Bearing Failure Analysis," J. Jpn. Soc. Fract. Mat., 5, p 75.
- 14) Maeda, K. and Tsushima, N. (1986), "Influence of Preexisting Residual Stress on Rolling Contact Fatigue Life," International Conference on Residual Stress, p 899.
- 15) Maeda, K., Nakashima, H. and Tsushima, N. (1992), "The Influence of Residual Stress in Radial Direction upon Rolling Contact Fatigue Life," International Conference on Residual Stress, ICRS-3, p 1371.
- 16) Muro, H. (1953), "Considerations on Strength of Quenched Ball Bearing Steel (in Japanese)," NTN Bearing Eng., 3, p 286.
- 17) Sato, Y., Miyauchi, S. and Mori, T. (1977), "Disking of Brittle Materials with Lateral Fluid Pressure (in Japanese)," J. Mat. Sci. Soci. Jpn., 14, p 280.
- 18) Hamatani, T. (1968), "Fractures and Countermeasures of Cold Forging Tools (in Japanese)," Metal Mat., 8, 7, p 54.

Appendix: Calculation Program of Residual Stress by MURO

Residual stress and strain calculations in this article were performed using Muro's program⁹⁾. Here Muro's calculation is briefly described.

We assume that the stress distribution along the rolling direction from $x = -2b$ to $+2b$ i. e., at 41 points, $x = X_1, X_2, \dots, X_{41}$ apart from each other with $0.1b$ distance for a given depth is

$$\begin{aligned} & X_1 (\sigma_{x1}, \sigma_{y1}, \sigma_{z1}, \tau_{xz1}, \tau_{yz1}, \tau_{xy1}), \\ & X_1 (\sigma_{x2}, \sigma_{y2}, \sigma_{z2}, \tau_{xz2}, \tau_{yz2}, \tau_{xy2}), \\ & \dots \\ & X_n (\sigma_{xn}, \sigma_{yn}, \sigma_{zn}, \tau_{xzn}, \tau_{yzn}, \tau_{xyn}), \\ & \dots \\ & X_{41} (\sigma_{x41}, \sigma_{y41}, \sigma_{z41}, \tau_{xz41}, \tau_{yz41}, \tau_{xy41}) \end{aligned}$$

where $\sigma_x, \sigma_y,$ and σ_z are normal stresses in $x, y,$ and z directions, respectively, and $\tau_{xz}, \tau_{yz},$ and τ_{xy} are shear stresses on $xz, yz,$ and xy planes, respectively. Then the von Mises equivalent stress σ_M at a point X_n is

$$\sigma_{Mn} = \{ [(\sigma_{xn} - \sigma_{yn})^2 + (\sigma_{yn} - \sigma_{zn})^2 + (\sigma_{zn} - \sigma_{xn})^2 + 6(\tau_{xzn}^2 + \tau_{yzn}^2 + \tau_{xyn}^2)] \div 2 \}^{1/2}$$

Then we assume that during rolling contact, at a given point, contact stresses P_1, P_2, \dots, P_{41} are successively applied; here P_1, P_2, \dots, P_{41} correspond to the stresses of X_1, X_2, \dots, X_{41} , respectively.

Stresses σ_{xn}, σ_{yn} and σ_{zn} at a given point are divided into respective elastic deviatoric stresses s_{xn}, s_{yn}, s_{zn} , and hydrostatic pressure s_n . Thus, $\sigma_{xn} = s_{xn} + s_n, \sigma_{yn} = s_{yn} + s_n, \sigma_{zn} = s_{zn} + s_n$, where $s_n = (\sigma_{xn} + \sigma_{yn} + \sigma_{zn})/3$. Therefore, $s_{xn} = \sigma_{xn} - s_n, s_{yn} = \sigma_{yn} - s_n, s_{zn} = \sigma_{zn} - s_n$. Then we assume that, if σ_{Mn} is greater than $\sqrt{3}$, elastic deviatoric stresses s_{xn}, s_{yn}, s_{zn} and shear stresses $\tau_{xzn}, \tau_{yzn}, \tau_{xyn}$ change by plastic deformation, depending on the value of σ_{Mn} , to $s_{xn} \times \sqrt{3}/\sigma_{Mn}, s_{yn} \times \sqrt{3}/\sigma_{Mn}, \dots, \tau_{xyn} \times \sqrt{3}/\sigma_{Mn}$. Residual stress is the difference between plastic deviatoric stress and elastic deviatoric stress.

Then, at a given point, when applied with a stress P_1 , if σ_{M1} is greater than $\sqrt{3}$, residual stress is created and each residual stress RS_{x1}, \dots, RS_{xy1} is calculated as follows:

$$\begin{aligned} RS_{x1} &= s_{x1}' - s_{x1} = s_{x1} \times (\sqrt{3}/\sigma_{M1}) - s_{x1} \dots\dots\dots [A1] \\ RS_{y1} &= s_{y1}' - s_{y1} = s_{y1} \times (\sqrt{3}/\sigma_{M1}) - s_{y1} \dots\dots\dots [A2] \\ RS_{z1} &= s_{z1}' - s_{z1} = s_{z1} \times (\sqrt{3}/\sigma_{M1}) - s_{z1} \dots\dots\dots [A3] \\ RS_{xz1} &= \tau_{xz1}' - \tau_{xz1} = \tau_{xz1} \times (\sqrt{3}/\sigma_{M1}) - \tau_{xz1} \dots\dots\dots [A4] \\ RS_{yz1} &= \tau_{yz1}' - \tau_{yz1} = \tau_{yz1} \times (\sqrt{3}/\sigma_{M1}) - \tau_{yz1} \dots\dots\dots [A5] \\ RS_{xy1} &= \tau_{xy1}' - \tau_{xy1} = \tau_{xy1} \times (\sqrt{3}/\sigma_{M1}) - \tau_{xy1} \dots\dots\dots [A6] \end{aligned}$$

where $s_{x1}, s_{y2}, \dots, \tau_{xy1}$ are elastic deviatoric stresses and $s_{x1}', s_{y1}', \dots, \tau_{xy1}'$ are plastic deviatoric stresses. $RS_{x1}, RS_{y1}, \dots, \tau_{xy1}$ are added to $\sigma_{x1}, \sigma_{y1}, \dots, \tau_{xy1}$, respectively, and if this new σ_{M1} is greater than $\sqrt{3}$, calculation of Eqs. [A1]–[A6] is repeated until new σ_{M1} becomes smaller than $\sqrt{3}$.

When the next stress P_2 is applied, those residual stresses RS_{x1}, \dots, RS_{xy1} , which have been created by Eqs. [A1]–[A6] are added to the stresses of P_2 , and another residual stress is created as in Eqs. [A7]–[A12] if $\sigma_{M2} > \sqrt{3}$:

$$\begin{aligned} RS_{x2} &= s_{x2}' - s_{x2} = s_{x2} \times (\sqrt{3}/\sigma_{M2}) - s_{x2} \dots\dots\dots [A7] \\ RS_{y2} &= s_{y2}' - s_{y2} = s_{y2} \times (\sqrt{3}/\sigma_{M2}) - s_{y2} \dots\dots\dots [A8] \\ RS_{z2} &= s_{z2}' - s_{z2} = s_{z2} \times (\sqrt{3}/\sigma_{M2}) - s_{z2} \dots\dots\dots [A9] \\ RS_{xz2} &= \tau_{xz2}' - \tau_{xz2} = \tau_{xz2} \times (\sqrt{3}/\sigma_{M2}) - \tau_{xz2} \dots\dots\dots [A10] \\ RS_{yz2} &= \tau_{yz2}' - \tau_{yz2} = \tau_{yz2} \times (\sqrt{3}/\sigma_{M2}) - \tau_{yz2} \dots\dots\dots [A11] \\ RS_{xy2} &= \tau_{xy2}' - \tau_{xy2} = \tau_{xy2} \times (\sqrt{3}/\sigma_{M2}) - \tau_{xy2} \dots\dots\dots [A12] \end{aligned}$$

After the final stress P_{41} is applied, created residual stresses are $RS_{x41}, RS_{y41}, RS_{z41}, RS_{xz41}, RS_{yz41},$ and RS_{xy41} .

Until this procedure, the method is almost the same as Merwin and Johnson's¹⁰⁾ except for the plastic deviatoric stress equation. Johnson used Prandtl-Reuss incremental theory for obtaining plastic deviatoric stress, which requires solution of differential equations. Solving differential equations led to considerable scatter of calculated values. Therefore, Muro used the simple method of multiplying the elastic deviatoric stress by a ratio of $\sqrt{3}/\sigma_M$ by the elastic deviatoric stress to obtain the plastic deviatoric stress.

According to Johnson, after unloading, the residual stress in the depth direction RS_{z41} is converted to RS_{x41} and RS_{y41} in the x and y directions by using the following equations, because no residual stress exists in the depth direction, keeping the strains in x and y axes the same:

$$\begin{aligned} (RS_{x41}) &= RS_{x41} - RS_{z41} \times \nu / (1 - \nu) \dots\dots\dots [A13] \\ (RS_{y41}) &= RS_{y41} - RS_{z41} \times \nu / (1 - \nu) \dots\dots\dots [A14] \\ (RS_{z41}) &= 0 \dots\dots\dots [A15] \end{aligned}$$

where $RS_{x41}, RS_{y41},$ and RS_{z41} are new residual stresses after conversion, and ν is Poisson's ratio. Residual strains are calculated from residual stresses.

Different from Johnson, Muro's program does not use this conversion of Eqs. [A13] and [A14] for the next loading, while using Eq. [A15]. In that case, it may deviate a little from theoretical values. When Eqs. [A13] and [A14] were used, calculated residual stresses were scattered significantly between values at a given loading cycle and the next loading cycle. Because RS_{x41} and RS_{y41} are negative and RS_{z41} is positive in Eqs. [A13] and [A14], not using Eqs. [A13] and [A14] means that smaller residual compressive stresses are given for the next loading. This stabilizes the residual stress calculation.

Author's Comment

It is very important for the simulation of a phenomenon that the calculating value asymptotically converges to one value. Plastic deformation includes a wide variety of many factors such as yield point, work hardening, change of contact stress due to plastic deformation, material flow, creation of residual stress, and loading cycles. Therefore, it is very difficult to express it in an exact formulation. The author thinks that Muro's residual stress calculation method used in this article can produce reasonable values similar to the actual value as stated in the text (compare **Table 4** and **Fig. 2**).

There may be other methods to calculate residual stress by rolling contact, such as the finite element method. However, as just mentioned, it is not easy to simulate exactly a phenomenon that is affected by many factors even if we used a precise tool. Muro's program can be performed on an ordinary personal computer. In this meaning, the author thinks such a program is very useful.



Author who gets Hunt Award from STLE President, D. McCoy

Photo of author



Noriyuki TSUSHIMA

Former Bearing Engineering
R&D Center

The 2006 Japan Society of Mechanical Engineers Young Engineers Award

Logarithmic Profiles of Rollers in Roller Bearings
and Optimization of the Profiles*Hiroki FUJIWARA**
Tatsuo KAWASE**

When a bearing roller is in contact with raceways, excessive pressure peaks occur at the ends of the contact rectangles. This is called edge loading. Roller and/or raceway profiles are usually crowned to prevent edge loads. Lundberg developed a logarithmic function for a crowned profile. The profile gives an axially uniform pressure distribution. Johns-Gohar improved the function for the convenience of manufacturing. However, the Johns-Gohar profile yields edge loading when the roller is tilted. In addition, the profile allows no straight portion on the roller surface although it is desirable to have a flat region from the viewpoint of machining. In this study, we modified the Johns-Gohar logarithmic function to exclude edge loading even when the roller is tilted, allowing a flat region. Three parameters, K_1 , K_2 and z_m , are introduced into the Johns-Gohar function. K_1 is coefficient of load, K_2 is ratio of crowning length to effective contact length, and z_m is crown drop at edge of effective contact length zone. In addition, a mathematical optimization method is used to efficiently determine a set of the parameters. An optimization problem is considered to minimize the maximum contact pressure P_{max} , or to maximize the rolling fatigue life L_{10} . A Rosenbrock method is also adopted as the optimization algorithm. This method requires no evaluation of gradients of the objective function. Pressure distribution is calculated by making use of a multilevel method. Some examples are demonstrated to verify the proposed method for both P_{max} and L_{10} .

1. Introduction

It is known that when a cylindrical surface or conical surface comes in contact, concentrated stress occurs at the end portion of the contact with the resultant contact pressure becoming excessive. This excessive contact pressure at the end portions is called edge stress. In a common roller bearing the roller rolling surface and/or the raceway surface of the race is crowned to avoid edge stress. Fig. 1 schematically shows a cylindrical roller bearing whose roller is crowned. The amount of decrease in the radius generated by crowning is called the drop.

Shapes of crowning include a straight line, a single circular arc or a combination of multiple circular arcs. However, Lundberg worked out a shape of crowning expressed in a logarithmic function (hereinafter referred to as logarithmic crowning)¹⁾. When a Lundberg curve is used, the distribution of contact

pressure can be made axially uniform. However, this curve has an infinite drop at the end of the effective contact length.

Lundberg gives a finite value as an approximation to the drop at the end. However, this method has its disadvantageous in that the shape becomes discontinuous depending on design conditions. Johns-Gohar presented a logarithmic functional formula obtained by improving Lundberg's method.²⁾

Incidentally, the housing and the shaft of a roller bearing are not exactly parallel to each other, with a certain misalignment present. In addition, the misalignment varies depending on the deflection of the shaft caused by the loading condition. Under these conditions, the roller rotates about the x-axis as shown in Fig. 1 and slants against the inner or outer ring; this is called tilt. In the Johns-Gohar curve, the tilt of a roller causes edge stress to occur.

Reusner states that forming a crowned part in a

*This paper is reprinted from the original paper (in Japanese) carried in the Proceedings of the Japan Society of Mechanical Engineers Part C, Vol.72 (2006), pp.3022 - 3029

**Elemental Technological R&D Center

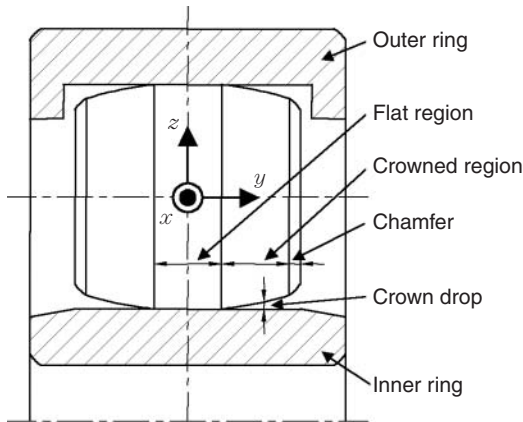


Fig. 1 Schematic drawing of a crowned roller in a cylindrical roller bearing

logarithmic shape prevents edge stress from occurring even under the presence of misalignment, resulting in a long service life³⁾. However, he does not show the specific shapes.

Takata et al. propose a crowning shape formed by combining Lundberg's logarithmic curve and circular arcs that brings a long service life under the presence of misalignment⁴⁾. This method has a drawback of complicated calculation that express the amount of crowning corresponding to misalignment by means circular arc, which is different than that of Lundberg's contact theory.

Paying attention to inner stress, Kamamoto et al. present a functional formula that gives an optimum shape⁵⁾. In other words, according to their theory, when Mises' equivalent stress or Tresca's equivalent stress appear near the contact area between the roller and the race, the stress will become axially uniform, which will minimize the damage the material undergoes as well as elongate bearing life. However, the functional formula that Kamamoto et al. has given to represent crowning curves does not take into account the effect of misalignment.

Urata has proposed a crowning shape formed by combining two or more circular arcs whose curvatures diminish as they move from the center to the end of the roller⁶⁾. Although he shows the crowning technique, edge stress does not appear in the crowning shape even under the presence of misalignment; the design method does not take misalignment into consideration, with tolerable amount of misalignment not made clear.

In addition, all of the reports above do not give detailed descriptions of the methods for optimum crowning design. The purpose of this report is to propose a logarithmic functional formula that can be

designed easily and to give the technique of optimizing it. To be more specific, we propose a design technique, based on improving Johns-Gohar's equation that will prevent edge stress due to misalignment. A functional formula is introduced in which the degree of freedom is improved by introducing three design parameters into Johns-Gohar's equation. Using this formula, one can set a straight section of an arbitrary length in the contact area. In addition, these parameters can be optimized through the use of a mathematical optimization method, which is shown below.

2. Johns-Gohar's logarithmic functional formula and its improvement

Johns-Gohar improved Lundberg's formula, showing the following equation²⁾:

$$z(y) = \frac{2Q}{\pi l E'} \ln \frac{1}{1 - (1 - 0.3033b/a) (2y/l)^2} \dots (1)$$

where

a : 1/2 of the effective contact length

b : Half width of contact

E' : Equivalent Young's modulus $\left(= \frac{E}{1 - \nu^2} \right)$

E : Young's modulus

ν : Poisson's ratio

l : Effective contact length

Q : Load

y : Position in the axial direction

$z(y)$: Drop at the position in the axial direction y

However, when this equation is applied, carrying out the calculation using the technique to be described later results in edge stress occasionally. This trend becomes more remarkable under the presence of misalignment. Providing a cylindrical roller or conical roller with a straight section may be desirable for machining or functional reasons; however, using this equation does not allow a straight section to be set up.

To solve this problem, three design parameters, K_1 , K_m , and z_m , are introduced into equation (1) written it into equation (2):

$$z(y) = \frac{2K_1Q}{\pi l E'} \times \ln \frac{1}{1 - \left(1 - 0.3033K_m \frac{b}{a} \right) \left\{ \frac{y - (a - y_m)}{l/2} \right\}^2} \quad (2)$$

where y_m denotes the length of the straight section and is given by

$$y_m = \frac{1}{2} \sqrt{\frac{1 - \exp\left(-z_m \frac{\pi l E'}{2K_1 Q}\right)}{1 - 0.3033 K_m b/a}} \dots\dots\dots (3)$$

As described above, a straight section is set up on the roller of a cylindrical roller bearing in some cases. If equation (3) is used, the length of crowning y_m can be established by specifying K_1 , K_m , and z_m ; however, directly giving y_m as a design parameter is more convenient. Therefore, let us determine K_m on the basis of equation (3) by substituting K_m into equation (2), which gives

$$z(y) = \frac{2K_1 Q}{\pi l E'} \times \ln \frac{1}{1 - \left\{1 - \exp\left(-\frac{z_m \pi l E'}{2K_1 Q}\right)\right\} \left\{\frac{y - (a - y_m)}{y_m}\right\}^2} \quad (4)$$

Further, defining K_2 as shown below

$$y_m = K_2 a$$

which gives the following equation:

$$z(y) = A \ln \frac{1}{1 - \left\{1 - \exp\left(-\frac{z_m}{A}\right)\right\} \left(\frac{y - a}{K_2 a} + 1\right)^2} \dots (5)$$

where, $A = \frac{2K_1 Q}{\pi l E'}$

In this equation, the design parameters have the following meanings:

- K_1 : Multiple of Q
- K_2 : Ratio of the crowning length to a
- z_m : Drop at the end of the effective contact length

K_1 corresponds to the curvature of the crowned section geometrically. Fig. 2 shows the portion that each parameter represents and the corresponding shape.

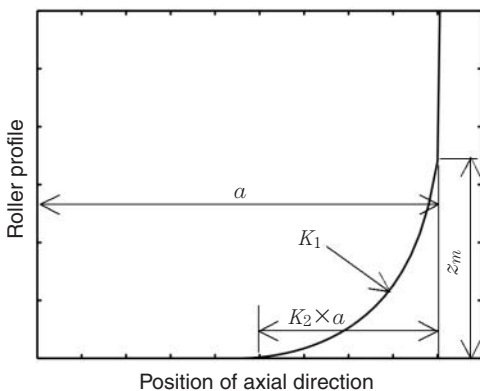


Fig. 2 Logarithmic profile parameters

Selecting these design parameters adequately makes it possible to design a logarithmically crowned shape that will not produce edge stress even if the roller is tilted.

3. Method of calculating contact pressure

Fig. 3 shows the schematic diagram of the cross section at the contact area. Pressure occurs at the area where two surfaces come in contact with each other and no pressure occurs where there is no contact. In other words, if the distance between the two surfaces is supposed to be $h(x, y)$, the following relationships are obtained:

$$\begin{aligned} h(x, y) > 0, p(x, y) = 0 & \text{ Non-contact area} \dots\dots (6) \\ h(x, y) = 0, p(x, y) > 0 & \text{ Contact area} \end{aligned}$$

When the elastic proximity amount between two bodies is given by $h_0 (< 0)$, the surface shape of a semi-infinite elastic body is given by $g(x, y)$ and the displacement of the surface of the semi-infinite elastic body is given by $u(x, y)$ then distance between two surfaces $h(x, y)$ can be expressed in the following equation:

$$h(x, y) = h_0 + g(x, y) + u(x, y) \dots\dots\dots (7)$$

The contact pressure $p(\eta, \zeta)$ and the displacement $u(x, y)$ are in a relationship given by the following equation

$$u(x, y) = \frac{2}{\pi E'} \int_{-\infty}^{\infty} \int_{-\infty}^{\infty} \frac{p(\eta, \zeta) d\eta d\zeta}{\sqrt{(x - \eta)^2 + (y - \zeta)^2}} \dots\dots (8)$$

In the above equation, (η, ζ) is the coordinate on the xy -plane. In other words, equation (8) means that the displacement at (x, y) is affected by the contact pressure p at all points and that the magnitude of the effect is inversely proportional to the distance between (x, y) and (η, ζ) .

In addition, since the surface integral of the contact

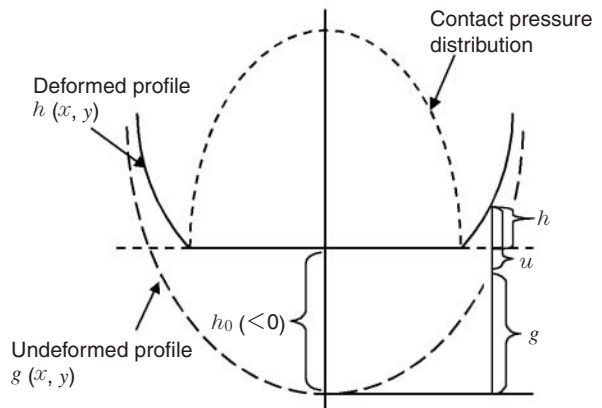


Fig. 3 Contact deformation and pressure distribution

pressure is equal to the normal load Q , the following equation holds:

$$Q = \int_{-\infty}^{\infty} \int_{-\infty}^{\infty} p(x, y) dx dy \dots\dots\dots (9)$$

The above simultaneous equations are solved numerically by means of the iteration method. The common iteration method has a drawback in that it is difficult for long-wavelength error components to converge against lattice spacing established in the space for which calculation is to be carried out. Furthermore, in the common calculation method, if the number of lattice points is set at n , the calculation of equation (8) will take a time on the order of $O(n^2)$. To handle this problem, the numerical calculation was made faster through the use of the multi-level method⁷⁾. The multi-level method is a high-speed arithmetic algorithm combining the multi-grid method that speeds up the convergence calculation of simultaneous equations by means of the iteration method and the multi-level multi-integration (MLMI) method that executes the double integration of equation (8) at a speed of $O(n \log n)$.

4. Contact pressure distribution on a logarithmically crowned roller

The contact between the cylindrical roller and the inner ring shown in Fig. 4 is considered. It is assumed that the roller alone is crowned. It is also assumed that both the roller and the inner ring are made of bearing steel. The calculation lattices are formed by dividing the system into 256 sections in the axial direction and the tangential direction into 32 sections.

Fig. 5 shows the relationship between the crowned shape and the contact pressure distribution for a tilt angle of 0 rad. When crowning is not provided, an extremely large edge stress of 10.7 GPa occurred at the end of the effective contact length of the roller.

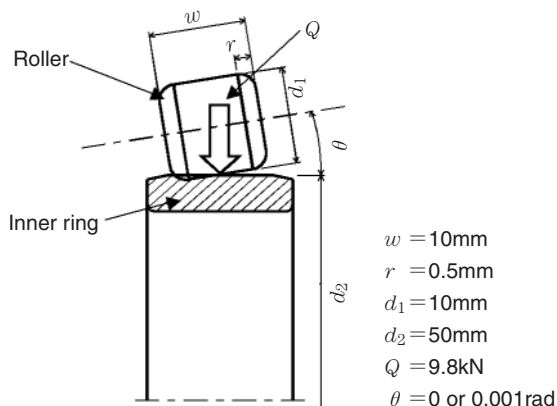


Fig. 4 Schematic drawing of a roller and an inner ring used in contact pressure calculation

Even on Johns-Gohar's curve, edge stress having a maximum value of 3.75 GPa has occurred. On Johns-Gohar's curve in the case of absence of crowning, the value of edge stress is reduced to 1/3. However, since the edge stress value depends on the size of calculation lattice, a simple comparison between values is not allowed. However, since calculation lattices of the same size are used in this case, a discussion on relative sizes does not pose a problem.

On the other hand, in the case of crowning according to equation (2), under the conditions of Fig. 4, if the conditions are

$$K_1 = 1, K_2 = 1, z_m = 12.7 \mu m$$

The same values as Johns-Gohar's curve is achieved. However, if the conditions are

$$K_1 = 1.4, K_2 = 1, z_m = 14 \mu m$$

edge stress does not occur.

Setting K_2 at 1 means providing the entire domain of the effective contact length with crowning. If the crowned domain is made into a domain half of "a" by setting K_2 at 0.5, the contact pressure distribution exhibits a decrease at the middle of the contact area and a slight increase at both ends. However, this increase in the contact pressure is not a spike-shaped increase in the contact pressure resulting from the contact of the intersection of the crowned part with the chamfer, thus differing from edge stress.

Fig. 6 shows the contact pressure distribution with the roller tilted by 0.001 rad. On Johns-Gohar's curve, the occurrence of edge stress is noted as in the case where the tilt angle is 0 rad.

Under the conditions of $K_1 = 1.4, K_2 = 0.5$, and $z_m = 14 \mu m$, edge stress did not occur, but under the condition of the tilt angle of 0.001 rad, edge stress occurred. Solve this problem by increasing z_m from 14 mm to 17 mm, which results in the conditions of $K_1 =$

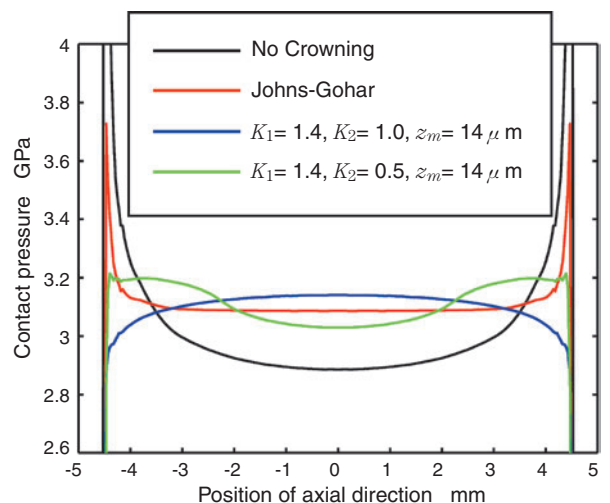


Fig. 5 Contact pressure distributions when the tilting angle is 0 rad

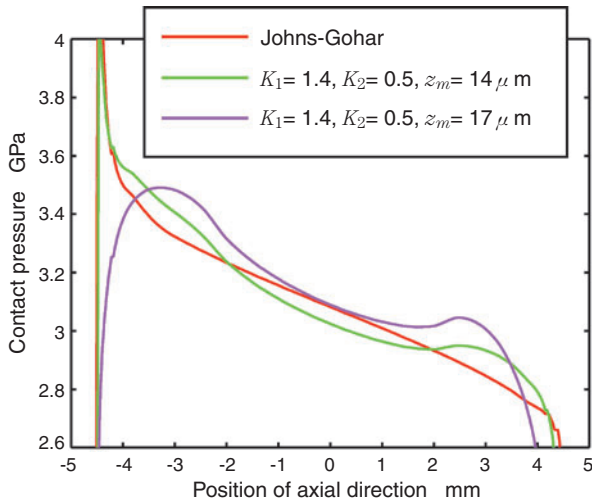


Fig. 6 Contact pressure distributions when the tilting angle is 0.001 rad

1.4, $K_2 = 0.5$, and $z_m = 17$ mm, and this prevents the edge stress from occurring.

5. Optimization of design parameters

5.1 Optimization algorithm

As described above, it is possible to decrease the maximum contact pressure by changing design parameters. However, it is difficult to give the optimum value by means of an analytical method. For this reason, a technique of optimizing design parameters by means of a computer is considered.

Various algorithms including the conjugate gradient method, annealing method and genetic algorithm are proposed as optimization algorithms. In solving this problem, for example, if the maximum contact pressure or rolling fatigue life is selected as the objective function it is impossible to analytically derive its derivative function with numerical differentiation accompanied by difficulty. For these reasons, we adopt the Rosenbrock method⁸⁾, a direct retrieval method. Its outline is as follows:

- (1) A directional vector is defined in the space of variables and the value of a variable is changed along the directional vector.
- (2) When a change in the variable improves the objective function, the change is accepted. If the objective function is degraded, the change is discarded.
- (3) If convergence occurs after repeating steps (1) and (2), the operation is finished. If not, the directional vector is modified and the operation goes back to step (1).

Not only the Rosenbrock method but also other optimization techniques have strong dependence on

the initial value in terms of the convergence of a solution. The convergence of a solution means the convergence solution itself and the amount of calculation required before the convergence solution is obtained. It is important to determine a favorable initial value in solving an optimization problem.

In this study, the initial value is determined in the following method: Not only the contact pressure but also the rolling fatigue life can be used as objective functions. In the following description, the maximum contact pressure P_{\max} is used as the objective function.

- (1) The limits of design parameters within which the initial values are retrieved and the number of values for each parameter within the limits are specified.
- (2) When numbers of values of K_1 , K_2 , and z_m are l , m , and n , ($l \times m \times n$) combinations of design parameters are defined. The calculation for the contact pressure is carried out for all combinations to determine P_{\max} .
- (3) The combination yielding the smallest P_{\max} is adopted as the initial value for optimization.

5.2 Example of optimization

In the following, an example of optimization calculation of the crowning of a cylindrical roller bearing is shown. When only the roller is crowned, the maximum contact pressure between the roller and the inner ring is greater than that between the roller and the outer ring. For this reason, when one considers the optimization of crowning, considering the contact between the roller and the inner ring suffices. It is assumed that a crowned roller is tilted by half the amount of misalignment against the inner ring under a misalignment condition.

In the following, the calculation example uses the geometrical shape and load condition shown in Fig. 4, and it is assumed that both the roller and the inner ring are made of bearing steel.

5.2.1 Case where the tilt angle is 0 rad

The optimization was carried out under the conditions shown in Table 1. Fig. 7 shows, in 3D contour lines, the relationship between the design parameters obtained by initial value retrieval and the

Table 1 Optimizing condition No. 1

Objective function	Maximum pressure
Roller tilting angle	0 rad
Initial value searching area of K_1	1 ~ 3
Initial value searching area of K_2	0 ~ 1
Initial value searching area of z_m	5 ~ 20 μ m

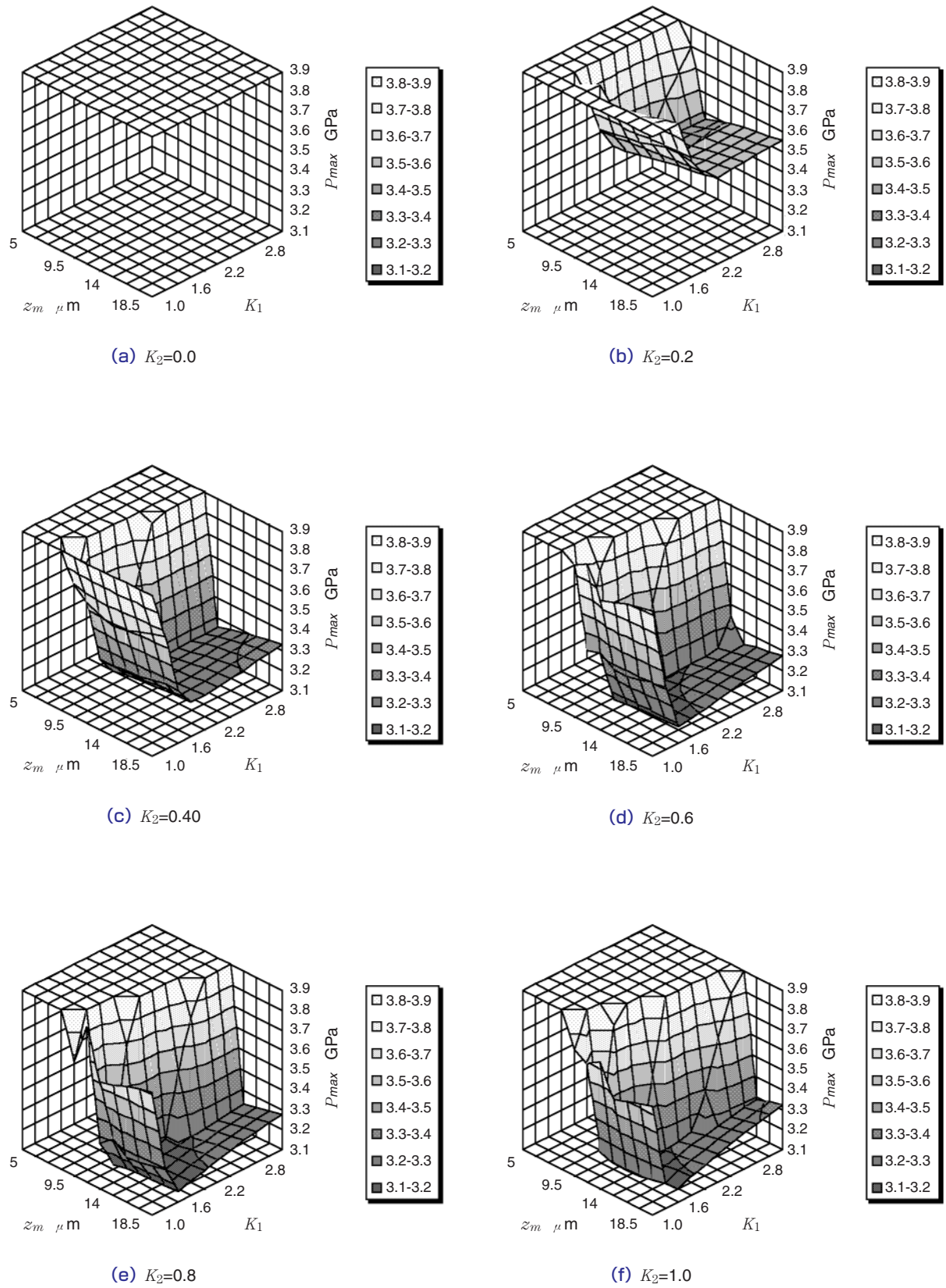


Fig. 7 Design parameters and maximum pressure under the optimizing condition No.1

maximum contact pressure. In **Figs.7 (a) to 7 (f)**, K_2 is changed in increments of 0.2 between 0 and 1. The individual graphs show the relationship among K_1 , z_m , and P_{max} for different K_2 values.

The best initial values are the following ones as shown in **Fig. 7 (e)**.

$$K_{10} = 1.4$$

$$K_{20} = 0.8$$

$$z_m = 12.5 \mu\text{m}$$

As a result of the optimization based on the Rosenbrock method, the optimum design parameters are obtained as shown below:

$$K_1 = 1.295$$

$$K_2 = 0.879$$

$$z_m = 12.684 \mu\text{m}$$

When a crowning operation is carried out using the optimum design parameters, the contact pressure distribution is almost uniform along the axis as shown in **Fig. 8**.

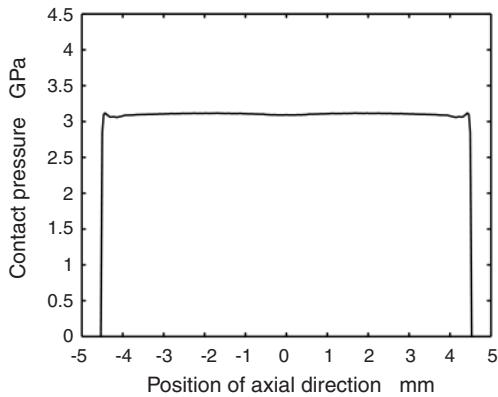


Fig. 8 Pressure distribution of the optimized profile under the condition No.1 ($K_1 = 1.295$, $K_2 = 0.879$, $z_m = 12.684 \text{ mm}$)

5. 2. 2 Case where the tilt angle is 0.001 rad

We consider a case where the roller was tilted and a straight section was provided. In other words, K_2 is fixed at 0.5 to be excluded from the objects to be optimized. The optimization conditions for this setting are shown in **Table 2**.

The best initial values are:

$$K_{10} = 2.8$$

$$z_{m0} = 16 \mu\text{m}$$

The best possible design parameter values are obtained through optimization.

$$K_1 = 2.779$$

$$z_{m0} = 16.253 \mu\text{m}$$

The contact pressure distribution then is as shown in **Fig. 9**.

The presence of a tilt causes the maximum contact pressure to occur at a negative position in the axial direction, and the provision of a straight section

Table 2 Optimizing condition No. 2

Objective function	Maximum pressure
Roller tilting angle	0.001 rad
Initial value searching area of K_1	2 ~ 4
Initial value searching area of z_m	10 ~ 30 μm

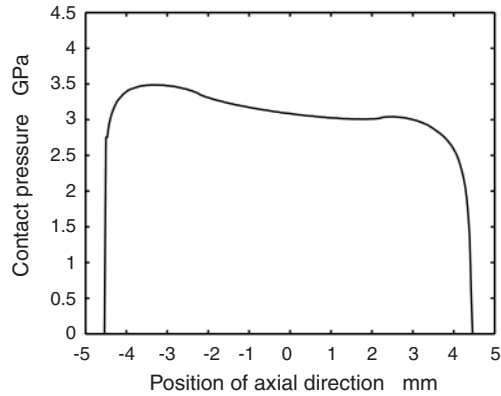


Fig. 9 Pressure distribution of the optimized profile under the condition No.2 ($K_1 = 2.779$, $K_2 = 0.5$, $z_m = 16.253 \text{ mm}$)

causes the contact pressure distribution in the middle to become concave.

In this way, this technique allows the optimum logarithmic crowning to be designed in cases where a tilt or straight section exists.

5. 2. 3 Case where life is taken as the objective function

The rolling fatigue life of the roller can be used as the objective function for the optimization. The life is calculated using Harris' method⁹⁾. **Table 3** shows the conditions for optimization.

The best initial values are:

$$K_{10} = 1.2$$

$$K_{20} = 0.9$$

$$z_m = 11 \mu\text{m}$$

The following values are obtained as the best possible design parameters through optimization:

$$K_1 = 1.065$$

$$K_2 = 0.982$$

$$z_m = 10.799 \mu\text{m}$$

Under the optimization conditions adopted here, edge stress is allowed to occur. The contact pressure distribution then is as shown in **Fig. 10** with edge stress occurring at both ends.

5. 2. 4 Shape formed as a result of logarithmic crowning

Fig. 11 shows the shape formed as a result of logarithmic crowning optimized under the conditions described above. Comparing "optimization conditions

Table 3 Optimizing condition No. 3

Objective function	Rolling fatigue life
Roller tilting angle	0 rad
Initial value searching area of K_1	1 ~ 3
Initial value searching area of K_2	0 ~ 1
Initial value searching area of z_m	5 ~ 20 μ m

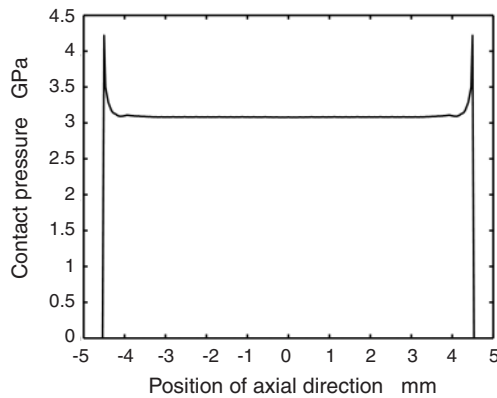


Fig. 10 Pressure distribution of the optimized profile under the condition No.3 ($K_1 = 1.065$, $K_2 = 0.982$, $z_m = 10.799$ mm)

1 (objective function: maximum contact pressure; tilt angle: 0 rad)" and "optimization conditions 3 (objective function: life; tilt angle: 0 rad)" reveals little difference between the shapes. However, when the life is taken as the objective function, edge stress occurs as shown in **Fig. 10**. **Fig. 7** shows that, with K_2 fixed at a value, the maximum contact pressure increases abruptly when K_1 or z_m becomes slightly smaller than the optimum point for the case where the maximum contact pressure is taken as the objective function. This increase in the maximum contact pressure is generated by the occurrence of edge stress. Qualitatively speaking, the greater the contact

pressure is, the shorter the life is; however, an increase in local contact pressure like edge stress has only a small effect according to Harris' method of calculating the life. For these reasons, whether edge stress occurs or not depends on which of the maximum contact pressure and life is adopted as the objective function for the optimization regardless of the similarity of the shape of rollers.

6. Conclusion

We made a proposition regarding a method of determining design parameters in the design of logarithmic crowning for roller bearings, by introducing the design parameters into a logarithmic crowning equation and using a numerical optimization method.

Specifically, we improved Johns-Gohar's functional formula to present a logarithmic crowning equation with an improved degree of design freedom. The design parameters introduced are the three that follow:

K_1 : Scale factor for design load, which affects the curvature of a crowned part in terms of geometry

K_2 : Ratio of the crowned part to the length from the home position to the chamfered part

z_m : Drop at the end of the effective contact length

K_2 may be defined at the time of designing the basic shape; in such a case, K_1 and z_m only are optimized.

The optimization condition is either the maximum contact pressure at its lowest or the maximum life. The Rosenbrock method is used as the optimization algorithm. By numerically optimizing these design parameters, the optimum logarithmic crowning for a roller bearing can be obtained even under the presence of misalignment.

In the following, the features of this technique are

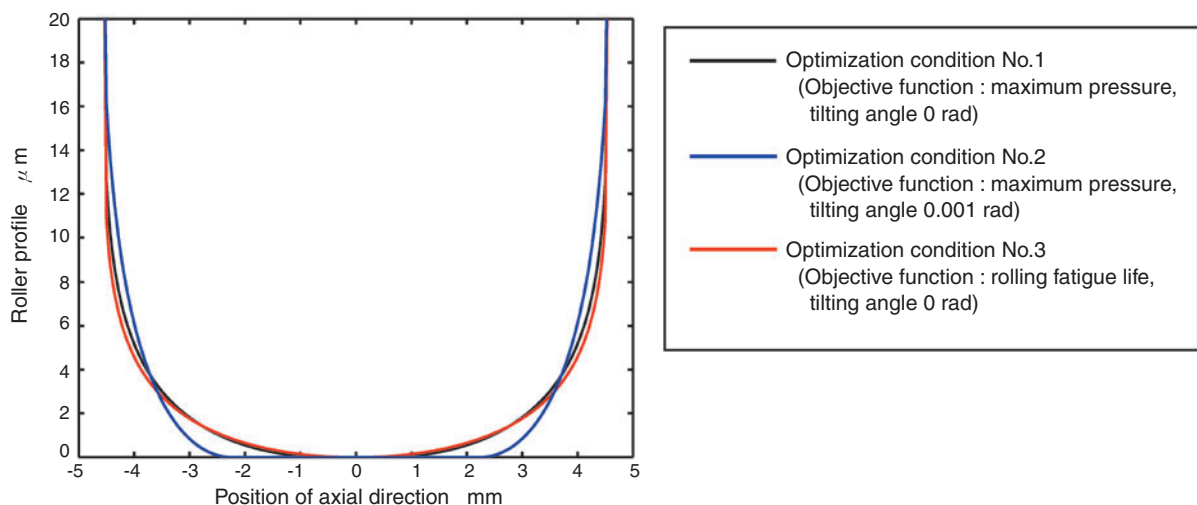


Fig. 11 Optimized roller profiles under the conditions No. 1 to 3

summarized:

- (1) In considering misalignment in the design of logarithmic crowning, the effect of the misalignment is treated independently of the logarithmic function. Contrary to this, this technique treats the effect as a design parameter and incorporates it into the logarithmic equation.
- (2) With the three design parameters corresponding to the crowning shape, the features of a crowned shape can be expressed by the parameter values only.
- (3) Incorporating the straight section into a design parameter enables the straight section to be combined with logarithmic crowning easily and with a greater degree of freedom.
- (4) A new design technique is proposed of incorporating the numerical value optimization technique into logarithmic crowning design.

References

- 1) Lundberg, G., Elastic Contact Between Two Semi-Infinite Bodies, *Forschung auf den Gebiete des Ingenieurwesen*, 5(1939), pp.201-211. (in German)
- 2) Johns, P. M. and Gohar, R., Roller bearings under radial and eccentric loads, *Tribology International*, 14(1981), pp.131-136.
- 3) Reusner, H., The logarithmic roller profile — the key to superior performance of cylindrical and taper roller bearings, *Ball Bearing Journal*, 230(1987), pp.2-10.
- 4) Takata, H. et al., Experimental Study of Fatigue Life of Profiled Roller Bearings, *NSK Technical Journal*, 653(1992), pp.1-7. (in Japanese)
- 5) Kamamoto, S. et al., Research on Crowning Profile to Obtain The Maximum Load Carrying Capacity for Roller Bearings, *KOYO Engineering Journal*, 159(2001), pp.44-51.
- 6) Urata, S., Investigation of Optimum Crowning Profile of Cylindrical Roller Bearings Part 2, *FUJIKOSHI Engineering Review*, 56(2000), pp.14-23. (in Japanese)
- 7) Venner, C. H. and Lubrecht, A. A., *Tribology Series, 37 Multilevel Methods in Lubrication*, (2000), Elsevier Science B. V.
- 8) Bazarra, M. S. et al., *Nonlinear Programming*, (1993), p.291, John Wiley & Sons.
- 9) Harris, T. A., *Rolling Bearing Analysis*, Forth Edition, (2000), pp.728-729, John Wiley & Sons.

Photos of authors



Hiroki FUJIWARA

Elemental Technological
R&D Center



Tatsuo KAWASE

Elemental Technological
R&D Center

Run-out Analysis for Rolling Element Bearing

Tomoya SAKAGUCHI*

1. Introduction

This is a commentary on rotational accuracy analysis of rolling bearings. The commentary introduces an example of study on effects of shape errors in balls and inner and outer rings and of angular intervals between balls on rotational deflections in the three axial directions of the inner ring; the study is based on quasi-static analysis that takes into consideration translational displacement of balls and inner rings on the radial plane in ball bearings. The commentary also presents the result of study on rotational accuracy.

This commentary was carried in Journal of Japan Society for Design Engineering, Vol.40, No.10, 2005. The Society commended the commentary as the most interesting among the articles other than treatises carried in the journal in the year. The analytical technique introduced in the article is as described in our Review No.69.

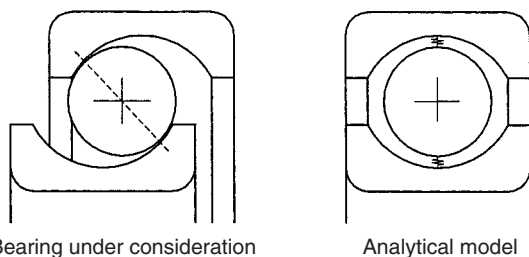


Fig. 1 Sections of an actual ball bearing with an axial load and the simplified model

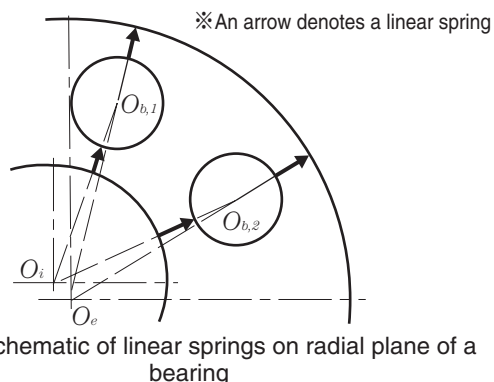


Fig. 2 Schematic of linear springs on radial plane of a bearing

2. Summary of the commentary

To analyze effects of errors in geometries of bearing components and of angular intervals of balls on rotational accuracy of ball bearings, a simulation program was developed in which the contact force between a rolling body and the raceway surface is modeled by a linear spring on a radial plane (**Figs. 1 and 2**) and the angular position of balls can be arbitrarily set up.

Through experimental verification, the validity of this simulation was confirmed. In addition, the result of a study on the relationship between errors in the shape of components and the rotational accuracy revealed that the rotational accuracy deteriorates when raceway surface deviations from a perfect circle with waviness orders Z and $Z \pm 1$ exist, where Z denotes the number of balls.

When no misalignment exists under pure axial load, it is thought that the practically sufficient rotational accuracy of a ball bearing can be estimated. It is anticipated that, in future, technologies for analyzing rotational accuracy under radial loading will evolve with the aim of reducing noise of increasingly fast-rotating machines.

Photo of author



Tomoya SAKAGUCHI

Elemental Technological
R&D Center

The Fourth Monozukuri Parts Grand Prix, Incentive Award

Improving Rolling Contact Fatigue Life of Bearing Steels Through Grain Refinement "Development of the FA bearing"

Chikara OHKI*

Summary

Improvement in strength for iron-based materials through reinforcement by means of grain refinement according to Hall-Petch's law is well known, notably in the ferrite phase. It has already been confirmed that the same principle applies to austenite and martensite phases. In ferrite and austenite-based materials, grain refinement is relatively easy to perform with successful commercialization in the field of controlled rolling. On the other hand, it is difficult to put martensite-based materials like bearing materials, which need a quenching process in their heat treatment, to grain refinement. As for specific methods for grain refinement, two examples are the Grange method that is based on repeated quenching and the ausforming method, but there are also several others that can be listed. However, all of these processes need excessive man-hours, which is not a practical industry practice.

The FA treatment developed this time does not need a large amount of man-hours. Through the improvement of heat treatment the results are enhanced grain refinement, enhanced solid solution of nitrogen, and enhanced precipitation. Fig. 1 shows prior-austenite grains subjected to the standard heat treatment and the FA treatment. The steel type is SUJ2. Compared with the grain boundary after standard heat treatment, the grain boundary of FA treatment shows that the average grain size of prior-austenite grains has been reduced to about 5 μ m, which is half of the prior size. The FA-treated product

exhibited an improvement in breaking stress and indentation forming contact pressure (the maximum contact pressure that causes the residual indentation depth to reach 1/10000 of the diameter of the rolling element when it is pressed to the surface), which also increased the rolling fatigue life. Table 1 shows an overview of the performance.

It is certain that the development of structural metal materials will advance toward grain refinement, and this technology is expected to be unfolded broadly. By considering future world trends, it can be said that it is not desirable to increase steel strength by adding alloy elements or through inefficient manufacturing processes. Our goal is to reduce the environmental impact and conserve energy through widespread use of FA-treated bearings.

Table 1 A summary of characteristics

	Ratio of a characteristic of an FA-treated product to that of a conventional carbo-nitriding-treated one*1
Breaking stress	1.2
Indentation forming contact pressure*2	1.1
Change in dimensions due to aging*3	0.7
Lubrication life with mixed foreign bodies*4	2

*1 Referred to a characteristic of a conventional carbo-nitriding-treated product set at 1

*2 Maximum contact pressure that causes the residual indentation depth to reach 1/10000 of the diameter of the rolling element when it is pressed to the surface

*3 A product showing a smaller value after having been held at 120°C for 2500 hours is a better one.

*4 Tapered bearing 30206; contact pressure: 2.5 GPa
Foreign bodies: One g/L of gas-atomized HV800 (50 μ m or smaller: 100-180 μ m = 9:1) mixed in the lubricant

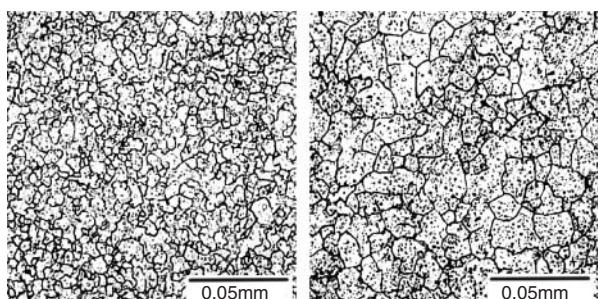


Fig. 1 Prior austenite grain boundary

Photo of author



Chikara OHKI

Elemental Technological R&D Center

Outstanding Prize, the 12th Advanced Display of the Year 2007

LCD Color Filter Repair System (NRS-3000 Series)

1. Introduction

In 1990, NTN commercialized devices to repair bridging defects on liquid crystal TFT (thin-film transistor) electrodes by laser-cutting them, making its way into the field of defect repair devices for FPDs (flat panel displays). Since then, NTN has accumulated a number of track records and many years of experience through the development of functions of applying ink on micro-domains stably and other functions of repairing defects.

Recently, NTN was given the ADY Outstanding Prize in recognition of its contribution to energy conservation in FPD manufacturing processes. NTN's contribution resulted from its efforts to develop an ink application mechanism that enables the quality of repair to be improved and repair tact time to be reduced and also from its efforts develop a function to automatically repair defects produced on color filters for liquid crystal display use.

This award is given to commend, by section of specialization, outstanding FPD-related devices sold in the past year. The color filter repair device was commended in the inspection, repair, and measurement section. **Photo** shows the appearance of the device. (Approximate dimensions of the device: 3 m in width × 4 m in depth × 3 m in height)



Photo Appearance of the device

2. Outline of the color filter repair device

In the manufacturing process of color filters for liquid crystal displays, clear defects (color dropout), opaque defects (mixed colors), and particle defects (sticking of dust) occur occasionally. A color filter repair device is intended for repairing such defects.

Clear defects are repaired by coating clear portions with ink having the same color as the original pixel color. Opaque defects are repaired by first cutting defective portions with YAG laser to change them into clear defects and then coating them with ink. Particle defects are repaired by first cutting defective portions with laser in the same way as in repairing opaque defects and then covering them with ink or

grinding them partially.

Equipped with an ink application mechanism that was greatly improved series NRS-3000, commended this time—shortens the repair tact time to one third of the time a conventional NTN device takes. In

addition, to achieve an improvement in the quality of repair, the tip of the application needle, used to apply ink, was specially processed to permit the quantity of ink application to be controlled in a range between several pico liters and several tens of pico liters (a pico liter is a trillionth of a liter) depending on the time during which a substrate remains in contact with the application needle. This enables us to respond to the recent requirement for ever increasing resolution for liquid crystal displays.

In addition, the repair process was considered to be difficult to automate and operators checked defects to determine repair conditions. However, NTN developed a unique image processing algorithm, being the first to achieve the automatization of the repair process in the industry. This innovation has made it possible to remove an operator needed for each device in the conventional process.

3. Summary

In addition to the color filter repair device presented in this commentary, NTN has developed and expanded a number of repair devices for FPDs including defect repair devices for plasma displays. Recently, new displays such as SEDs (surface-conduction electron-emitter displays), organic EL (organic electroluminescence) displays, and electronic paper are being developed rapidly and put into mass production. NTN will continue its effort in developing devices that will contribute to the progress of such new displays.

Photo of author



Akihiro YAMANAKA
Product Engineering Department
Precision Equipment Division

Akihiro YAMANAKA*

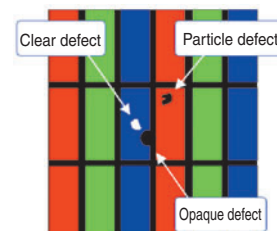
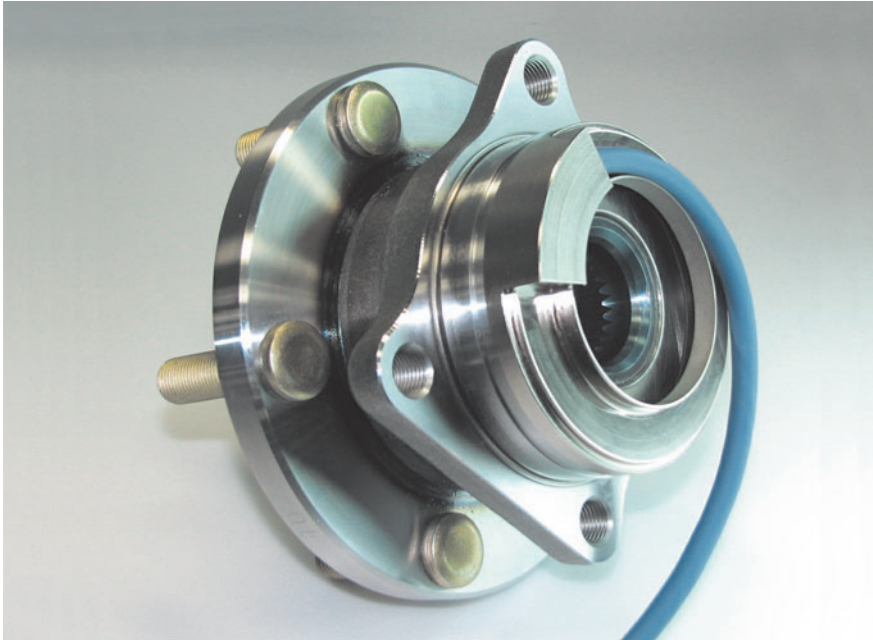


Fig. Defects in a CF panel



Hub bearing equipped with high resolution rotational sensor

Contributing to better vehicle safety control



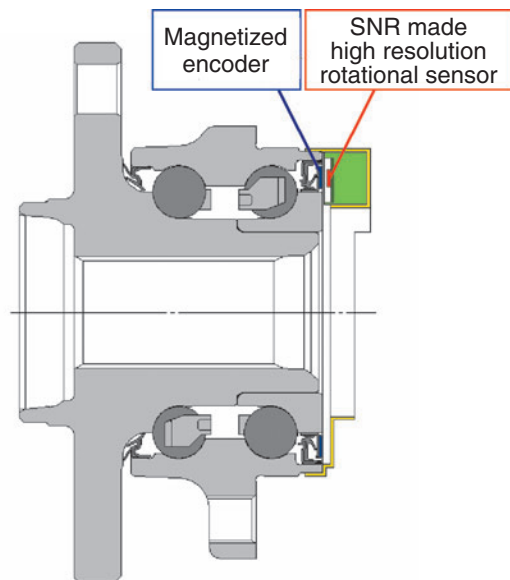
Features

- (1) High resolution rotational signal (40 times higher relative to conventional types; magnetic encoder is the same as conventional types)
- (2) A & B phase pulse output allows detection of rotational direction
- (3) External dimensions are the same as conventional hub bearings and can be applied to both driven and non-driven wheels

Applications

- Hub bearings for passenger vehicle use

Construction



Environment-friendly roller bearing

Using **biodegradable materials** to make the cage, seal and grease, the new roller bearing reduces environmental loading after being discarded



Features

- (1) The biodegradability of the cage and seal is over 60%.
[A product eligible for a **Green Pla Mark**]
- (2) The biodegradability of the grease is over 60%.
[A product eligible for an **Eco Mark**]
- (3) Working temperature limits: -30 to 70°C
- (4) Allowable number of revolutions: dmn value: 350,000
(about the same as that of existing general-purpose products)

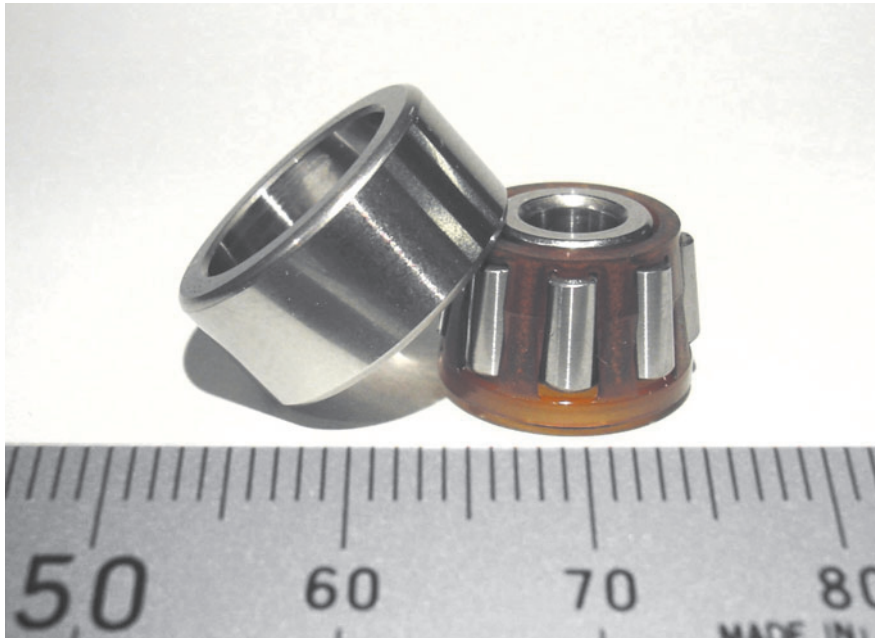
Construction

- The cage and seal are made up of a polyester-based biodegradable resin having improved strength and heat resistance.
- The grease is made up of a base oil composed of an ester-based synthetic oil having a 60% biodegradability.

- ※ **Green Pla Mark**: An official certification mark given to a biodegradable plastic product.
- ※ **Eco Mark**: An official certification mark given to a biodegradable material (other than plastics) or a commodity using such material.

World's smallest tapered roller bearing

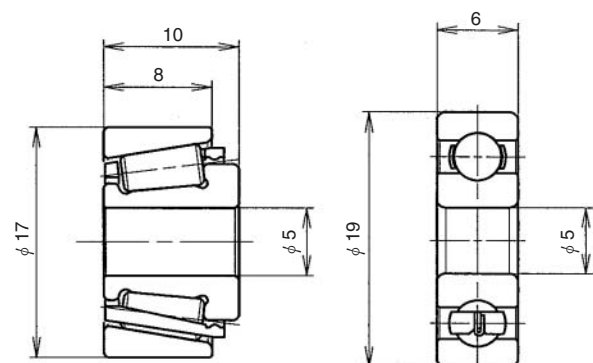
A tapered roller bearing with a **bearing inside diameter of five mm** achieves a longer life and higher rigidity than similar ball bearings



Features

- (1) **Tapered roller bearing with the world's smallest diameter**
Five-mm inside diameter ϕ 17-mm
outside diameter ϕ 10-mm width
- (2) **Longer life**
Fourteen-time longer life than that of similar ball bearings
- (3) **Higher rigidity**
Five-time greater axial rigidity than that of similar ball bearings

Construction

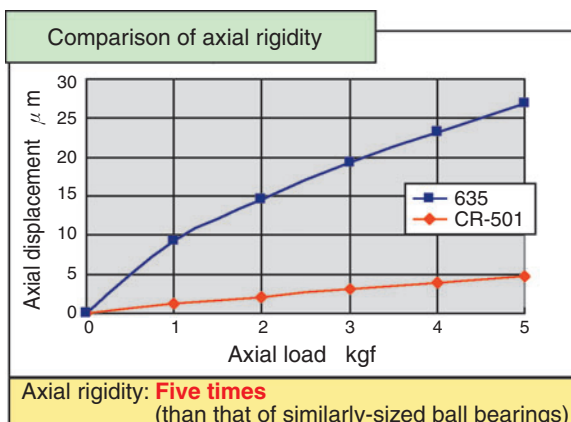


[Cross-section of the developed product]

[Cross-section of a similar ball bearing]

Applications

- Reducers, medical equipment, robot joints, and the like



MQCJ lubrication angular contact ball bearing

The world's highest speed angular contact ball bearing has been realized through the adoption of a new jet lubrication scheme equipped with inner ring cooling and a mechanism for best minimum quantity lubrication for the raceway



Features

- (1) High-speed operation at **the world's highest speed**
 - Constant pressure pre-load:
 d_{mN} value: 5 million
(90% increase in the conventional air/oil lubrication ratio)
 - Constant position pre-load:
 d_{mN} value: 3.6 million
(40% increase in the conventional air/oil lubrication ratio)
- (2) Power loss: on the same level as that of air/oil lubrication
- (3) Simplification of the oil supply / discharge system
The outer cylinder cooling oil serves also as the bearing lubrication oil.

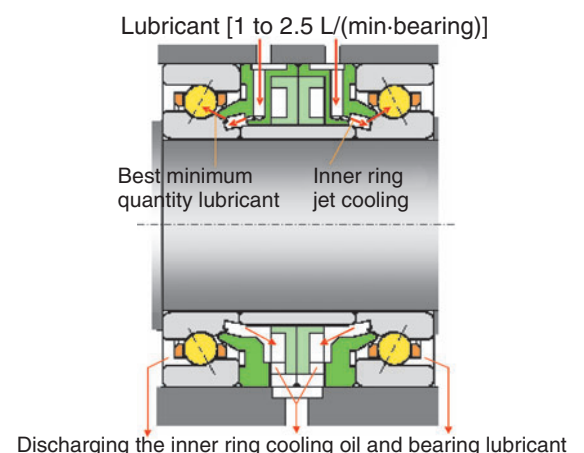
Applications

- Ultra-high-speed main spindle for machine tools (machining centers for die machining and aluminum machining)

*MQCJ stands for Minimum Quantity and Cooling Jet

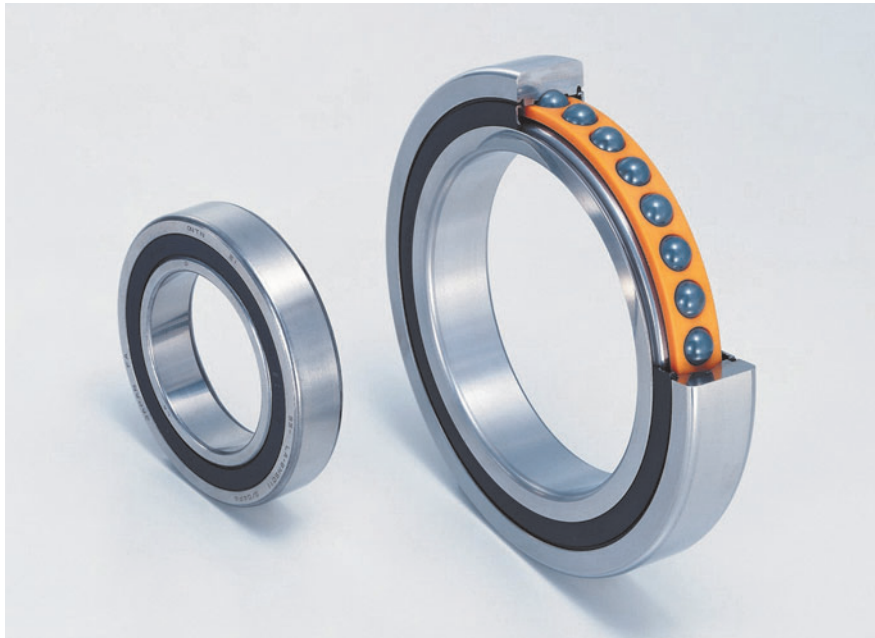
Construction (means of realization)

1. The adoption of inner ring cooling scoop grooves and special nozzle spacers has realized inner ring cooling and best lubrication.
2. Optimization of the bearing interior design has realized ultra-high speed and high rigidity.
3. Special inner/outer ring materials excel in durability under high-speed, high-contact-pressure operation.



Angular contact ball bearing with ultra-high-speed seal

The new grease SE-1 and optimization of internal design have realized ultra-high-speed operation at the world's highest level



Features

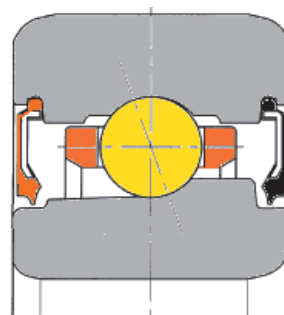
- (1) Angular contact ball bearing with seal having high-speed rotation performance at **the world's highest level**
 d_{mn} value: **1.7 million**; 20% improvement compared to the performance of conventional similar products
- (2) The bearing washing process before mounting and the grease filling process are not necessary.
- (3) External lubricant feeders are not necessary.

Applications

- Machining tool main spindle (machining centers and tapping machines)

Construction

1. Optimization of internal design
 ⇒High speed and low heat generation
2. Adoption of the newly developed grease SE-1
 ⇒High speed and long life
3. Adoption of a specially developed material for the race
 ⇒Improved seizure resistance



Cross-section of an angular contact ball bearing with ultra-high-speed seal

New high-speed specification bearing unit for rolling stocks (New RCT bearing)

The bearing maintenance interval is lengthened more than twice



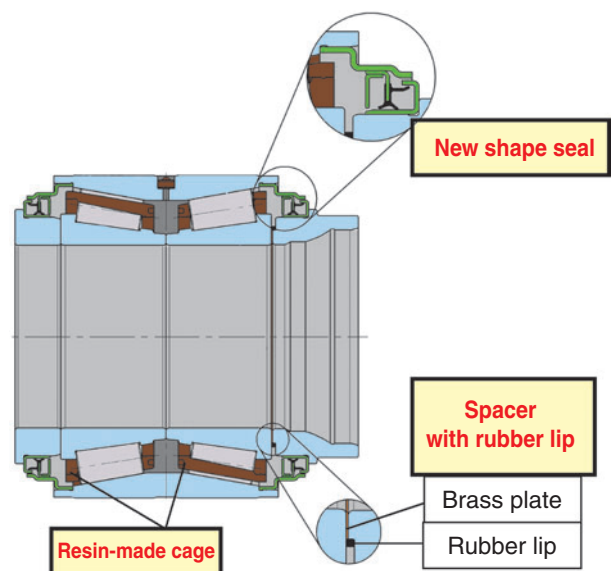
Features

- (1) **Special-resin-made cage**
Longer lubrication life as a result of the adoption of a special, anti-shock resin and the suppression of abrasion loss
- (2) **Spacer with rubber lip**
Suppression of fretting between the inner ring and the back cover due to dynamic deflection of a shaft
- (3) **New shape seal**
Longer lubrication life as a result of reduced temperature rise

Applications

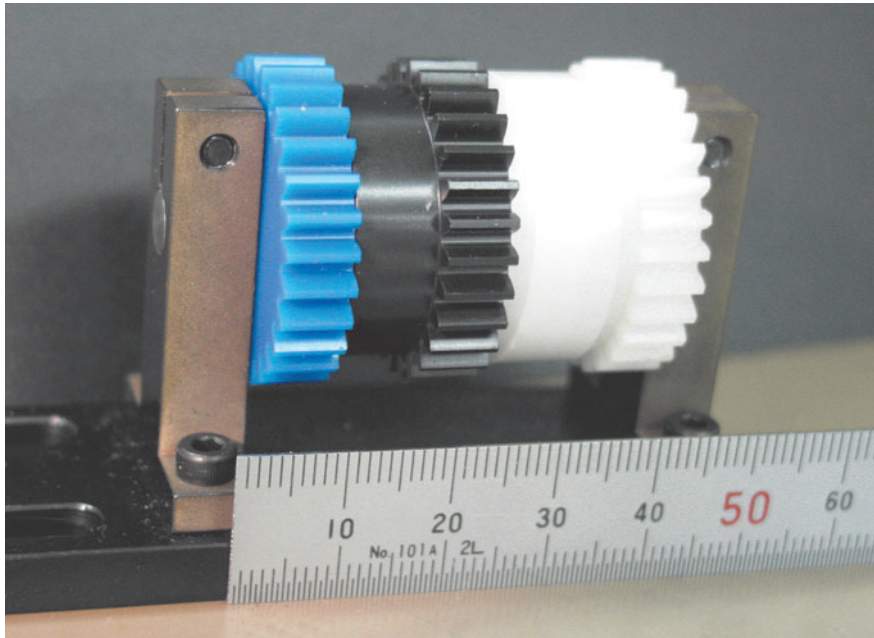
- Shaft support bearings for rolling stock use

Construction



Office equipment paper-reversing unit

Smooth paper feed without a reversing motor in the double-side printing mechanism for printing and copying machines



Features

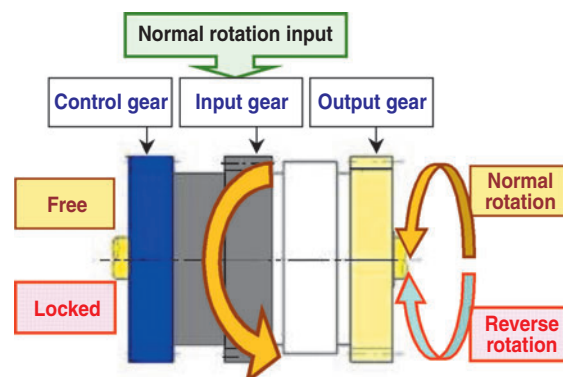
- (1) The output gear can be rotated both clockwise and counterclockwise at the same speed with that of the input gear.
- (2) A dedicated reversing motor is not needed.

Applications

- Paper feed direction switchover mechanisms for copying machines and printers capable of both side printing

Construction

- The unit consists of three gears, namely, an input gear, an output gear, and a control gear, with the input gear always rotating in one (normal) direction.
- When the control gear is not braked (free), both the control and the output gear rotate in the normal direction (the same direction as that of the input gear).
- On the other hand, when the control gear is braked to a halt (locked), the output gear rotates in the direction opposite to that of the input gear.



Color filter automatic repair machine

Automatic repairing of defects in color filters for flat panel displays improves labor efficiency, saving labor



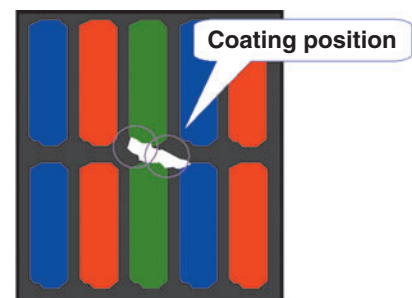
Features

- (1) NTN's unique image processing technology is used to locate a defect, automatically remove (laser-cutting) the defect and coat it according to its type and color.
- (2) Automatic repairing improves labor efficiency, saving labor.

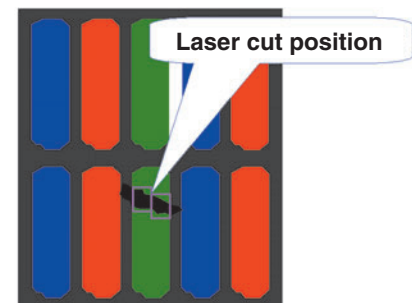
Applications

- Color filter defect repair
(Opaque defects, clear defects, mixed colors)

Defect repair methods



Clear defect repairing
(The circle denotes the result of the automatic coating location calculation.)



Opaque defect repairing
(The square denotes the result of the laser cutting location calculation.)

HEADQUARTERS

NTN CORP. URL <http://www.ntn.co.jp>

Head Office / 3-17, 1-chome, Kyomachibori, Nishi-ku, Osaka 550-0003 Japan
Phone: 81-6-6443-5001 Telex: J63750, NTN CORP. Fax: 81-6-6445-8581
Tokyo Headquarters / TOC Building, 6th Floor, 22-17, 7-chome, Nishi-Gotanda,
Shinagawa-ku, Tokyo 141-0031 Japan Phone: 81-3-5487-2815

NTN USA CORP.

1600 E. Bishop Court, P.O. Box 7604, Mount Prospect, IL 60056-7604, U.S.A.
Phone: +1-847-298-7500 Fax: +1-847-294-1209

SALES NETWORK

NTN BEARING CORP. OF AMERICA

Head Office / 1600 E. Bishop Court, P.O. Box 7604, Mount Prospect, IL 60056-7604,
U.S.A.
Phone: +1-847-298-7500 Fax: +1-847-699-9744
Central Sales Office / 111 West Washington Street Suite 310, East Peoria, IL 61611 U.S.A.
Phone: +1-309-699-8600 Fax: +1-309-699-8670
Eastern Sales Office / 191 Sheree Blvd., Suite 101, Exton, PA 19341, U.S.A.
Phone: +1-610-524-1477 Fax: +1-610-524-1571
South Eastern Sales Office / 5475 Peachtree Industrial Blvd., Norcross, GA 30092,
U.S.A.
Phone: +1-770-448-4710 Fax: +1-770-448-6969
Western Sales Office / 2251 SW Grapevine Parkway, Grapevine, TX 76051, U.S.A.
Phone: +1-817-329-1818 Fax: +1-817-329-4711
Great Lakes Sales Office / 1600 E. Bishop Court, P.O. Box 7604, Mount Prospect,
IL 60056-7604, U.S.A.
Phone: +1-847-699-4060 Fax: +1-847-294-1364
NTN Automotive Center / 39255 W. 12 Mile Road, Farmington Hills, MI 48331-2975,
U.S.A.
Phone: +1-248-324-4700 Fax: +1-248-324-1103

NTN BEARING CORP. OF CANADA LTD.

Head Office / 305 Courtneypark Drive West, Mississauga, Ontario, L5W 1Y2, Canada
Phone: +1-905-564-2700 Fax: +1-905-564-7749
Vancouver Branch / 201-669 Ridley Place Annacis Island Delta, B.C., V3M 2Y9 Canada
Phone: +1-604-517-1777 Fax: +1-604-517-1794
Edmonton Branch / 4608-97th Street, Edmonton, Alberta T6E 5N9, Canada
Phone: +1-780-435-6200 Fax: +1-780-435-3600
Toronto Branch / 305 Courtneypark Drive West, Mississauga, Ontario L5W 1Y4,
Canada
Phone: +1-905-564-9600 Fax: +1-905-564-9609
Montreal Branch / 4973 Levy Street, Ville, St-Laurent, Quebec, H4R 2N9, Canada
Phone: +1-514-333-8054 Fax: +1-514-333-1078

NTN WÄLZLAGER (EUROPA) G.m.b.H.

Head Office / Nordrhein-Westfalen Branch /
Max-Planck-Strasse 23, 40699 Erkrath, F.R. Germany
Phone: +49-211-2508-0 Fax: +49-211-2508400
Stuttgart Branch / Schurwaldstrasse 13, 73765 Neuhausen, F.R. Germany
Phone: +49-7158-17040 Fax: +49-7158-170460
München Branch / Geretsrieder Strasse 10A, 81379 München, F.R. Germany
Phone: +49-89-7488630 Fax: +49-89-786382
Hamburg Branch / Barkhausweg 7, 22339 Hamburg, F.R. Germany
Phone: +49-40-536962-0 Fax: +49-40-53696215
Italy Branch / Via Maestri del Lavoro, 3/A, 40138 Bologna, Italy
Phone: +39-051-535174 Fax: +39-051-538492

NTN BEARINGS (UK) LTD.

Wellington Crescent, Fradley Park, Lichfield, Staffordshire, WS13 8RZ, U.K.
Phone: +44-1543-445000 Fax: +44-1543-445035

NTN FRANCE S.A.

Head Office / Z.I. Sablière BP 338 Schweighouse Sur Moder 67507 Haguenau Cedex, France
Phone: +33-3-88-53-22-22 Fax: +33-3-88-73-46-95
Lyon Branch / Parc Technologique 2 Pace Berthe Morisot 69792 Saint-Priest
cedex, France
Phone: +33-4-72-04-0044 Fax: +33-4-72-04-4456
Paris Branch / Boulevard De Beaubourg B.P. 27 Emerainviller, 77313 Marne-la-
vallee Cedex 2, France
Phone: +33-1-64-80-4747 Fax: +33-1-64-80-4778

NTN BEARING-SINGAPORE (PTE) LTD.

Head Office / No.9 Clementi Loop Singapore 129812
Phone: +65-64698066 Fax: +65-64695400
Philippine Representative Office / Unit 1002 Philippine Axa Life Centre Condominium
Corporation
Sen. Gil Puyat Ave Corner Tindalo Street Makati City, Philippines
Phone: +63-2-759-4407 Fax: +63-2-759-4409
India Representative Office / 805, International Trade Tower, Nehru Place, New Delhi
110019, India
Phone: +91-11-51513234 Fax: +91-11-51513236

NTN CHINA LTD.

Head Office / Rm. 1914-1915, Park-in Commercial Centre, 56, Dundas Street,
Mongkok, Kowloon, Hong Kong
Phone: 852-2385-5097 Fax: +852-2385-2138
Guangzhou Liaison Office / Room 7306, CITIC Plaza, No.233 Tian He North Road,
Guangzhou, China. 510613
Phone: +86-20-8626-6766 Fax: +86-20-8626-6630
Shanghai Liaison Office / Unit 2212, Shanghai Maxdo Centre, 8 Xing Yi Road,
Changning District Shanghai, 200336, China
Phone: +86-21-5208-1006 Fax: +86-21-5208-1016
Beijing Representative Office / Unit 08, EF Floor, East Tower, Twins Tower, B12
Jianguom enwai Da Jie, Chaoyang Dist., Beijing 100022, China
Phone: +86-10-6568-3069 Fax: +86-10-6568-2278

NTN BEARING-THAILAND CO., LTD.

Head Office / 12th Floor, Panjathani Tower, 127/15 Nonsee Road, Chongnonsee
Yannawa, Bangkok 10120, Thailand
Phone: +66-2-681-0401 Fax: +66-2-681-0408
Khon Kaen Branch / 189-191 Ruen Rom Road Tambon Nai-Muang, Amphur
Muang, Kohn Kaen, 40000, Thailand
Phone: +66-43-223679 Fax: +66-43-223061
Haad Yai Branch / 198-198/1 Nipat U-Thid 2 Road, Amphur Haad Yai, Songkhla,
90110, Thailand
Phone: +66-74-236568 Fax: +66-74-231520
Bangna Sales Office / 35/35 Bangna-Trad Road, KM11 Bangplee, Samutprakarn,
10540, Thailand
Phone: +66-2-7501732 Fax: +66-2-7501731
Chiangmai Sales Office / 94. 94/1 Chayapoom Road, Tumbolsripoom, Amphur
Muang, Chiang Mai 50200, Thailand
Phone: +66-53-874328 Fax: +66-53-874330

NTN BEARING-MALAYSIA SDN. BHD.

Head Office / No.2, Jalan Arkitek U 1/22, Hicom Glenmarie Industrial
Park, 40150 Shah Alam, Selangor, Malaysia
Phone: +60-3-55696088 Fax: +60-3-55690200
Butterworth Branch / 4700, Jalan Permatang Pauh, 13400 Butterworth, Malaysia
Phone: +60-4-3328312 Fax: +60-4-3324407
Ipoh Branch Office / 65, Medan Kidd, Kinta Mansion, 30200 Ipoh, Malaysia
Phone: +60-5-2547743 Fax: +60-5-2538077
Kuantan Branch / B-72, Ground Floor, Jalan Beserah 25300 Kuantan, Malaysia
Phone: +60-9-5141132 Fax: +60-9-5141164
Johor Bahru Branch / 51 Jalan, Sri Bahagia 5, Taman Sri Bahagia, Tampoi, 81200
Johor Bahru, Malaysia
Phone: +60-7-2364929 Fax: +60-7-2370897

NTN-CBC (AUSTRALIA) PTY. LTD.

3, The Crescent, Kingsgrove, NSW 2008, LOCKED BAG 1800, Kingsgrove 1480.
NSW Australia
Phone: +61-2-9502-1833 Fax: +62-2-9502-4013

NTN DE MEXICO, S.A.

Guadalajara Office / Calle 22 No.2465, Esq. Calle 3, Zona Industrial, C.P. 44940
Guadalajara, Jalisco, México
Phone: +52-33-3145-1490 Fax: +52-33-3145-1594
México Office / Calle Emilio Cardenas No.158, Fracc.Industrial San Nicolas
C.P.54030 Tlalnepantla, Estado De Mexico
Phone: +52-55-5565-5562 Fax: +52-55-5565-8638

NTN SUDAMERICANA, S.A.

World Trade Center Panama
Calle 53 Este, Urbanización Marbella Piso NO.16, Oficina 1601
Apartado Postal 832-0487, Panamá, Rep.de Panamá
Phone: +507-269-4777 Fax: +507-264-5592

NTN DO BRASIL LTDA.

Av. Moema, 94-9 Andar-conj. 92a94 CEP 04077-020-Indianópolis-São Paulo-SP,
-Brasil
Phone: +55-11-5051-0600 Fax: +55-11-5051-2807

NTN KOREA CO., LTD.

Head Office / 10th Floor, Press Center, 25, Taepyeong-Ro 1-GA, Jung-Gu, Seoul
100-745, Korea
Phone: +82-2-720-3665 Fax: +82-2-720-3669
Pusan Branch / Rm.707, 7th Floor, Daerim Bldg., 341-5 Bjeon 1-Dong, Busanjin-
Gu, Busan, Korea, 614-843
Phone: +82-51-811-1351 Fax: +82-51-811-1353

NOTE : The appearance and specifications may be changed without prior notice
if required to improve performance. Although care has been taken to
assure the accuracy of the data compiled in this catalog, NTN does not
assume any liability to any company or person for errors or omissions.

NTN TECHNICAL REVIEW No.75

Printed and published in October 31, 2008

Editor **Kenji OKADA**

Publisher **Keiji OOHASHI**

Published by NTN Corporation
3-17, 1-chome, kyomachibori, Nishi-ku, Osaka, J apan

Printed by
NISSHA Co., Ltd

**No part of this publication may be reprinted or reproduced
without the prior permission of the copyright owner.**